

**Optical Measurement of
Nitric Oxide and Hydroxyl Radicals Distributions
in Combusting Diesel Sprays**

ROMAIN DEMORY

COPYRIGHT

Attention is drawn to the fact that copyright of this thesis rests with its author. This copy of the thesis has been supplied on condition that anyone who consults it is understood to recognise that its copyright rests with its author and that no quotation from the thesis and no information derived from it may be published without the prior written consent of the author.

This thesis may be made available for consultation within the University Library and may be photocopied or lent to other libraries for the purposes of consultation.

ABSTRACT

The development and combusting behaviour of a diesel spray were investigated to provide a deeper understanding of the formation of nitric oxide (NO) in diesel engines.

To characterise the spray, the nozzle flow was measured by the rate tube technique. The sensitivity of the flow to injection pressure was shown to follow the theoretical behaviour. Penetrations of the liquid spray were measured by means of high speed video imaging. The innovative measurements of the liquid penetration during the combustion allowed combustion phases and liquid jet lengths to be associated.

Hydroxyl (OH) radicals were acquired by planar laser-induced fluorescence (PLIF). Combined with high speed videos of the flame natural luminosity, they were used to identify precisely the evolution of combustion in time and space. The measured OH distributions compared favourably with results from simulations using the KIVA code. The OH radicals were shown to be present mainly in the mixing controlled phase, distributed in a thin layer around the vapour fuel in the jet, within the diffusion flame location. OH radicals could be seen as early as 0.4 ms before the pre-mixed heat-release spike and until the end of apparent heat release. In the conditions studied, the diffusion flame, therefore, spanned most of the combustion process, starting very soon after auto-ignition.

Finally distributions of NO were acquired by LIF and compared with the evolution of combustion. NO was found to appear 0.5 to 1 ms after the development of the diffusion flame, on the lean side of the flame front, outside the region with a high density of OH radicals but also later on, downstream the spray, on the outskirts of the zone with high soot density. The formation rate of NO was found almost constant during the mixing-controlled combustion, with a small increase at the end of injection, when the flame collapsed on the fuel spray. The observed increase was linked to a rapid cooling of the flame plume and the associated freezing of the thermal-NO mechanism. Varying injection pressures did not significantly affect the overall formation rate although peak NO densities were seen to gradually move downstream the flame plume with increased injection pressure. NO formation increased with the in-cylinder pressure in accordance with a higher density of air and higher local temperatures.

CONTENTS

COPYRIGHT	II
ABSTRACT	III
CONTENTS.....	IV
LIST OF TABLES	VIII
LIST OF FIGURES	IX
LIST OF FIGURES	IX
ACKNOWLEDGEMENTS.....	XIV
DECLARATION.....	XV
NOMENCLATURE.....	XVI
1. INTRODUCTION	1
1.1. BACKGROUND ON DI DIESEL COMBUSTION PROCESSES	2
1.2. DIESEL ENGINE POLLUTION	8
1.3. OUTLINE	9
2. POLLUTANTS FORMATION.....	11
2.1. OH FORMATION	11
2.2. NITRIC OXIDE FORMATION	16
2.3. OBJECTIVES	24
3. DIAGNOSTIC TECHNIQUES FOR MOLECULAR CONCENTRATIONS	27
3.1. PHYSICAL PROBING	27
3.1.1. <i>Cylinder dumping method</i>	29
3.1.2. <i>In-cylinder sampling method</i>	30
3.2. OPTICAL DIAGNOSTICS.....	30
3.2.1. <i>Background information</i>	31
3.2.1.1. Atomic electronic structure.....	31
3.2.1.2. Molecular spectroscopy	32
3.2.2. <i>Laser diagnostics techniques for the measurement of species densities</i>	39
3.2.2.1. Laser-induced fluorescence (LIF).....	39
3.2.2.2. Raman scattering	40
3.2.2.3. Coherent anti-Stokes Raman spectroscopy (CARS)	41
3.2.2.4. Degenerate four-wave-mixing (DFWM)	43
3.2.2.5. Conclusion	44
3.2.3. <i>Laser-Induced fluorescence (LIF)</i>	44
3.2.3.1. From molecular spectra to LIF	44
3.2.3.2. Deactivation pathways	46

3.3.	LASER-INDUCED FLUORESCENCE OF HYDROXYL RADICALS AND NITRIC OXIDE	49
3.3.1.	<i>Fluorescence signal evaluation</i>	49
3.3.1.1.	Fluorescence yield	49
3.3.1.2.	Boltzmann fraction	51
3.3.1.3.	Overlap integral	52
3.3.2.	<i>Experimental setup</i>	58
3.3.2.1.	Excitation sources	58
3.3.2.2.	Optics	61
3.3.2.3.	Optical engine	62
3.3.2.4.	Collection system	63
3.3.3.	<i>Excitation/collection schemes for OH-LIF</i>	64
3.3.3.1.	The $A^2\Sigma^+-X^2\Pi$ (0,0) excitation band scheme	64
3.3.3.2.	The $A^2\Sigma^+-X^2\Pi$ (3,0) excitation band scheme	64
3.3.3.3.	The $A^2\Sigma^+-X^2\Pi$ (1,0) excitation band scheme	65
3.3.3.4.	Conclusion	65
3.3.4.	<i>Excitation/collection schemes for NO-LIF</i>	68
3.3.4.1.	The $D^2\Sigma^+-X^2\Pi$ (0,1) excitation band scheme	68
3.3.4.2.	The $A^2\Sigma^+-X^2\Pi$ (0,2) excitation band scheme	70
3.3.4.3.	The $A^2\Sigma^+-X^2\Pi$ (0,0) excitation band scheme	71
3.3.4.4.	Conclusion	72
4.	APPARATUS AND SETUP	75
4.1.	HIGH-PRESSURE SPRAY RIG	75
4.2.	FUEL INJECTION EQUIPMENT	79
4.3.	LASERS	82
4.3.1.	<i>Description</i>	82
4.3.2.	<i>Calibration</i>	83
4.3.3.	<i>Synchronization</i>	85
4.4.	OPTICS	87
4.5.	COLLECTION SYSTEM	88
4.5.1.	<i>Description</i>	88
4.5.2.	<i>Exposure time</i>	89
4.6.	LIF EXPERIMENTAL SETUP	90
4.7.	FUEL	92
4.8.	CORRECTION PROCEDURE FOR THE RAW LIF DISTRIBUTIONS	97
4.8.1.	<i>Potential sources of error</i>	100
4.8.2.	<i>Distribution analysis of the on-line signal</i>	100
5.	COMBUSTING DIESEL SPRAY CHARACTERISATION	105
5.1.	SPRAY AND FLAME DEVELOPMENT	105
5.1.1.	<i>Nozzle flow calculation</i>	105
5.1.2.	<i>Nozzle flow measurements</i>	106

5.1.3.	<i>Spray penetration</i>	111
5.1.4.	<i>Flame development</i>	114
5.1.5.	<i>Cycle analysis</i>	119
5.1.5.1.	Heat release rate.....	119
5.1.5.2.	Vaporisation.....	121
5.1.6.	<i>Conclusions</i>	123
5.2.	LIF SIGNAL PROCESSING	124
5.2.1.	<i>Calculation of the volume of the flame</i>	125
5.2.2.	<i>Calculation of the temperature</i>	125
5.2.3.	<i>Calculation of the molar fractions</i>	127
5.2.4.	<i>Mixing</i>	128
5.2.5.	<i>Limitations</i>	128
5.2.6.	<i>Results and discussion</i>	129
6.	LASER INDUCED FLUORESCENCE OF HYDROXYL RADICALS	134
6.1.	EXCITATION.....	134
6.2.	COLLECTION	135
6.3.	CALIBRATION OF OH-LIF WITH A CANDLE LIGHT.....	135
6.4.	RESULTS AND DISCUSSION	138
6.4.1.	<i>Effect of injection pressure</i>	144
6.4.2.	<i>Effect of in-cylinder pressure</i>	146
6.5.	CONCLUSIONS.....	150
7.	LASER-INDUCED FLUORESCENCE OF NITRIC OXIDE	151
7.1.	EXCITATION.....	151
7.2.	COLLECTION	153
7.3.	CALIBRATION OF NO-LIF WITH A SPECTROMETER	155
7.4.	RESULTS AND DISCUSSION	157
7.4.1.	<i>Exhaust gas analysis</i>	157
7.4.2.	<i>In-cylinder nitric oxide distributions</i>	160
7.4.2.1.	Effect of injection pressure.....	164
7.4.2.2.	Effect of in-cylinder pressure.....	167
7.5.	CONCLUSIONS.....	171
8.	CONCLUSIONS	172
8.1.	FUTURE WORK	178
	REFERENCES.....	179
	PAPERS PUBLISHED BY THE AUTHOR.....	190
	JOURNALS	190
	CONFERENCES.....	190

APPENDIX A	191
HEAT RELEASE RATE	191
APPENDIX B	193
EMISSION STANDARDS	193
APPENDIX C	201
RAW OH DISTRIBUTIONS.....	201

LIST OF TABLES

Table 1 – Rate constants for NO formation / destruction.....	21
Table 2 – Nomenclature of l , L , Λ	36
Table 3 – Laser diagnostics techniques for species measurement (adapted from Eckbreth (1996))	39
Table 4 – Excited states lifetimes.....	45
Table 5 – Collisional cross sections of OH $A^2\Sigma^+(v'=1)$ and NO $A^2\Sigma^+(v'=0)$ (Battles and Hanson, 1995, Paul et al., 1994).....	50
Table 6 – Signal strengths of different OH-LIF schemes (Ketterle et al., 1992).....	66
Table 7 – Summary of OH-LIF publications (diesel-like conditions are highlighted by a white background).....	67
Table 8 – Four lowest states of NO (Daily, 1997)	68
Table 9 – Oscillator’s strength for the <i>NO</i> molecule (Legris and Domingues, 2004)	69
Table 10 – Absorption of the laser beam 13°c.a. after ignition in a gasoline engine for an equivalence ratio of 1.0 (Schulz et al., 1997)	72
Table 11 – Summary of NO-LIF publications (diesel-like conditions are highlighted by a white background).....	74
Table 12 – Rapid compression machine operating conditions	76
Table 13 – Engine control and reading parameters	78
Table 14 – Nozzle library.....	79
Table 15 – Photochemical stabilities of dyes (Brackmann, 2000)	83
Table 16 – Best laser-engine synchronizations	87
Table 17 –Camera specifications	89
Table 18 – Fuel characteristics (some data adapted from Pickett & Siebers (2003)).....	94
Table 19 – Frequency distributions of the on-peak signal.....	101
Table 20 – Summary of published fuel choices and respective justifications	104
Table 21 – Heat of vaporisation and specific heat of some hydrocarbons of interest (Heywood, 1988) .	121
Table 22 – Heat release rate decomposition for two injection pressures (30 mm ³ of GE80 injected at 60/160 MPa in an in-cylinder pressure and temperature of 5 MPa and 680 K).....	126
Table 23 – Hardware and settings used for OH-PLIF.....	134
Table 24 – Lasing Performance of the Coumarin 153 (left) and Rhodamine 590 (right) (Brackmann, 2000).....	136
Table 25 – Hardware and settings used for NO-PLIF.....	151
Table 26 – Exhaust gas analysis data	158
Table 27 – EU emission standards for passenger cars [g.km ⁻¹].....	193
Table 28 – Summary of the parameters for the ECE and EUDC cycles	195
Table 29 – Japanese emission standards for diesel passenger cars [g/km].....	196
Table 30 – EPA Tier 1 emission standards for passenger cars [g/miles]	198
Table 31 – EPA Tier 2 emission standards [g/miles]	199
Table 32 – Summary of the parameters for the FTP-75 cycle.....	200

LIST OF FIGURES

Figure 1 – Idealised diesel and otto diagrams for a 4-stroke engine	1
Figure 2 – Typical rate of heat release diagram	6
Figure 3 – Two-dimensional schematic of diesel combustion (adapted from Dec (1997) and Flynn <i>et al.</i> (1999))	7
Figure 4 – Schematic view of the flame front from the top of the spray	14
Figure 5 – OH detection timing in diffusion flames	15
Figure 6 – Effect of reduction in oxygen concentration by different diluents (exhaust gas, CO ₂ , N ₂) on NO _x emissions in DI diesel. Bore = 140 mm, stroke = 152 mm, r _c =14.3, speed = 1300 rev/min, fuel rate = 142 mm ³ /stroke, injection timing at 4° BTC	23
Figure 7 – Schematic representation of a chemiluminescence analyser (adapted from Ferguson & Kirkpatrick (2001))	29
Figure 8 – Harmonic oscillator model	34
Figure 9 – Rigid rotor model	35
Figure 10 – The vibrational progression of the band formed during electronic absorption from the ground (v''=0) state to a higher state (adapted from Banwell and McCash (1994))	37
Figure 11 – <i>P</i> , <i>Q</i> and <i>R</i> branches	38
Figure 12 – LIF experimental setup (adapted from Hanson <i>et al.</i> (1990) and Taylor (1993a))	40
Figure 13 – Raman scattering experimental setup (adapted from Taylor (1993a) and Eckbreth (1996)) ..	41
Figure 14 – CARS experimental setup (adapted from Taylor (1993a))	42
Figure 15 – DFWM experimental setup (adapted from Eckbreth (1996))	43
Figure 16 – Deactivation pathways for an excited molecule (adapted from the Jablonski diagram)	47
Figure 17 – Resonant, Stokes shifted and anti-Stokes shifted fluorescence for an excitation of NO at 236 nm. Adapted from (Bessler <i>et al.</i> , 2003b)	48
Figure 18 – Vibrational population distribution of NO X ² Π with temperature (Luque and Crosley, 1999)	52
Figure 19 – Collisional broadening and shift for OH at 283 nm (left) and NO at 226 nm (right). Simulated conditions are from the top: 0.1, 0.5, 1 and 2 MPa. All spectra simulated at 700 K, shift is too small to be apparent (e.g. 0.01 nm at 2 MPa for NO) (Luque and Crosley, 1999)	54
Figure 20 – Decrease in the overlap integral with line broadening	56
Figure 21 – NO overlap integral between two Gaussian lineshapes (top), and between a Gaussian laser lineshape and a simulated absorption lineshape (bottom)	57
Figure 22 – General laser-induced fluorescence experimental set-up	58
Figure 23 – A typical arrangement for dye lasers (adapted from Hecht (1986))	59
Figure 24 – Laser dyes range (from Brackmann (2000))	60
Figure 25 – Parametric oscillator (adapted from Hecht (1992))	61
Figure 26 – Measured transmittances for fused-silica, sapphire and BK 7 (spectrograph study of 20 mm thick windows)	62
Figure 27 – Design of the optical chamber	75

Figure 28 – Glass holder design (Crua, 2002).....	77
Figure 29 – Fouling of fused-silica windows.....	77
Figure 30 – Rate tube comparison of multi- and single-hole nozzles. The area under the curve is proportional to the quantity of fuel injected. Above: corresponding rail pressure drops.....	80
Figure 31 – Nozzle types.....	81
Figure 32 – Injection current pulse from the custom made FIE controller.....	82
Figure 33 – Measurement error.....	84
Figure 34 – Dye laser spectrum acquired with narrowband sweeps of a spectrometer for the dye laser set at 3 different wavelengths: 225.5, 226.0 and 226.5 nm.....	85
Figure 35 – Synchronization laser-engine.....	86
Figure 36 – Sheet forming optics.....	88
Figure 37 – Comparison between Rayleigh scattering (non-filtered) and fluorescence (filtered) signal timings. Signals collected during the NO-LIF investigation on the CCD chip at different times after the original trigger for a 20 ns opening of the intensifier.	90
Figure 38 –LIF experimental setup.....	91
Figure 39 – White diesel fuel (top) and GE80 (bottom) absorption and fluorescence spectra (absorption of GE80 below 300 nm is unavailable because of the interference of hexane absorption).....	95
Figure 40 – Fuel fluorescence.....	96
Figure 41 – Sum of the standard deviation over the images for different number of captures on-line (top) and off-line (bottom) (30 mm ³ of GE80 injected at 100 MPa in an in-cylinder pressure and temperature of 5 MPa and 700 K).....	98
Figure 42 – OH- and NO-LIF signal to noise ratio (30 mm ³ of GE80 injected at 100 MPa in an in-cylinder pressure and temperature of 5 MPa and 700 K).....	99
Figure 43 – Standard deviation of the spatially averaged on-peak distributions (top: NO, bottom: OH).....	103
Figure 44 – Rate tube measurements for different injection pressures (30 mm ³ injected volume in an in-cylinder pressure and temperature of 5 MPa and 680 K, averaged over 100 cycles).....	108
Figure 45 – Onset of injection – the hesitation visible on the single-hole nozzle (top row), is not seen on the multi-hole nozzle (bottom row) (injection of 30 mm ³ of fuel at 160 MPa in an in-cylinder pressure and temperature of 6 MPa and 700 K– the images where taken at regular intervals between 0.42 and 0.65 ms aSOI).....	109
Figure 46 – Working principle of a common-rail injector (adapted from (Dietsche et al., 2005)).....	109
Figure 47 – Evolution of the rail pressure and flow rate at needle lift (30 mm ³ injected volume in an in-cylinder pressure and temperature of 5 MPa and 680 K, averaged over 100 cycles, injection pressures are 160, 140 MPa on first row and 100, 60 MPa on second row).....	110
Figure 48 – High-speed video imaging of spray development.....	111
Figure 49 – Liquid fuel penetration evolution with time and injection pressure (60, 100 and 160 MPa from top to bottom – 30 mm ³ of GE80 injected in an in-cylinder pressure and temperature of 5 MPa and 680K, single cycle).....	113
Figure 50 – Evolution of the spectral radiance of a black-body with temperature.....	115

Figure 51 – High speed videos of the spray and flame development (30 mm ³ of GE80 injected at 160 MPa in an in-cylinder pressure and temperature of 5 MPa and 700K). The bright regions at the top of the images are due to liquid scattering of the side illumination whereas the bottom bright regions are due to natural luminescence of flame.	117
Figure 52 – High speed videos of spray and flame development at three injection pressures (30 mm ³ of GE80 in an in-cylinder pressure and temperature of 5 MPa and 720 K). The bright regions at the top of the images are due to liquid scattering of the side illumination whereas the bottom bright regions are due to natural luminescence of flame.	118
Figure 53 – Computed heat release rate and average in-cylinder temperature (30 mm ³ of GE80 at 160 MPa in a in-cylinder pressure and temperature of 5 MPa and 680 K).....	120
Figure 54 – Evaluation of the evaporated mass (30 mm ³ of GE80 injected at 160 MPa in an in-cylinder pressure and temperature of 5 MPa and 680 K).....	122
Figure 55 – Evaporation and heat release rates (30 mm ³ of GE80 injected at 160 MPa in an in-cylinder pressure and temperature of 5 MPa and 680 K).....	123
Figure 56 – Computed chamber (green 1/100), pre-mixed flame (blue) and diffusion flame (red) volumes (30 mm ³ of GE80 injected at 160 MPa in an in-cylinder pressure and temperature of 5 MPa and 680 K).....	125
Figure 57 – Heat release decomposition (30 mm ³ of GE80 at 60 MPa (top) / 160 MPa (bottom) in an in-cylinder pressure and temperature of 5 MPa and 680 K).....	127
Figure 58 – Individual frames of flame high speed video, 1.9 ms aSOI (left) and 2.4 ms aSOI (right), the frames were included into a background representing the complete chamber volume (160 MPa IP, 5 MPa motored ICP, 30 mm ³).....	128
Figure 59 – Example of computed temperature (top row, colour coding in K), CO ₂ molar fractions (middle row) and H ₂ O molar fractions (30 mm ³ of GE80 injected at 100 MPa in an in-cylinder pressure and temperature of 5 MPa and 700 K). The figures on the vertical and horizontal axes correspond respectively to the distance from the nozzle and the centre axis of the chamber in mm.	130
Figure 60 – Maximum (left) and average (right) computed temperatures (30 mm ³ of GE80 injected at 100 MPa in an in-cylinder pressure and temperature of 5 MPa and 700 K).....	131
Figure 61 – Population effects on the LIF signal with time for 3 injection pressures (30 mm ³ of GE80 injected in an in-cylinder pressure and temperature of 5 MPa and 700 K).....	132
Figure 62 – Fluorescence yield effects on the OH- and NO- LIF signal with time for 3 injection pressures (30 mm ³ of GE80 injected in an in-cylinder pressure and temperature of 5 MPa and 700 K).....	133
Figure 63 – Filters for OH-LIF	135
Figure 64 – Experimental candle flame and simulation spectra of OH.....	137
Figure 65 – Negative of OH-LIF on a candle with Coumarin 153 (left) and Rhodamine 590 (right).....	138
Figure 66 – Reference image of	138
Figure 67 – Normalised colour and black & white maps used in distributions.....	139
Figure 68 – Raw OH-LIF on-line distributions and spray and flame (30 mm ³ of GE80 injected at 100 MPa in an in-cylinder pressure and temperature of 5 MPa and 630 K)	140

Figure 69 – Comparison of the measured OH distributions with the natural flame luminosity. The top row shows OH distributions from the KIVA 3 simulation by Dr Abdelghaffar (private communication)	141
Figure 70 – Spatially averaged luminosity and OH signal compared to the heat release rate	142
Figure 71 – Vertical intensity profile of OH distributions, 3 ms aSOI (30 mm ³ of GE80 injected in an in-cylinder pressure and temperature of 5 MPa and 700K)	144
Figure 72 – Evolution of OH radicals distribution with time for four injection pressures. The white arrows indicate the liquid fuel penetration, as observed from high-speed videos (no data for 140 MPa) ..	145
Figure 73 – Horizontal intensity profile of OH distributions, 3 ms aSOI (30 mm ³ of GE80 injected in an in-cylinder pressure and temperature of 5 MPa and 700K)	146
Figure 74 - In-cylinder pressure scaling of OH levels (30 mm ³ of GE80 injected at 160 MPa in an in-cylinder temperature of 700 K).....	147
Figure 75 – Evolution of OH radicals distribution with time for three motored in-cylinder pressure (30 mm ³ of GE80 injected at 160 MPa in an in-cylinder temperature of 700 K, 670 K for 6 MPa)	148
Figure 76 – Vertical intensity profile of OH distributions, 3 ms aSOI (30 mm ³ of GE80 injected at 160 MPa in an in-cylinder temperature of 700 K (670 K for 6 MPa))	149
Figure 77 – Horizontal intensity profile of OH distributions, 3 ms aSOI (30 mm ³ of GE80 injected at 160 MPa in an in-cylinder temperature of 700 K (670 K for 6 MPa))	149
Figure 78 – Experimental absorption spectrum against NO (Luque and Crosley, 1999) and O ₂ (Bessler et al., 2003b) simulated spectra	152
Figure 79 – Filters for NO-LIF	154
Figure 80 – Set of reflective filters in front of UV lens, intensifier and camera	155
Figure 81 –Rotational structures of the OH (top) and NO (bottom) transitions at 283 nm ($A^2\Sigma^+ - X^2\Pi(1,0)$) and 226 nm ($A^2\Sigma^+ - X^2\Pi(0,0)$) at 0.1 MPa/300 K (Luque and Crosley, 1999).....	156
Figure 82 – Simulated (top) and measured (bottom) NO vibrational spectra (Luque and Crosley, 1999).....	157
Figure 83 – NO _x emission trends with oxygen level in air	159
Figure 84 – Heat release rates for different injection pressures (injection of 30 mm ³ of GE80 in an in-cylinder pressure and temperature of 5 MPa and 700K)	160
Figure 85 – Evolution of NO distributions with flame development (the white arrows represent the liquid fuel penetration).....	161
Figure 86 – Superimposition of non-simultaneous distributions of OH (white edges) and NO. The colour bar on the right of each picture represents the flame luminosity vertical profile.....	163
Figure 87 – Superimpositions of non-simultaneous distributions of OH (white edges) and NO for different injection pressures. The colour bar on the right of each picture represents the flame luminosity vertical profile (no data for 140 MPa)	165
Figure 88 – Evolution of the average intensity (top) and attenuation coefficient (bottom) with time	166
Figure 89 – Superimpositions of non-simultaneous distributions of OH (white edges) and NO for different in-cylinder pressures	168

Figure 90 – Heat release rates for different in-cylinder pressures (injection of 30 mm ³ of GE80 at 160 MPa in an in-cylinder temperature of 700K).....	169
Figure 91 – In-cylinder pressure scaling of NO levels (30 mm ³ of GE80 injected at 160 MPa in an in-cylinder temperature of 700 K).....	170
Figure 92 – Spatially averaged luminosity, OH and NO signal compared to the heat release rate	172
Figure 93 – Combustion process model	177
Figure 94 – ECE 15 cycle	194
Figure 95 – EUDC Cycle	195
Figure 96 – 10-15 mode cycle.....	197
Figure 97 – FTP-75 cycle.....	200
Figure 98 – Raw OH on-line distributions – 1.75 ms aSOI, initial development of the diffusion flame (injection of 30 mm ³ of GE80 at 100 MPa in an in-cylinder pressure and temperature of 5 MPa and 700 K).....	202
Figure 99 – Raw OH on-line distributions – 2 ms aSOI, initial development of the diffusion flame (injection of 30 mm ³ of GE80 at 100 MPa in an in-cylinder pressure and temperature of 5 MPa and 700 K).....	203
Figure 100 – Raw OH on-line distributions – 2.5 ms aSOI, static diffusion flame (injection of 30 mm ³ of GE80 at 100 MPa in an in-cylinder pressure and temperature of 5 MPa and 700 K).....	204
Figure 101 – Raw OH on-line distributions – 3.5 ms aSOI, flame collapse (injection of 30 mm ³ of GE80 at 100 MPa in an in-cylinder pressure and temperature of 5 MPa and 700 K).....	205
Figure 102 – Raw OH on-line distributions – 4.5 ms aSOI, flame collapse (injection of 30 mm ³ of GE80 at 100 MPa in an in-cylinder pressure and temperature of 5 MPa and 700 K).....	206
Figure 103 – Raw OH on-line distributions – 5 ms aSOI, flame collapse (injection of 30 mm ³ of GE80 at 100 MPa in an in-cylinder pressure and temperature of 5 MPa and 700 K).....	207

ACKNOWLEDGEMENTS

First of all, I would like to acknowledge with many thanks my supervisors, Dr. Cyril Crua and Professor Morgan Heikal for their assistance and support.

I wish to express my deepest gratitude to the mechanical and electrical technicians of the School of Engineering William Whitney, David Stansbury, Ken Maris, Tony Brown and Brian Maggs.

I want to thank Kourosh Karimi, Benoit Oger, Thomas Fischer, Dr. Walid Abdelghaffar and Dr. Eric Domingues who helped in gathering some data for this project and all the members of the Internal Combustion Group for their useful suggestions and comments.

I cannot fail to acknowledge the financial and technical support of Ricardo UK Plc. and Delphi Diesel Systems. Special thanks are due to Dr. Martin Gold.

DECLARATION

I declare that the research contained in this thesis, unless otherwise formally indicated within the text, is the original work of the author. The thesis has not been previously submitted to this or any other university for a degree, and does not incorporate any material already submitted for a degree.

Romain Demory

NOMENCLATURE

Roman symbols

A.....	Constant dependent on the fuel [-]
	First excited electronic state
A_{ji}	Einstein coefficient for a spontaneous emission from state j to state i [-]
B.....	Second excited electronic state
c.....	Speed of light in vacuum: 3.108 m.s^{-1}
c_p, c_v	Specific heats at constant pressure and constant volume [$\text{J.kg}^{-1}.\text{K}^{-1}$]
C.....	Third excited electronic state
D.....	Fourth excited electronic state
E.....	Energy [J]
EA.....	Apparent activation energy [J]
$F_v(J)$	Rotational Energy [J]
G.....	Dynode gain [A.s.photon^{-1}]
$G(v)$	Vibrational energy [J]
h.....	Planck's constant : $6.626.10^{-34} \text{ J.s}$
i.....	Current intensity [A]
J.....	Total angular momentum quantum number [-]
	Rotational state [-]
k_{i+}, k_{i-}	Rate constants [$\text{cm}^3.\text{mol}^{-1}.\text{s}^{-1}$]
l.....	Azimuthal or orbital quantum number [-]
L.....	Resultant orbital angular momentum quantum number [-]
n.....	Constant dependent on the fuel [-]
	Number of moles [-]
	Principal quantum number [-]
N_i	Population of state i [m^{-3}]
\dot{N}_p	Photon arrival rate [photo.s^{-1}]
m.....	Mass [kg]
	Magnetic quantum number [-]
P.....	Pressure [Pa]
	Branch for transitions from a rotational level to the next lower corresponding level
Q.....	Heat [J]

Branch transitions from a rotational level to the corresponding level

R Universal Gas constant [$\text{Pa}\cdot\text{m}^3\cdot\text{kg}^{-1}\cdot\text{K}^{-1}$]

Branch for transitions from a rotational level to the next upper corresponding level

r_v Compression ratio [-]

s Spin quantum number [-]

S Resultant spin quantum number [-]

t Time [s]

T Temperature [K]

U Internal energy

v Vibrational state [-]

V Volume [m^3]

Potential energy [J]

X Ground electronic state

Greek symbols

α Load Ratio [-]

γ Ratio of specific heats $\frac{c_p}{c_v}$ [-]

ε Efficiency of the collection optics [-]

η Quantum efficiency of the photocathode [-]

η_i Thermodynamic efficiency [-]

λ Wavelength [nm]

Quantum number for the axial component of the orbital momentum [-]

Λ Total axial electronic angular quantum number [-]

v Wave number [cm^{-1}]

π Number Pi [-]

Σ Total spin quantum number resultant [-]

τ_{id} Ignition Delay [ms]

Φ Fuel-Air Equivalence Ratio [-]

$\Phi(v)$ Normalized line shape function [-]

$\Phi F(v)$ Fluorescence radiant power [W]

ψ Wave Amplitude [m]

Ω Quantum number for the total axial momentum [-]

ΩC Solid angle of the collection optics [sr]

ω_iFrequency [Hz]

Subscripts

e.....Electronic
F.....Fluorescence
id.....Ignition delay
n.....Neat
Otto.....Otto engine type
p.....Photon
Diesel.....Diesel engine type
r.....Rotational
tot.....Total
v.....Vibrational

Acronyms

AFR.....Air Fuel Ratio
aSOI.....After Start Of Injection trigger
aTDC.....After Top Dead Centre
a.u.....Arbitrary Units
BBO.....Beta Barium Borate
BK7.....Borosilicate crown optical glass
bSOI.....Before Start Of Injection trigger
bTDC.....Before Top Dead Centre
c.a.....Crank Angle
CARS.....Coherent Anti-Stokes Raman Spectroscopy
CCD.....Charge Coupled Device
CFD.....Computational Fluid Dynamics
CMOS.....Complementary Metal Oxide Semiconductor
CN.....Cetane Number
DFWM.....Degenerate Four-Wave Mixing
DPF.....Diesel Particulate Filter
EET.....Electronic Energy Transfer
EGR.....Exhaust Gas Recirculation

EHN	2-ethylhexyl nitrate
FIE.....	Fuel Injection Equipment
FTIR	Fourier Transform InfraRed
FWHM	Full Width at Half Maximum
HCCI.....	Homogeneous Charge Compression Ignition
HMN	Heptamethylnonane
ICCD	Intensified Charge Coupled Device
ICP	In-Cylinder Pressure
KL	Optical Thickness
LIF.....	Laser-Induced Fluorescence
LII.....	Laser-Induced Incandescence
LIS.....	Laser-Induced Scattering
Nd:YAG	Neodymium Yttrium-Aluminium Gasket
NO _x	Nitrogen Oxides
PAHs	Polycyclic Aromatic Hydrocarbons: phenanthrene, fluorenes, naphthalenes, pyrenes and fluoranthrenes
ppm.....	Parts Per Million
RCM.....	Rapid Compression Machine
RET	Rotational Energy Transfer
TDC.....	Top Dead Centre
TPGME	Tripropylene Glycol Monomethyl Ether
UV	Ultra-Violet
VCO	Valve Covering Orifice
VET.....	Vibrational Energy Transfer

1. INTRODUCTION

In 1893, Rudolf Diesel published a book entitled “Theory and Construction of a Rational Heat Engine to Take Place of the Steam Engine and of all Presently Known Combustion Engines”. In this book, he sets the basic principles of what is known nowadays as the diesel engine.

All internal combustion engines aim at converting, in the most efficient manner, the thermal energy of a air/fuel mixture into a mechanical work. The conversion process efficiency can be evaluated through the study of the thermodynamic cycle followed by the fluid. Diesel’s initial programme was to build an engine capable of realizing the ideal Carnot cycle. This imaginary engine would have an efficiency far above those of existing engines and especially far above the efficiency of the otto – or petrol – engine, previously demonstrated by Nikolaus August Otto (1867). Diesel quickly realised that it was unfortunately technically impossible to follow the Carnot Cycle. Nevertheless he presented in 1897 an engine that follows the cycle presented in Figure 1.

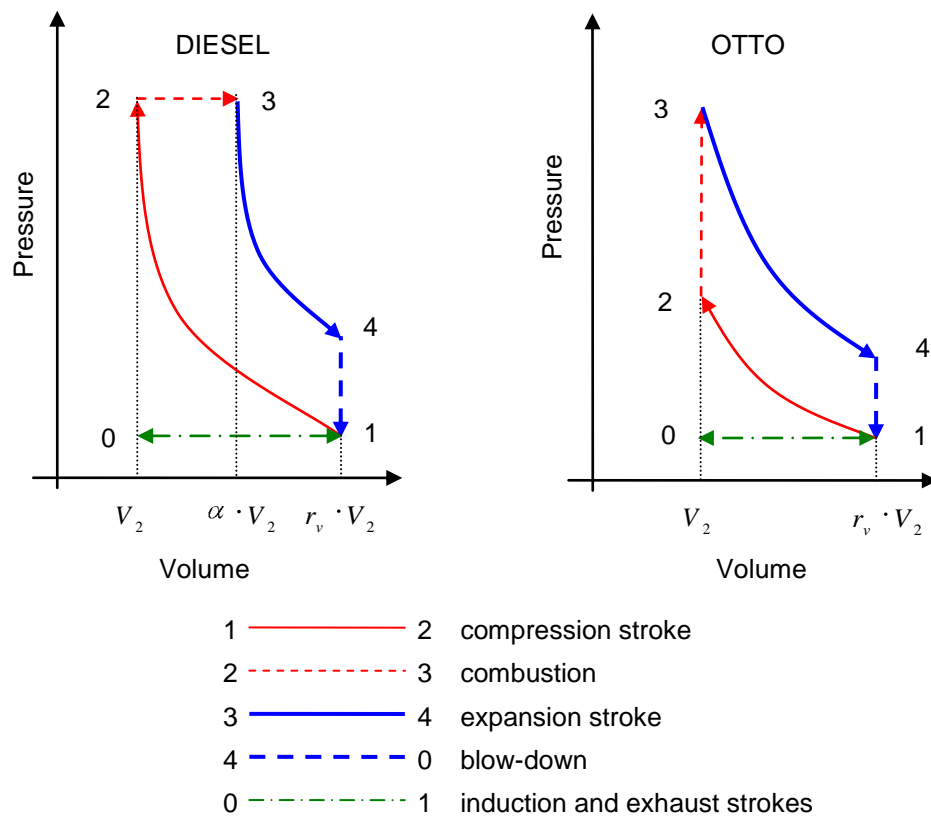


Figure 1 – Idealised diesel and otto diagrams for a 4-stroke engine

From these cycles, an overall efficiency can be computed. They stand as follow for the otto and the diesel engines:

$$\eta_{Otto} = 1 - \frac{1}{r_v^{\gamma-1}} \quad (1)$$

$$\eta_{Diesel} = 1 - \frac{1}{r_v^{\gamma-1}} \cdot \left[\frac{\alpha^\gamma - 1}{\gamma \cdot \alpha - 1} \right] \quad (2)$$

r_v , α and γ are respectively called the compression ratio and the load ratio and the ratio of specific heat capacity. They depend on the engine geometry, operating conditions and gas properties. Within the range of these parameters the term in bracket in the diesel efficiency remains greater than unity. This means that for the same compression ratio, diesel efficiency is lower than otto efficiency. Diesel apparently did not reach his initial goal of following a more efficient thermodynamic cycle. However, if one looks at the effective thermodynamic cycle followed by these engines, things look a lot better for Diesel's engine. Its working principle makes the use of high compression ratios (r_v) possible. A quick analysis of the equations (1) and (2) indicates that this corresponds to an efficiency advantage over otto engines.

Despite this efficiency advantage, diesel engines have long been restricted to heavy transportation applications. This is mainly due to the technical requirements associated with the diesel cycle:

- i. Combustion is obtained through autoignition of the air-fuel mixture. This is only achievable for high pressures, implying a very robust and heavy architecture.
- ii. The fuel is injected just before maximum pressure is reached and has very little or no time to mix with the air. The poor performances of injection systems have traditionally made high power density diesel engines unfeasible.

Recently, the joint use of downsizing and high pulverisation injection systems has allowed diesel engines to match gasoline engine performances in passenger cars. With similar driveability, lower consumption and, in most countries, a favourably taxed fuel, the diesel penetration of the passenger car western European market in 2003 increased to 44% (Hayden and Cooper, 2004).

1.1. Background on DI diesel combustion processes

First in the diesel combustion sequence is the injection of fuel toward the end of the compression stroke in a small volume of high-pressure, high-temperature gases. The performance of the injection system is crucial as the nature of the combustion process is

mainly determined by the quality of the fuel spray and its distribution and mixing within the combustion chamber (Crua, 2002, Kohse-Höinghaus and Jeffries, 2002). The best systems aim to allow fuel to reach most of the combustion chamber. The fuel-air equivalence ratio (Φ) is a measure of the relative amount of fuel and air. If the ratio is locally too high, the air-fuel mixture is said to be rich. The fuel-air mixing process during combustion produces soot particles in the highly rich regions of each fuel spray. (Sher, 1998). A good distribution of the fuel in the chamber volume is therefore sought to decrease emissions and/or to increase the amount of fuel for optimum combustion hence increasing the power output. For this reason fuel injectors always have multi-hole nozzles, resulting in separate sprays. Similarly, high injection pressures and small nozzle orifices are used in order to disperse the fuel as widely as possible in the air (Stone, 1999).

The processes described hereafter take place in each fuel spray in a closely comparable though not necessarily identical manner. Each fuel spray consists of a cold, liquid core surrounded by a mixture that contains fuel droplets and vaporised fuel. In order to burn, the fuel must first be in a vapour state. This process – called vaporisation – is enhanced if the liquid fuel is already scattered in small droplets. Consequently, a second important criterion for injection systems is their pulverisation (or atomisation) capacity.

When the temperature and pressure are high enough, autoignition of the fuel occurs in the regions where the fuel-air equivalence ratio is appropriate. An indication of the mixture strength limits suitable for autoignition can be assessed through the study of flammability limits (Sazhina et al., 1999). The theoretical flammability limits of diesel fuel are of 0.6 and 5.5% fuel by volume (Heywood, 1988). This corresponds to a range of fuel-air equivalence ratio of 0.3 - 3.5. From photographic studies, Rife & Heywood (1974) state that autoignition occurs at an equivalence ratio close to or leaner than stoichiometric ($\Phi \leq 1$) in the air-fuel mixture at the edge of the spray. On the other hand, laser-based diagnostics allowed Dec (1997) to claim that the pre-mixed burn flame occurs in fuel-rich regions ($\Phi > 1$). It is observed that at this time the vapour has barely penetrated beyond the liquid, so the first natural emission of light must be coming from the sides of the jet. The equivalence ratio of these regions is found to be between 2 and 4, which is at the upper limit of the flammability range.

The delay between the onset of injection and autoignition is called the *ignition delay*. It consists of the physical and the chemical delays. The former depends on the processes such as atomisation, vaporisation and mixing of the fuel vapour with air. The latter is

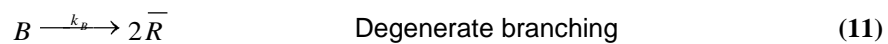
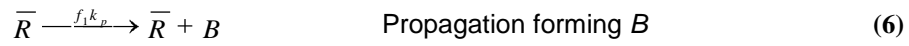
dependent on the precombustion reactions (Heywood, 1988). For a given engine and fuel, the chemical delay is mainly dependent on the gas temperature and pressure and a simple estimation is given by the Arrhenius type equation:

$$\tau_{cd} = A \cdot p^{-n} \cdot \exp \frac{E_A}{R \cdot T} \quad (3)$$

Where τ_{cd} is the chemical delay, E_A the apparent activation energy, R the universal gas constant and A, n are constants dependent on the fuel and the engine.

Although equation (3) is very useful for practical applications, it does not take into account some important phenomena such as cool flames. They have been observed in rapid compression machine experiments (Minetti et al., 1995, Mohamed, 1998) and they play an important role in the autoignition process and modes of combustion such as HCCI.

The autoignition of air/fuel mixtures can be modelled by a detailed kinetic mechanism as a sequence of elementary chemical reactions. In the case of diesel fuel however, the number of intermediate species and possible reactions is very large and becomes prohibitive in terms of computer efficiency. Halstead *et al.* (1977) have published a simplified model that regroups all possible species under a limited number of generic species and reactions. The sequence of reactions considered is:



Where R, B and Q are generic species, RH is an alkane fuel C_nH_{2m} where $m = n+1$, k_p, k_t and k_B are the kinetic rate coefficients augmented by the factors f_1, f_3 and f_4 . The associated mathematical model results in a system of coupled ordinary differential equations describing the concentrations of the chemical species that influence heat

release in the autoignition process, and the system temperature. It should be observed that the differential equation for fuel concentration was presented by Halstead *et al.* (1977) in an algebraic form (equation (16)).

$$\frac{1}{V} \frac{dn_R}{dt} = 2 \cdot k_q \cdot RH - O_2 \pm k_B \cdot B - k_t \cdot \bar{R}^2 - f_3 \cdot k_p \cdot \bar{R} \quad (12)$$

$$\frac{1}{V} \frac{dn_B}{dt} = f_1 \cdot k_p \cdot \bar{R} \pm f_2 \cdot k_p \cdot Q - \bar{R} - k_B \cdot B \quad (13)$$

$$\frac{1}{V} \frac{dn_Q}{dt} = f_4 \cdot k_p \cdot \bar{R} - f_2 \cdot k_p \cdot Q - \bar{R} \quad (14)$$

$$\frac{1}{V} \frac{dn_{O_2}}{dt} = -p \cdot k_p \cdot \bar{R} \quad (15)$$

$$n_{RH} = \frac{n_{O_2} \cdot h_{O_2, \tau=0}}{p \cdot m} + h_{RH, \tau=0} \quad (16)$$

The next equation is the energy balance equation which yields the rate of temperature rise:

$$\frac{dT}{dt} = \frac{1}{C_v \cdot n_{tot}} \cdot (Q_K - Q_L - W_P) \quad (17)$$

Where $[M]$ and n_M correspond to the concentration and number of moles of the various species M , p and q are respectively the number of moles of oxygen consumed and the exothermicity per cycle, Q_K is the chemical heat release term, Q_L is the heat loss term and W_P is the work term due to the piston motion. Although this model should not be expected to be genuinely predictive, it is able to correctly represent trends as observed in experimental investigations (Sazhina *et al.*, 1999).

The flame spreads rapidly along the premixed portions of air-fuel charge that had enough time to evaporate and mix during the ignition delay. The most common way to analyse the rate of energy released by the fuel is to compute the so-called heat release rate. The rate of net heat release under assumptions specified in Appendix A can be written as:

$$\frac{dQ_n}{dt} = \frac{\gamma}{\gamma - 1} \cdot P \cdot \frac{dV}{dt} + \frac{1}{\gamma - 1} \cdot V \cdot \frac{dP}{dt} \quad (18)$$

Where γ is the ratio of heat capacities $\frac{c_p}{c_v}$.

During the ignition delay, the fuel temperature in Diesel spray increases to that of the surrounding hot gas. This will cause onset of endothermic pyrolysis reactions and cracking of the fuel resulting in a short period of negative heat release. After the onset of autoignition the pre-mixed flame takes on and the heat release rises sharply (see Figure 2). The jet continues to grow and penetrate across the chamber through the remainder of the pre-mixed burn.

Once most of the premixed fuel has been burned, the heat release rate drops. From then on, combustion is controlled by turbulent mixing of fuel and air at the outskirts of the spray. In most cases, only part of the fuel has been injected by then and freshly injected fuel will evaporate and mix within the pre-mixed combustion products. This is the source of a specific diesel combustion process called the *diffusion flame*. Unlike the pre-mixed flame, this flame is not spreading in the chamber burning the air-fuel mixture on its way. The diffusion flame is a fairly static sheath surrounding the periphery of the spray. The fuel – or decomposed fuel – is diffusing out of the spray, mixing with the outside air and burning.

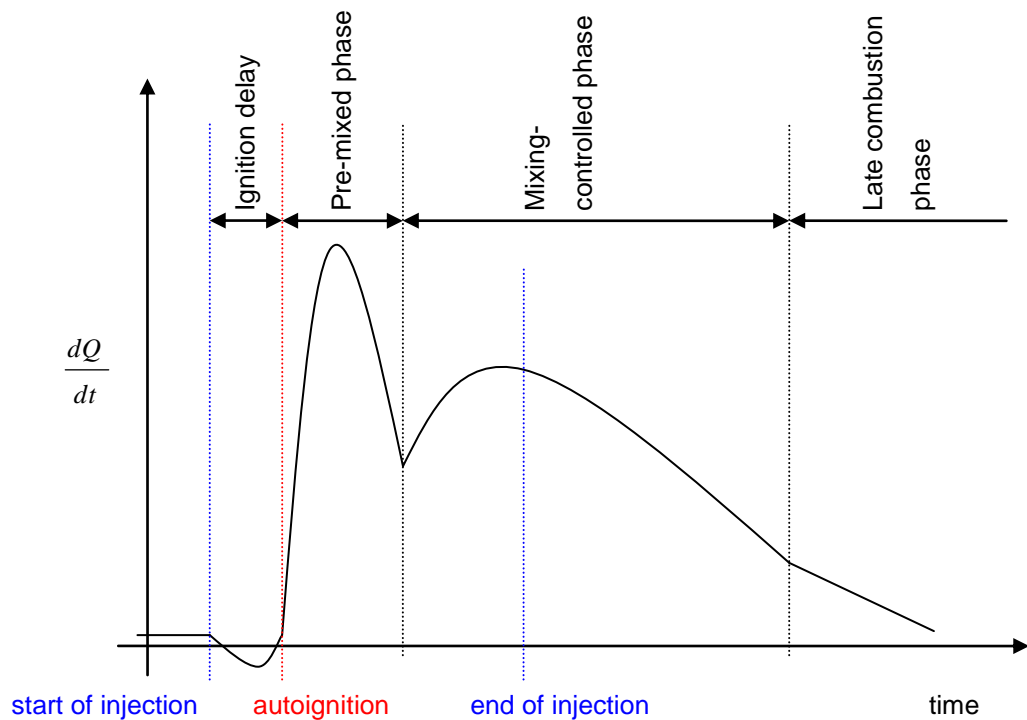


Figure 2 – Typical rate of heat release diagram

There can be small amounts of oxygen in the spray plume. Considering the equivalence ratio of the premix burn, this oxygen is more likely to be a result of the turbulent mixing

than leftovers of the pre-mixed flame. The plume is very fuel-rich though and only partial combustion of the fuel vapour is possible. During this longer *mixing-controlled phase*, the heat release rises to a second, lower peak and then decreases gradually. In fact, the burning rate is controlled by the rate at which the mixture becomes available for burning. The mixture becomes available after the processes of atomisation, vaporisation, mixing of the fuel vapour with the air and pre-flame chemical reactions. Heywood (1988) has reported the mixing of fuel vapour with air as the controlling process (the one with the largest characteristic time). Figure 3 presents the typical geometry of diesel combusting sprays.

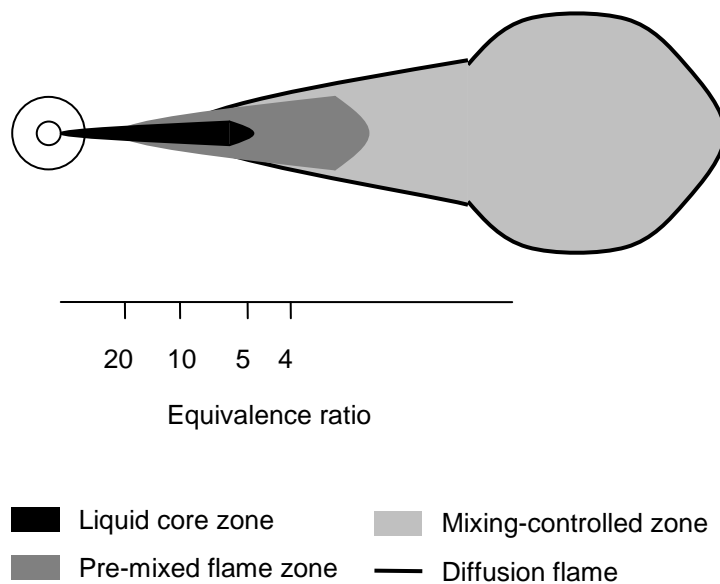


Figure 3 – Two-dimensional schematic of diesel combustion (adapted from Dec (1997) and Flynn *et al.* (1999))

Researchers usually identify another phase of combustion: the *late combustion phase*. Although the combustion process is still a mixing-controlled type, this phase is characterised by a lower rate of heat release. The injection has stopped at this time and this phase lasts well into the expansion stroke. The fuel or the incomplete combustion products – which together can account for approximately 20% of the total fuel energy (Stoffels, 1999) – burn at a slower rate as the temperature of the cylinder gases falls during expansion.

The complex combustion process described here can unfortunately lead to the formation of pollutants. The next paragraph introduces some of the issues associated with engine pollution and the actual status on legislation and clean engine technology.

1.2. Diesel engine pollution

Pollution from internal combustion engines was first studied in the 1950's, in an attempt to explain the apparition of smoggy skies over big cities. Photochemical smog episodes are widespread phenomena in urban regions worldwide where increased levels of nonmethane hydrocarbons (NMHC) and nitrogen oxides (NO_x) may be found from various anthropogenic sources (Rappenglück et al., 2000). Meteorological influences such as sunny and warm weather conditions, along with stagnant wind patterns, favour the formation of secondary pollutants, that is, ozone (O₃) and peroxyacetyl nitrate (PAN) through effective photochemical consumption of NMHC and NO_x. Exhaust gases have since proved to be a key player in several polluting processes resulting in:

- i. Expansion of acid rain, destruction of the ozone layer and global warming.
- ii. Apparition of “smog” and ozone over big cities.
- iii. Potential headaches, breathing difficulties, asthma, memory or learning disorders and lung cancer on a small geographical scale (Solomon and Balmes, 2003).

The main pollutants from internal combustion engines have been classified in 4 categories:

- i. Carbon monoxide (CO)
- ii. Hydrocarbons (HC)
- iii. Nitrogen oxides (NO_x)
- iv. Particulates (PM)

In 1970, the US congress adopted the Clean Air Act, giving the Environment Protection Agency (EPA) responsibility for regulating motor vehicle pollution. European Union regulations for new light duty vehicles were originally specified in the directive 70/220/EEC and were amended a number of time since. A similar agency sets vehicle emission limits in Japan.

Each regulation contains emission limits and testing cycles, the details of the regulations for Europe, USA and Japan can be seen in Appendix B. As can be seen from the emission standards, gasoline and diesel engines do not have to comply with the same limits. Due to different combustion processes, the two engine types have different emission rates. While extensive use of catalytic after treatment is a possible answer to comply with emission limits for gasoline engines, the lean combustion of diesel engines and their high emission rates of particulates set a major challenge.

Because the diesel combustion is lean, oxygen can still be found in exhaust gases. This oxidising medium boosts the efficiency of catalytic after-treatment on compounds like carbon monoxide and hydrocarbons. However, nitrogen oxides can hardly be reduced in this medium. A number of advanced technologies have been proposed to achieve an effective post-treatment of nitrogen oxides (selective catalytic reduction, NO_x absorbers...), but these are expensive and prone to wear and failure.

Similarly, the diesel specific mixing-controlled combustion results in the production of soot, which grows into particulate matter by absorbing organic compounds. These particulate matters cannot be easily oxidised by catalytic after treatment. Diesel particulate filters (DPF) need to be installed in the tailpipe. However they are expensive and tend to decrease fuel economy.

An alternative way of dealing with these pollutants is to act directly on their formation in the engine chamber. By addressing the formation of pollutants, the need for complex and costly after-treatment can be minimised (Cooper et al., 2004). Different technological modifications allow influencing the combustion. These modifications can involve the chamber geometry, the injection system or the intake air content. The aim of this thesis is to pave the way to such modifications by improving our global understanding of diesel combustion.

1.3. Outline

Before the emergence of laser-based diagnostics, the combustion process details could only be assumed (Heywood, 1988, Stone, 1999). Without a complete knowledge of the flame geography, it was difficult to act efficiently on pollution formation. Optical combustion diagnostics is now a mature field of research and a number of techniques have been developed for the investigation of combustion (Taylor, 1993b, Eckbreth,

1996, Kohse-Höinghaus and Jeffries, 2002). Results from laser-based diagnostics have proved some of the former views of the combustion wrong. This is especially true for the location of nitrogen oxides and particulate matter formation sites as well as for the liquid/vapour distribution of the fuel.

Some researchers (Dec, 1997, Stoffels, 1999, Flynn et al., 1999) have already proposed new ideas on the combustion process but have not produced a full concept. A review of the original and new ideas on pollution formation is given in Chapter 2. The project presented here intends to investigate the formation of hydroxyl radical and nitric oxide for a broader set of conditions. In particular, several injection and in-cylinder configurations will be explored. The results will be compared to the published literature. Whereas Chapter 2 reviews the global physical processes believed to be the source of the main diesel pollutants and details the objectives of our investigations, Chapter 3 covers the review of the measurement techniques specific to hydroxyl radical and nitric oxide. The selected techniques were applied with the experimental apparatus presented in Chapter 4. The work undertaken and the results achieved are included in Chapters 5, 6 and 7. Chapter 5 presents the spray and flame visualisation and modelling whereas Chapter 6 and 7 introduce the hydroxyl radicals and nitric oxide investigations respectively. Finally, to come back to the inter-dependent physical processes of Chapter 2, the conclusions drawn from this project are presented in Chapter 8.

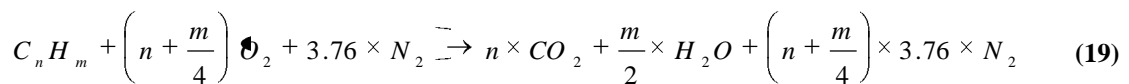
2. POLLUTANTS FORMATION

In this chapter a review of the original and new ideas on pollutants formation and combustion chemistry are presented. In particular, the current knowledge on the chemistry of hydroxyl radicals and nitric oxide formation and destruction is presented.

2.1. OH formation

Intermediate reactions and radicals

Combustion of fuel in an internal combustion engine is often said to follow the reaction:



In fact, this reaction only represents the global balance of the combustion process. There are a number of intermediate elementary reactions involving reactive intermediates. The most abundant species taking part in the pyrolysis or oxidation reactions are H, O and OH (Barlow et al., 1990), but many other radicals (CH, C₂, CN, CH...) can also play a role in the process. All these radicals are suitable for the study of flame development as they can be found at super-equilibrium concentrations in the flame front (e.g. 3 to 5 times the chemical equilibrium concentrations). Their concentration can be linked to the intensity of combustion activity and gradually drops off away from the flame. This gradual drop becomes sharper at higher pressure, leading to very thin zones of super-equilibrium concentrations in the case of high-pressure diesel engines.

Among the many existing radicals, OH combines the following appealing characteristics:

- i. It is present in relatively large concentrations in most flames
- ii. It has been detected in high-pressure flames – i.e. up to 5 MPa (Barlow et al., 1990, Bechtel et al., 1984, Eckbreth, 1996, Dec, 1997, Kohse-Höinghaus, 1994).
- iii. Its spectroscopy is well-known and within the range of standard optical diagnostic devices.

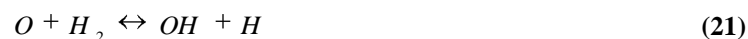
- iv. It is also believed that OH radicals play an important role in soot oxidation (Kosaka et al., 1996, Dec and Coy, 1996) and NO formation (Lavoie et al., 1970)

Because the signal from simple videos or images of the flame is integrated along the line of sight, it is inappropriate for the study of the flame structure. In contrast, two dimensional distributions of OH can effectively be used for this purpose (Meier et al., 2000) and would improve our knowledge of combustion. For these reasons, a large number of investigations on flame kinetics involve preferably the OH radical. Dec & Coy (1996) reported for instance, that although the CH radical can be used to visualise reaction zones, it does not yield a signal as strong as OH and the wavelength and pulse duration needed are difficult to achieve.

OH peak concentration appears on the lean-side of the stoichiometric mixture fraction, where the temperature is at its maximum (Stone, 1999). Hydroxyl radicals are produced via rapid two-body reactions and disappear via slower three-body recombination reactions. The excessive number of intermediate elementary reactions for the combustion of diesel fuel does not allow their complete description to be given. However, the reactions for hydrogen/air combustion give a good introduction to two- and three-body reactions.

OH formation/destruction in a simple case

Two body reactions for hydrogen/air flames radicals (Barlow et al., 1990):



Three-body recombination reactions for hydrogen/air flames radicals (Barlow et al., 1990):





Representative time scales for the two-body reactions have been found to be 150 times shorter than those of the three-body reactions.

Review of published experimental results

Investigations of OH distributions are very common for premixed steady flames and spark ignition engine conditions. In comparison diesel-like conditions or diffusion flame studies are rare. The vast majority of the published research involves laser-based diagnostics. The radical lifetimes are indeed inherently short and present in localised regions. Therefore a very high temporal and spatial resolution is needed and laser techniques are more appropriate than physical probing. In Section 3 a detailed comparison of physical probing and optical diagnostics, and a review of the experimental schemes applied are presented.

In her early global review, Kohse-Höinghaus (1994) reported more than 20 investigations on optical diagnostics of OH radicals of which only few concerned diffusion-type combustion. However, some information can be drawn from other types of combustion. Nygren *et al.* (2001) reported for example that, in their gasoline engine, the flame front was easily identified as the sharp gradient in OH distributions. This was confirmed in a Bunsen flame investigation by Nguyen *et al.* (1996) in which the radial profiles of species concentrations (OH, NO, CH₄, O₂, CO, CO₂, H₂O...) and temperature proved that both OH and NO are in the high temperature flame front. The peak of OH although higher in mole fraction was found narrower than the NO peak.

More interesting are the results of a diffusion flame investigation in a high pressure combustor (Allen *et al.*, 1995). Comparisons of OH distributions at different pressures were given. Increasing the combustor pressure had the following consequences:

- i. A decrease in the thickness of the OH zones.
- ii. A contraction of the spray angle.
- iii. A substantial decrease in the characteristic size of the reaction-zone convolutions.

The two latter conclusions confirm that in-depth combustion knowledge can be learnt from OH-LIF results. Still, the highest pressure investigated remains low (0.95 MPa) and the absorption problems encountered combined with the limitations of the LIF

technique at high pressures (see section 3.2.3.2) are a concern for real diesel-like investigations.

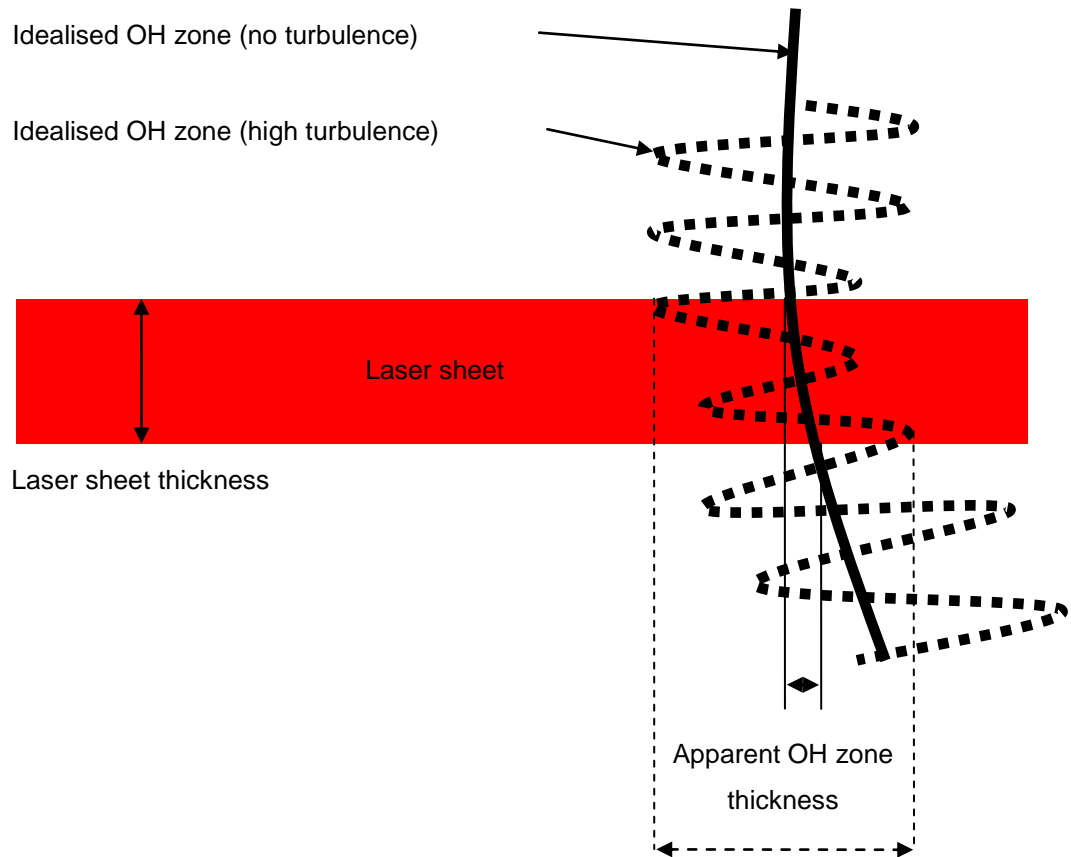


Figure 4 – Schematic view of the flame front from the top of the spray

Recently published studies have proved that these problems could be – at least partially – overcome. Kosaka *et al.* (1996) monitored the correlation between OH and soot distributions in a rapid compression machine at pressures up to 2.9 MPa. Soot appeared later than OH and existed mainly in the central region of the spray. OH surrounded the soot at the periphery of the flame but the two hardly coexisted in a diesel flame. This was later confirmed by Nakagawa *et al.* (1997) who, in his diesel engine experiment, found that OH radicals were only present in a band-like zone outside of the flame luminescence. Dec & Coy (1996) found this band-like zone to be 120 μm thick in low turbulence regions at a pressure of 5 MPa. From the distributions, it appears that the thickness was larger for Kosaka *et al.* who were working at a lower pressure (2.9 MPa). However, Nakagawa’s distributions are fairly thick despite the relative high pressure (5 MPa). This can be linked to the laser sheet thickness (0.5 mm for Nakagawa *et al.*, 0.25 mm for Dec & Coy). In the case of high levels of turbulence, the thickness of the

OH band will be artificially increased by that laser sheet thickness as shown in Figure 4. Hall *et al.* (1997) have demonstrated the importance of OH in the oxidation of soot. They reported that the high soot oxidation observed in their laminar diffusion flame can only be explained by the presence of superequilibrium concentrations of oxidising hydroxyl radicals (McEnally *et al.*, 1998, Smooke *et al.*, 2005). The globally very thin and localised band of OH means that oxidation of soot by hydroxyl radicals, will preferably take place at the outskirts of the central region containing soot. Finally, the use of different sooting fuels confirmed that the qualitative trends on OH distribution do not change drastically with the change of total soot amount in the flame (Kosaka *et al.*, 1996).

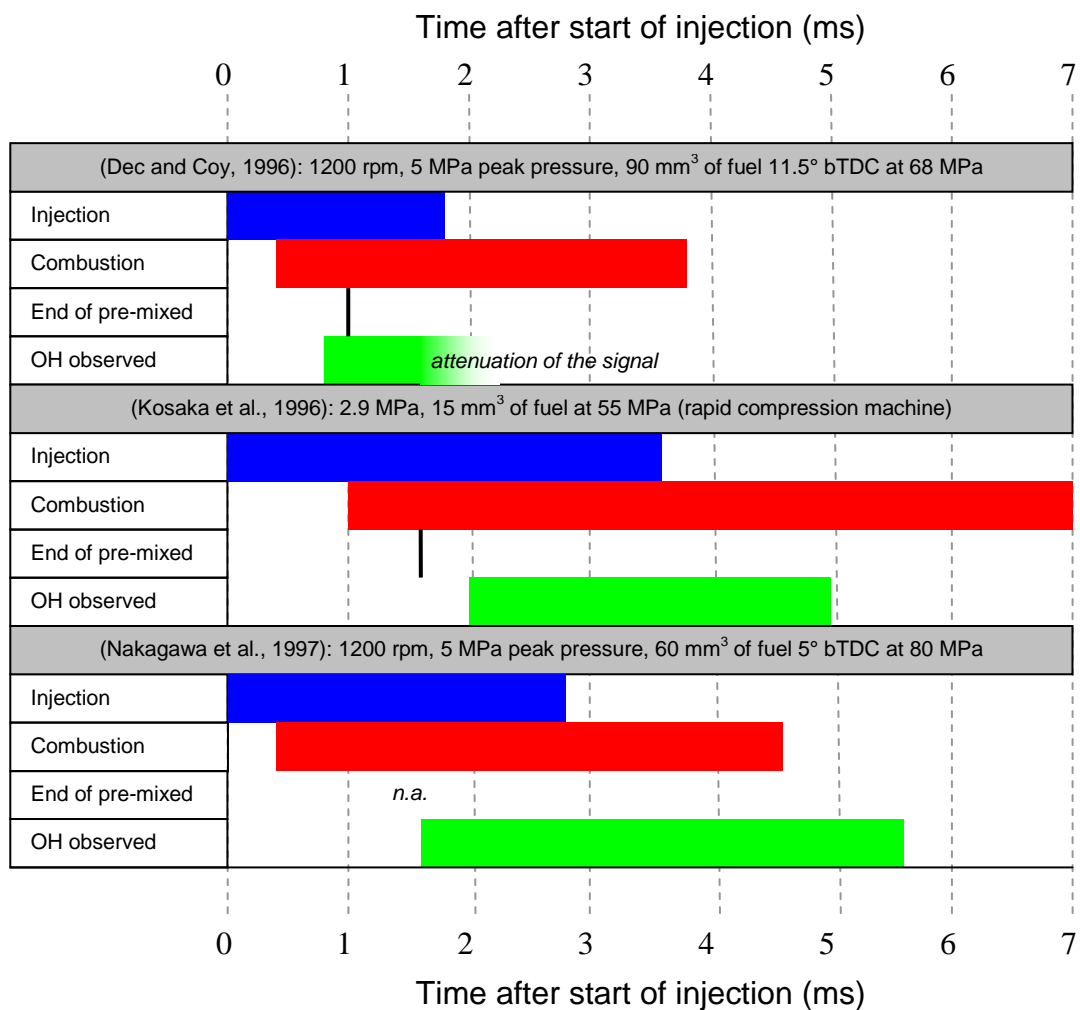


Figure 5 – OH detection timing in diffusion flames

Dec reported that concentrations in the premixed-burn were too low to be detected. This was related to the very high equivalence ratio of this first part of the combustion. OH

appeared 0.8 ms after the start of injection (aSOI) in the diffusion flame and laser attenuation affected the results after 1 ms aSOI. OH was still visible up to 1.5 ms aSOI. Kosaka *et al.* observed OH between 2 ms aSOI (start of the diffusion flame identified by the heat release rate) and 5 ms aSOI (late stage of combustion). Nakagawa *et al.* found that OH appeared shortly after ignition and was present until 5.5 ms aSOI when the luminescence of the flame was no longer observed. Figure 5 is a summary of the different observations. The period while OH is observed depended not only on the actual presence of OH but also on the changing optical conditions in the chamber, hence timings in Figure 5 appear fairly mixed.

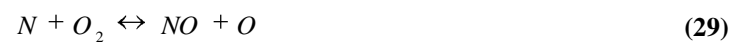
2.2. Nitric Oxide formation

The two main nitrogen oxides (collectively known as NO_x) in diesel exhaust gases are nitric oxide (NO), and nitrogen dioxide (NO₂). Their respective proportion varies with engine load and speed but nitrogen dioxide never accounts for more than 30% of the nitrogen oxides.

Nitric oxide is believed to have three possible origins known as the thermal-NO, the prompt-NO and the fuel-NO mechanisms.

Thermal-NO mechanism

It is also known as the extended Zeldovich mechanism as Zeldovich was the first one to identify equation (28) and (29) as sources of nitrogen oxides (Zeldovich, 1946). The last equation has been found to be contributing significantly (Lavoie *et al.*, 1970):



The rate constants for the reactions are highly dependent on temperature. From this observation and from the equilibrium equations above, it can be presumed that high temperature (hence the name “thermal”) and oxygen concentration are necessary prerequisites for the formation of NO (since nitrogen is always abundant in any possible condition). Thermal NO formation is therefore maximal for local equivalence ratio on the lean side of the stoichiometry (i.e. where high temperatures and presence of oxygen

are combined) or in extremely hot lean post flame gases (above 1800K). From the kinetic rates of Table 1, Bowman (1975) derives the NO rate equation:

$$\frac{d NO}{dt} = \frac{6 \cdot 10^{16}}{T^{1/2}} \exp\left(\frac{-69090}{T}\right) \cdot O_2^{1/2} \cdot N_2 \quad (31)$$

Where $d[NO]/dt$ is the rate of formation of NO [mol/cm³.s], T is the local temperature [K], and $[S]_e$ is the equilibrium concentration of species S [mol/cm³].

Within the steady-state assumption for the N atom and for $[NO]/[NO]_{\text{equilibrium}} \ll 1$, the extended Zeldovich mechanism can be reduced to a single global step (Chen and Kollmann, 1992):



The formation rate then becomes:

$$\frac{d NO}{dt} \approx 3.68 \cdot 10^{14} \exp\left(\frac{-38370}{T}\right) \cdot O \cdot N_2 \cdot W_{NO} \quad (33)$$

Where $d[NO]/dt$ is the rate of formation of NO [g/cm³.s], T is the local temperature [K], [S] is the concentration of species S [mol/cm³] and W_{NO} is the molecular weight of NO [g/mol].

The reactions can be “quenched” before their equilibrium by mixing with colder fresh gases or because of the temperature decrease due to expansion. Likewise, investigators have reported measured NO formation rates significantly larger than predicted by equilibrium reactions (28)-(30) in the combustion zone.

Furthermore, researchers have reported high discrepancies between measured NO formation rates in the combustion zone and rates predicted by equation (31). To account for these variations, the effects of super-equilibrium concentrations of O and OH radicals have been proposed. Nevertheless, Fenimore (1971) argued that the concentrations of radicals required were significantly larger than partial equilibrium values. He suggested that, in the case of fuel-rich mixtures, reactions involving hydrocarbon species played an important role in the NO formation process, a mechanism termed “prompt-NO”.

Prompt-NO mechanism

Whereas thermal-NO is believed to happen in lean regions only, the prompt-NO (or Fenimore) mechanism takes place over the width of the flame. This mechanism is governed by (Bowman, 1975, Stone, 1999):



Further reactions similar to (28)-(30) or involving the cyano compounds (HCN, CN) and oxygenated species lead to NO production. Prompt-NO is not the formation of intermediate species (cyano compounds, nitrogen atoms) in the rich flame, followed by the transport and the subsequent oxidisation of these species in leaner regions. All these reactions take place in the “primary reaction zone” as defined by Fenimore (Fenimore, 1971). Formation rates in the vicinity of the flame can be large but the quantity of NO formed remains usually small compared to the thermal-NO production. Therefore prompt-NO is only significant when combustion temperatures are low enough (<2000K) for thermal-NO to be negligible.

Table 1 summarises the values on the reaction rate constants for the thermal and prompt NO mechanisms. The reader is referred to Hanson & Salimian (1984) and Miller & Bowman (1989) for more in depth surveys of the rate constants in the N/H/O system.

Fuel-NO mechanism

Nitrogen traces as amines and ring compounds (e.g. pyridine, quinoline and carbazoles) can be found in the fuel if the distillation is not of good quality. These compounds can be decomposed to smaller molecules as NH₃, HCN and CN during the temperature increase. NH₃ and HCN react very quickly in lean flames to form NO. In rich conditions, the species undergo a more complicated cycle of reactions that can result in their reduction to N₂.

This mechanism is fuel-dependent and efforts have been put into fuel distillation in order to decrease the nitrogen concentrations. The levels of nitrogen compounds in nowadays' diesel fuel render fuel-NO negligible.

Review of the experimental results published

Although three sources of NO have been identified, thermal-NO appears as the main NO producing mechanism. Different experimental schemes have been designed to characterize and verify the thermal-NO mechanism. A review of the specific

methodologies employed to this purpose is not included in this section which focuses on the results. Nevertheless they are later presented in section 3.

The chronologically first NO measurement techniques to be used were physical probing techniques. For instance, the blow-down technique is a temporally but not spatially precise technique used by Voiculescu & Borman. In 1978, they reported that NO usually accounts for 80% of the engine cylinder NO_x. Increasing loads were characterized by a rise in the NO levels, although loads were only increased up to a global fuel-air equivalence ratio (ϕ) of 0.6 (Voiculescu and Borman, 1978). Aoyagi *et al.* (1980) conducted a similar investigation but employing a sampling technique that gave both temporally and spatially precise measurements of NO. They found that as the local fuel-air equivalence ratio approaches 1, the measured NO levels tend to decrease. Indeed, although the temperature is expected to increase as the mixture approaches stoichiometric conditions, the rarefaction of the oxygen hinders the formation of NO. In both investigations, the level of NO decreased with retarded injection. This can be related to the reduced maximum temperature associated with a shorter ignition delay. Likewise, the bulk of the NO was found to be produced during the early and middle combustion period (first 15 to 25° crank angle of combustion). These results belied the early predictions of Zeldovich (1946) who stated that since the NO formation rate was much slower than the combustion rate, most of the NO would be formed after completion of combustion.

Whereas the blow-down technique gave maximum global levels of NO about 2000 ppm (parts per million) for a conventional injection timing, Aoyagi's sampling valve method gave, for the same conditions, maximum local levels of NO lower than 1000 ppm. This illustrates the difference in absolute levels of emissions between two engine designs. Aoyagi *et al.* found the highest NO concentration at the flame tip which was swept by the air swirl. The levels of exhausted NO are measured as a third or two thirds of the maximum levels.

More recently, techniques employing laser-based diagnostics have made more temporal and spatial precise results available. Despite the practical difficulties to obtain clear, high-signal distributions, formation of nitric oxide was found to last longer than in the previous studies. Alatas *et al.* reported a formation starting early during combustion and practically stopping around 40° c.a. after top dead centre (Alatas et al., 1993). This meant that the pre-mixed phase did not produce the bulk of the NO (Stoffels, 1999).

Some researchers claimed that the pre-mixed phase does not produce any NO since it has an equivalence ratio of 2-4 – i.e. too high for the production of NO (Dec and Canaan, 1998). Furthermore, the maximum local temperature reached by this partial oxidation of fuel is estimated around 1600K (Flynn et al., 1999). Borman & Ragland (1998) noted that the equivalence ratio of the pre-mixed burning was indeed very high for a turbocharged engine because of the shorter ignition delay. In a naturally aspirated engine however, evidence from sampling and radiation measurements lead them to think that the reactants were lean or stoichiometric during the pre-mixed burn. Furthermore, some NO could be produced in a very rich pre-mixed flame via the prompt-NO mechanism. Verbiezen *et al.* (2006) for instance reported a small production of NO inside the jet plume, during the pre-mixed phase.

Nevertheless, the bulk of the NO is still believed to be produced via the thermal-NO mechanism, during the mixing-controlled phase. Thus, in their quantitative investigation, Verbiezen *et al.* (2006) saw an increase in the molar fractions of NO in the jet plume from 450 ppm to 2500 ppm with the appearance of the diffusion flame. In fact, even higher molar fractions of NO were measured slightly outside the jet plume – i.e. on the lean side of the diffusion flame. The diffusion flame, with temperatures well above 2000 K was indeed expected to be a major source of thermal-NO formation. Stoffels *et al.* (1999) also found high number densities of NO slightly outside of the flame luminescence zone, in a thin layer at the tip of the spray – as identified by Aoyagi *et al.* – as well as on the side of it. This however was not always clear in the published distributions. In most cases the nitric oxide number densities appeared fairly homogeneous across the jet plume and no specific pattern appeared as in the OH-LIF case (Dec and Canaan, 1998). The NO number densities tended to increase in the latter period of the combustion process (Nakagawa et al., 1997). As the jet structure disappeared, NO was formed throughout the portion of the combustion chamber where the reacting fuel jet has travelled. Strikingly, this could confirm the early statement of Zeldovich (1946) that nitric oxide is formed after the fuel has completely burned (locally). Dec & Canaan also reported a formation of NO after the end of injection that can amount to one-third of all NO produced. Finally the NO content curve declined towards larger crank angles. This is often associated with the formation of nitrogen dioxide, however Stoffels *et al.* argued that this process only cannot explain the decrease in NO levels.

Table 1 – Rate constants for NO formation / destruction

Reaction	$k_i^+ (cm^3 / mol \cdot s)^*$	$k_i^- (cm^3 / mol \cdot s)^*$	Reference
$O + N_2 \leftrightarrow NO + N$	$7.6 \cdot 10^{13} \cdot \exp \frac{-38.000}{T}$	$1.6 \cdot 10^{13}$	(Bowman, 1975)
	$1.8 \cdot 10^{14} \cdot \exp \frac{-38370}{T}$		(Hanson and Salimian, 1984)
$N + O_2 \leftrightarrow NO + O$	$6.4 \cdot 10^9 \cdot T \cdot \exp \frac{-3150}{T}$	$1.5 \cdot 10^9 \cdot T \cdot \exp \frac{-19.500}{T}$	(Bowman, 1975)
	$1.6 \cdot 10^{10} \cdot T \cdot \exp \frac{-4470}{T}$	$3.8 \cdot 10^9 \cdot T \cdot \exp \frac{-20820}{T}$	(Hanson and Salimian, 1984)
$N + OH \leftrightarrow NO + H$	$4.1 \cdot 10^{13}$	$2.0 \cdot 10^{14} \cdot \exp \frac{-23.650}{T}$	(Bowman, 1975)
	$5.4 \cdot 10^{13} \cdot \exp \frac{-1720}{T}$	$1.7 \cdot 10^{14} \cdot \exp \frac{-24560}{T}$	(Hanson and Salimian, 1984)
$CH + N_2 \leftrightarrow HCN + N$	$4.3 \cdot 10^{12} \cdot \exp \frac{-11060}{T}$		(Warnatz et al., 2001)
$N_2 + O + M \leftrightarrow N_2O + M$	$1 \cdot 10^{14} \cdot \exp \frac{-9100}{T} \dagger$	$8 \cdot 10^{14} \cdot \exp \frac{-29850}{T}$	(Stoffels, 1999)
$N_2O + O \leftrightarrow 2NO$	$4.22 \cdot 10^{13} \cdot \exp \frac{-12077}{T}$		(Lavoie et al., 1970)
	$6.91 \cdot 10^{13} \cdot \exp \frac{-13400}{T}$		(Hanson and Salimian, 1984)
$O + N_2O \leftrightarrow N_2 + O_2$	$3.61 \cdot 10^{13} \cdot \exp \frac{-1207}{T}$		(Lavoie et al., 1970)
	$1 \cdot 10^{14} \cdot \exp \frac{-14100}{T}$		(Hanson and Salimian, 1984)
$H + N_2O \leftrightarrow N_2 + OH$	$3.01 \cdot 10^{13} \cdot \exp \frac{-5435}{T}$		(Lavoie et al., 1970)
	$7.59 \cdot 10^{13} \cdot \exp \frac{-7600}{T}$		(Hanson and Salimian, 1984)
$NO + HO_2 \leftrightarrow NO_2 + OH$	$2.09 \cdot 10^{12} \cdot \exp \frac{-241}{T}$		(Hanson and Salimian, 1984)
$NO_2 + O \leftrightarrow NO + O_2$	$1.0 \cdot 10^{13} \cdot \exp \frac{+300}{T}$		(Hanson and Salimian, 1984)

Nitrous oxide

At low temperatures, the presence of a number of chemical radicals, due to fuel decomposition is the origin of another nitrogen oxide: nitrous oxide (Stone, 1999)



* , k_i^+ , k_i^- defined by: $\frac{d P_i^-}{dt} = \nu_{P_i} \cdot \left(k_i^+ \cdot \prod_{i=1}^n R_i^{\nu_{R_i}} - k_i^- \cdot \prod_{i=1}^m P_i^{\nu_{P_i}} \right)$

Where n it the number of reactants R_i , m it the number of products P_i , ν_{P_i}, ν_{R_i} , respectively the stoichiometric coefficients of product P_i and reactant R_i and P_i^-, R_i^- respectively the concentrations of product P_i and reactant R_i

†, $(cm^6 / mol^2 \cdot s)$

Nitrous oxide can in turn be a source of nitric oxide through the reactions (Merola et al., 2004, Lavoie et al., 1970):



Chen and Kollmann (1992) remarked that this pathway is only important for a high-pressure combustion because the intermediate N_2O is formed by a three-body reaction.

Nitrogen dioxide formation

Although chemical kinetic models suggest that the production of NO_2 is negligible at typical combustion conditions, investigators have reported substantial $\frac{[NO_2]}{[NO]}$ ratios in the flame zone. The origin of this nitrogen dioxide has been linked to significant levels of HO_2 via (Bowman, 1975, Heywood, 1988, Ladommatos et al., 1996, Kohse-Höinghaus, 1994, Dec and Coy, 1996)



A rapid conversion of NO_2 back to NO takes place in the presence of atomic oxygen:



Once again, quenching of the reactions may lead to significant levels of NO_2 in the exhaust gases (up to 20% of the NOx as reported above).

As in most cases, the main source of nitrogen oxides seems to be thermal-NO, temperature, oxygen concentration and combustion duration are the main issues. Therefore, an obvious improvement would be to replace part of the atmospheric oxygen by some inert gas. Using a high specific heat capacity gas would lead to even higher decrease in nitrogen oxides production.

Exhaust gas recirculation

The effect of reduction in oxygen concentration was studied for different gases, Heywood (1988) reported the results presented in Figure 6 for exhaust gas, carbon dioxide and molecular nitrogen:

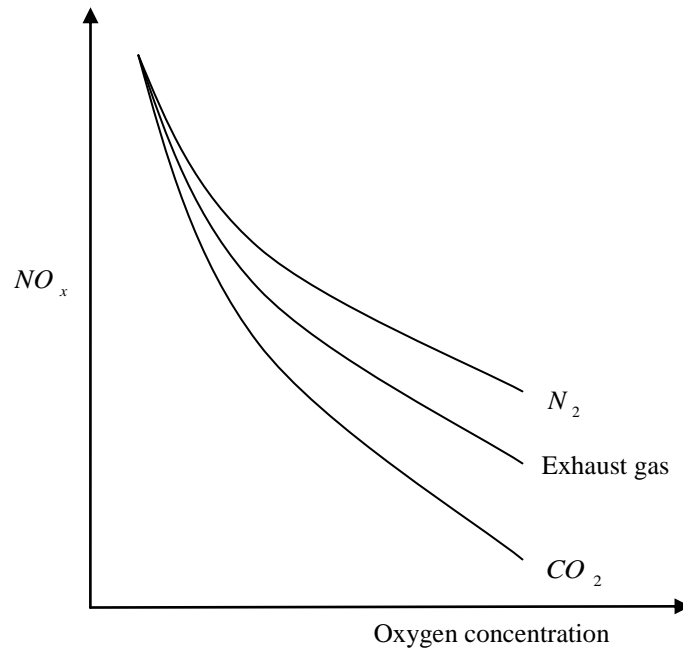


Figure 6 – Effect of reduction in oxygen concentration by different diluents (exhaust gas, CO_2 , N_2) on NO_x emissions in DI diesel. Bore = 140 mm, stroke = 152 mm, $r_c=14.3$, speed = 1300 rev/min, fuel rate = $142 \text{ mm}^3/\text{stroke}$, injection timing at 4° BTC

The only gas readily available in the environment of an internal combustion engine is exhaust gas. Therefore engines have recently been fitted with exhaust gas recirculation (EGR) systems. Using EGR is equivalent to replacing some of the nitrogen and oxygen by carbon dioxide and water vapour. The system works in a feedback loop, the EGR valve position being controlled to fulfil the desired oxygen level.

Reducing oxygen concentration affects the chemical kinetic time τ_{chem} , slowing down the combustion speed. The equilibrium flame temperature is inversely proportional to this characteristic time τ_{chem} . Several justifications have been given to explain the decrease of τ_{chem} . They can be summarised in the following five effects (Ladommatos et al., 1996):

- i. Dilution effect: reduction in oxygen concentration
- ii. Thermal effect: introduction of higher specific heat capacity molecules
- iii. Chemical effect: dissociation of CO_2 and H_2O at high temperature
- iv. Inlet temperature effect: change in inlet temperature
- v. Thermal throttling effect: change in volumetric efficiency

Whereas the first three effects listed above tend to reduce nitrogen oxides production, the last two are unwanted side effects that can be avoided by cooling the recirculated gases. It has been found (Ladommatos *et al.*, 1996) that the prevailing decreasing effect is the dilution effect, the chemical and thermal effect being responsible for only up to 10 % of the fall in nitrogen oxides levels. The reduction in NO_x formation associated with the dilution effect was then linked with a decrease in the combustion speed and τ_{chem} .

However, a reduction in oxygen concentration not only affects τ_{chem} but also the production of soot. As a result of this increased soot concentration, the radiation absorption of the in-cylinder charge raises. In their numerical implementation of the P-1 model for thermal radiation transfer, Sazhina *et al.* (2000) showed that, although radiation in a typical diesel flame has no significant effect on the heat release rate, it can lower the maximum temperature enough to appreciably decrease NO_x formation.

The dilution effect identified by Ladommatos *et al.* could therefore be not only the result of a reduced flame speed but also of an increased radiation level.

The well-known trade-off between NO_x and soot emission levels could be partially explained by the beneficial effect of soot radiation on peak temperatures and NO_x formation.

2.3. Objectives

The investigation presented here aims at providing a deeper understanding of the formation of nitric oxide. Although the latest in situ studies on nitric oxide revealed part of the details of this mechanism, some questions lay unanswered.

The mixing-controlled phase has been identified as the main source of nitric oxide. Within this phase the periphery of the diffusion flame has been hypothesised as a main source. Indeed, this region combines elevated temperatures and high concentrations of oxygen. Nevertheless, this zone does not clearly stand out in the published nitric oxide distributions. Most of the nitric oxide is produced after the heat release rate peaks, when temperatures have started to decrease.

The diffusion flame time and spatial evolution can be analysed by the study of hydroxyl radicals (OH) distributions. These radicals have been shown to be mainly present in the mixing controlled phase, distributed in a thin layer around the flame plume, where the diffusion flame takes place (Allen et al., 1995, Kosaka et al., 1996, Dec and Coy, 1996, Nakagawa et al., 1997). If the hypothesis of a high production of nitric oxide in the diffusion flame is correct, the distributions of hydroxyl radicals and nitric oxide should match.

In some cases, formation of nitric oxide was recorded as long as 7 ms aSOI hence implying a long lifetime for the radicals N, O or OH. The presence of hydroxyl radicals after the end of apparent combustion is investigated here.

Adjusting the injection pressure is a convenient and effective way to influence the combustion process. An elevated injection pressure is often sought for better atomisation and to increase the rate of injected mass. However, the influence of injection pressure on NO_x levels is unclear. The evolution of local nitric oxide concentrations with increased injection pressure is presented here.

Recent studies have shown that auto-ignition occurs in regions where the mixture has become, through turbulent mixing, nearly homogeneous. The combustion of such mixtures is a potential source of thermal-NO only if the fuel-air equivalence ratio is close to stoichiometric. However a substantial number of amines and cyano compounds could be produced through the prompt-NO mechanism in rich mixtures. Furthermore, investigations of advanced combustion strategies as HCCI, for which the mixing controlled flame is very short, have reported a substantial production of NO_x (Laguitton, 2005). No direct link between the equivalence ratio and NO formation in premixed flames has been established. The effects of equivalence ratio on the NO formation in pre-mixed flames will be studied through the variation of the injection and in-cylinder pressure.

Models for the prediction of NO formation are based on this thermal (extended-Zeldovich) mechanism. Although they are able to reproduce experimental NO history remarkably well, as noted by Borman and Ragland (1998), such models are very sensitive to the ignition and turbulence models so that excellent agreement may be caused by fortuitous combinations of these submodels. The two-dimensional distributions of NO obtained experimentally could be the first step in a wider evaluation of models for the prediction of NO formation in CFD codes.

In most of the published investigations, the laser beam was cut by the piston around TDC. Therefore no information was available for as much as 20 c.a. before and after TDC. The current investigation in the Proteus rapid compression machine (RCM) is not subjected to this drawback. Likewise, the published results are mostly based on measurements with the laser beam propagating upstream the spray, often severely affected by attenuation at the tip of the flame. In the Proteus RCM, the side of the flame can be observed in more details as the laser beam travels perpendicular to the spray axis. Other technical features such as the choice of the fuel and the method employed will be discussed in Section 3.3.

To be able to fulfil these objectives, proper investigation techniques must be selected. The next chapter presents a brief review of the possible options. The technical issues associated with the most appropriate techniques are listed and final conclusions on the technique details for each investigation are given.

3. DIAGNOSTIC TECHNIQUES FOR MOLECULAR CONCENTRATIONS

This chapter reviews the techniques currently available for the measurement of molecular concentrations, and their associated technical requirements. The selected techniques and the specific details of the investigations are then further described in Section 3.3.

3.1. Physical Probing

Physical probing techniques have been extensively used before the availability of commercial lasers. Laser and optical techniques have then progressively developed and are now more widely used, for the reasons outlined below (Bechtel et al., 1984, Kohse-Höinghaus, 1994, Eckbreth, 1996, Dec, 1997).

- i. Whereas laser techniques, if appropriate precautions are taken, can be considered as remote, physical probing is intrusive and is likely to alter the flame behaviour. Indeed, the combustion could be catalytically modified or modified by the introduction of flow or thermal disturbances. Moreover, the physical probe could act as a flame holder when working with flow recirculation. Likewise the probe is subjected to temperature and pressure limits, which reduce the range of possible studies.
- ii. The physical probing measurements are not in situ but far removed from the sampling location. A great care has to be put in their design to avoid chemical transformation in the lines. Because this is not always possible, correction models have to be built to evaluate the real species concentrations. Such models tend to decrease the accuracy of the results.
- iii. Lastly, the spatial resolution and temporal response of such measurements cannot compete with the high spatial and temporal precision of laser techniques. High spatial precision is essential for the understanding of primary reaction zone and close-to-surface behaviour. Pulsed lasers can be as short in time as considered instantaneous compared to the combustion time scale.

Nevertheless, physical gas removal is often used when no particular spatial or temporal resolution is needed. It is, for example, applied to verify the compliance of a vehicle with emission standards. The application of this technique for nitrogen oxides will be described and two different high resolution methods will then be discussed. Physical probing of hydroxyl radicals is rare and difficult to perform, hence it will not be reviewed.

A number of specific physical probing techniques have been developed to measure molecular concentrations in combustion environments. But whether the in-cylinder sampling, cylinder dumping or direct exhaust gas method is used, every physical probing technique relies on exhaust gas analysis.

The collected mixture composition can be determined by use of Fourier transform infra red spectrometers – known as FTIR spectrometers (Donahue et al., 1994), or non-dispersive infrared analyzers – know as NDIR analyzers. In the specific case of nitrogen oxide measurements however, the most commonly employed analysers are chemiluminescence analysers – know as CLA (Voiculescu and Borman, 1978).

CLAs are based on the detection of light emitted by the reaction between nitric oxide and ozone (Stone, 1999). Nitric oxide reacts with ozone to become nitrogen dioxide in an electronically excited state (denoted by the asterisk):



The excited nitrogen dioxide can then be deactivated either by emission of a photon or by collision with any other molecule (denoted M):



Writing the conservation equation for the global chemical evolution, Ferguson & Kirkpatrick (2001) conclude that the photon intensity is proportional to the concentration of nitric oxide for the following conditions:

- i. The system is at steady state: the rate of change of species concentrations in the reactor is zero.
- ii. The ozone flow rate is large compared to the sample flow rate.
- iii. The reactor temperature and pressure are fixed.

Since there is often more interest into overall nitrogen oxides concentrations (NO_x : $\text{NO} + \text{NO}_2$), a catalytic converter is usually inserted in the sample line to convert nitrogen dioxides into nitric oxides.

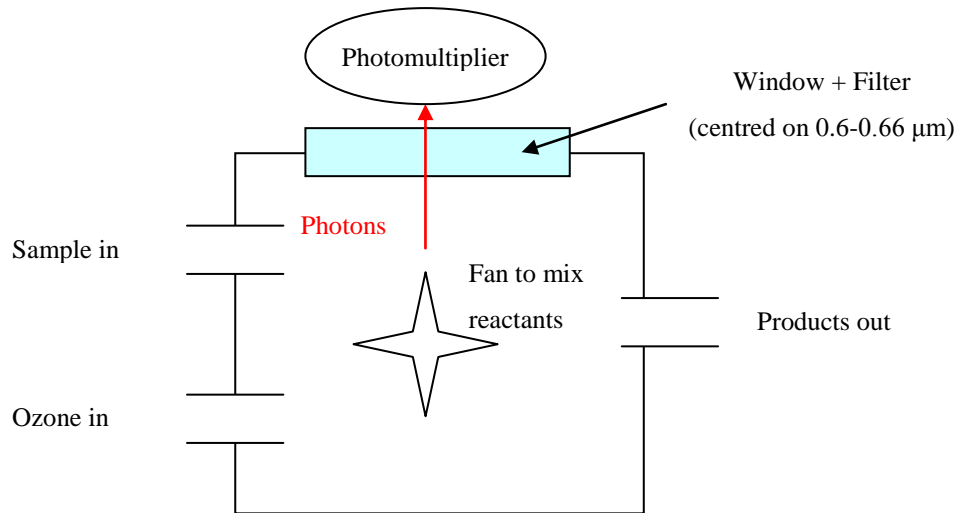


Figure 7 – Schematic representation of a chemiluminescence analyser (adapted from Ferguson & Kirkpatrick (2001))

3.1.1. Cylinder dumping method

This technique gives the spatially averaged composition of the cylinder gas for a given crank angle. A port linked to a collection chamber is fitted in the cylinder head. At a chosen crank angle, the port opens hence enabling the combustion gases to transfer to the collection chamber. The collected gases are subsequently analysed by the standard exhaust gas analysis described above. For the concentration histories to be correct, two conditions have to be fulfilled (Voiculescu and Borman, 1978):

- i. The chemical reactions have to be quenched when the collection port opens. In the case of nitrogen oxides, this could be interpreted by a necessary rapid decrease of temperature.
- ii. The collection sample must be such a large portion of the cylinder gas that it cannot be significantly biased.

The gradual temperature drop that in fact takes place at the port opening leads to some shift of the measured concentration. Therefore, the experimental concentration curve is slightly advanced by a few crank angles.

3.1.2. In-cylinder sampling method

Gas-sampling probes suck gas from a point in the combustion chamber and transfer it to an on-line gas analysis or to a sample bottle for subsequent analysis. This technique allows analysing samples of gas coming from some specific location in the combustion chamber (Aoyagi et al., 1980). Because a sampling valve is used, a hole has to be drilled in the cylinder head and sample locations are limited (Taylor, 1993a).

3.2. Optical diagnostics

As presented before, in a number of cases, optical and especially laser techniques are more appropriate to combustion studies than physical probing. Nevertheless, they have their own intrinsic drawbacks, the most obvious being the requirement for optical access. Furthermore, there is no single technique capable of measuring all species and temperatures simultaneously, and most of them tend to be applicable to small molecules only. Finally, although optically achievable spatial resolution is high, the measurement resolution is primarily determined by signal level considerations. In the following paragraphs two Raman based approaches and two electronic resonance techniques will be described. The processes involved are inelastic, i.e. there is an energy exchange between the incoming electromagnetic wave and the molecules.

For these techniques to be fully understood, some qualitative understanding of molecular electronic structure is useful. Thus, a brief introduction to electronic energy levels determination is presented hereafter. Because introducing multi-atoms multi-electrons structure at once may be confusing, a step by step presentation will be given.

3.2.1. Background information

3.2.1.1. Atomic electronic structure

Hydrogen energy states

Stationary wave states of valence electrons can be described through the Schrödinger wave equation (Eckbreth, 1996):

$$\nabla^2 \psi + \frac{8 \cdot \pi^2 \cdot m}{h^2} \cdot (E - V) \cdot \psi = 0 \quad (44)$$

Where E is the total energy, V the potential energy, m the particle mass, h Planck's constant ($h = 6.626 \cdot 10^{-34} \text{ J.s}$) and ψ the so-called wave function.

The equation can be solved for a number of discrete values of E_n , called eigenvalues. These values correspond to the allowed main orbits the electron can follow. To differentiate the possible orbits a first quantum number has been introduced.

n : principle quantum number (possible values: 1,2,3,4...)

For each total energy eigenvalues E_n , a degenerate set of eigenfunctions can be derived from the equation. These eigenfunctions represent the allowed angular momentum and spatial orientation for each energy state. To represent the possible momentum and orientation, two quantum numbers have been introduced.

l : azimuthal or orbital quantum number (possible values: 0,1,2,..., $n-1$)

m : magnetic quantum number (possible values: $l, l-1, \dots, 0, \dots, -l$)

Inspection of the energy states of some alkali metal atom spectra revealed that some states consist of two states of almost equal energy. To account for this structure, it is necessary to introduce another degree of internal freedom to the atom, the electron spin, designated as the quantum number s .

s : spin quantum number

Multi-electron atom energy states

Because most atoms possess more than one valence electron, a global atomic description of the energy configuration had to be developed. In order to differentiate quantum numbers associated to one electron orbital and quantum numbers associated to multi-electron atoms, the latter are chosen among the capital letters alphabet. The

following three quantum numbers have been introduced in order to describe the atomic electronic configuration.

L : resultant orbital angular momentum quantum number

For instance, for two electrons with orbital quantum numbers l_1 and l_2 :

$$L = l_1 + l_2, l_1 + l_2 - 1, \dots, |l_1 - l_2|$$

S : resultant spin quantum number

For instance, for two electrons with spin quantum numbers s_1 and s_2 :

$$S = s_1 + s_2, s_1 + s_2 - 1, \dots, |s_1 - s_2|$$

J : total angular momentum quantum number

$$J = L + S, L + S - 1, \dots, |L - S|$$

An atom electronic configuration is then fully defined by the notation:

$$n^{2S+1} L_J \quad (45)$$

$2S + 1$ is called multiplicity and n is often omitted. The nomenclature of L can be found in Table 2.

Since the interest here is to introduce all the necessary background for an overall understanding of the optical techniques applied to the measurement of molecules concentrations, the case of atomic electronic configuration is not sufficient and molecular electronic description has to be presented. In order to differentiate quantum numbers associated to atoms and quantum numbers associated to molecules, the latter are chosen among the Greek alphabet.

3.2.1.2. Molecular spectroscopy

Molecular electronic structure

From the previous definition another quantum number is introduced to define the axial component of the orbital angular momentum of one electron. For electrons of given n and l quantum numbers, but with different m values, the quantum number λ is employed. It can take on values of $|m|$.

λ : quantum number for the axial component of the orbital momentum.

$$\lambda = l, l - 1, \dots, 0$$

The description of the global molecule electronic structure is defined by the following three quantum numbers:

$$\Lambda = \left| \sum \lambda_i \right| : \text{total axial electronic angular quantum number}$$

$$\Sigma = \left| \sum s_i \right| : \text{total spin quantum number resultant}$$

$$\Omega = \left| \Lambda + \Sigma \right| : \text{quantum number for the total axial momentum}$$

The molecule electronic state is then fully described by the following notation:

$${}^{2S+1}\Lambda_{\Omega} \quad (46)$$

$2S + 1$ is called multiplicity. The nomenclature of Λ can be found in Table 2.

Vibrational and rotational degrees of freedom

The analogy between atomic and molecular energy levels is however not complete. Because the molecular nucleus has a capacity to rotate and vibrate, molecules have more degrees of freedom than atoms. These extra degrees of freedom have been taken into account by the introduction of new quantum numbers:

ν : the vibrational quantum number

J : the rotational quantum number

Each of these degrees of freedom corresponds to a potential energy fluctuation. The approximate orders of magnitude of the change in energy are as follows (Banwell and NcCash, 1994):

$$\Delta E_{elec} \approx \Delta E_{vib} \times 10^3 \approx \Delta E_{rot} \times 10^6 \quad (47)$$

Where E is expressed in cm^{-1}

Vibrational dynamics

The vibrational dynamics of a diatomic molecule can be pitched in the classical “dumbbell” model shown in Figure 8. The model consists of two distinct masses connected by a spring. In this case, the motion of atoms is that of a simple harmonic oscillator where they alternate between moving toward and away from each other.

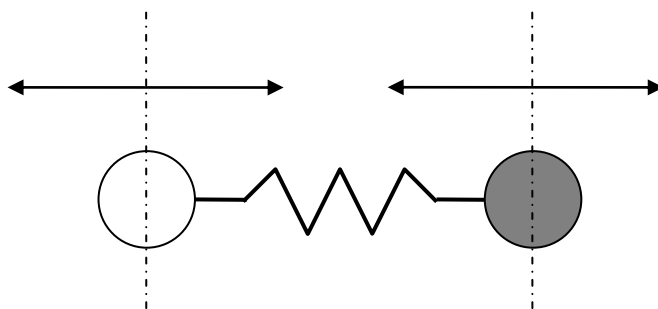


Figure 8 – Harmonic oscillator model

For the simple harmonic motion of a single mass, m , on a spring, the Hooke's law is:

$$F = -k \cdot x \quad (48)$$

Where x is the distance from equilibrium and k is the spring constant. The frequency of oscillation is then given by:

$$\nu = \frac{1}{2 \cdot \pi} \cdot \sqrt{\frac{k}{m}} \quad (49)$$

The corresponding frequency of oscillation for a dumbbell system is identical except that m is replaced by the reduced mass, μ with:

$$\frac{1}{\mu} = \frac{1}{m_1} + \frac{1}{m_2} \quad (50)$$

From equation (48), the potential energy of a simple harmonic can be written as:

$$V = 2 \cdot \pi^2 \cdot \mu \cdot \nu^2 \cdot x^2 \quad (51)$$

Replacing the potential in the Schrödinger equation, the quantified energies of oscillation, or vibrational energies of the molecule are (Greenhalgh, 1994):

$$E_{vib} = h \cdot \nu \cdot (v + \frac{1}{2}) \quad (52)$$

Where v is the vibrational quantum number ($v = 0,1,2,\dots$), ν the frequency of oscillation and h Planck's constant.

Rotational dynamics

In addition to vibrating as a simple harmonic oscillator, diatomic molecules have rotational dynamics as pictured in Figure 9. The energies associated with this rotation will also be quantised.

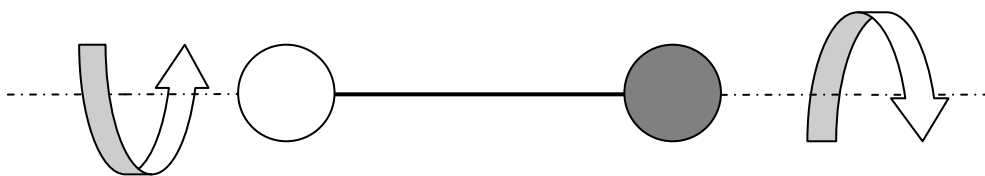


Figure 9 – Rigid rotor model

Beginning again with the dumbbell model, the vibrational degree of freedom is ignored and the two atoms are connected by a massless rigid rod. The classical energy for this rigid motion is given by:

$$E = \frac{L^2}{2 \cdot I} \quad (53)$$

Where L is the angular momentum and I is the moment of inertia about the axis of rotation. Substituting into the Schrödinger equation:

$$\frac{L^2}{2 \cdot I} \cdot \psi = E \cdot \psi \quad (54)$$

Where ψ is an eigenfunction of L^2 with eigenvalues $\hbar^2 J(J+1)$ with J , the rotational quantum number ($J=0,1,2,\dots$). The rotational energies can be written as (Greenhalgh, 1994):

$$E_{rot} = h \cdot c \cdot B \cdot J \cdot (J + 1) \quad (55)$$

Where B is called the rotational constant and given by: $B = \frac{h}{8 \cdot \pi^2 \cdot c \cdot I}$

Total molecular energy

To summarise, energy and total angular momentum of the molecule involve three modes of excitation: electronic, rotational and vibrational. By following the Born-Oppenheimer approximation, the total energy of the molecule may be written as:

$$E = E_{elec} + E_{vib} + E_{rot} \quad (56)$$

Where E_{vib} and E_{rot} are the vibrational and rotational energies. If the molecule is assumed to be a harmonic oscillator and a perfect rotator, these energies are given by equations (52) and (55).

Electronic structure and molecular spectrum

The energy variations described hitherto can be acquired / released by absorption / emission of an electromagnetic wave. Planck's equation gives the link between the absorbed / emitted radiation frequency and the quantum of energy acquired / released:

$$E = h \cdot \nu \quad (57)$$

Where E is the exchanged energy, h Planck's constant and ν the radiation frequency.

In molecular spectroscopy, the ground electronic state is called the X-state, the lowest excited state the A-state, the second lowest excited state the B-state etc.

Historically the different levels have been denoted Σ ($\Lambda = 0$), Π ($\Lambda = 1$), Δ ($\Lambda = 2$) and Φ ($\Lambda = 3$) – see Table 2. For the Σ states of homonuclear molecule, it is common to subscript the term symbol with g (for the German word *gerade*) or u (*ungerade*) instead of Ω , which indicate if the orbital is either respectively symmetric or asymmetric, relative to inversion through the molecular centre. The Σ states of both homonuclear and heteronuclear molecules are further distinguished by being symmetric (Σ^+ state) or antisymmetric (Σ^- state) with respect to a reflexion in the plane of symmetry axis.

Table 2 – Nomenclature of l , L , Λ

		0	1	2	3	4	...
Quantum number	l	s	p	d	f	g	...
	L	S	P	D	F	G	...
	Λ	Σ	Π	Δ	Φ	Γ	...

The lower vibrational and rotational states are distinguished by a double prime (v'', J''), while the upper states carry only a single prime (v', J'). Likewise, transitions for which $J' = J'' + 1$, $J' = J''$ and $J' = J'' - 1$ are termed R-, Q- and P-branch, respectively (Figure 11). Therefore, rotational transitions are usually labelled as $R(J'')$, $Q(J'')$ or $P(J'')$.

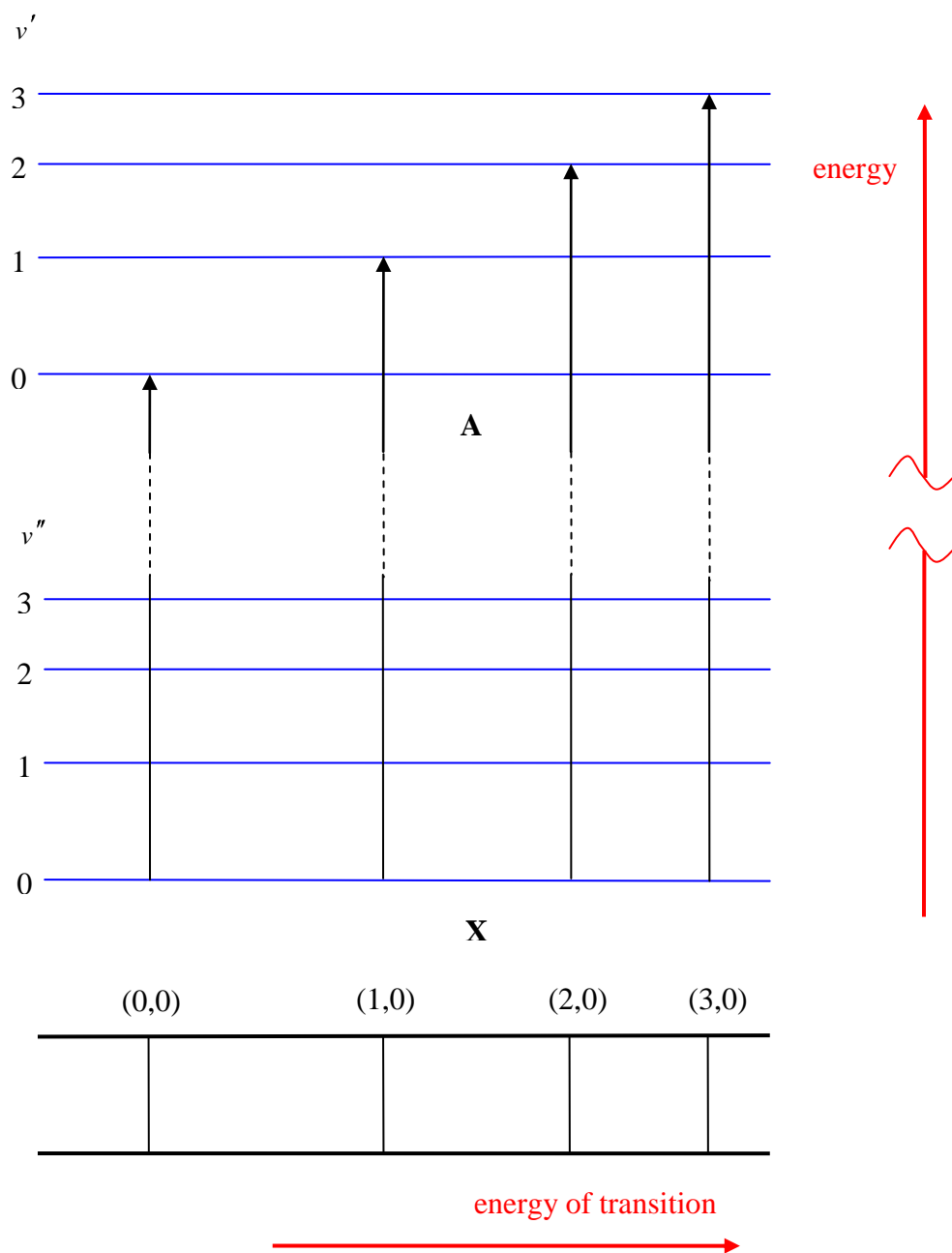


Figure 10 – The vibrational progression of the band formed during electronic absorption from the ground ($v''=0$) state to a higher state (adapted from Banwell and McCash (1994))

Whereas the selection rules restrict the possible changes in electronic quantum numbers (hence possible transitions), there is no selection rule for v when a molecule undergoes an electronic transition (Figure 10). However, all transitions (v', v'') do not have the same probability. The Frank-Condon principle states that an electronic transition takes

place so rapidly that a vibrating molecule does not change its internuclear distance appreciably during a transition (Banwell and McCash, 1994, Eckbreth, 1996). As a general rule, the transition probabilities are the greatest for the Q-branch, and fall off with increasing change in rotational quantum number (Daily, 1997).

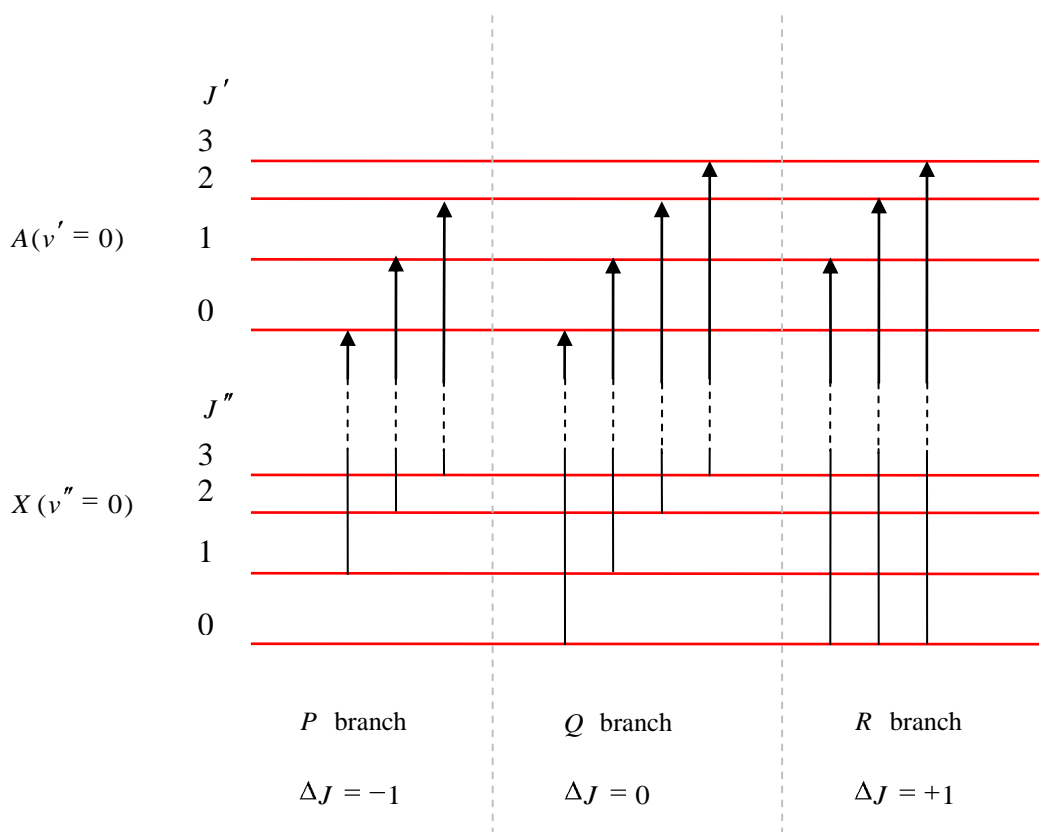


Figure 11 – P , Q and R branches

Measurements techniques exploiting the electromagnetic properties of molecules have been developed. Depending on the properties used, the signal can be radiated in all directions (full solid angle) or as a laser-like beam. The techniques are then respectively termed incoherent and coherent Table 3. The techniques can also be fluorescence or Raman based. When light is scattered from a molecule, most photons are elastically scattered (Rayleigh scattering). The scattered photons have the same energy, and therefore, wavelength as the incident photons. However, a small fraction of light (approximately 1 in 10 million photons (Taylor, 1993a)) is scattered at a different wavelength from, and usually lower than, the wavelength of the incident photons. This

phenomenon, Raman scattering, can be seen as the subsequent fluorescence to an excitation to a virtual energy level. It is the basis of a number of measurement techniques.

The first technique considered here will be the most widely used: laser-induced fluorescence (LIF). Two Raman based techniques will then be introduced, and finally, the electronic resonant degenerate four-wave mixing technique will be presented.

Table 3 – Laser diagnostics techniques for species measurement (adapted from Eckbreth (1996))

	Incoherent	Coherent
Major species (>0.1%)	Raman based approach	
	Raman scattering	CARS
Minor constituents (<0.1%)	Electronic resonance techniques	
	LIF	DFWM

3.2.2. Laser diagnostics techniques for the measurement of species densities

3.2.2.1. Laser-induced fluorescence (LIF)

The LIF technique (Figure 12) is based on the accurate excitation of molecules to an upper energy level and the monitoring of the subsequent radiation. As reported in Table 3, LIF is an incoherent technique. Thus, only part of the emitted signal will be collected, in general at an angle of 90° to the incident laser beam. However, incoherent techniques allow the capture of two-dimensional distributions if the incoming laser beam is shaped into a thin sheet. The technique is then called planar laser-induced fluorescence or PLIF.

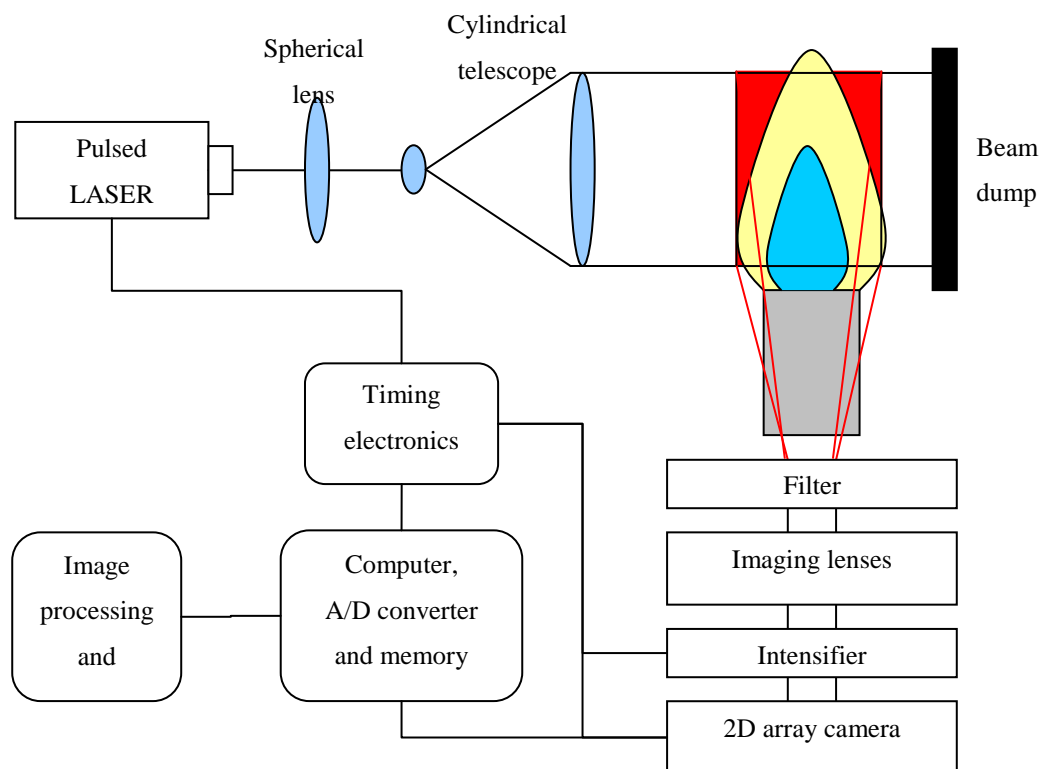


Figure 12 – LIF experimental setup (adapted from Hanson et al. (1990) and Taylor (1993a))

The visible and ultraviolet spectral regions (200 to 600 nm) are of great interest in LIF as they are mostly free from interferences from broad emissions of stable molecules such as CO_2 , CO and H_2O . The temporal resolution of the measurement is controlled by the laser source with 5-10 ns pulse lengths being typical whereas the spatial resolution is set by the sensor array which often contains more than 1 million pixels.

3.2.2.2. Raman scattering

Raman scattering has received early attention because of its simple experimental setup (Figure 13): a single laser can indeed be used to monitor all the species of interest without having to be tuned to a specific wavelength (e.g. resonance wavelength).

The scattered signal subsequent to Raman process is species specific and linearly proportional to the species number density. Spectral interferences between the vibrational Raman bands of different gases are rare, and scattered intensity from a given constituent is independent of the surrounding. Since the process is insensitive to collisional quenching (see 3.2.3 for a discussion on collisional quenching), quantitative measurements can easily be achieved.

The collected signal is however very low and limits the applicability of the technique to high concentration species. In an attempt to increase the proportion of collected signal, a coherent technique based on Raman scattering is often preferred and will therefore be presented hereafter.

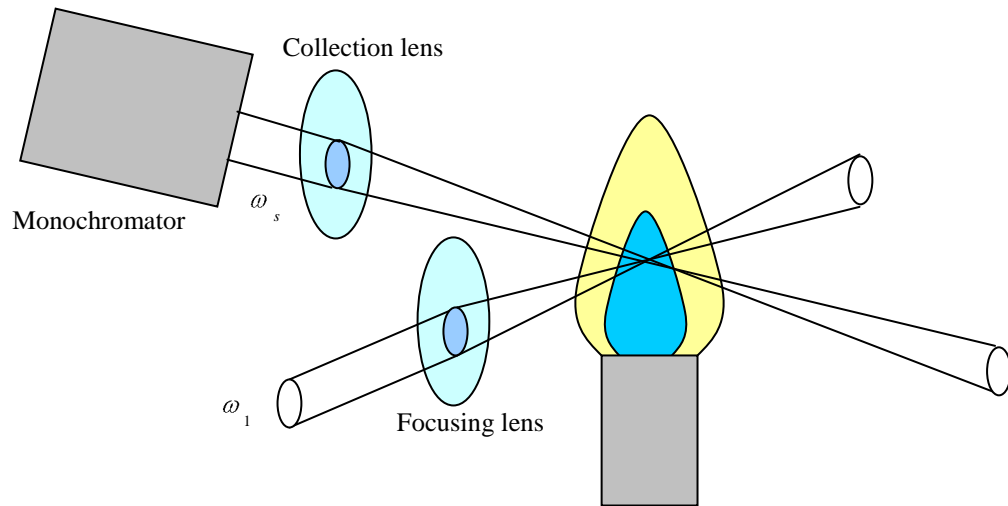


Figure 13 – Raman scattering experimental setup (adapted from Taylor (1993a) and Eckbreth (1996))

3.2.2.3. Coherent anti-Stokes Raman spectroscopy (CARS)

Simple CARS experiments utilise two beams of frequency ω_1 and ω_2 respectively called the pump and Stokes (for it is downshifted in frequency) fields. The geometry of the mixing scheme is such that the two incoming fields are phase-matched and generate a coherent CARS signal at $\omega_3 = 2 \cdot \omega_1 - \omega_2$ (Figure 14). This non-linear four wave mixing process requires a precise angular alignment of the pump and Stokes field (Eckbreth, 1996).

It is highly important to ensure that CARS signal generated at one location will be in phase with that generated at other locations for constructive signal growth to occur.

The oscillating polarization at ω_3 rises from the medium third-order non-linear susceptibility, which density and temperature dependency allows CARS to be used as a diagnostic tool.

Different molecular constituents can be scanned by tuning the frequency difference $\omega_1 - \omega_2$ to a particular Raman resonance. Whereas the temperature can be probed by

analysis of the spectral shape, the strength of the signal is related to the species concentration.

A similar process – coherent Stokes Raman scattering – is obtained when the Stokes beam is replaced by an anti-Stokes beam. However, since CARS spectra lie in the anti-Stokes region, interferences with fluorescence spectra are less likely.

Due to its high signal to noise ratio (one photon in 10 thousand is scattered (Taylor, 1993a)), and its coherent properties, harsh dirty flame environments with a strong fluorescent or luminous background can be probed.

This extension of the domain of applicability is at the cost of a heavier experimental setup: CARS is indeed a double-ended technique requiring line of sight optical access. Furthermore, multiple laser sources are required for single species study. The CARS signal spectra comprehend both constructive and destructive interference effects and exhibits quadratic dependence upon density and laser power.

Finally, dye laser noise and spatial resolution have also proved to be limiting factors in the application of CARS to practical, high gradient combustions (Greenhalgh, 1988, Greenhalgh, 1994).

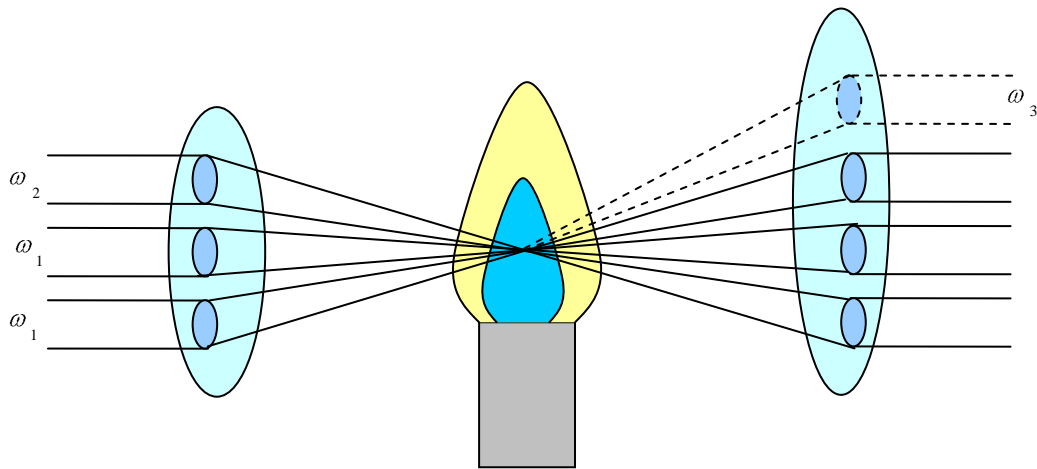


Figure 14 – CARS experimental setup (adapted from Taylor (1993a))

To conclude, even in the case of the coherent process, Raman techniques applications to minor species remain unfortunately difficult. Radical species (e.g. OH , CH , NH , CN , C_2) and pollutants (e.g. NO , CO) with concentrations below 1000 ppm can hardly be detected.

3.2.2.4. Degenerate four-wave-mixing (DFWM)

DFWM is another third-order nonlinear optical process that has been initially developed as a tool to calculate the reflectivity of the phase conjugate mirror. Its development as a combustion diagnostic tool is fairly recent. DFWM requires a single laser to produce three input beams at frequency ω . The appropriate orientation of the three beams generates, at mixing point, a signal beam also at frequency ω (Figure 15). This single input frequency makes DFWM simpler to setup than CARS, but still, a correct phase-matching geometry has to be applied. As for the CARS technique, correct phase-matching geometry is hard to maintain because of the occurrence of refractive index gradients through the in-cylinder mixture.

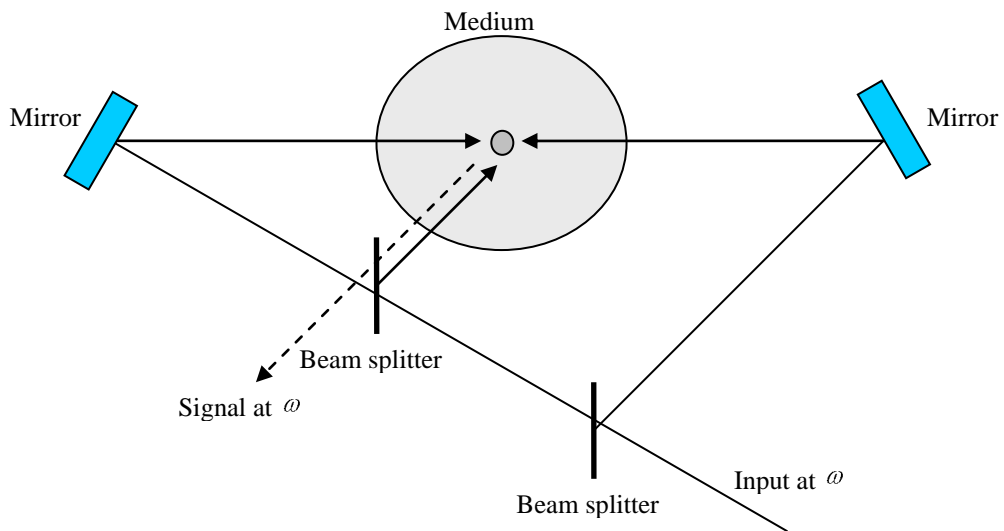


Figure 15 – DFWM experimental setup (adapted from Eckbreth (1996))

The signal spectra essentially follow the electrons absorption spectrum of the species being probed. Because the signal is at the same frequency as the input, input light scattering could be interfering. However, the signal being coherent and with some spatial filtering, spurious scattering can easily be isolated.

DFWM is not sensitive to quenching – one of the major issues with laser induced fluorescence (3.2.3). Finally the intrinsic inaccuracy of DFWM could be less than the inaccuracy of LIF with a bad knowledge of the background environment at elevated pressures.

3.2.2.5. *Conclusion*

As seen before, the Raman-based techniques are not sensitive enough to measure concentrations down to hundreds of ppm. On the other hand, both electronic resonant techniques presented here could be used to obtain radical or pollutant distributions.

The DFWM technique appears best suited if quantitative measurements are sought. Its insensitivity to quenching and coherent signal makes it the tool of preference for high-pressure, low-signal conditions. However, its complex excitation/collection setup (Figure 15) and its sensitivity to beam alignment are considerable drawbacks when limited optical access and vibration of the test-rig are considered.

In contrast, the literature shows that the LIF technique has been applied successfully to the extreme conditions found in diesel engines. Moreover, LIF offers the opportunity to capture two-dimensional distributions of the probed molecules.

Therefore, the LIF technique was selected to obtain qualitative two-dimensional distributions of OH radicals and NO in a combusting diesel spray. In the next section, the theoretical basis of the technique is further described.

3.2.3. Laser-Induced fluorescence (LIF)

3.2.3.1. From molecular spectra to LIF

The selectivity property is the basis of LIF technique: as every molecule has a unique set of energy levels, it has unique absorption and emission spectra. Thus, molecule spectra are as explicit as identification cards.

The LIF technique relies on the following reflection: by accurately choosing the excitation wavelength, only the targeted molecules will be excited. If the excited states have very short lifetimes (Table 4), the molecule will rapidly return to the ground state. With appropriate monitoring devices, the associated fluorescence radiation can be visualised and the molecules concentration linked to the emission intensity.

Table 4 – Excited states lifetimes

Molecule	Ground State	Excited State	Fluorescence lifetime [ns]	Real lifetime [ns] (limited by)	Reference
<i>OH</i>	$X^2\Pi_i$	$A^2\Sigma^+$	700	2 ns at 1 bar (quenching)	(Ketterle et al., 1992)
	$X^2\Pi_i$ $v'' = 0,1$	$A^2\Sigma^+$ $v' = 0$		2 ns	(Arnold et al., 1990)
			700	2 ns at 1 bar (quenching)	(Ketterle et al., 1992)
	$X^2\Pi_i$ $v'' = 0$	$A^2\Sigma^+$ $v' = 3$		0.1 ns	(Arnold et al., 1990)
				0.1 ns below 10 bar (predissociation)	(Ketterle et al., 1992)
<i>NO</i>	$X^2\Pi_r$	$A^2\Pi_r$	210 ± 10		(Luque and Crosley, 1999)
			250		(Daily, 1997)
	$X^2\Pi_r$	$D^2\Pi_r$	20		(Daily, 1997)

In the linear regime, the measured fluorescence radiant power F subsequent to an excitation is proportional to the quantity of absorbed light (Eckbreth, 1996):

$$F = I_{\nu_0} \cdot N_1^0 \cdot V_c \cdot B_{12} \cdot \frac{h \cdot \nu_0}{c} \cdot \frac{\Omega_c}{4\pi} \cdot \varepsilon \cdot g_{\nu_0} \cdot f_{B_1} \cdot \Phi \quad (58)$$

where I_{ν_0} is the laser irradiance at ν_0 , N_1^0 is the population density of the probed molecule in state 1 prior to laser excitation, V_c is the probed volume, B_{12} is the Einstein rate constant for stimulated absorption from state 1 to state 2, h is Planck's constant, ν_0 is the optical frequency of the absorption transition, Ω_c is the solid angle of the collection optics, ε is the efficiency of the collection optics (includes the detection electronic gain, the quantum efficiency of the detector and any loss of signal due to the optics), g_{ν_0} is the spectral overlap integral between the excitation and absorption lineshapes, f_{B_1} is the Boltzmann fraction representing the population of initial state 1 and Φ is the fluorescence yield, the proportion of absorbed energy radiated in fluorescence.

3.2.3.2. Deactivation pathways

In general, a number of competing phenomena make Φ difficult to evaluate and quantitative measurements difficult to achieve. These phenomena are summarised in Figure 16. Furthermore, the population of the ground rotational states are not always in equilibrium with the surrounding rotational states (Bessler et al., 2003b). In this case, the complex rotational energy transfer (RET) controls the number of absorbing molecules and must therefore be taken into account. The other pathways from the upper to the lower levels include:

- i. Collisional quenching, which is caused by energy exchange between colliding molecules and is consequently dependent on temperature and pressure.
- ii. In some cases internal conversion between two states of same multiplicity can occur without any emission of radiation. This is likely to happen when the lower vibrational levels of the higher electronic state have approximately the same energy as the higher vibrational levels of the lower electronic state.
- iii. Intersystem crossing between two energy levels of different multiplicity lead to phosphorescence, hence late radiation. Indeed, phosphorescence electronic excited states have a longer lifetime (over 10^{-4} sec) than fluorescence electronic excited states (lower than 10^{-5} sec).
- iv. For large enough excitation energies, the transition can become saturated with a fluorescence signal no longer proportional to the excitation energy. Likewise, depending on the molecule structure, ionisation or photodissociation can happen.

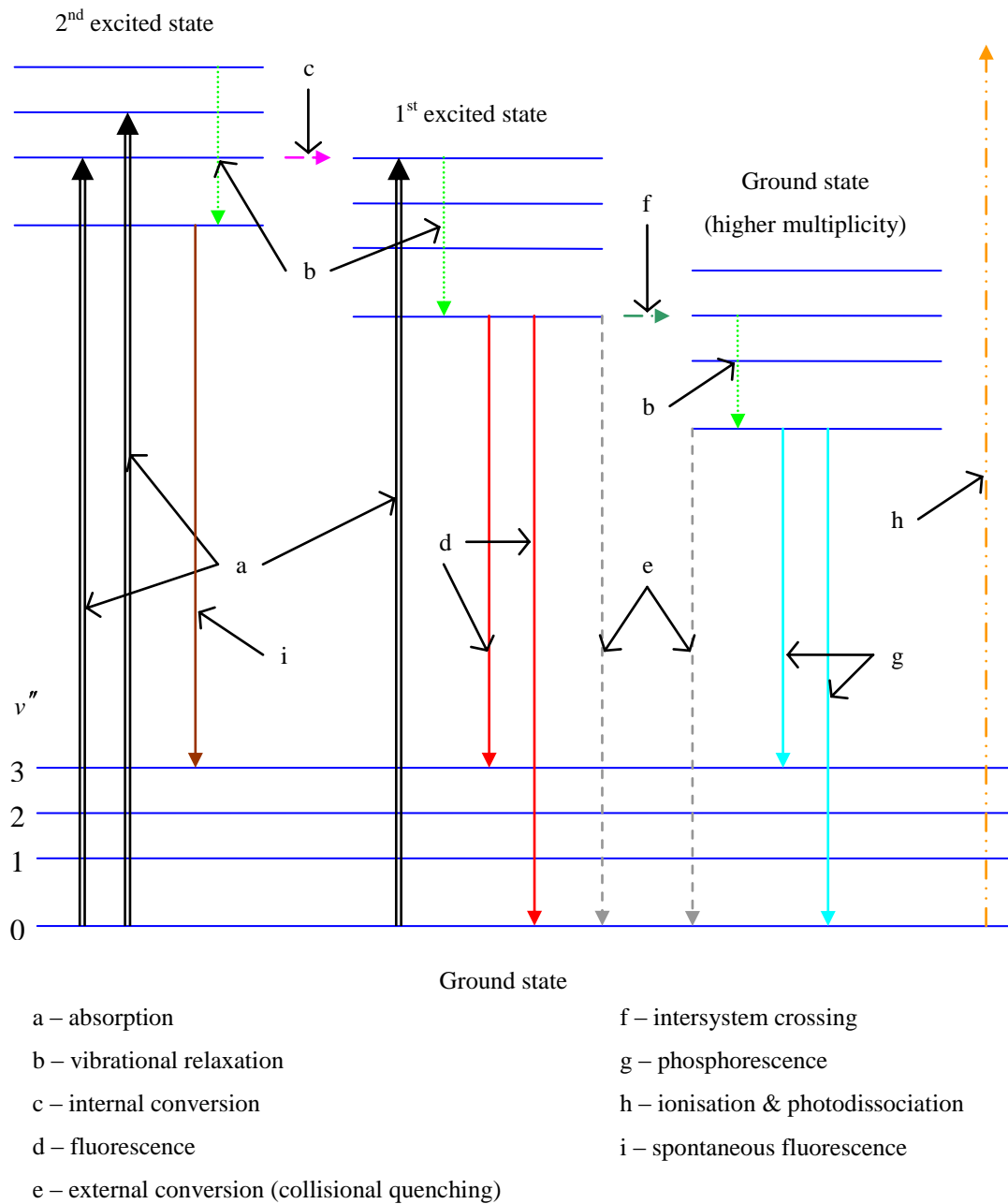


Figure 16 – Deactivation pathways for an excited molecule (adapted from the Jablonski diagram)

Since these phenomena are difficult to evaluate in the case of an engine-like combustion, quantitative applications of LIF have been very limited in the past. The so called “quenching” corrections involve knowing partial pressures of all species present, the local temperature as well as the rates of deactivation of the excited state and their dependence to pressure. Several different experimental approaches such as saturated or predissociative (LIPF) LIF have been developed to facilitate quantitative measurements.

Likewise, the effects of quenching are sometimes calibrated by adding a known quantity of the fluorescent molecule to the inlet air (de Sercey et al., 2006).

Because the excited molecule can gain or lose small amounts of energy via additional pathways, the fluorescence emission wavelength can vary. In most cases, vibrational relaxation will take place and the fluorescence will be Stokes-shifted (shifted towards higher wavelength). However, some amount of anti-Stokes shifted fluorescence can also be emitted. Emission at the excitation wavelength is termed resonance fluorescence (Figure 17).

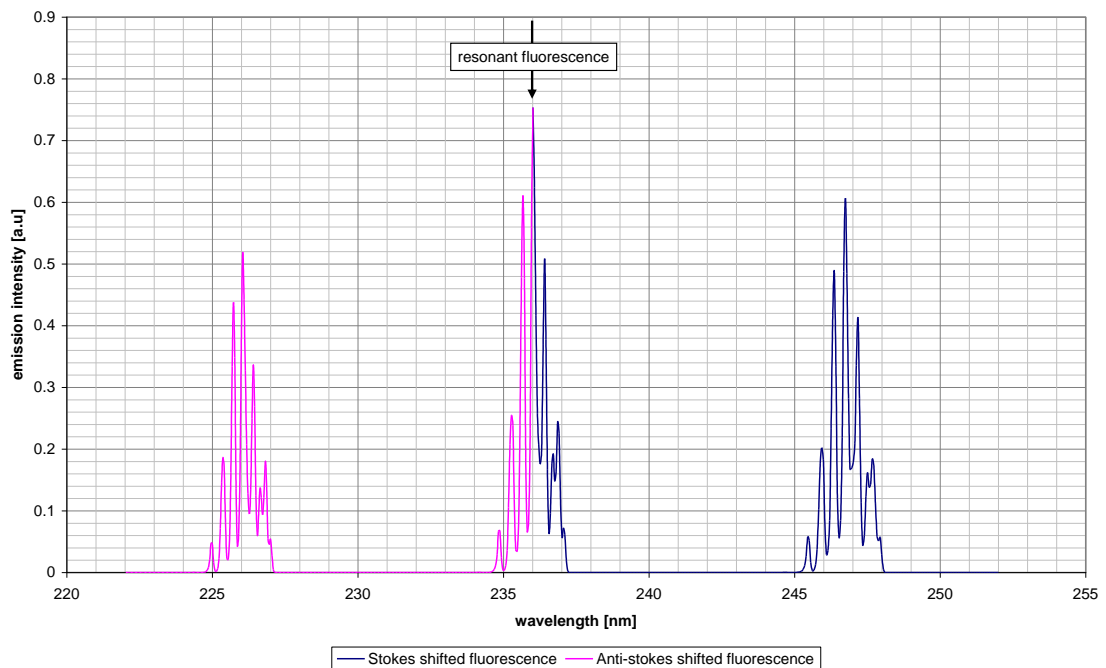


Figure 17 – Resonant, Stokes shifted and anti-Stokes shifted fluorescence for an excitation of NO at 236 nm. Adapted from (Bessler et al., 2003b).

Techniques based on LIF have also been used to access information such as species temperature (two-line temperature) or pressure-temperature-velocity (line shape measurements).

In the following section, the specific details of the OH- and NO-LIF techniques applied to diesel combusting sprays will be introduced.

3.3. Laser-Induced Fluorescence of hydroxyl radicals and nitric oxide

3.3.1. Fluorescence signal evaluation

3.3.1.1. Fluorescence yield

For the excitation/emission schemes considered, some of the deactivation pathways reported above can be ruled out.

In the considered applications of LIF to the measurement of OH and NO density distributions, the applied power density is rather low, at $\sim 5 \text{ kW/cm}^2$. Investigations on saturation levels for schemes with similar or lower absorption cross-sections have reported saturation thresholds higher than this figure (see for instance Andresen *et al.* (1988), Kosaka *et al.* (1996) for OH saturation and Vyrodiv *et al.* (1995) for NO saturation). The hypothesis of linear regime is therefore verified and equation (58) applies.

The electronic transitions considered are not likely to be affected by intersystem crossing and ionisation. One scheme only ($A^2\Sigma^+ - X^2\Pi (3,0)$ of OH, see page 64) involves a high rate of predissociation. In this case, the fluorescence yield is independent of the quenching rate ($Q_{21} \ll P_{21}$) and can be written as:

$$\Phi = \frac{A_{21}}{A_{21} + P_{21}} \quad (59)$$

Where A_{21} and P_{21} are respectively the Einstein rate coefficient for spontaneous emission and the rate coefficient for predissociation.

As a general rule, in the very high pressure environment of a diesel combustion chamber, collisional quenching can be considered as the main competing deactivation process. Therefore, the fluorescence yield can be written as:

$$\Phi = \frac{A_{21}}{A_{21} + Q_{21}} \quad (60)$$

Where A_{21} and Q_{21} are respectively the Einstein rate coefficient for spontaneous emission and the rate coefficient for electronic quenching.

The possible colliding species in a diesel-like combustion are CO₂, H₂O, O₂, N₂, fuel molecules, combustion intermediates and radicals. Battles & Hanson (1995) and Paul *et al.* (1994) have identified the main colliders for OH and NO-LIF. Whereas for the former the main source of quenching comes from H₂O followed by CO₂ and O₂, for the latter CO₂ is the major concern, H₂O and O₂ collision cross sections being half as high. Overall, the collision cross sections are twice higher for NO than for OH. For temperatures above 1000 K, the collision cross sections of H₂O, CO₂ and O₂ with OH and NO stayed fairly constant. Collisional quenching of OH and NO can therefore be considered as temperature independent.

Table 5 – Collisional cross sections of OH A²Σ⁺(v'=1) and NO A²Σ⁺(v'=0) (Battles and Hanson, 1995, Paul et al., 1994)

	σ _{CO₂}	σ _{H₂O}	σ _{O₂}
OH [Å ²] (1000 K < T < 2500 K)	20	27	10
NO [Å ²] (1000 K < T < 2500 K)	55	28	25

The collisional quenching rate can be expressed as (Battles and Hanson, 1995):

$$Q_{21} = \frac{P}{k \cdot T} \sum_i \chi_i \cdot \sigma_i \cdot \sqrt{\frac{8 \cdot k \cdot T}{\pi \cdot \mu_i}} \quad (61)$$

Where χ_i is the mole fraction of colliding species i , σ_i , the collisional cross-section of colliding species i , $\mu_i = m_i \cdot m_{NO} / (m_i + m_{NO})$, the reduced mass of the colliding species i ,

Replacing equation (61) into equation (60), the fluorescence yield Φ is found to be proportional to:

$$\Phi \propto \sqrt{T} / P \cdot \sum_i \frac{\chi_i \cdot \sigma_i}{\sqrt{\mu_i}} \quad (62)$$

For proper qualitative comparisons of signal strength, one needs to know the local temperature and gas composition in order to evaluate collisional quenching. This information is however not easily available hence only few publications include a correction for collisional quenching. Barlow *et al.* (1990), for instance, calculated the local temperature and gas composition from Raman scattering data while many others

bracketed these values between a perfectly homogeneous and an heterogeneous combustion process (Dec and Canaan, 1998, Stoffels, 1999, Fissenewert et al., 2005). The temperature gradients can be very high during the mixing-controlled phase. Flynn *et al.* (1999) for instance reported temperatures inside the flame plume of 1600 K, compared to 2700 K for the diffusion flame. In both their modelling of heptane and oxygenated fuel chemistry, although the heat release rate of the pre-mixed phase was not negligible, the amount of H₂O and especially CO₂ produced during this phase was not as proportionally important since mainly intermediate species were formed. On the other hand, concentrations of CO₂ and H₂O were expected to be high in the vicinity of the diffusion flame.

3.3.1.2. Boltzmann fraction

The temperature affects the fluorescence signal through the Boltzmann population distribution (f_{B_i} in equation (58)). The Boltzmann fraction of the quantum state (n,v,J) at a specific temperature T is given by (Ingle and Crouch, 1988):

$$F_{n,v,J}(T) = \frac{2J+1}{Q(T)} \cdot \exp\left(\frac{-E(n,v,J)}{k \cdot T}\right) \quad (63)$$

Where $g=2J+1$ is the statistical weight of state (n,v,J) , $Q(T)$ is the partition function and $E(n,v,J)$ is the excitation energy relative to the ground state.

In fact, the higher the OH or NO temperature is, the more high energy levels will be populated. Therefore, if the excitation scheme aims at the commonly most populated level (i.e. the lowest), higher temperature will mean lower population and hence lower excitation rate. Figure 18 shows for instance the vibrational population distribution of NO X²Π between 700 and 2200 K. All excitation lines do not have the same sensitivity to temperature. For instance, Berckmüller (1996) noticed that the Q2(22.5) transition in the A²Σ⁺-X²Π (0,0) band of NO has a ground state population which varies by only 2% over the temperature range 350 to 700K. However, this absorption line is very weak and would not fit the present investigation.

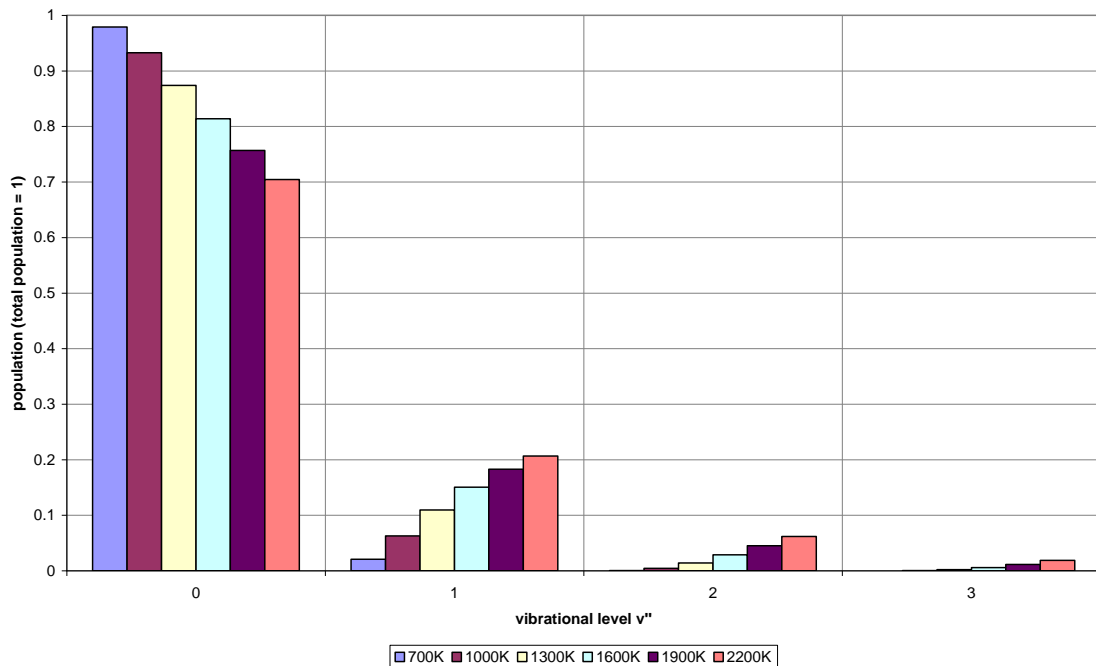


Figure 18 – Vibrational population distribution of NO X²Π with temperature (Luque and Crosley, 1999)

3.3.1.3. Overlap integral

Collisions between molecules are responsible for phenomena called pressure or collisional broadening and collisional shift, which widens absorption lineshape and alters the centreline frequency of the absorption lineshape respectively. The collision width is proportional to pressure. At high pressure, the peaks are then wider (in terms of frequency) and easier to tune on. However, the spectrum becomes less structured and can make it more difficult to discriminate fluorescence from background noise. This problem is especially critical for NO as it combines an already dense spectrum at low pressures and unusually large broadening coefficients. Chang *et al.* (1992) reported that broadening of NO is considerably larger than those for electronic transitions of other diatomic molecules, of which OH is somewhat more typical.

The collisional width can be evaluated as the sum of collider-dependent collision widths per unit pressure, weighted by the partial pressure of each collider species:

$$\Delta \nu_c = \sum_i 2 \cdot \gamma_i \cdot p_i \quad (64)$$

Where $2\gamma_i$ is the broadening coefficient of collider species i [$\text{cm}^{-1} \cdot \text{atm}^{-1}$], and p_i is the partial pressure of species i [atm].

Likewise, the collisional shift is proportional to pressure and the collisional shift coefficient can be written as:

$$\Delta \nu_s = \sum_i \delta_i \cdot p_i \quad (65)$$

Where δ_i is the shift coefficient of collider species i [$\text{cm}^{-1} \cdot \text{atm}^{-1}$], and p_i is the partial pressure of species i [atm].

The collisional broadening coefficients of NO in nitrogen and argon as found by Chang *et al.* (1992) and confirmed by Vyrodov *et al.* (1995) are:

$$2 \cdot \gamma_{NO-N_2} = 0.585 \cdot \left(\frac{295}{T} \right)^{0.75} \quad (66)$$

$$2 \cdot \gamma_{NO-Ar} = 0.505 \cdot \left(\frac{295}{T} \right)^{0.65} \quad (67)$$

In comparison, the coefficients found by Davidson *et al.* (1996) for OH are noticeably smaller:

$$2 \cdot \gamma_{OH-Ar} = 0.140 \cdot \left(\frac{300}{T} \right)^{0.75} \quad (68)$$

The collisional shift coefficients of NO and OH also show discrepancies:

$$\delta_{NO-N_2} = -0.180 \cdot \left(\frac{295}{T} \right)^{0.56} \quad (69)$$

$$\delta_{NO-Ar} = -0.160 \cdot \left(\frac{295}{T} \right)^{0.58} \quad (70)$$

$$\delta_{OH-Ar} = -0.0305 \cdot \left(\frac{300}{T} \right)^{0.45} \quad (71)$$

Figure 19 illustrates the effects of collisional broadening and shift on the NO and OH spectra.

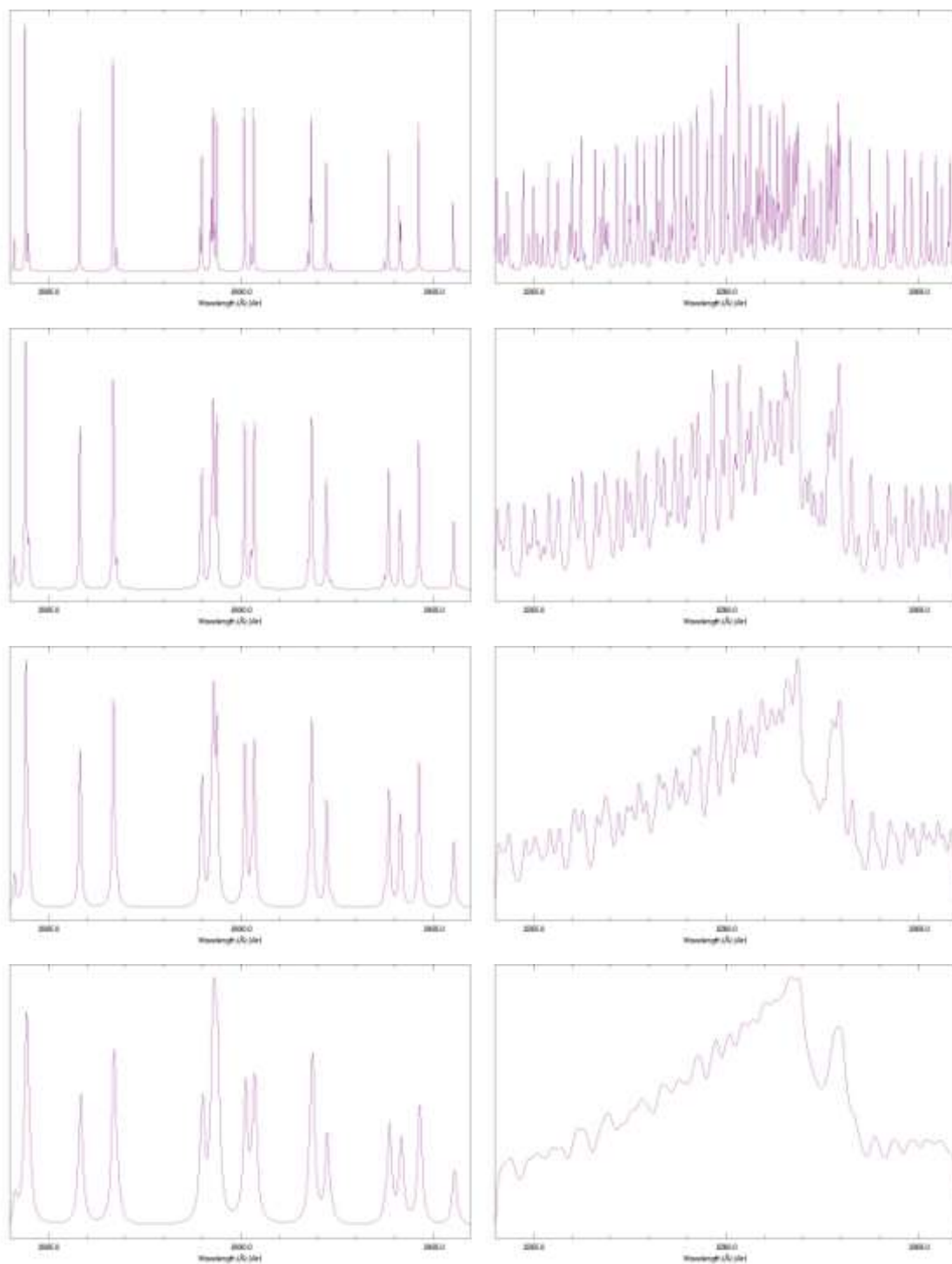


Figure 19 – Collisional broadening and shift for OH at 283 nm (left) and NO at 226 nm (right). Simulated conditions are from the top: 0.1, 0.5, 1 and 2 MPa. All spectra simulated at 700 K, shift is too small to be apparent (e.g. 0.01 nm at 2 MPa for NO) (Luque and Crosley, 1999)

In a similar manner, the thermal motion of molecules results in broadening due to the Doppler effect. The Doppler broadening coefficient is given by (Eckbreth, 1996):

$$\Delta \nu_D = \frac{2 \cdot \nu_0}{c} \cdot \sqrt{\frac{2 \cdot \ln 2 \cdot k \cdot T}{m}} \quad (72)$$

Where $\Delta \nu_D$ is the transition width, ν_0 , the transition centre frequency, c , the speed of light, m , the molecular mass, k , Boltzmann's constant and T , the temperature.

Doppler broadening is dominant at low pressures when collisional broadening is negligible. In the case of diesel combustion however, Doppler broadening is one order of magnitude smaller than collisional broadening.

In practise, the presence of broadening means that the overlap integral – i.e. g_{ν_0} in Equation (58)– between the sharp laser bandwidth and the widened molecule peak decreases (Bessler et al., 2003a, Legris and Domingues, 2004). The overlap integral in the case of a dominant collisional broadening (i.e. Lorentzian absorption lineshape) can be written as (Battles and Hanson, 1995):

$$g = \int_{-\infty}^{+\infty} \phi_{abs}(\nu, \nu_0 + \Delta \nu_s, \Delta \nu_c) \cdot \phi_{las}(\nu, \nu_0, \Delta \nu_{las}) \cdot d\nu \quad (73)$$

Where Φ_{abs} and Φ_{las} are the absorption and laser lineshape functions, ν_0 , the central frequency, $\Delta \nu_s$, the collisional shift, $\Delta \nu_c$, the collisional broadening and $\Delta \nu_{las}$, the spectral FWHM of the laser lineshape

A lower fraction of the molecules can be excited with the same laser bandwidth. This problem is illustrated in Figure 20 where the widths of the same peak are represented for two broadening levels. The two peaks have the same area but the overlap integral is more than twice lower for the broaden peak. Moreover, the absorption line shape may vary because of changing temperature and collisional partners in the measurement plane. Whereas at low pressure these variations stay within the laser bandwidth, at high pressure they can change the result of the overlap integral and the fluorescence yield (Allen et al., 1995).

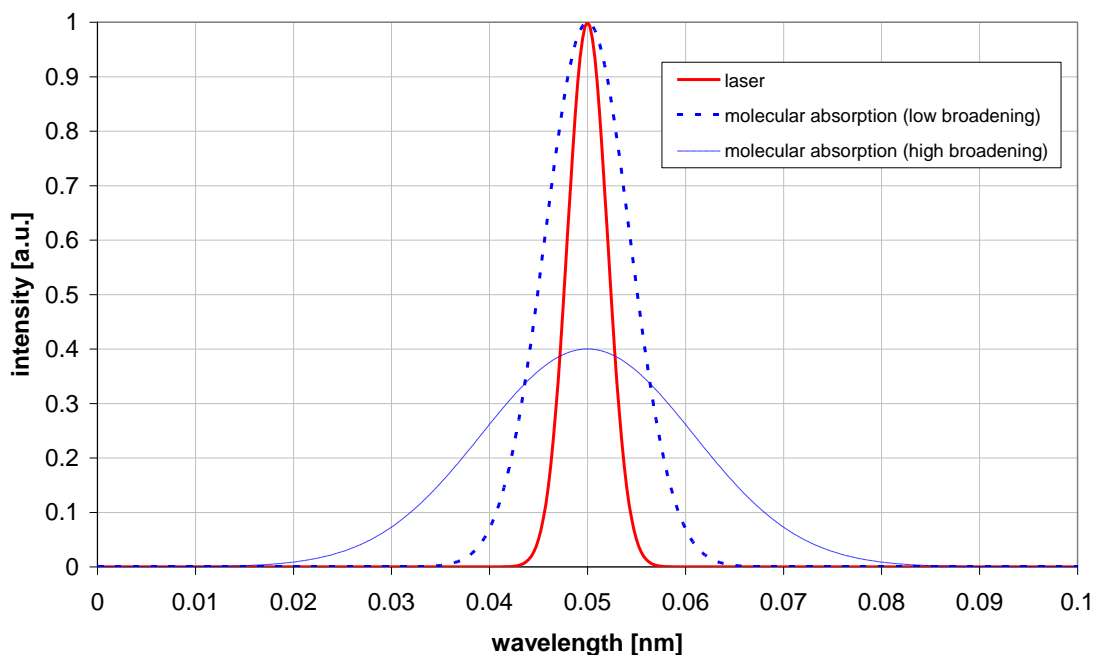


Figure 20 – Decrease in the overlap integral with line broadening

Taking into account the broadening and shifting effects cited above, a series of spectra were obtained at specified pressures with the LIFSim database (Bessler et al., 2003b). The overlap integral was then calculated assuming the laser pulse to be of Gaussian lineshape with a FWHM of 0.002 nm (manufacturer’s specifications). The results show that the overlap can be considered constant over the pressure range of interest. Indeed the absorption peaks of NO and OH are already very broad at the minimum encountered pressure. Moreover, the combination of rather dense absorption spectra and broadband collection means that the laser light can be indifferently absorbed by several transitions. This explains also the differences observed between the two graphs presented in Figure 21.

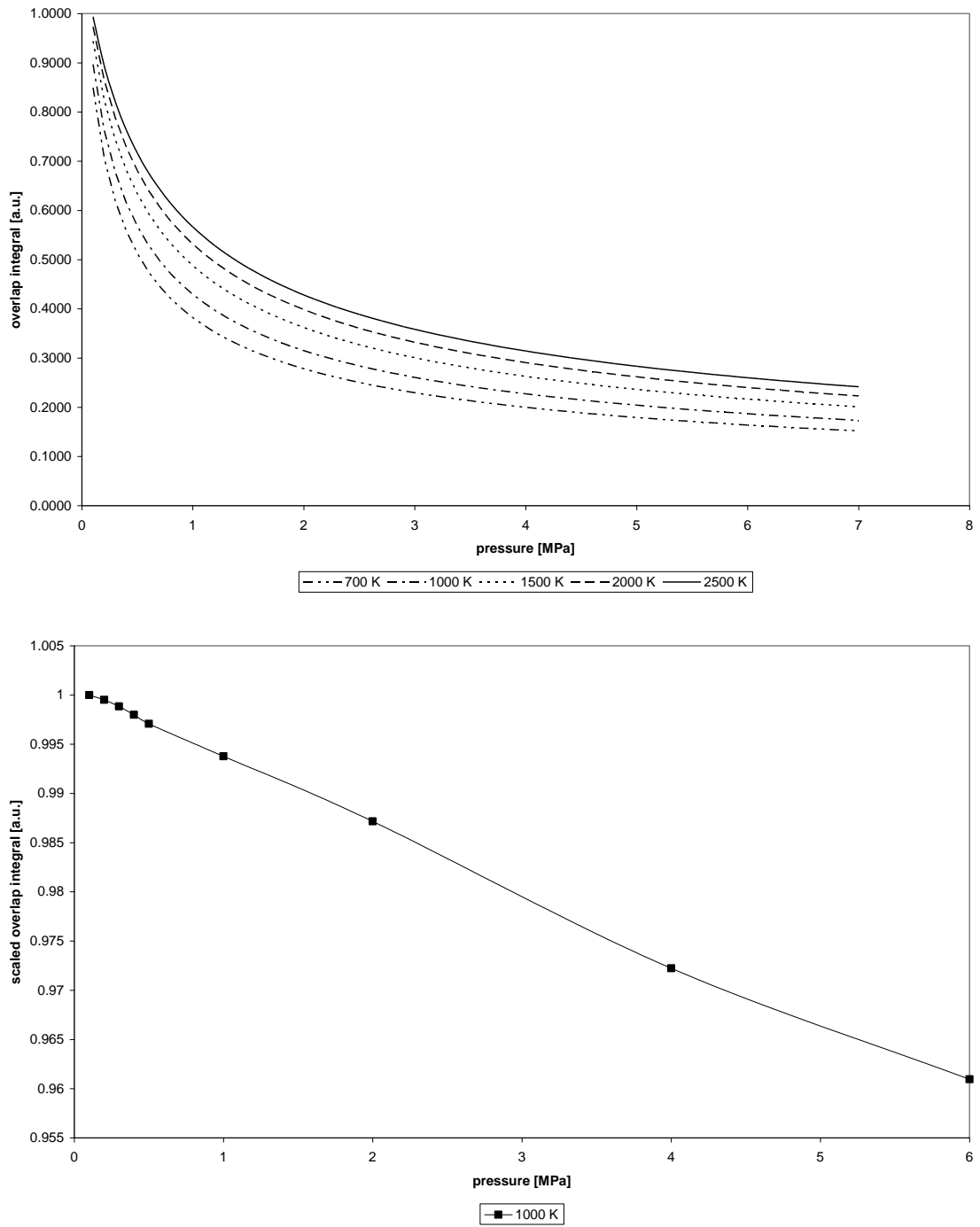


Figure 21 – NO overlap integral between two Gaussian lineshapes (top), and between a Gaussian laser lineshape and a simulated absorption lineshape (bottom)

In the next section a general review of the specific OH- and NO-LIF methodology and associated equipment is given.

3.3.2. Experimental setup

A general experimental setup for the application of planar LIF to combustion is shown in Figure 22.

The engine is generally fitted with quartz windows at the top of the liner to enable the beam to enter the chamber. An optical piston bowl is used and the emission is monitored through it.

If two-dimensional distributions are sought, the laser beam is shaped into a thin sheet, typically 25 mm wide and 0.5 mm thick. The collection system is designed to monitor the fluorescence and filter the interferences.

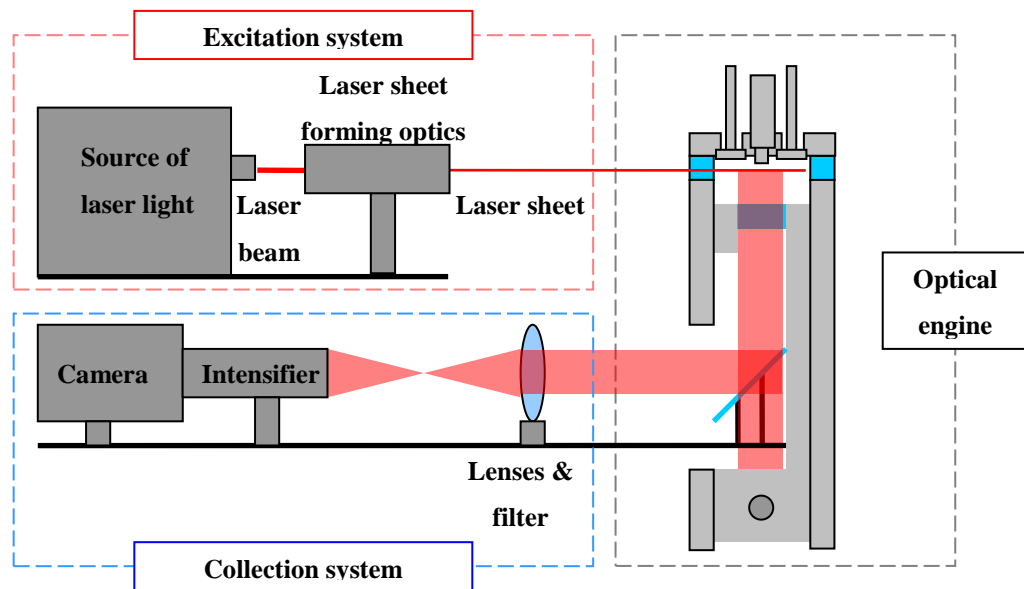


Figure 22 – General laser-induced fluorescence experimental set-up

3.3.2.1. Excitation sources

The excitation scheme is successful if it combines a good selection of transitions and high excitation energy. A good transition must have a highly populated lower level, a low absorbance/interference of the medium at these wavelengths, a low lifetime of the excited state in order to avoid quenching and high oscillator strength to maximize the rate of fluorescence yield. If the transition is considered good enough, it is then necessary to check if any high energy excitation source can be used at the specified

By selecting carefully the dye compound, almost any wavelength from high ultraviolet to infrared can be obtained (see Figure 24). However dye compounds in ultraviolet are either inexistent or have low fluorescence yield rate. Therefore a frequency doubling crystal, either Beta Barium Borate (BBO) or Potassium Dihydrogen Phosphate (KDP), is often used. The output frequency of the laser beam is then doubled and any ultraviolet frequency can be reached. This ensures that the best transitions for OH or NO can be used.

The combined fairly low efficiencies of the dye laser (10-40% depending on the dye compound) and the doubling crystal (typically 20%) lead to laser pulse energies of the order of 10 mJ (Daily, 1997), well below the excimer lasers output. This low energy is the main concern with the use of dye lasers.

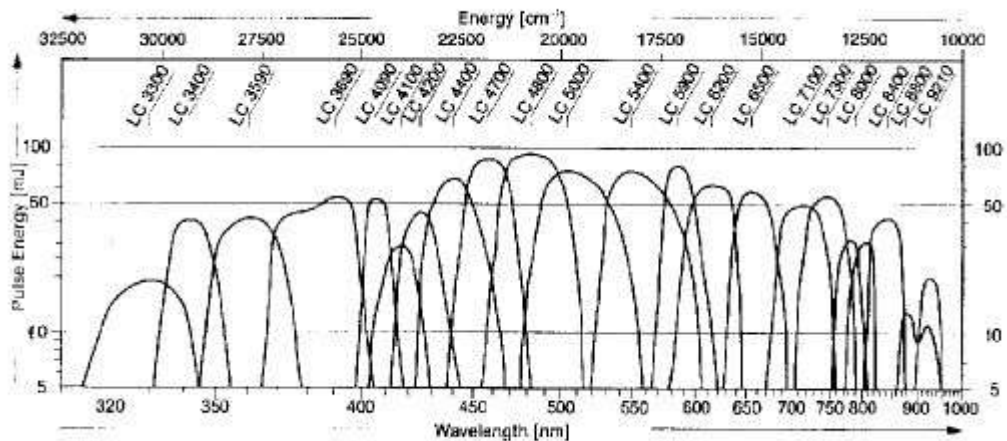


Figure 24 – Laser dyes range (from Brackmann (2000))

Optical parametric oscillators

OPOs are not strictly speaking lasers since they are involving no stimulated emission of light. Their working principle relies on the pumping of a non-linear crystal as Potassium Titanyl Phosphate (KTP). The pump beam enters the crystal at the high frequency ω_{pump} and parametric amplification generates two beams at ω_{signal} and ω_{idler} such that $\omega_{pump} = \omega_{signal} + \omega_{idler}$. The non-linear crystal is placed between two mirrors and resonance of one or both of the generated beam waves in the cavity enhances the interaction in the non-linear crystal (Hecht, 1992). The frequencies ω_{signal} and ω_{idler} can be tuned either by changing the nature of the crystal or its orientation inside the cavity.

OPOs, like dye lasers need to be used in combination with a frequency doubling crystal in order to reach the required wavelengths for OH or NO-LIF.

Although OPOs have a higher efficiency than dye lasers, they are much more sensitive to adjustments and to changes in the working environment. They need to be installed in an atmosphere controlled room and on a vibration damping support.

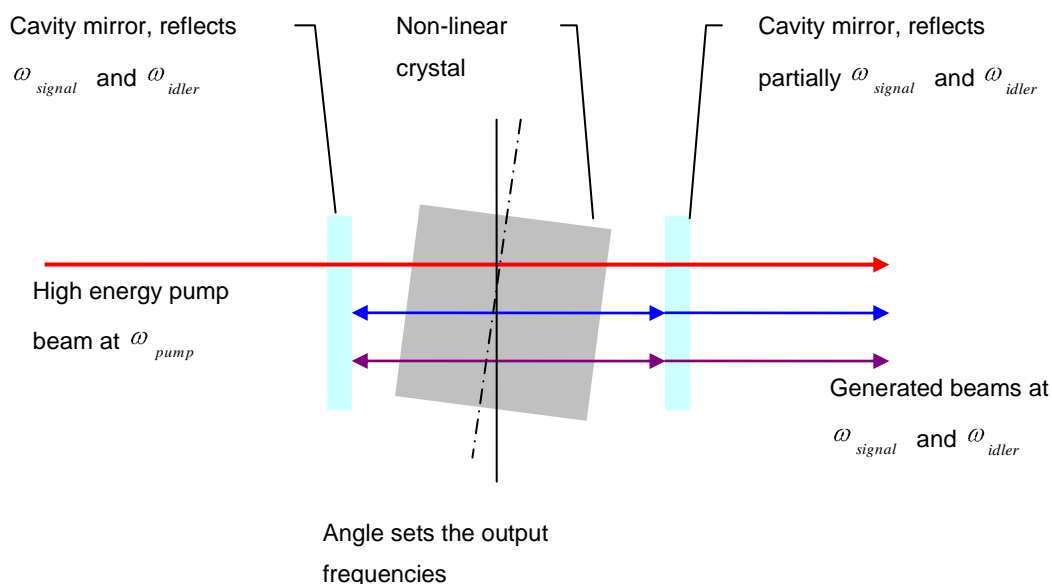


Figure 25 – Parametric oscillator (adapted from Hecht (1992))

3.3.2.2. Optics

Sheet forming optics

Sheet forming optics are composed of several cylindrical lenses which shape the incoming circular cross-section beam into a rectangular cross-section beam. This is the basis for two-dimensional laser-induced fluorescence. Clearly, the thinner the sheet is, the less inaccurate the two-dimensional assumption is. There is however a trade off on the height of the sheet as a smaller sheet allows higher laser energy densities but restricts the region investigated.

3.3.2.3. Optical engine

For PLIF, the engine must have at least two optical accesses at a respective angle of 90°. This is most often achieved by fitting a piston extension on one of the engine cylinders (see Figure 22). The laser sheet enters the chamber horizontally and the fluorescence radiates through the transparent piston. A static mirror at the bottom of the piston extension allows the fluorescence to be monitored for any crank angle.

Windows

The four main requirements for the windows are:

- i. To provide sufficient optical access
- ii. To withstand high pressure and temperature
- iii. To be transparent in the wavelength region of interest
- iv. To be easily cleanable

There are three main materials used for optical windows: fused silica, sapphire and BK7. Their respective transmittances are shown in Figure 26. In most investigations, a skip-fire strategy is applied to reduce window fouling by soot.

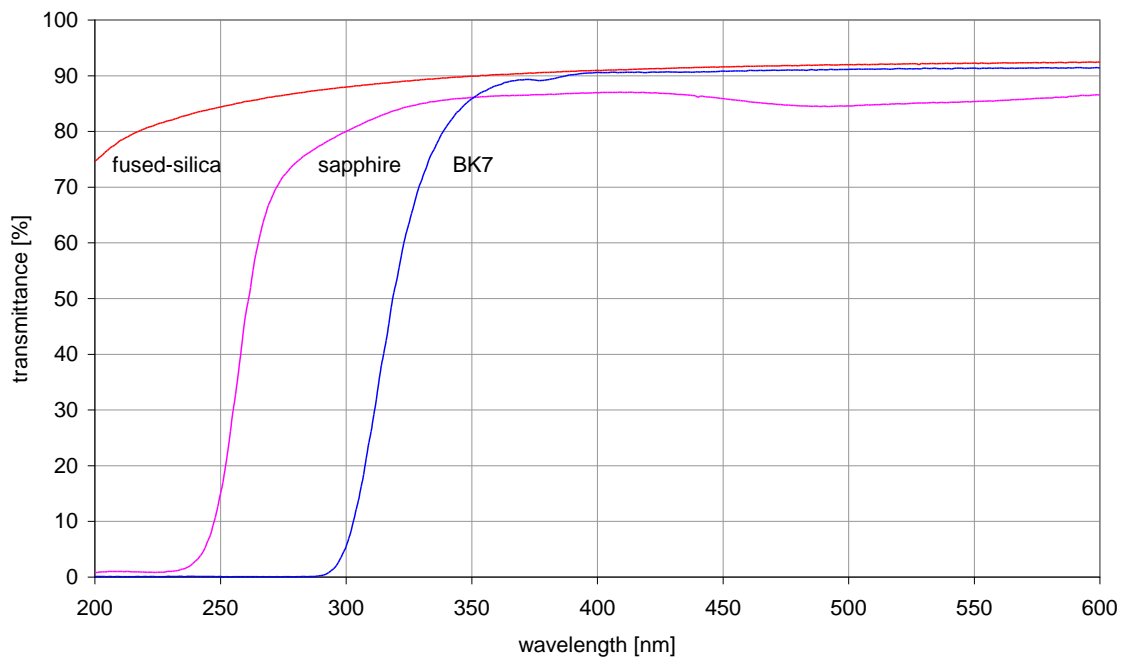


Figure 26 – Measured transmittances for fused-silica, sapphire and BK 7 (spectrograph study of 20 mm thick windows)

3.3.2.4. Collection system

Lens

The lens is selected to maximize the quantity of light collected. Depending on the collection system geometry, their focal length can vary. Still, low $f/\#$ numbers are usually sought.

Intensifier

Intensifiers have two main roles:

- i. They are primarily used to increase the intensity of the signal. They convert the photonic information into an electric signal through a photocathode surface, amplify the signal and convert it back to photons through a phosphor plate.
- ii. Their ability to be gated for very short time allows almost instantaneous pictures to be taken.

Detection

Photomultiplier tube (PMT)

They are composed of a vacuum tube which contains a photosensitive cathode and a collection anode separated by a series of electrodes called dynodes. Their current output is given by:

$$i = \eta \cdot G \cdot \dot{N}_p \quad (74)$$

Where η is the quantum efficiency of the photocathode [-], G , the dynode gain [A.s/photon] and \dot{N}_p , the photon arrival rate [photon/s].

They are extremely sensitive, have fairly low rise times (e.g. 0.1 ns) and a large dynamic range. They are therefore often used for one-dimensional measurements.

Charge coupled camera (CCD)

They consist of arrays of individual CCD detectors. The detectors are made of conducting electrodes overlaying and insulating layer which separates the electrodes from a doped silicon region used for generating the photo-induced charge. As they have satisfactory characteristics, are relatively low-priced and have high spatial resolution

(up to the order of 10^6 elements), CCD arrays are often chosen for two-dimensional optical diagnostics.

The next section presents the relevant OH and NO electronic transition for laser excitation. A summary of the published experimental setups can be found in Table 7 and Table 11.

3.3.3. Excitation/collection schemes for OH-LIF

Even at high temperatures and pressures, the vibrational level with the highest population is the $X^2\Pi v'' = 0$ level. Three different schemes have been designed to take advantage of this feature.

3.3.3.1. The $A^2\Sigma^+ - X^2\Pi (0,0)$ excitation band scheme

OH can be excited from the $X v'' = 0$ level to the $A v'' = 0$ level by photons at around 308 nm. This scheme is popular since 308 nm lies in the range of a high power laser source: the XeCl excimer laser. In general the fluorescence of the red-shifted (0,1) band is monitored. Böckle *et al.* (1999) note that the fluorescence of the blue-shifted (1,0) band is stronger and explains this phenomenon by collisionally induced populations. Although stronger, this fluorescence band is problematic because it is inherently dependent on gas composition, temperature and pressure.

3.3.3.2. The $A^2\Sigma^+ - X^2\Pi (3,0)$ excitation band scheme

The transition from the $X v'' = 0$ to the $A v'' = 3$ level is interesting because of its high predissociation rate. If the pressure is sufficiently low (below 1 MPa according to Ketterle *et al.* (1992)), fluorescence is mainly competing against predissociation and quenching effects can be neglected. This is highly interesting since the rate of predissociation depends only on the nature of the excited molecule whereas quenching depends on gas composition, temperature and pressure (Andresen *et al.*, 1990). Therefore quantitative laser-induced predissociative fluorescence (LIPF) is easier to achieve than quantitative LIF. Here again, an excimer laser output is compatible with the wavelength requirements (KrF excimer at around 248 nm).

However, the ratio of effective fluorescence per excited molecules is lower for LIPF than for LIF (10^{-4} against 10^{-3} in Andersen *et al.* (1990)). Moreover, at very high pressures (above 1 MPa), neglecting quenching is questionable (Ketterle *et al.*, 1992). Finally, the (3,0) vibrational transition is very weak (Dieke and Crosswhite, 1962).

3.3.3.3. *The $A^2\Sigma^+ - X^2\Pi (1,0)$ excitation band scheme*

The last scheme is based again on a transition from the $X v'' = 0$ level, but this time OH is excited to its $A v'' = 1$ level. The major drawback on this scheme is the absence of high power laser sources at the required wavelength (around 283 nm). Dye lasers with their higher tuneability but lower power output have to be used. Fortunately, the fluorescence emission of two different vibrational transitions can be monitored: the A-X (1,1) and (0,0) transitions. The existence of a strong (0,0) emission indicates extensive energy transfers (Allen *et al.*, 1995). This scheme has been extensively applied to gasoline engines (Murase *et al.*, 1998, Nygren *et al.*, 2001), diffusion flames (Bengtsson, 1996, Allen *et al.*, 1995) as well as real diesel engines (Dec and Coy, 1996, Kosaka *et al.*, 1996, Nakagawa *et al.*, 1997). The investigators methodology is remarkably similar and details are summarized in Table 7.

3.3.3.4. *Conclusion*

OH-LIF appears as a quite mature technique and different schemes have been successfully applied. In their comparative investigation, Ketterle *et al.* (1992) concluded that the relative signal strength S of a detection scheme is given by:

$$S = q_{12} \cdot q_{23} \cdot \tau_{eff} \cdot E_v \quad (75)$$

q_{12} and q_{23} are the Frank-Condon factors between the initial (1) excited (2) and final (3) states. τ_{eff} is the effective lifetime of the excited state, limited by predissociation or collisional quenching [s]. E_v is the spectral fluence of the laser, limited by saturation [$\text{J}\cdot\text{cm}^{-2}\cdot\text{s}^{-1}$]. Taking into account the different sources of laser light, the signal strengths can be computed and stand as reported in Table 6.

Table 6 – Signal strengths of different OH-LIF schemes (Ketterle et al., 1992)

λ_{exc} [nm]	λ_{em} [nm]	q_{12}	q_{23}	τ_{eff} [ns]	E_v [J.cm ⁻² .s ⁻¹]	S
248	295	0.011	0.52	0.1	250	0.14
308	343	1	0.004	2	250	2.0
281	312	0.33	0.59	2	30	11.7

It appears that the scheme based on the dye laser, despite its low fluence, exhibits high signal strength. Furthermore, three major investigations of diesel combustion following this scheme have been published. In order to compare results with these publications, the A-X (1,0) scheme was selected.

3.3.4. Excitation/collection schemes for NO-LIF

NO-LIF has been confined for a long time to low-pressure, often seeded, idealised combustion processes (Wodtke et al., 1988, Schulz et al., 1995, Tsujishita et al., 1999, Kanazawa et al., 2001). Although proving the potential of the technique, these experiments did not reach engine-like conditions, especially in terms of pressure and their results were considered to be of limited validity. At high pressure, attenuation of the laser and fluorescence light is a major concern. This explains the lack of early studies in optical diesel engines.

Table 8 – Four lowest states of NO (Daily, 1997)

Electronic State		Energy [keV]	Degeneracy
${}^2\Pi_{\frac{1}{2}}$	X	0	2
${}^2\Pi_{\frac{3}{2}}$		121	2
${}^2\Sigma^+$	A	43.965	2
${}^2\Pi$	B	45.930	4

Nevertheless, these idealised studies brought up some useful conclusions like the potential danger of having interference from hot oxygen (Wodtke et al., 1988, Battles and Hanson, 1995, Schulz et al., 1995), absorption from carbon dioxide and water vapour (Bessler et al., 2003a, Legris and Domingues, 2004), intermediate hydrocarbons interfering with nitric oxide fluorescence or double photon fluorescence and Raman scattering of molecules such as N_2 or H_2O and finally absorption due to high local concentration of NO. Therefore a careful choice of the excitation and collection wavelengths is necessary. From a preliminary review, the less appropriate schemes can be eliminated. For instance, the two-photon technique was put aside despite its high selectivity and collection simplicity. The technique, which consists in exciting the NO molecule in two steps (e.g. two photons at 452 nm), gives indeed signals 50 times lower than single photon LIF. Three main excitation/collection schemes have been thoroughly considered and are presented hereafter.

3.3.4.1. The $D^2\Sigma^+ - X^2\Pi(0,1)$ excitation band scheme

Arnold *et al.* (1992) applied the method previously designed by Wodtke *et al.* (1988) to a direct injection diesel optical engine. The scheme used the D-X (0,1) electronic-

vibronic transition of nitric oxide with an excitation wavelength at 193 nm. This excitation light could easily be obtained from an ArF excimer laser. Moreover, the oscillator's strength of this transition band was the strongest (see Table 9) meaning that the ratio of fluorescence over excitation for a given population should be higher.

Table 9 – Oscillator's strength for the NO molecule (Legris and Domingues, 2004)

Oscillator's strength	Transition band	
4 to $6 \cdot 10^{-4}$	A-X(0,0) to A-X(0,2)	γ -band
$7 \cdot 10^{-5}$	B-X(7,0)	β -band
$3 \cdot 10^{-3}$	D-X(0,1)	ε -band

Despite the relative high energy of the laser pulses (6 mJ), nitric oxide distributions were found only for low pressures (0.5 and 1 MPa). It appeared that the 193 nm laser sheet was especially attenuated in the chamber. Several possible origins to this phenomenon have been identified:

- i. This wavelength is overlapping low energy/high population levels ($v' = 2,3$) of oxygen.
- ii. In their S.I. study, Bräumer *et al.* (1995) reported that absorption of the exciting laser beam at 193 nm was mainly due to intermediates such as unsaturated hydrocarbons, partially oxidized hydrocarbons and PAH molecules.
- iii. Hildenbrand *et al.* (2001) on the other hand, found that almost all the loss of transmission below 300 nm could be attributed to hot CO₂ absorption.

Similarly, Bräumer *et al.* warned that since the transition started from $v'' = 1$, the signal showed a strong temperature dependence. A correction for laser intensity was therefore needed if accurate concentrations were sought.

Following this conclusion, the scheme was applied and improved by several researchers. Brugman *et al.* (1993, , 1998, Brugman, 1998) and later Stoffels *et al.* (1998, , 1999, Stoffels, 1999) proved that, with sufficient energy, carefully selected excitation and collection wavelengths and an appropriate attenuation correction, useful distributions could be obtained.

Brugman *et al.* reported that the transition did not appear to be saturated with a laser energy of 20 mJ/pulse. The use of *n*-heptane instead of diesel fuel did not improve the signal level as expected. This would mean that absorption of laser radiation is similar for both fuels. The signal intensity was reported to increase rapidly as the pressure dropped during the expansion stroke, demonstrating the weight of collisional quenching

at high pressures. The excitation wavelength of 193.377 nm, which corresponds to the rotational $R_1(26.5)/Q_1(32.5)$ transitions, was believed to be free of O₂ absorption.

Another interesting detail is the increase of oxygen concentration in the intake air. It was increased up to 40% in order to reduce soot formation and likewise window fouling. However, oxygen concentration has a very important effect on nitric oxide formation. Considering oxygen enrichment as an opposite measure to exhaust gas recirculation, a consistent outcome is a boosted nitric oxide formation. After all, an EGR level of 30%, sufficient to reduce significantly the NO_x emissions, only reduces the oxygen concentration in the gases to around 16%. Although boosting the oxygen content to such high levels has the enviable consequence of increasing the fluorescence signal, the conditions could deviate from real diesel combustion conditions.

Stoffels *et al.* identified the O₂ $B^3\Sigma_u^+ \leftarrow X^3\Sigma_g^- v'' = 2,3$ fluorescence lines at 211, 217.5 and 225 nm. Although those lines are very close to the NO emissions at 208, 216, 225 nm, their narrow doublet structures allow differentiation. Likewise, the O₂ emission, due to its fast predissociation, is less sensitive to pressure changes than NO. The proportion of O₂ fluorescence in the signal will then be highest around TDC.

3.3.4.2. The $A^2\Sigma^+ - X^2\Pi(0,2)$ excitation band scheme

More recently, Hildenbrand *et al.* (2000a, , 2000b) focused on the use of the A-X (0,2) electronic-vibronic transition of nitric oxide. Once again, the study was based on a former low-pressure scheme (Schulz et al., 1995). As the excitation wavelength of this band is around 248 nm, KrF excimer lasers were an appropriate source of excitation. The relatively high energy output of these lasers (as much as twice the one of ArF) gave the approach a solid basis. The originality of the scheme came from the monitored wavelength. In order to avoid the high fluorescence contribution of hot oxygen (above 250 nm) and intermediate hydrocarbons (above 260 nm), a choice was made to monitor fluorescence shifted toward shorter wavelengths i.e. emission from the (0,1) band at 237 nm. This was necessary as analysis of emission spectra showed that fluorescence interference was especially high above 255 nm. This collection scheme was affected by the high dependence of anti-Stokes emissions on collisional background. The fluorescence signal strength would still be a function of NO densities but to an increasing extent (yet an unknown extent) of local conditions. Here again, oxygen concentration was boosted (up to 28%).

Some averaged NO-LIF distributions were obtained without oxygen enrichment for different injection configurations. The general signal level was low but increasing with injection pressure and a correction for laser attenuation was applied. The systematic error in the NO concentration due to local temperature variations was found to be $\pm 20\%$ between 1800 K and 2500 K. This scheme was less sensitive to temperature deviations than the D-X (0,1) scheme. Interestingly, the attenuation correction is scaled on a study of O₂ B-X (2,7) band fluorescence.

3.3.4.3. The $A^2\Sigma^+ - X^2\Pi (0,0)$ excitation band scheme

The third and last excitation/collection scheme was initiated by Alatas *et al.* (1993). The scheme consisted of exciting the first vibrational level of the ground state into the lowest excited electronic state i.e. through the A-X (0,0) electronic-vibronic transition at 226 nm. The first vibrational level of the ground state was more populated than the second or third, as used in the two other schemes (Figure 18). This should result in stronger signals for comparable excitation power. Unfortunately, no excimer laser has an output range including 226 nm and another technical solution had to be selected.

Alatas *et al.* used a dye laser, but because dyes fluorescing in ultra violet are rare and of low efficiencies, a frequency conversion unit was used to double the output frequency. To maximize the output power of this assembly, a Neodymium - Yttrium Aluminium Gasket (Nd:YAG) laser was chosen to pump the dye.

Nakagawa *et al.* (1997) followed a similar scheme. Both studies were impeded by low signal due to laser attenuation, especially in the early phase of combustion. In both cases, oxygen concentration in the inlet air was boosted in order to increase the signal. Alatas *et al.* report an increase of nitric oxide in the tailpipe from 120 ppm to 1100 ppm when the oxygen content of air was boosted to 29%. Interference from laser-induced polycyclic aromatic hydrocarbons (PAH) fluorescence was a concern only for early crank angles after top dead centre (TDC). Nakagawa *et al.* (1997, , 1998) reported that data from five combustion cycles had to be added to obtain exploitable distributions of nitric oxide.

In 1993, Alatas *et al.* concluded that additional work was necessary with required improvements in the detection sensitivity and laser pulse energy.

One of the most interesting studies on nitric oxide distribution in an optical diesel engine was published by Dec & Canaan (1998). The A-X (0,0) electronic-vibronic

transition scheme was followed with the innovative use of an optical parametric oscillator (OPO) instead of the dye-laser. The OPO is more complicated than a classic dye-laser but the authors claim output energies 5 times higher than those of Alatas *et al.* and Nakagawa (i.e. 12-15 mJ/pulse). This was a direct solution to one of the problems identified 4 years earlier by Alatas *et al.*. This high energy combined with a high sensitivity collection system gave this investigation a major advantage on its predecessors: there was no need for oxygen enrichment.

The excitation wavelength - 226.035 nm, the same as for Battles & Hanson (1995) and Di Rosa *et al.* (1996) despite the higher pressure - has been chosen to minimise oxygen absorption while being close to peak nitric oxide absorption. Polycyclic aromatic hydrocarbons (PAH) fluorescence was found of very low intensity and a series of filters were carefully selected to properly collect the targeted spectrum (see Table 11).

3.3.4.4. Conclusion

This review brings out the absorption of the laser sheet/signal as the main problem to overcome. Therefore, longer excitation wavelength are preferable and the D-X (0,1) band scheme had to be crossed off the list (see Table 10).

Table 10 – Absorption of the laser beam 13°c.a. after ignition in a gasoline engine for an equivalence ratio of 1.0 (Schulz et al., 1997)

Wavelength [nm]	Absorption [%·cm ⁻¹]
193	95
225	25
248	5

Despite the low population of the second vibrational level of the ground state, the A-X (0,2) scheme appears as the most appropriate with very low levels of absorption and the high energy of KrF lasers.

The A-X (0,0) band scheme may be more sensitive at low temperatures and concentrations of NO but the absence of high energy laser sources at 226 nm is a major concern. However, because of the availability of a dye laser, it has been decided to implement the A-X (0,0) band scheme. The optimisation of the dye laser power output and of the collection efficiency should allow signal-to-noise ratios to be high enough. The careful selection of the wavelength – with the help of a spectrometer – will allow

O₂ interferences to be avoided. If necessary, the in-cylinder conditions can be tuned to minimize absorption. Finally, as the flame will be investigated from side to side, the laser sheet should encounter only small amounts of high absorption burnt gases before the flame, resulting in lower absorption levels than those reported in Table 10. Likewise, the NO distribution of half of the flame only will be necessary if symmetry is assumed. Table 11 summarizes the published NO-LIF investigations of interest.

The next chapter presents the details of the equipment used to apply the selected techniques.

4. APPARATUS AND SETUP

In this chapter the apparatus employed during the investigation is presented. In addition, its limitations, the necessary calibrations and some methodology characteristics are introduced.

4.1. High-pressure spray rig

The rapid compression machine is a modified single-cylinder engine with a bore of 135 mm and a stroke of 150 mm first described and tested by Kennaird *et al.* (2000). It was converted to two-stroke cycle operation and an optical chamber was incorporated between the cylinder and the head increasing the displacement to 2.2 litres (Figure 27).

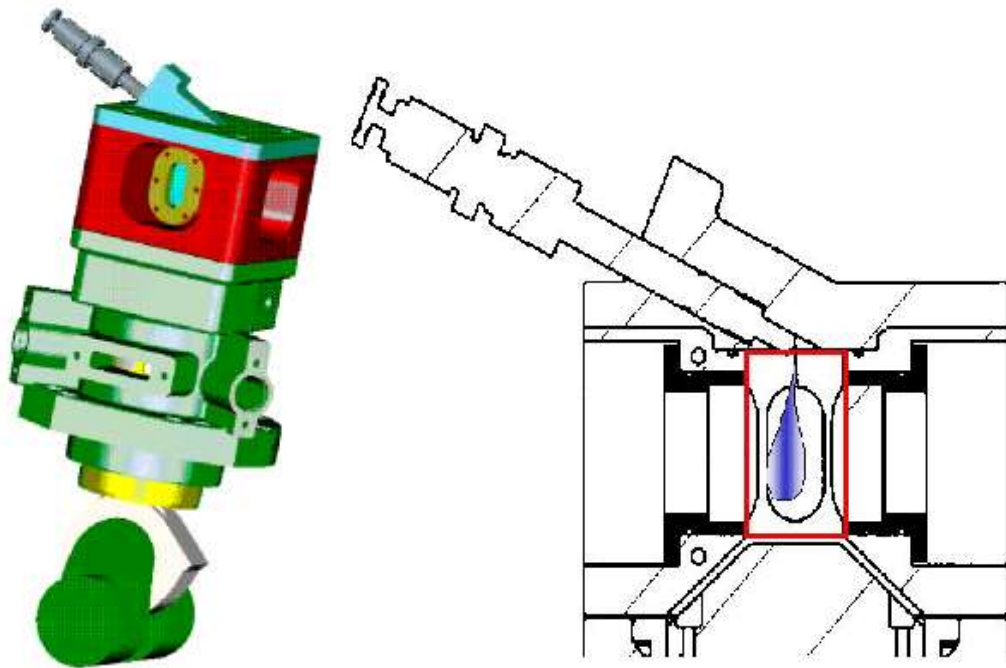


Figure 27 – Design of the optical chamber

Because of this larger combustion chamber, the compression ratio dropped to 9:1. In order to keep engine-like conditions during injection (around TDC), the intake air was boosted up to 0.8 MPa and the temperature up to 373 K. These corrections allow a TDC pressure of 12 MPa and temperature of 721 K to be reached. The RCM was run at a constant speed of 500 rpm. The in-cylinder pressure was monitored on an oscilloscope and manually fine-tuned by controlling the boost pressure. A back-pressure valve could

be closed to limit the quantity of compressed air needed. This valve also controlled the amount of internal gas recirculation. Further details of the RCM and the operating conditions are presented in Table 12.

The optical chamber was 80 mm in height and 50 mm in diameter. This allowed a single fuel spray to be injected vertically without any impingement on the walls or the windows. The chamber was designed to obtain near-quiet conditions so that the air flow dependence of the spray development would be negligible. Once again, to maintain engine-like conditions, a water jacket was designed to heat the cylinder head up to 95°C. Emersion heaters were fitted in the crank case to heat the sump oil up to 60°C. These temperatures and a number of other parameters (Table 13) were controlled by the use of

Table 12 – Rapid compression machine operating conditions

Type	Two-stroke, one-cylinder DI
Bore	135 mm
Stroke	150 mm
Displacement	2.4 l
Compression ratio	9:1
Exhaust port opening	85°c.a.
Inlet port opening	95°c.a.
Speed	500 rpm
Water temperature	90°C
Oil temperature	60°C
Firing rate	Every 10th cycle
Start of injection	15°c.a. bTDC
Injection pressure	60-160 MPa
Motored TDC pressure	4-7 MPa
Motored TDC temperature	720 K
Intake air temperature	393K
Intake air pressure	0.2-0.3 MPa absolute
Injection system	Bosch 2 nd gen. common rail
Injector / nozzle	Bosch single hole Ø0.2 VCO
Cone angle	135°
Injected volume	30 mm ³
Injection duration	2.4 ms-4.2 ms (160- 60 MPa)

transducers, PID controllers and a custom-built software. The windows were designed to be easily removable for cleaning and replacement. The optical access was measured as 25 mm wide and 55 mm high (Figure 28). Windows with different optical materials (BK7, sapphire, fused-silica) have been manufactured.

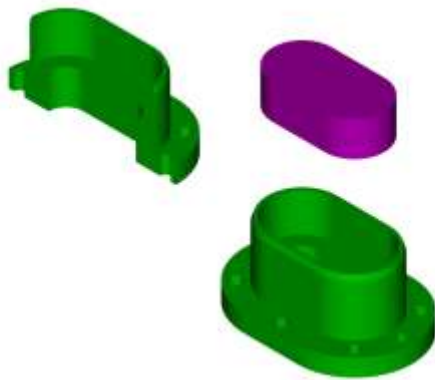


Figure 28 – Glass holder design (Crua, 2002)

The windows had to be cleaned frequently. Whereas fouling was not always apparent at visible wavelength, a spectrograph analysis proved that the absorption of the windows at the wavelengths of interest was increasing rapidly with the number of engine cycles (see Figure 29). An extensive investigation revealed that the fouling was caused by oil coming from the sump past the piston rings. An additional piston ring was fitted and the fouling problem solved. A sapphire window was specifically installed in the laser path to make sure that the remaining laser UV. light would not exit the combustion chamber or be scattered.

The windows had to be cleaned frequently. Whereas fouling was not always apparent at visible wavelength, a spectrograph analysis proved that the absorption of the windows at the wavelengths of interest was increasing rapidly with the number of engine cycles (see Figure 29). An extensive investigation revealed that the fouling was caused by oil coming from the sump past the piston rings. An additional piston ring was fitted and the fouling problem solved. A sapphire window was specifically installed in the laser path to make sure that the remaining laser UV. light would not exit the combustion chamber or be scattered.

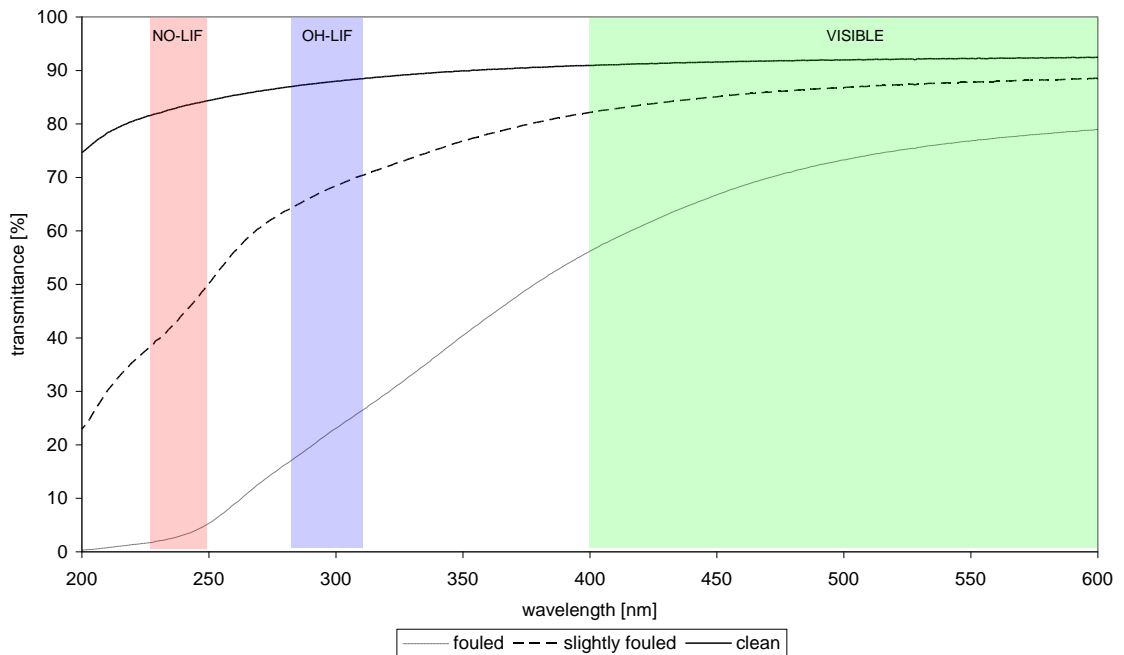


Figure 29 – Fouling of fused-silica windows

Table 13 – Engine control and reading parameters

Parameter	Transducer	Type	Range	Control		
				Actuator	Type	Typical variations
Water temperature	Thermocouple	Type K	200°C	Emersion heater	PID	±2°C
Sump oil temperature	Thermocouple	Type K	200°C	Emersion heater	PID	±10°C
Plenum air temperature	Thermocouple	Type K	200°C	Air heaters	PID	±3°C
Exhaust gases temperature	Thermocouple	Type K	700°C		No	
Oil circuit pressure	Silicon diaphragm sensor	Druck PDCR 810-0799	7 bar		No	±0.3 bar
Plenum pressure	Silicon diaphragm sensor	Druck PDCR 810-0799	10 bar	Boost valve	Manual (Oscilloscope)	±0.1 bar
Barrel pressure	Piezoresistive sensor	Kistler 4045A10	10 bar		No (depends on Plenum pressure)	
In-cylinder pressure	Water-cooled Piezoresistive sensor	Kistler 6061	250 bar		No (depends on Plenum pressure)	±2 bar at TDC
Exhaust pressure	Piezoresistive sensor	Kistler 4045A10	10 bar		No (depends on Plenum pressure)	
Rail pressure	Piezoresistive sensor	Kistler 4067A2000	2000 bar	Fuel pump duty cycle	Calibrated	±30 bar
Injection current	Current clamp	Chauvin Arnoux E3N	100 A		Calibrated	±0.2A
Engine speed	encoder	3600 pulses per revolution		Dyno control	Manual	±1%

4.2. Fuel injection equipment

A high-pressure, second generation Bosch common rail, fuel injection equipment (FIE) was fitted with different available injectors and nozzles (Table 14). Single-hole nozzles were mounted on injectors inclined at an angle of 67.5° , such that the fuel spray would be oriented vertically (Figure 27). High speed video and injection rate studies have proved the behaviour of these single-hole nozzles comparable to the one of multi-hole nozzles (Kennaird et al., 2000, Morgan et al., 2001, Crua, 2002). There are discrepancies at the start of injection due to needle oscillation but the main part of the injection is identical, apart from a lower volumetric flow of fuel for the single-hole nozzles (see Figure 30).

Table 14 – Nozzle library

	Micro-Sac	Mini-Sac	VCO
Hole size [μm]	100	100	100
	140	160	150
	160	200	200
	180		
	200		

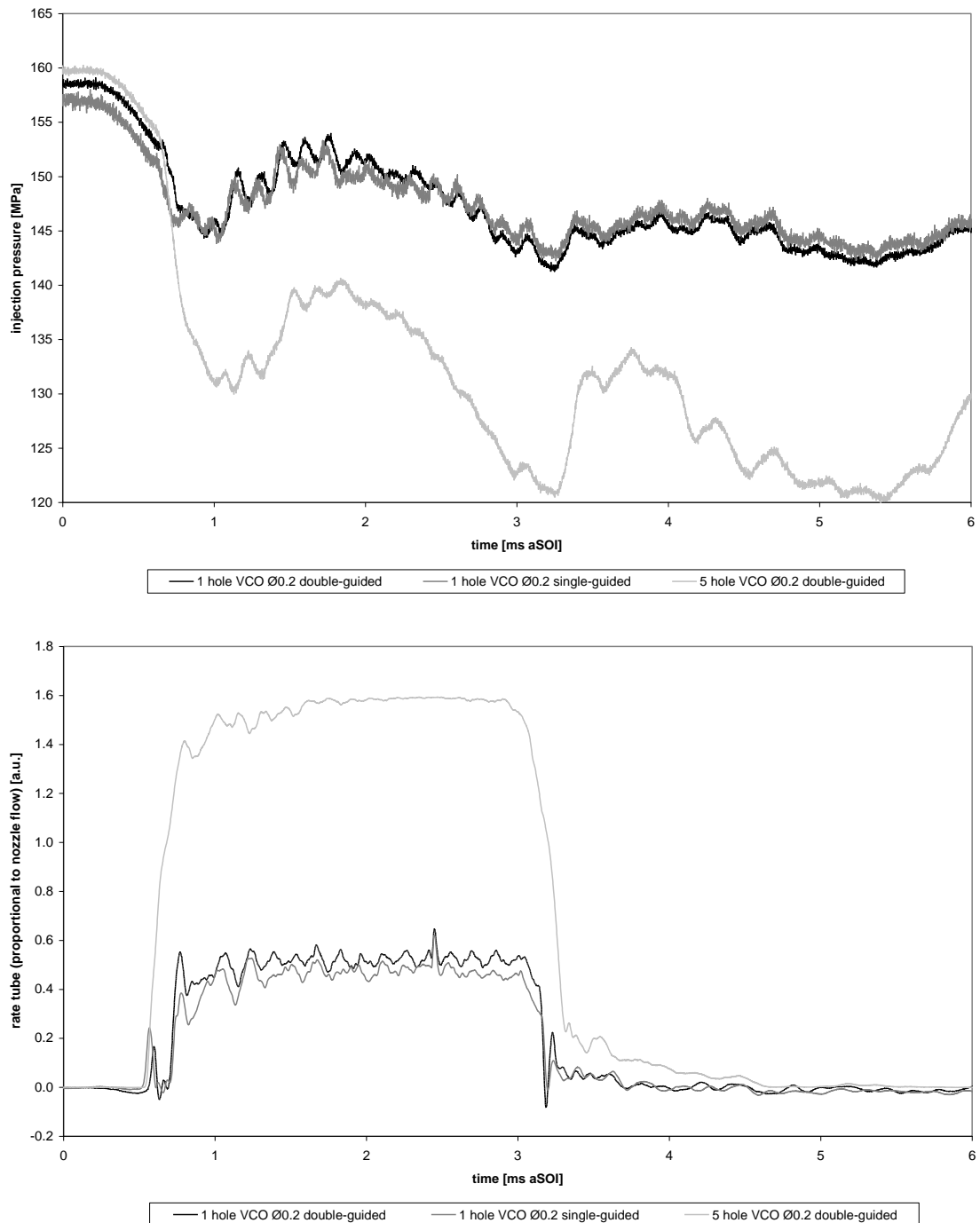


Figure 30 – Rate tube comparison of multi- and single-hole nozzles. The area under the curve is proportional to the quantity of fuel injected. Above: corresponding rail pressure drops

Nozzles of the VCO, mini-sac and micro-sac type were used. Although the VCO nozzles have very precise deliveries in terms of timing and quantity, they introduce discrepancies in spray formation between the different holes. This can be explained by the architecture of the nozzle itself. In VCO nozzles the holes lead directly to the needle

seat area (hence the name VCO: valve covered orifice) and are therefore shut by the needle itself. Consequently, the injections are very sensitive to needle/nozzle concentricity.

To increase injections consistency, mini-sac nozzles were introduced (Figure 31). In this design the constant volume of fuel existing between the needle and the holes ensures a better repartition of the fuel flow. Unfortunately, the fuel in the sac can result in fuel droplets leaving the injector after the needle has shut. For that reason manufacturers have been trying to reduce the volume of the sac by introducing micro-sac nozzles.

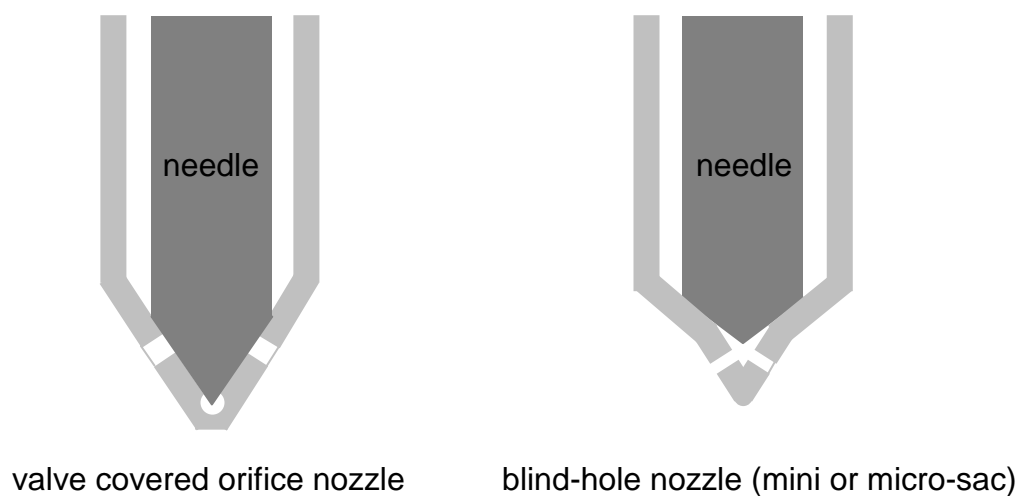


Figure 31 – Nozzle types

The custom-built FIE controller was calibrated thanks to measurements from a Lucas rate gauge and the pressure readings from the Kistler inserted in the fuel pipe. The controller allows single as well as multiple injections with variable timings. The injection current pulse was calibrated to be identical to a standard Bosch ECU pulse (see Figure 32). To allow a flexible control of the injection pressure, the fuel pump was powered by an electric motor running at 1430 rpm. This ensured a stable, independent controlled, rail pressure with minimal fluctuation.

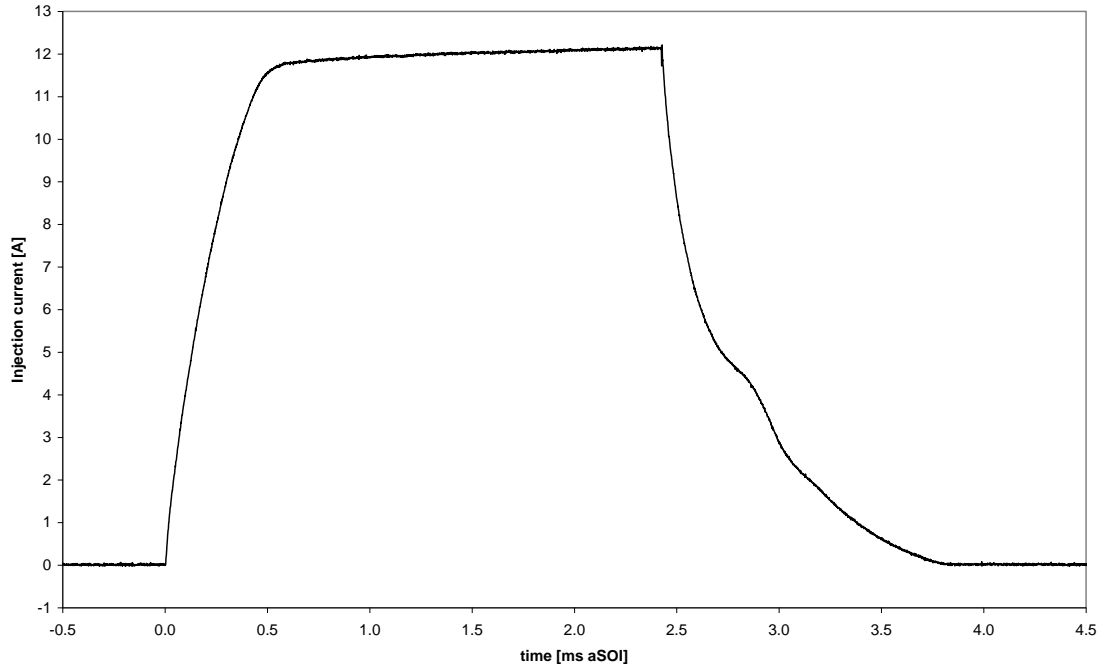


Figure 32 – Injection current pulse from the custom made FIE controller

4.3. Lasers

4.3.1. Description

A Nd:YAG (Neodymium Yttrium Aluminium Garnet) laser was used either to pump the dye laser for the LIF studies. The laser was a Spectra-Physics Quanta-Ray® GCR 150, capable of delivering pulses of 300 mJ at 532 nm (155 mJ at 355 nm) at a frequency of 10 Hz. The laser pulses were spatially and temporally Gaussian with a beam diameter of 8.7 mm and pulse length of 6-7 ms at FWHM. The laser manufacturer quoted a pulse-to-pulse energy fluctuation less than 3% and long term power drift less than 5% over 8 hours.

As previously mentioned, a 3-stage dye laser was pumped for the LIF studies. The Precision Scan® Sirah dye laser equipped with the 3000 lines/mm groove density single grating yield output with linewidth of ± 0.001 nm. The overall efficiency of the resonator, pre-amplifier and amplifier is specific to the dye pumped. The polarised output beam divergence is less than 0.5 mrad. In order to reach the desired UV

wavelength for the LIF investigations, the laser was equipped with a second harmonic generator. It consisted of a non-linear UV crystal (BBO – beta barium borate) and a compensator that corrected the parallel displacement of the laser beam due to the BBO. This second harmonic generator efficiency is limited to 20%.

4.3.2. Calibration

Due to the rather large changes in crystal temperature, the orientation of the crystal had to be adjusted not only when the wavelength was altered but at regular intervals in order to maintain an optimal energy output. Because this procedure could unfortunately not be done frequently enough, the energy output of the dye laser varied considerably. The crystal was therefore equipped with a temperature stabilisation system. The unit stabilises the crystal temperature with an accuracy of 0.1°C. Moreover, a laser pulse energy was recorded and associated with each camera capture.

The dye molecules can absorb so much energy that their binding energy is surpassed and the molecule dissociates, or at least changes its structure. The ability of the dye molecules to keep their fluorescing power at a high level determines how often they have to be replaced. Table 15 reports these photochemical stabilities for the dyes of interest.

Table 15 – Photochemical stabilities of dyes (Brackmann, 2000)

Dye	Centre of emission [nm] (after doubling-crystal)	Lifetime for half maximum efficiency [kW/l]	Lifetime for half maximum efficiency in this case study [h]
Coumarin 47	470 (235)	45	60
Rhodamine 6G	590 (295)	316	210

The dye laser calibration is ensured by fine adjustments of the position of the gratings and the output coupler. These adjustments were set at the delivery of the system and were not altered. The dye laser manual specifies a wavelength precision of < 30 pm and a bandwidth of 2 pm. An ICCD spectrometer was used to verify these specifications.

The spectrometer needed to be calibrated every time its gratings or optical alignments were changed. The most precise grating (2400 grooves/mm) gave a dispersion of 1.25 nm/mm, hence a maximum theoretical resolution of 30 pm. On the other hand the large band grating (150 grooves/mm) offered a dispersion of 20 nm/mm and a maximum theoretical resolution of 500 pm. The maximum theoretical resolutions were computed considering the CCD chip as the limiting component. The densest grating was

used to ensure maximum resolution. The spectrometer was calibrated to follow the peaks of a mercury lamp. It is obviously better to calibrate on a peak close to 226 nm, the closest usable peaks being at 253 nm and 404 nm. The error on the measurement is reported to be linear by the spectrometer's manufacturer. Figure 33 reports the measured error for a calibration at 253 nm and at 404 nm.

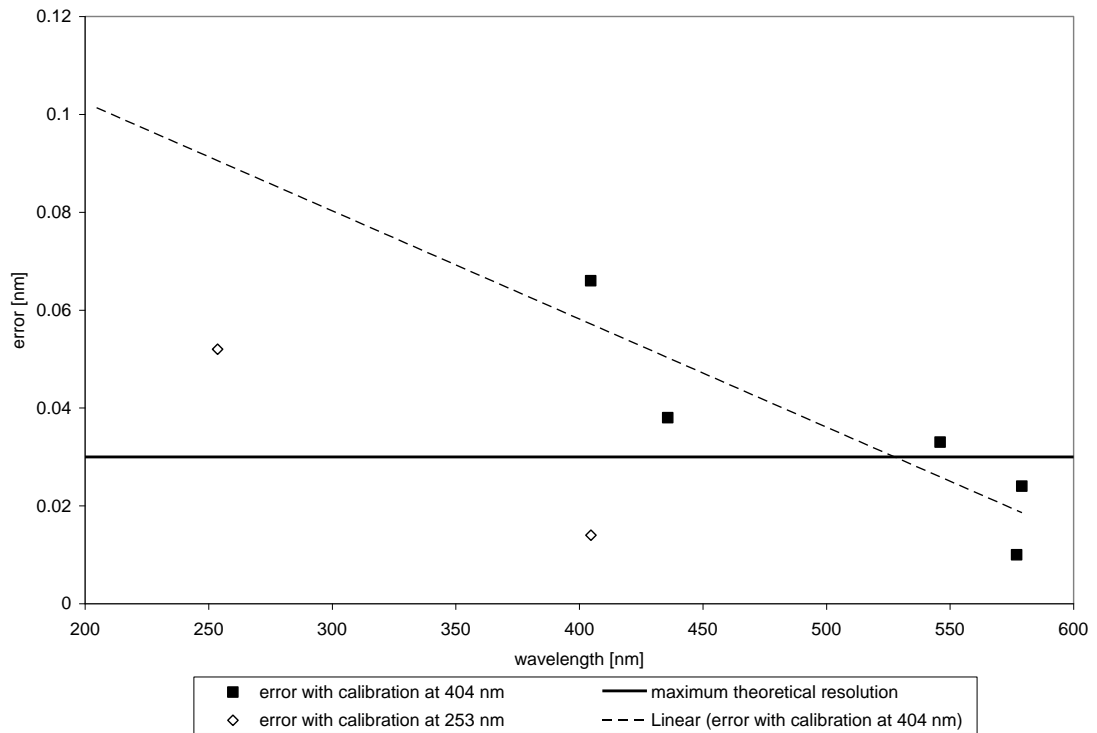


Figure 33 – Measurement error

It appeared that even in the best case, errors around 226 nm are in the range 0.05-0.1 nm. This is up to 3 times higher than the maximum theoretical resolution mentioned previously. Indeed, whereas the resolution of the spectrometer was relatively high, its accuracy was specified at ± 0.2 nm for a grating of 1200 grooves/mm. The figure of 0.1 nm with the 2400 grooves/mm grating seems then consistent.

The dye laser output was analysed at three wavelengths: 225.5, 226.0 and 226.5 nm. Three sets of spectrometer measurements for different calibrations were recorded for each wavelength (Figure 34). The dye laser wavelength output was around 0.1 nm away from the targeted wavelength. Considering the level of error on measurements, the calibration of the dye laser seems correct.

The linewidth of the dye laser peak was several orders too wide. This however was not linked to the accuracy but the resolution of the spectrometer. We previously said that

the maximum theoretical resolution of the densest grating is 30 pm. This is true if we consider the CCD chip as the limiting component. However it appeared that the optical resolution of the spectrometer was lower. This resolution was specified at 0.1 nm at 435.8 nm with a 1200 grooves/mm grating. It results that the linewidth of a laser cannot be verified with this spectrometer.

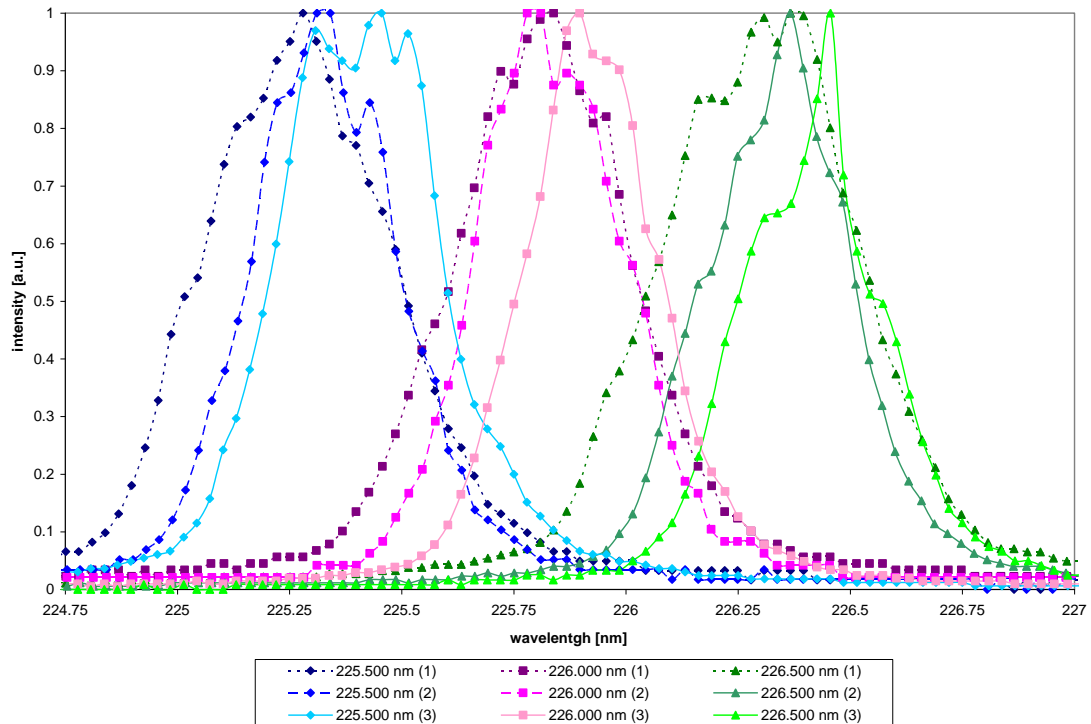


Figure 34 – Dye laser spectrum acquired with narrowband sweeps of a spectrometer for the dye laser set at 3 different wavelengths: 225.5, 226.0 and 226.5 nm

4.3.3. Synchronization

The Nd:YAG laser allowed a pulse frequency range from 9.30 to 10.90 Hz with an optimum frequency at 10 Hz. For the measurements to be averaged over several cycles it was necessary to synchronize the laser pulse with the injection timing. As previously mentioned, the two-stroke RCM was run at a constant speed of 500 rpm. Although the maximum frequency for injections was therefore 8.33 Hz, a skip-cycle strategy was usually applied and the firing frequency was therefore lower. The skip-cycle strategy's two main purposes were first to ensure full scavenging of burnt gases and secondly to reduce window fouling. Skipping cycles was also beneficial to the dye laser energy output. A longer time for dye circulation between two pulses improves both the dye

lifetime and the pulse energy level. The laser pulse frequency being higher than the injection frequency, several skip-cycle strategies were possible. Figure 35 illustrates the relation between the injections and the allowed laser frequencies. The first conclusion drawn from Figure 35 is that at least 3 cycles need to be skipped before the frequencies can match. From 3 cycles skipped on, all strategies are within the laser frequency range. However, moving away from the optimal frequency comes at a power output cost. Consequently the strategies closer to these optimal frequencies are preferable.

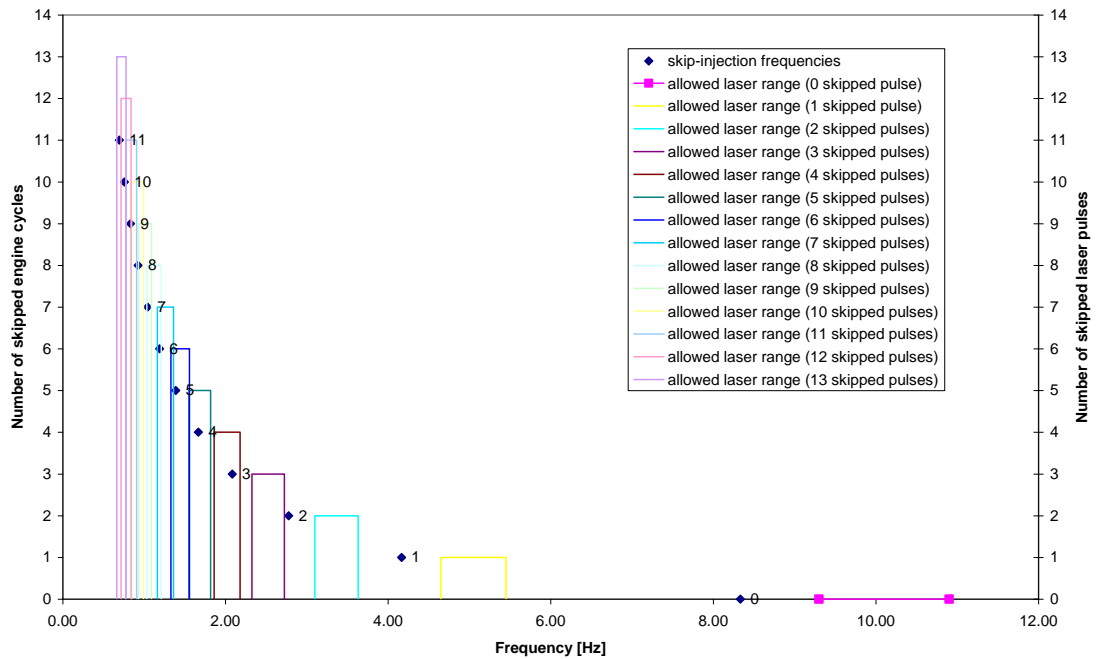


Figure 35 – Synchronization laser-engine

Table 16 relates the different strategies and their distance from an optimal laser frequency. The skip-cycle strategies following the $4 + 5 \times n$ relation – i.e. 4, 9, 14... - are exactly matching a natural laser frequency and are therefore the optimal combinations. The frequency of the laser system was altered by tuning its engine-synchronisation module (LaVision ‘YEX’ module).

Table 16 – Best laser-engine synchronizations

Number of skipped cycles [-]	Injection frequency [Hz]	Best synchronization		
		Number of skipped pulses [-]	Optimal laser frequency [Hz]	Frequency change [%]
0	8.33	-	-	-
1	4.17	-	-	-
2	2.78	-	-	-
3	2.08	4	2.00	4.17
4	1.67	5	1.67	0.00
5	1.39	6	1.43	2.78
6	1.19	7	1.25	4.76
7	1.04	9	1.00	4.17
8	0.93	10	0.91	1.85
9	0.83	11	0.83	0.00
10	0.76	12	0.77	1.52
11	0.69	13	0.71	2.78
12	0.64	15	0.63	2.56
13	0.60	16	0.59	1.19
14	0.56	17	0.56	0.00
15	0.52	18	0.53	1.04

4.4. Optics

The laser beam was directed towards the engine windows by a set of UV mirrors. A small fraction (up to 4%) of the beam energy was directed to an energy monitor and a pulse energy trace was associated to each recorded picture.

The beam was then shaped into a thin vertical sheet typically 0.5 mm thick and 40 mm high by a set of four lenses (Figure 36). The first lens expanded the laser beam vertically until the third lens collimated the resulting cone into a parallel laser sheet. As the beam diameter was rather large (2-3 mm), a second set of two lenses was necessary to produce a thin laser sheet. Therefore the second lens narrowed the thick sheet and the fourth lens collimated the laser into a thin sheet. The laser sheet entered the combustion chamber and crossed the vertical flame from side to side.

It quickly became evident that the laser pulse energy was restricted by the fouling of the mirrors and lenses. At u.v. wavelengths, up to 50% of the energy could be lost because of the dusty and polluted environment of the laboratory. Therefore optics and laser components were cleaned regularly with a fast evaporating chemical (isopropanol).



Figure 36 – Sheet forming optics

4.5. Collection system

4.5.1. Description

The collection system consisted of filters, lenses and an image acquiring device. Depending on the investigation, two different types of cameras were used.

- i. A high-speed video camera was used for the spray and flame descriptions. This Phantom® V7.1 camera from Vision Research Inc. was equipped with an 8 bit monochromatic CMOS chip. The resolution was kept low at 128x256 pixels to reach a frame rate of 41100 frames per second. The exposure time was set to 2 μ s in order to ensure sufficient image sharpness.
- ii. An ICCD DoubleShutter Sensicam® from Pulse Photonics Ltd was used for the LIF investigations. The camera could acquire monochromatic images up to 1280x1024 pixels with a resolution of 12 bits and a limited frame rate of 9 frames per second. An image intensifier was introduced between the lenses and the camera to improve the camera spectral range. The natural spectral sensitivity of the chip was indeed limited to the 340-700 nm FWHM range. The second advantage of the intensifier was its fast gate capabilities – i.e. its 5 ns minimum exposure time compared to the 100 ns of the camera. Very short exposure times were necessary to make sure that natural flame emission was blocked. All images presented in this thesis were obtained with a fixed sensitivity of 10 counts per photon (corresponding to a manufacturer gain setting of 80).

A 105 mm focal length UV-Nikkor lenses with a 4.5 f-number (f/4.5) was used to collect as much as possible of the incoherent fluorescence.

Table 17 –Camera specifications

	High-speed video camera	Intensified camera
Sensor type	CMOS	CCD
Sensor size	17.6x13.2 mm	8.6x6.9 mm
Sensitivity	4800 ISO/ASA	160 counts/photoelectron
Bit depth	8 bits	12 bits
Exposure time	2 μ s	50 ns
Resolution	128x256 pixels	1280x1024 pixels
Frame speed	41100 fps	1 / fired cycle

4.5.2. Exposure time

Although no time dependency explicitly appears in Equation (58), the fluorescence process is not instantaneous and its intensity follows an exponential pattern. The length of this decay is directly related to the fluorescence yield. In the case of low fluorescence yield – e.g. high collisional quenching – the fluorescence decay will be shorter. In the present investigation, the decay was found to be extremely short (Figure 37). Indeed, Ketterle *et al.* (1992) reported that although natural lifetime of OH $A^2\Sigma^+$ excited state is 700 ns, its real lifetime at 0.1 MPa is decreased to 2 ns due to collisional quenching. The intensifier gatewidth was adjusted to 50 ns in order to avoid the collection of flame luminosity.

The delay between the laser pulse and the gate opening/closing was adjusted carefully. The camera's dark current was systematically subtracted from the distributions of both OH and NO.

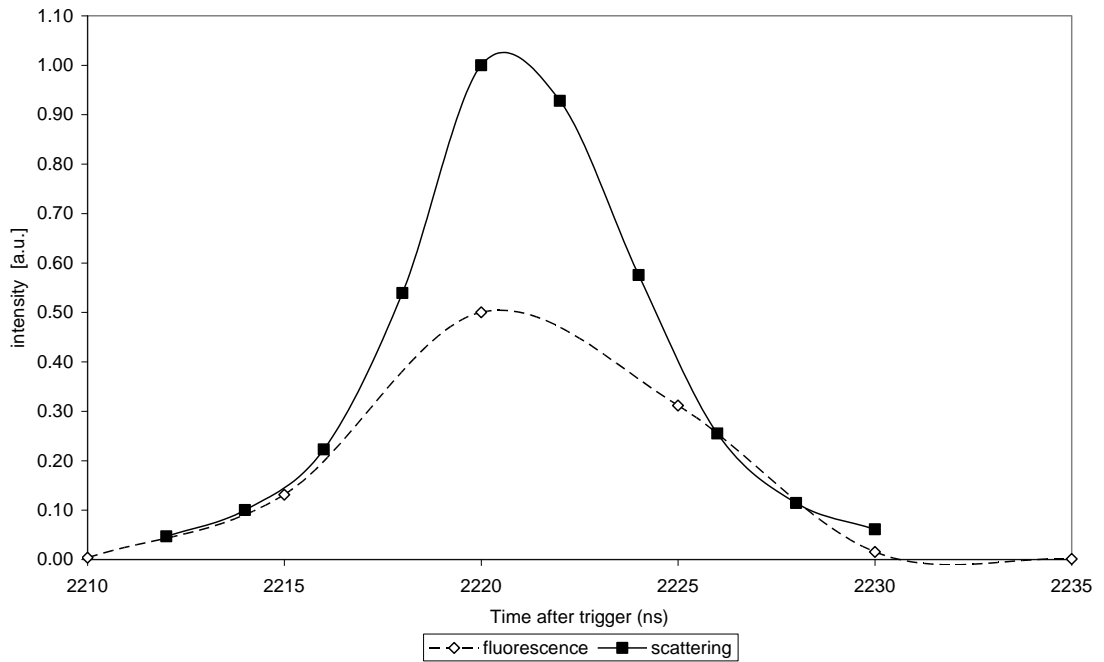
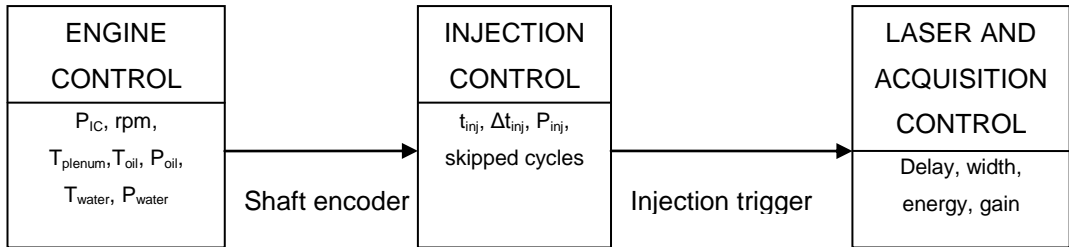
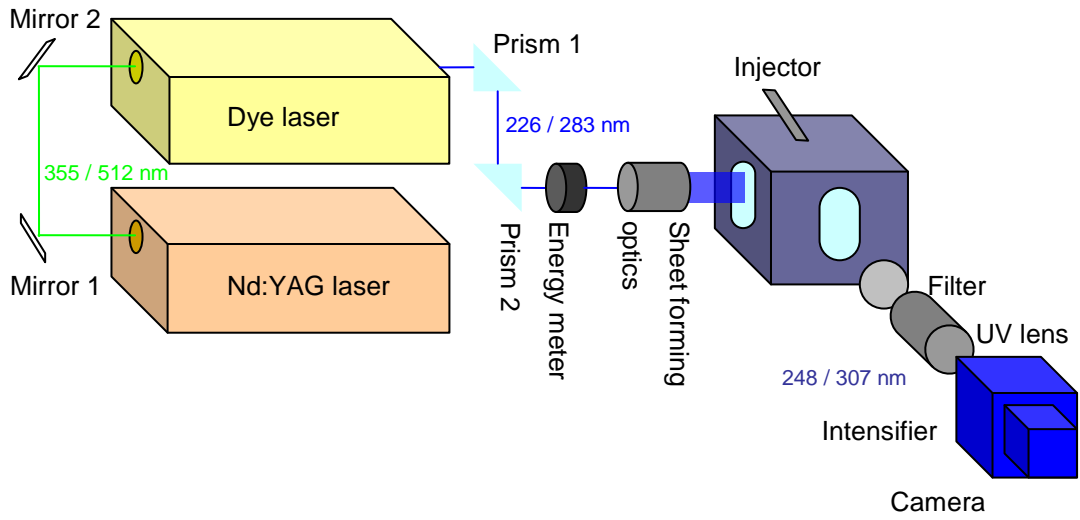


Figure 37 – Comparison between Rayleigh scattering (non-filtered) and fluorescence (filtered) signal timings. Signals collected during the NO-LIF investigation on the CCD chip at different times after the original trigger for a 20 ns opening of the intensifier.

4.6. LIF experimental setup

Figure 38 presents the global experimental setup of the OH and NO LIF experiments, including the interactions between the components described above. The injector was at an angle of 67.5° to the vertical axis, resulting in a vertical spray in the centre of the combustion chamber. The laser sheet position was adjusted to cut the combusting spray in its centreline.

Schematic of the facility



View from the sheet forming optics

Camera view

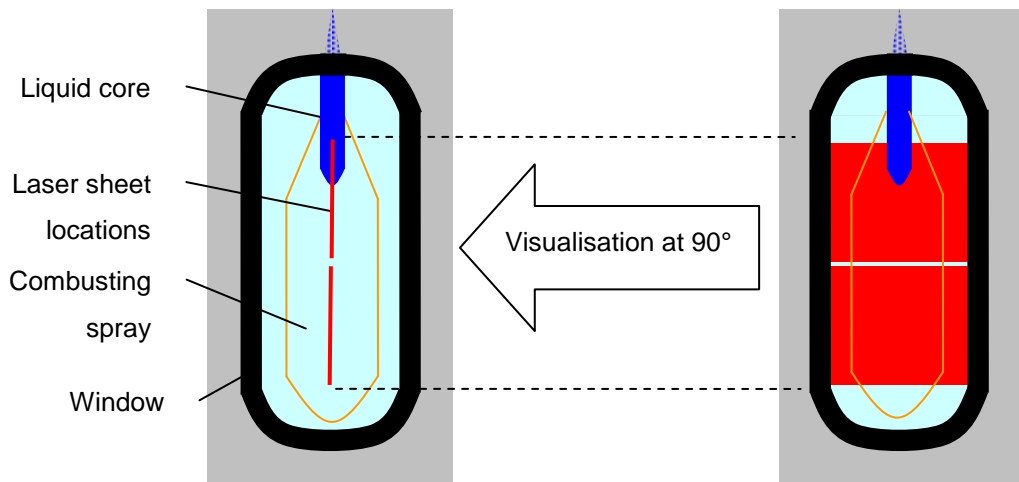


Figure 38 –LIF experimental setup

4.7. Fuel

The fuel can influence the LIF results in several ways. Firstly, high concentrations of soot are responsible for laser and fluorescence attenuation. For this reason, oxygenated fuels have been widely used either pure (Allen et al., 1995, Kosaka et al., 1996, Dec and Coy, 1996) or blended with another fuel (Nakagawa et al., 1997, Alatas et al., 1993, Kosaka et al., 1996, Dec and Coy, 1996, Dec, 1997). In the literature, the reported reductions of soot emission coming with the use of oxygenated fuel vary greatly. There is apparently no simple relation between soot emission and oxygen content of the fuel. Some researchers suggested that the molecular structure of the oxygenated fuel should be taken into account (Mueller and Martin, 2002). In particular, CO is believed to have a key role in soot oxidation. Therefore, fuels with carbon atoms that tend to be directly oxidised to CO₂ are less effective at attenuating soot levels. For instance, esters (functional group R'-COO-R''), with two oxygen atoms bound to a single carbon, have higher soot production levels than ethers (functional group R'-O-R''). Buchholz *et al.* (2004) concluded that an even distribution of the oxygen atoms within the fuel leads to lower soot levels.

Some researchers have used *n*-heptane as it is a pure compound having features (e.g. cetane number) similar to commercial fuel. For this reason, it has been widely employed in chemical kinetics models and a large amount of data on its combustion characteristics is available. Nevertheless, it is believed that even greater improvements in terms of soot production can be achieved with a more appropriate fuel. Several investigations have reported that *n*-heptane's sooting behaviour is similar to the one of commercial fuels (Brugman et al., 1993, Allen et al., 1995). The only advantage of *n*-heptane over commercial diesel fuel is its non aromatic nature. High aromatic contents have been linked with a higher production of soot.

Intermediate species can also be a source of laser/fluorescence attenuation. Poly-aromatic hydrocarbons (PAH) fluorescence in particular can interfere with NO and OH fluorescence. This signal to noise deterioration is likely to become more severe at shorter wavelengths associated with NO fluorescence (Allen et al., 1995). Since PAH are believed to play a role in soot formation, the same solution as for soot reduction (i.e. introduction of low-sooting fuels) is often chosen. Table 20 summarises some of the different solutions published and the authors' justifications.

It is believed that an oxygenated fuel blend is necessary to obtain useful LIF results and a justification of this is given hereafter. As found by Pickett & Siebers (2003), the optical thickness of the combustion gases decreased when a linear hydrocarbon blend replaced the diesel fuel: more than 50% decrease in the local KL^\ddagger number when a D2 fuel was replaced by a blend of hexadecane (cetane) and heptamethylnonane (HMN). However, the same study showed that further improvements could be obtained if a blend of oxygenated fuel was used. Likewise, Mueller & Martin (2002) report that the spatially integrated natural luminosity signal (approximately proportional to the soot concentration for a given temperature) could be decreased by up to 90% if the same blend of cetane and HMN was replaced by a specific oxygenated fuel blend. To identify this “specific” oxygenated fuel blend Natarajan *et al.* (2001) have screened 71 potential oxygenate compounds. Gonzales *et al.* (2001) investigated the “soot reduction” capacity of the selected oxygenates. They identified Tripropylene Glycol Mono-Methyl Ether (TPGME) and Di Butyl Maleate as two most promising candidates. TPGME was also the oxygenate yielding the highest soot reduction in the two optical studies mentioned before (Pickett and Siebers, 2003, Mueller and Martin, 2002). Therefore it was decided to select a blend of 80% of TPGME and 20% of HMN (fuel blend referenced as GE80 in Mueller & Martin (2002) and Pickett & Siebers (2003)). Along with very low soot levels, the combustion of this blend yielded normal levels of hydrocarbons and carbon monoxide, and slightly increased NOx levels. The major drawback of this fuel mix was its fairly high cetane number (Table 18). It was however decided not to increase the proportion of HMN in the mix in order to keep a high concentration of oxygen in the fuel and stay within the conditions explored in the publications mentioned above. The high cetane number would shorten the ignition delay and decrease the importance of the pre-mix combustion. Nevertheless, it was believed that the combustion processes would remain of the same nature and that the high cetane number would not affect the global trends of nitric oxide formation.

[‡] The KL number is representative of the optical thickness of the combustion gases measured by the

extinction ratio of a laser beam: $\frac{I}{I_0} = \exp(-K \cdot L)$

K: the extinction coefficient

L: the path length through the gases

Table 18 – Fuel characteristics (some data adapted from Pickett & Siebers (2003))

fuel	boiling temperature [K]	density at 20°C [-]	oxygen content [wt. %]	cetane number [-]	C/O ratio	H/C ratio	effective H/C ratio (H/[C-O])	lower heating value [MJ/kg]	stoichiometric air to fuel ratio	adiabatic flame temperature [K]
TPGME	243	0.96	31	96	2.5	2.2	3.67		11.5	
HMN	240		0	15	-	2.1 3	2.13		20.2	
GE80: 80% TPGME 20% HMN		≈0.92	25.8	80	3.2 5	2.2	3.15	30.5	13.2	1850
reference diesel	180-350	0.81	0	53.8	-	2.1 7	2.17	43.4	14.7	2240

Secondly, natural fluorescence of the fuel vapour can occur and interfere with the fluorescence of the species probed. Allen *et al.* (1995) reported, for instance, that methanol natural fluorescence obscured OH distributions, particularly at high pressures in the 0 to 10 bar range. The natural fluorescence of commercial diesel or other fuels was sometimes used for equivalence ratio studies (Tait and Greenhalgh, 1993). Since the complex mix of compounds that compose the fuel absorbs light on a large range of wavelengths, a number of high power laser sources could be used. Thus, diesel fuel fluorescence was obtained from an excitation at 355 nm/102 mJ (Pastor *et al.*, 2002), *iso*-octane fluorescence from an excitation at 248 nm/400 mJ (Andresen *et al.*, 1990) and *n*-heptane from an excitation at 308 nm/20 mJ (Arnold *et al.*, 1992). The best way to free the results from suspicion was to analyse the natural fluorescence of the fuel vapour with a spectrometer. This is rarely done in the published studies. It was then decided to investigate the fluorescence of diesel and GE80 fuel. A small quantity of GE80 (0.5% in volume) was mixed in hexane and analysed with both an absorption and a fluorescence spectrometer. Likewise, the absorption and emission spectra of the reference white diesel fuel were acquired. The spectra are presented in Figure 39. It appeared that for both fuels, whatever the excitation wavelength, the fluorescence started where the absorption range ended. This could be simply due to the rather high density of absorbing molecules in the test cell probed. Any fluorescence emitted in the absorption range could be reabsorbed and, through internal conversion, reemitted at a Stokes-shifted wavelength. In order to verify this assumption, the fluorescence spectrum of white diesel fuel in a gaseous phase was acquired.

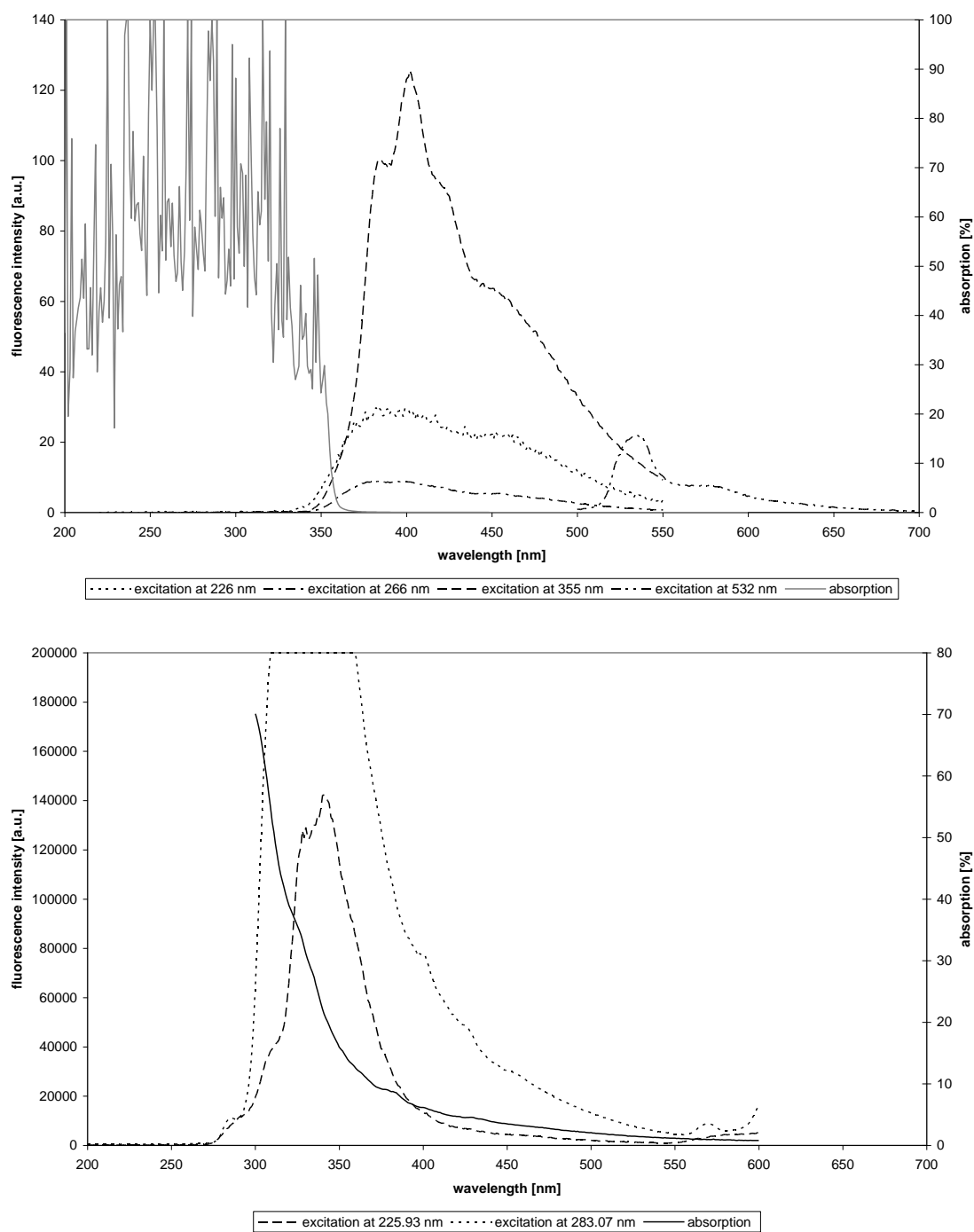


Figure 39 – White diesel fuel (top) and GE80 (bottom) absorption and fluorescence spectra (absorption of GE80 below 300 nm is unavailable because of the interference of hexane absorption)

Commercial white diesel fuel was evaporated on a hot plate. The laser train of pulses at 226 nm and of 1 mJ energy was directed through the vapour. The light collected at 90° was analyzed by an ICCD spectrometer. Five sets of data with and without laser

excitation were acquired. The intensities shown in Figure 40 are the background corrected averages.

The fuel fluoresced strongly between 275 nm and 400 nm. Results published by Arnold *et al.* (1990) using a XeCl excimer laser and by Pastor *et al.* (2002) using the third harmonic of a Nd:YAG laser – i.e. excitation at 308 nm and 355 nm respectively – showed a similar behaviour. This fluorescence range was lower than in Figure 39. The density of the absorbing species seemed to affect the wavelength range of emission. Interestingly, this would mean that the lower part of the fluorescence spectrum is representative of the average density of absorbing species in the line of sight. An appropriate comparison of the overall emitted signal with the shape of the spectrum at low wavelength could yield information on the level of absorbing species in the probed volume as well as in the line of sight.

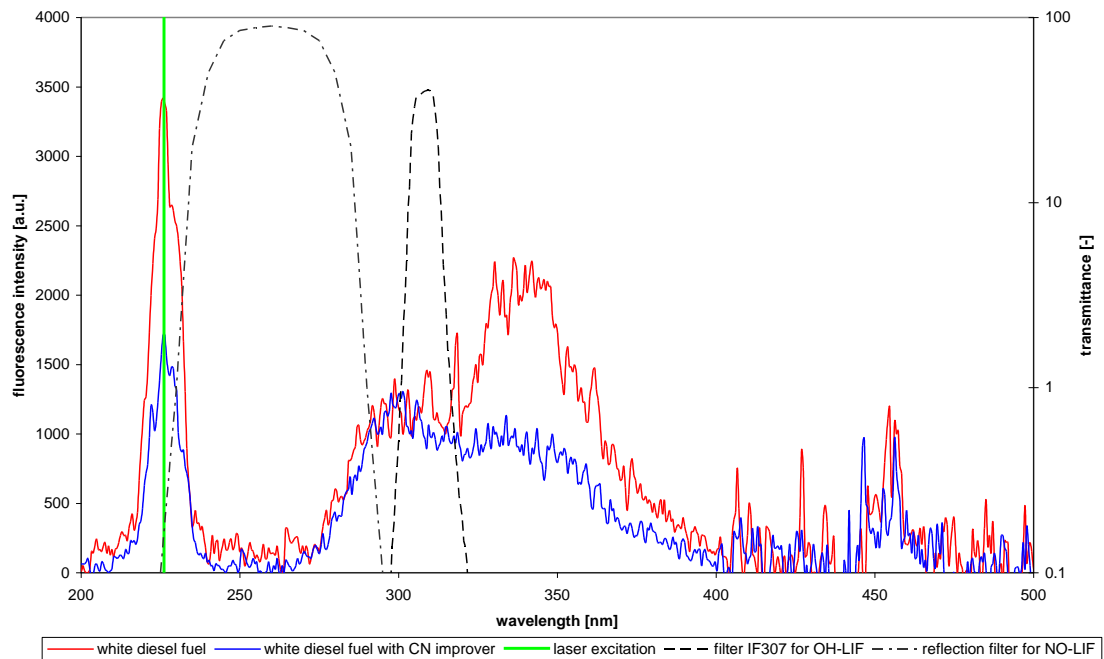


Figure 40 – Fuel fluorescence

In Figure 40, the emission peak centred on 226 nm was due to laser scattering. The disturbances in signal intensity beyond 400 nm were due to the ambient lighting (neon spectrum). The extra measurement with cetane number improver in the fuel (CN + 8) was recorded with a slightly modified laser energy. The CN improver (2-ethylhexyl nitrate – EHN) does not change the fuel fluorescence wavelength band and only affects the fluorescence intensity slightly. The sample containing the improver turned black

upon heating, a phenomenon well known for fuel containing EHN (Mueller and Martin, 2002), as this compound decomposes before boiling.

To conclude, laser attenuation may occur as a consequence of absorption by the fuel, soot or PAH. These conditions are often characterised by a clear asymmetry in the distributions, the side of the chamber from which the laser sheet comes being “brighter” than the other side.

Furthermore, some spurious signal may be captured – especially in the OH-LIF case – as some of the fuel fluorescence was within the collected wavelength range.

4.8. Correction procedure for the raw LIF distributions

The laser and fluorescence light are not only absorbed by nitric oxide, fuel molecules, soot or PAH as reported above, but also by a number of smaller molecules such as hot CO₂ (Hildenbrand and Schulz, 2001). Interferences from Raman and Rayleigh scattering of molecules such as N₂, O₂, CO₂, H₂O can also occur. Most of these interferences are affected by density and temperatures. The signal to noise ratio may then evolve with these parameters too. In particular, O₂ has a tendency to predissociate faster than to quench or broaden, its interfering fluorescence signal increases linearly with pressure (Schulz et al., 1997). Moreover, some molecules need their high energy vibrational level to be populated in order to absorb in the excitation bandwidth. Higher temperatures will then lead to higher absorption and interfering fluorescence. Therefore, the signal to noise ratio of OH-LIF and especially NO-LIF decreases dramatically with increasing pressure and temperature.

In order to free the results from broadband interferences, an off-line subtraction strategy was adopted. Series of images were acquired with the dye laser tuned on and off an absorption peak of OH and NO.

The corrected images presented hereafter are therefore average images corrected for off-line signal, but also for laser energy and background level.

It was first evaluated that a number of 30 and 15 captures were enough to compute a representative average of respectively the on- and off-line distributions. Figure 41 shows for instance the sum over the images of standard deviation for a number of capture counts. It can be seen that the standard deviation tends to a plateau above 20-30

on-line (10-15 off-line) images, meaning that the average image becomes meaningful above this limit.

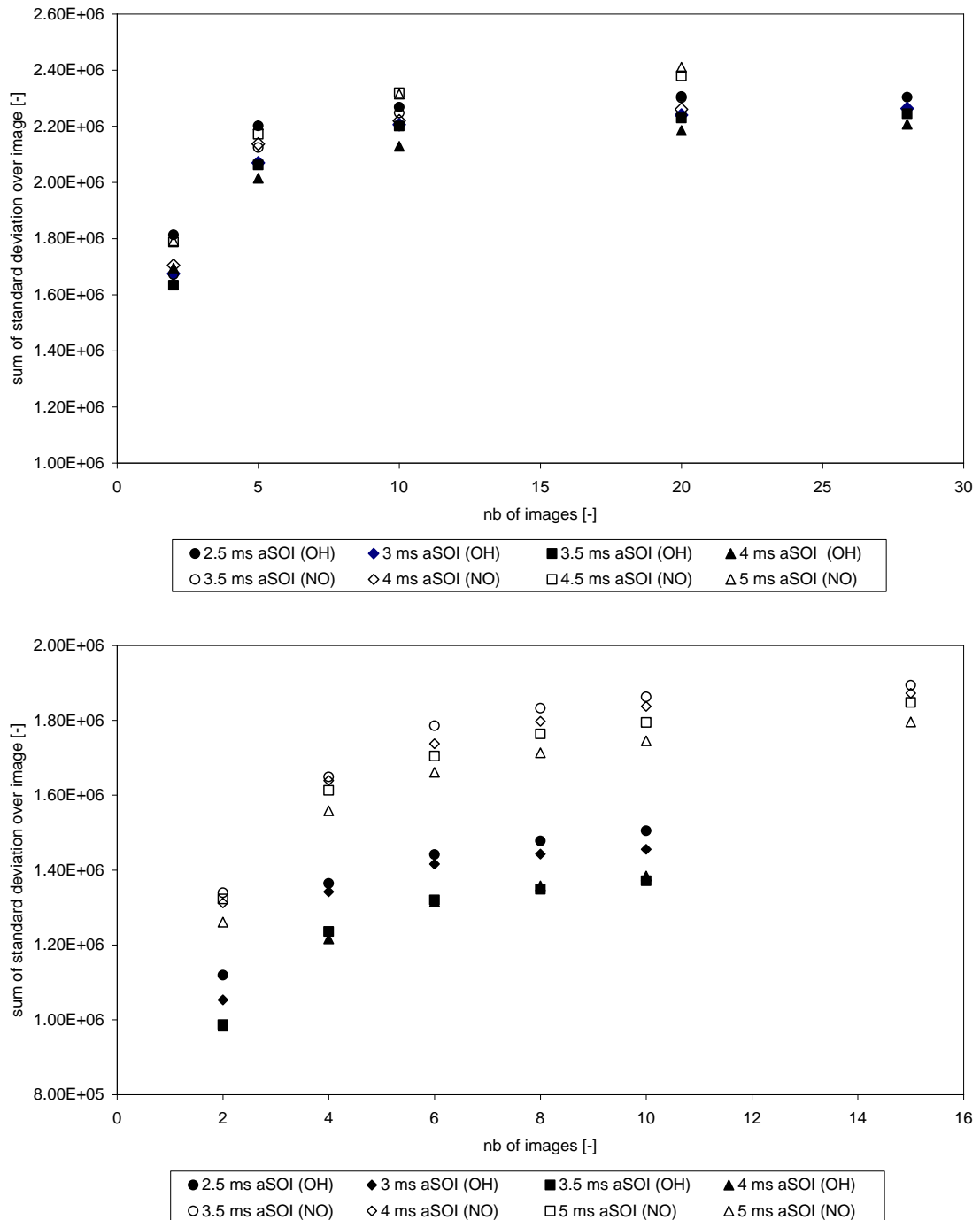


Figure 41 – Sum of the standard deviation over the images for different number of captures on-line (top) and off-line (bottom) (30 mm³ of GE80 injected at 100 MPa in an in-cylinder pressure and temperature of 5 MPa and 700 K)

Each of the 30 on-line and 15 off-line image intensities were normalised by the measured laser pulse energy. For each image, the mean background noise was computed

on a portion of the CCD chip that does not collect light from the combustion chamber. This background noise was then subtracted to the individual images. An average of the on- and off-line distributions was then computed. The average off-line signal was finally subtracted to the average on-line signal.

The laser energy profile is globally Gaussian but fairly uneven. Similarly, the collection optics efficiency and/or the camera sensitivity may not be homogeneous over the whole field-of-view. Unfortunately, it was impossible to apply a complete flat fielding correction because of the changing nature of the energy profile and the low signal to noise ratio in the region of low laser energy. Only a small region of the centre of the CCD chip was used to image the fluorescence and the collections efficiency and camera sensitivity were found to be homogeneous on this limited region.

Figure 42 presents the evolution of the corrected signal for OH and NO compared to the background noise. The noise being fairly constant, both signal to noise ratios increase with signal intensity reaching 10 to 30 in the presence of high densities of OH or NO.

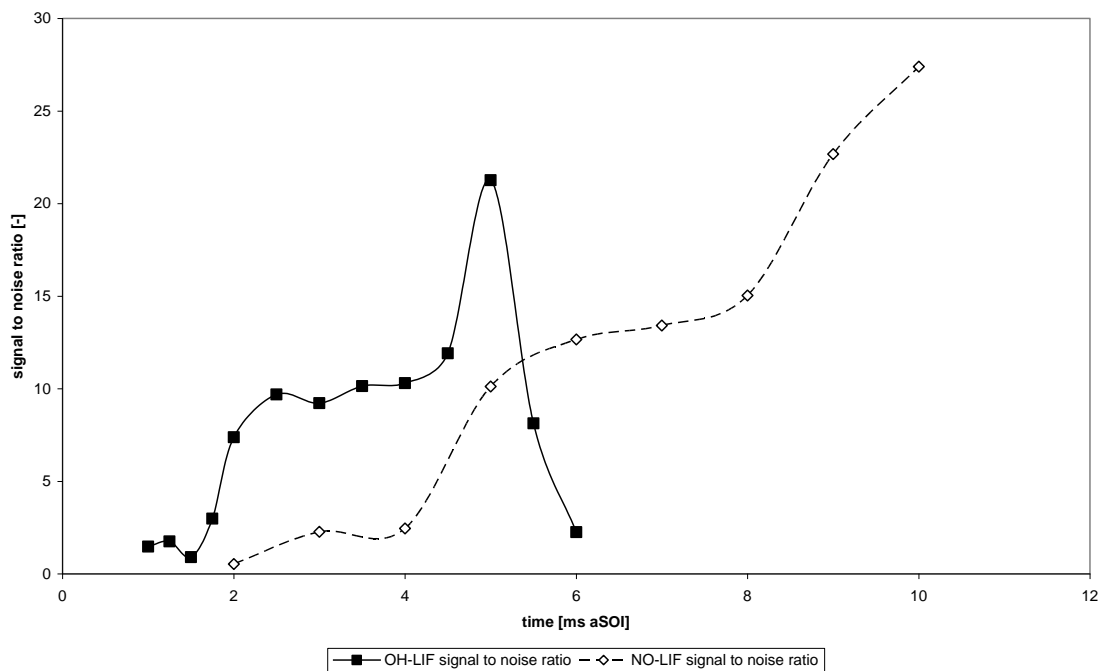


Figure 42 – OH- and NO-LIF signal to noise ratio (30 mm³ of GE80 injected at 100 MPa in an in-cylinder pressure and temperature of 5 MPa and 700 K)

4.8.1. Potential sources of error

The energy monitor used to associate a laser pulse energy to every captured image was tested against a reference calibrated laser energy meter. The output of the energy monitor was accurate within 4%. However, the main source of error was the attenuation of the laser energy between the energy monitor and the chamber. Although optics and windows were constantly cleaned to ensure optimal conditions, the laser energy could easily be reduced by some unpredictable fouling of the side window during the experiment. The associated error was evaluated at 10-15%.

A set of 100 on-line images were captured for a single set of conditions and the error introduced by limiting the collection to 30 images was estimated at 4%. Similarly, the off-line limitation to 15 images introduced a 4% uncertainty.

A series of black images were captured in order to evaluate the potential error introduced by the background subtraction. The dark current was found to be fairly constant over the CCD chip. The error introduced by subtracting a background noise computed on a small part of the chip was evaluated at 2%.

The biggest source of error remains the physical processes associated with fluorescence emission (notably quenching). Unfortunately, their exact impact was difficult to evaluate. A phenomenological model is presented in section 5.2 to try to understand their potential effect on the LIF distributions.

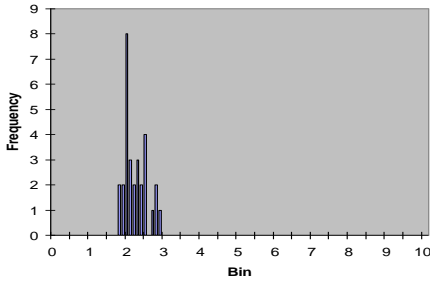
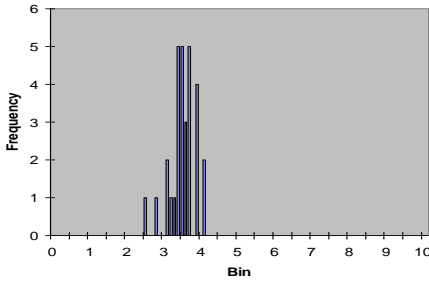
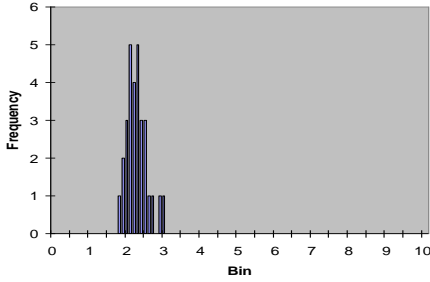
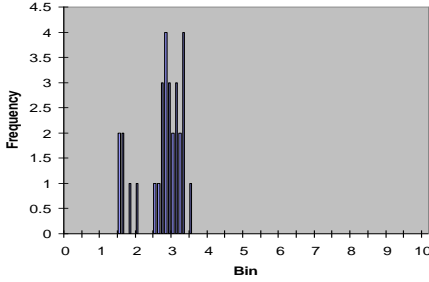
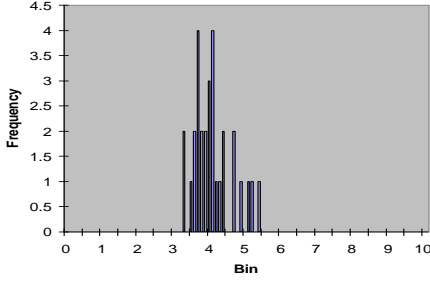
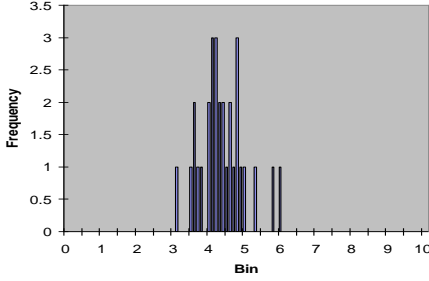
4.8.2. Distribution analysis of the on-line signal

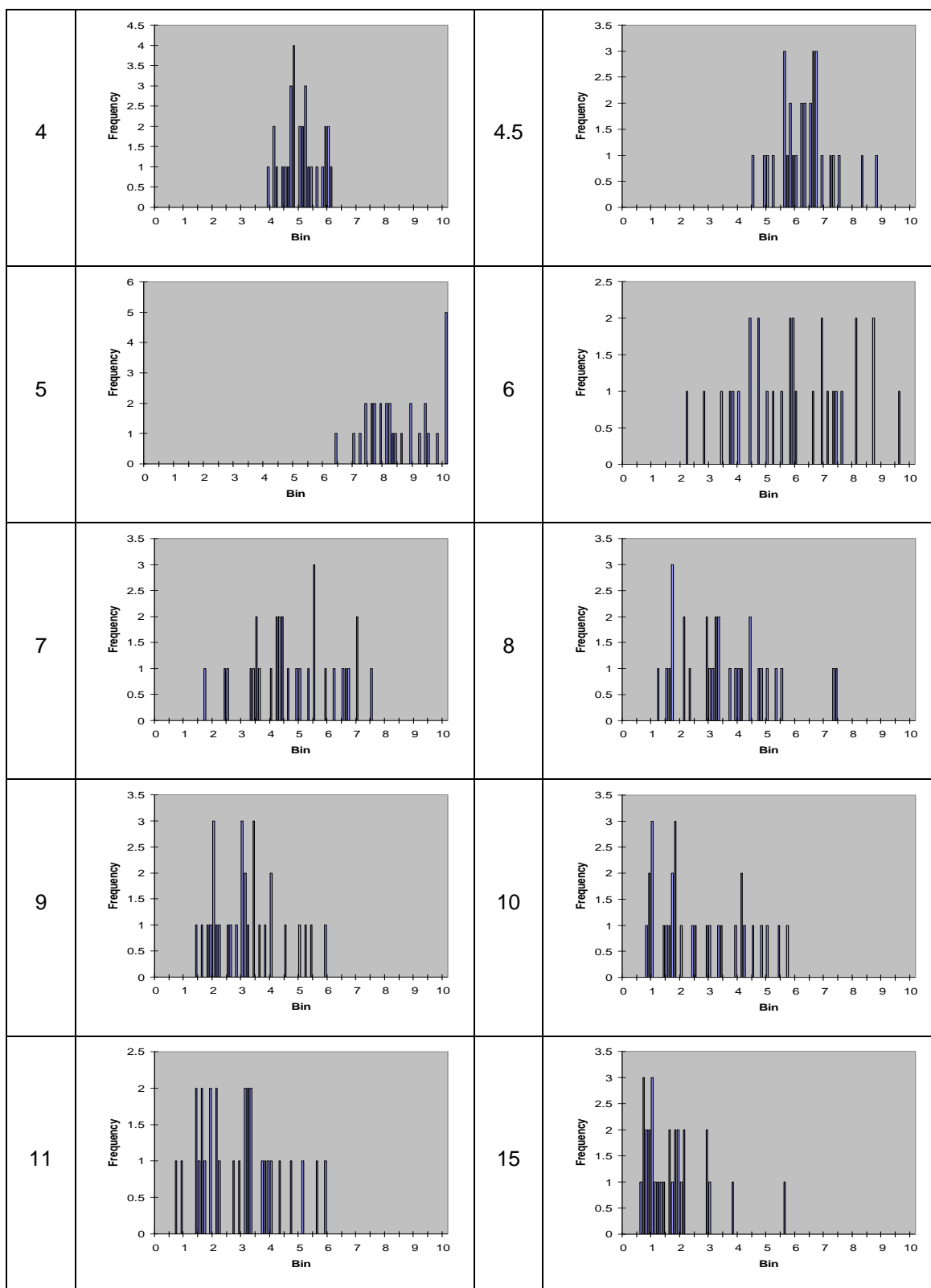
Early measurements showed that the cycle-to-cycle variations of the averaged intensities over the probing volume were greater for the on-line signal than for the off-line signal. Furthermore, for the on-line signal, the variation was more pronounced when fluorescence was dominant. The interferences appeared as a more stable source of light, barely varying from one cycle to another. From this observation it was hypothesised that the interferences component of the on-peak signal could be estimated by means of frequency distribution analysis. For instance, Table 19 presents the frequency distributions of on-line NO-LIF measurements. The intensities were averaged over a rectangle containing the laser sheet path. It appeared that between 1 and 4 ms aSOI the intensity distribution shifted to the higher intensities while keeping a narrow width. This evolution corresponded to the initial increase in interferences level. The intensity distribution then shifted back to a lower range at 5 ms aSOI. After 5 ms aSOI

this low intensity component of the distribution gradually decreased as the fluorescence signal increased. The fluorescence intensity distribution was wider and the histogram appears flatter. From 10 ms onward, the fluorescence component decreased and the intensity distribution returned to an “interference shape”.

The interference intensity distributions were then narrower than the fluorescence intensity distributions. Indeed, the concentrations and distributions of the sources of interferences (e.g. scattering from liquid, soot and radiation from combustion products and intermediates) were less affected by variations in the combustion processes than nitric oxide or hydroxyl radical fluorescence.

Table 19 – Frequency distributions of the on-peak signal

Time [ms aSOI]	Intensity histogram	Time [ms aSOI]	Intensity histogram
1.5		1.75	
2		2.5	
3		3.5	



In Figure 43, the inverse of the standard deviation of the on-line signal seems to follow the off-line signal intensity. This is clearer for NO-LIF as OH-LIF interferences are proportionally very small, leading to artificially high standard deviations whenever the fluorescence is not present. The match between the off-line signal and the inverse of the

on-line signal standard deviation can be used in cases where the off-line distributions cannot be acquired.

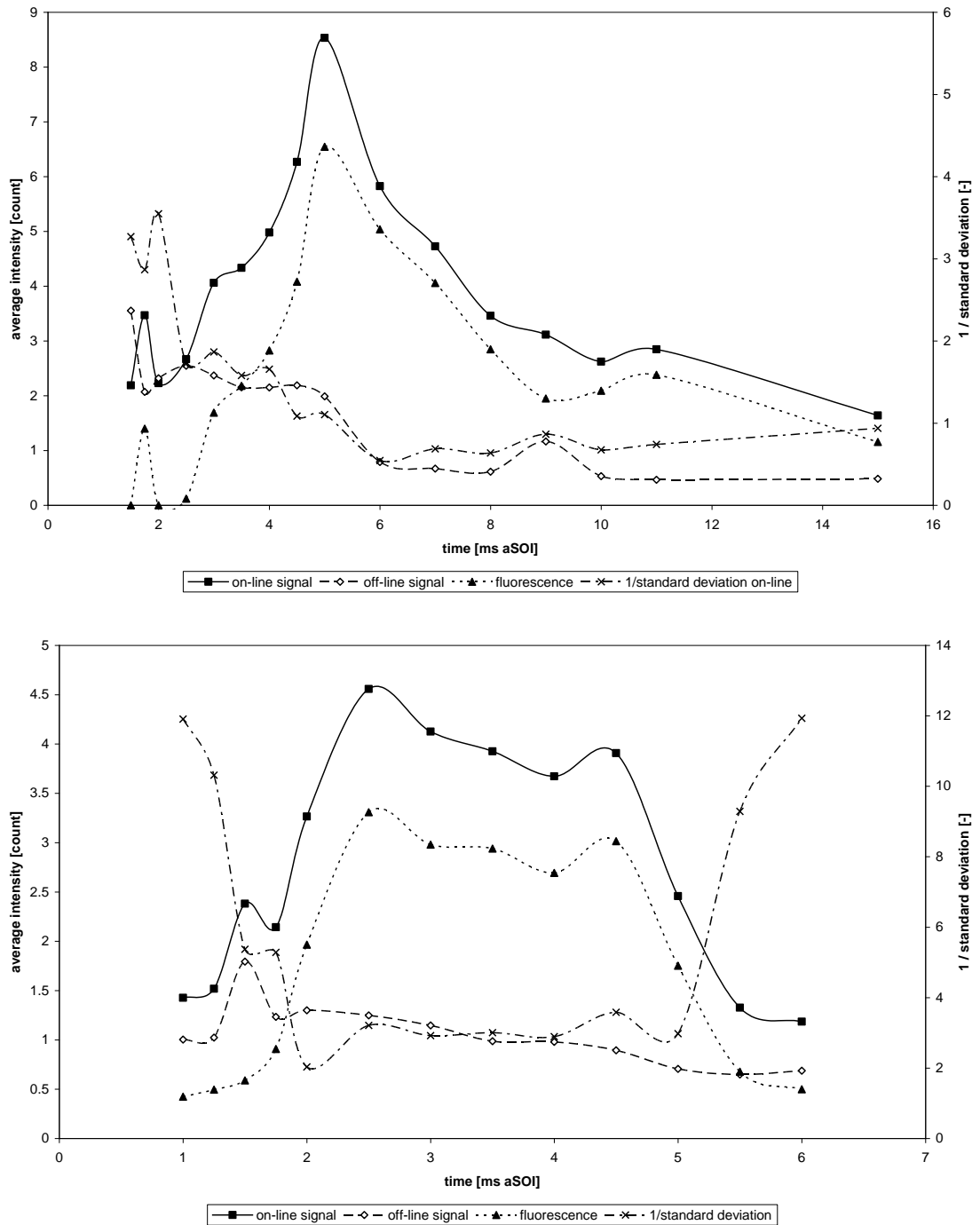


Figure 43 – Standard deviation of the spatially averaged on-peak distributions (top: NO, bottom: OH)

Table 20 – Summary of published fuel choices and respective justifications

Fuel	Used by	Justification	Cetane number	Carbon number
diesel	Brugman (NO), Stoffels (NO), Hindebrand (NO), Monkhouse (NO)	Excitation at 248 nm is favorable to IC engine applications...laser attenuation is minimized, and the possibility of detecting NO-LIF shifted towards shorter wavelengths strongly discriminates NO-LIF against contribution of interfering LIF caused by hot molecular oxygen and intermediate hydrocarbons (Hindebrand, 2000)	45-50	12--13
n-heptane	Arnold (OH-NO), Brugman (NO), Allen (OH)	Using n-heptane as fuel, the engine could be operated for many minutes before the windows became obscured with soot. On the other hand, with diesel as fuel, all windows were covered with soot within a few seconds (Arnold, 1992) The use of substitute fuels like n-heptane does not result in improved NO images, as was expected in view of increased absorption of laser radiation and emissions by many different components of Diesel fuel (Brugman, 1993). Laser attenuation observed with heptane was 3 times higher than with ethanol - at 10 bar. The attenuation observed for OH is likely to become more severe at shorter wavelengths associated with, for example, NO fluorescence near 225 nm (Allen, 1995)	56	7
iso-octane (50%) tetradecane (50%)	Alatas (NO), Nakagawa (OH-NO)	Less numerous absorbing and fluorescing components causing low transmission of the laser beam and a strong combustion background radiation in a large wavelength region (Brugman, 1993 about Alatas, 1993) To minimize the production of exhaust particles (Nakagawa, 1997)		8 (50%) 14 (50%)
ethyl alcohol (40%) n-dodecane (60%)	Nakagawa (OH-NO)	To minimize the production of exhaust particles (Nakagawa, 1997)	8 (40%)	2 (40%) 12 (60%)
ethanol	Allen (OH)	Aromatic hydrocarbons responsible for laser attenuation in heptane combustion are apparently absent in ethanol-air flames (Allen, 1995)	8	2
methanol	Allen (OH)	Methanol fuel was problematic as its natural fluorescence obscured OH distributions, particularly at high-pressures (Allen, 1995)	3	3
n-dodecane (20%) n-tridecane (50%) n-tetradecane (20%) polypropylene glycol (10%)	Kosaka (OH)	90% paraffin hydrocarbon reference fuel and polypropylene glycol was used to reduce the optical attenuation caused by dense soot cloud (Kosaka, 1996)	80 (90%)	12 (20%) 13 (50%) 14 (20%)
polypropylene glycol	Kosaka (OH)	For very low-sooting flame. Qualitative distribution of OH fluorescence in a diesel flame does not change drastically with the change of total soot amount in a flame (Kosaka, 1996)		
tetraethoxypropane (70%) heptamethylnonane (30%)	Dec (OH-NO)	Low-sooting fuel used to minimize both optical obscuration by the soot within the reacting fuel jet and window fouling by soot deposition (Dec, 1996, 1998)	42.5 54.28 (70%) 15 (30%)	11 (70%) 16 (30%)
tetraethoxypropane	Dec (OH)	Produces even less soot than the mix TEOP/HMN (Dec, 1996)	54	11
heptamethylnonane (67%) n-hexadecane (33%)	Dec (NO)	Reference fuel from another study, more soot (Dec, 1998)	42.5 15 (67%), 100 (33%)	16 (67%) 16 (33%)

In the next chapters, the results of the spray and flame development, OH-LIF and NO-LIF investigations are presented and discussed.

5. COMBUSTING DIESEL SPRAY CHARACTERISATION

In direct injection engines, the spray development has a major influence on combustion. In particular, the atomisation and vaporisation capabilities of the injection system influence the combustion timing, and the local equivalence ratios and therefore, the thermodynamic and chemical processes in the combustion chamber.

A number of experiments were therefore designed in order to characterise the spray and its combustion at the conditions of our OH- and NO-LIF investigations.

5.1. Spray and flame development

5.1.1. Nozzle flow calculation

In steady state, mass conservation requires that the mass flow rate be of equal magnitude in all cross sections of the injection circuit:

$$\dot{m} = \rho_1 \cdot A_1 \cdot v_1 = \rho_2 \cdot A_2 \cdot v_2 \quad (76)$$

Where \dot{m} is the mass flow through a cross section [$\text{kg}\cdot\text{s}^{-1}$], ρ_i , the density of the fluid at point i [$\text{kg}\cdot\text{m}^{-3}$], A_i the cross section area at point i [m^2] and v_i the velocity of the fluid at point i [$\text{m}\cdot\text{s}^{-1}$].

In the case of an incompressible fluid:

$$\rho_1 = \rho_2 = \rho \quad (77)$$

And:

$$A_1 \cdot v_1 = A_2 \cdot v_2 = \text{const} . \quad (78)$$

At the pressures investigated, the liquid fuel will change its volume with changes in pressure. Nevertheless, these changes are still small and in the case of computation of the nozzle flow, can be neglected.

From the law on energy conservation, Bernoulli's equation can be written:

$$p_1 + \frac{1}{2} \cdot \rho \cdot v_1^2 + \rho \cdot g \cdot h_1 = p_2 + \frac{1}{2} \cdot \rho \cdot v_2^2 + \rho \cdot g \cdot h_2 \quad (79)$$

Where p_1 , v_1 , h_1 and p_2 , v_2 , h_2 are respectively the pressures [Pa], velocities [m.s⁻¹] and altitude [m] of the fuel in the rail and at the nozzle outlet; ρ is the density of the fuel [g.m⁻³] and g the acceleration of gravity [m.s⁻²].

If we consider the effects of altitude negligible compared to the static and kinetic pressures, equation (79) becomes:

$$v_2^2 - v_1^2 = \frac{2}{\rho} \cdot (p_1 - p_2) \quad (80)$$

From the mass continuity equation (78):

$$v_2^2 \cdot \left(1 - \left(\frac{A_2}{A_1}\right)^2\right) = \frac{2}{\rho} \cdot (p_1 - p_2) \quad (81)$$

Considering the cross sections in the injector and in the rail, $\left(\frac{A_2}{A_1}\right)^2$ can be neglected:

$$v_2 = \sqrt{\frac{2}{\rho} \cdot (p_1 - p_2)} \quad (82)$$

To take into account the influence of the orifice shape and the friction losses, a velocity coefficient φ , sometimes called discharge coefficient C_D , is often added:

$$v_2 = \varphi \cdot \sqrt{\frac{2}{\rho} \cdot (p_1 - p_2)} \quad (83)$$

Where v_2 is the nozzle output velocity, p_1 , the pressure in the rail [Pa], p_2 , the in-cylinder pressure [Pa], ρ , the density of the fuel [kg.m⁻³] and φ the velocity coefficient [-]. p_2 being at least an order of magnitude smaller than p_1 , it is sometimes neglected.

5.1.2. Nozzle flow measurements

The nozzle flow can be indirectly measured by the use of a rate tube. In this experiment, the fuel is injected in a long tube filled with the same working fluid under pressure. The extra volume of fluid creates a pressure wave which travels along the tube.

Let's consider the injected fluid as a plane circular piston acting on the working fluid. For a piston moving uniformly with speed $U_0 \exp(j\omega t)$, the pressure at any field point is given by (Kinsler et al., 2000):

$$p(r, \theta, t) = j \cdot \rho_0 \cdot c \cdot \frac{U_0}{\lambda} \cdot \int_s \frac{1}{r'} \cdot e^{j(\omega t - kr')} dS \quad (84)$$

Where $p(r, \theta, t)$ is the pressure at point (r, θ) and time t , ρ_0 , the equilibrium density, c the speed of sound, U_0 , the piston speed amplitude, λ , the wavelength, r' , the distance to the source and ω the angular frequency.

Thus, at any point within the rate tube, the pressure is proportional to the piston speed i.e. the nozzle flow.

The rate tube outputs at different injection pressures are presented in Figure 44. A short isolated flow peak can be seen at the beginning of injection. This is a phenomenon well reported for single-hole nozzles and a complementary investigation proved that multi-hole nozzle do not show the same behaviour (Figure 45). It is believed to be due to needle oscillation subsequent to pressure differentials inside the nozzle. Nozzles with a higher number of holes are more likely to have a more symmetrical pressure distribution around the needle. This hesitation duration decreases with increasing injection pressure.

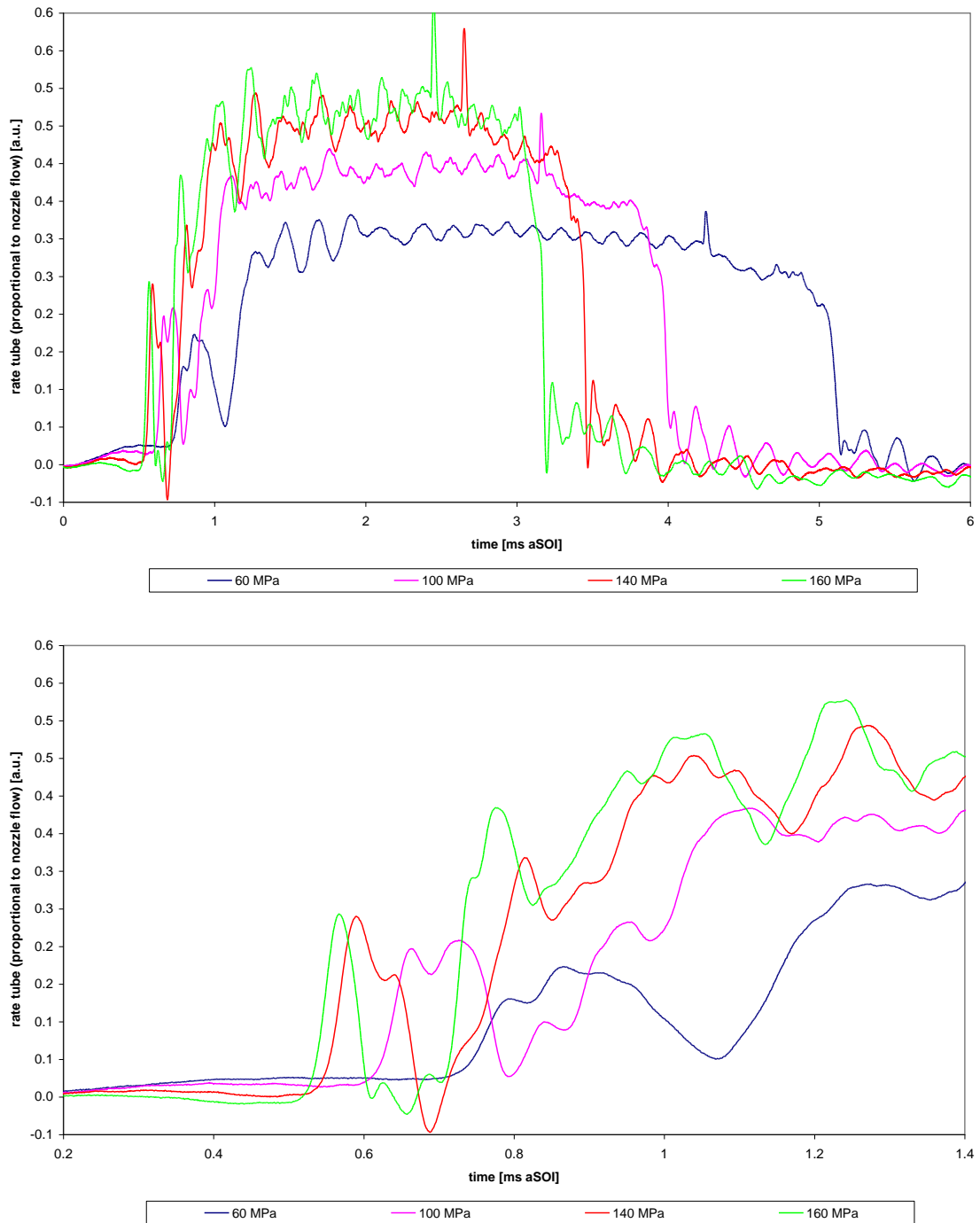


Figure 44 – Rate tube measurements for different injection pressures (30 mm³ injected volume in an in-cylinder pressure and temperature of 5 MPa and 680 K, averaged over 100 cycles)

Figure 46 is a diagram showing the working principle of a high pressure common rail injector. As can be seen, the solenoid coil does not act on the needle itself but on a valve constrained on one side by springs and on the other side by the fuel pressure. At the start of injection, the solenoid is triggered by the injection current. The balance of the

forces on the valve changes and the valve opens, lowering the fuel pressure at the top of the needle. Subsequently, the pressure differential between the top and the bottom of the needle changes and the needle lifts.

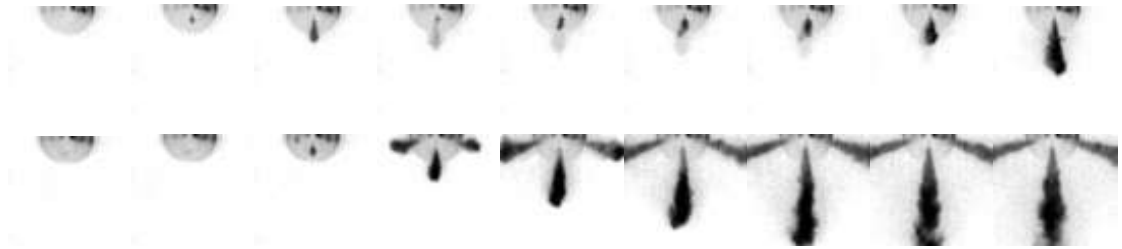


Figure 45 – Onset of injection – the hesitation visible on the single-hole nozzle (top row), is not seen on the multi-hole nozzle (bottom row) (injection of 30 mm³ of fuel at 160 MPa in an in-cylinder pressure and temperature of 6 MPa and 700 K– the images were taken at regular intervals between 0.42 and 0.65 ms aSOI)

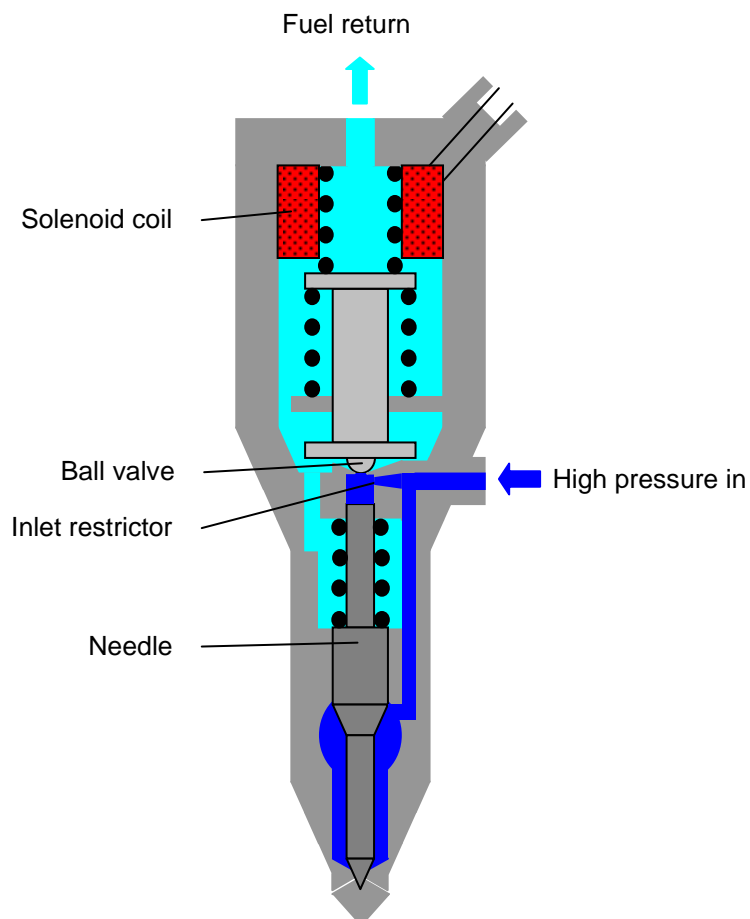


Figure 46 – Working principle of a common-rail injector (adapted from (Dietsche et al., 2005))

Corresponding short-wave oscillations are seen on the rail pressure and flow rate traces (Figure 47). The oscillation frequency changed with injection pressure and the oscillations are believed to be a consequence of the injector internal dynamics. The evolutions of the oscillation and hesitation durations with injection pressure were comparable. These phenomena could therefore share a common origin.

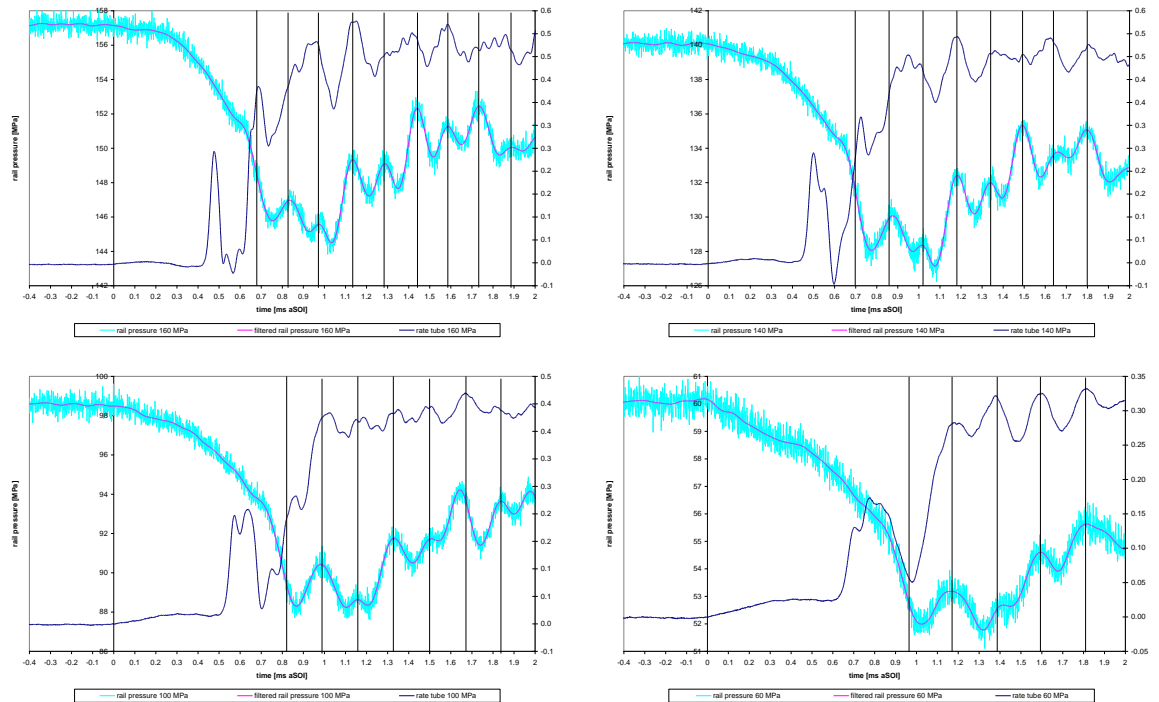


Figure 47 – Evolution of the rail pressure and flow rate at needle lift (30 mm³ injected volume in an in-cylinder pressure and temperature of 5 MPa and 680 K, averaged over 100 cycles, injection pressures are 160, 140 MPa on first row and 100, 60 MPa on second row)

To summarise, the fuel started to flow through the nozzle hole between 0.4 and 0.6 ms after the time of trigger (abbreviated here as time aSOI). After a small hesitation, the flow quickly reached its steady state value, as given by equation (83). The injection pressure influenced the delay between trigger and effective flow, the duration of the hesitation, the time necessary to reach maximum flow and the maximum flow itself. Thanks to the rate tube investigation, the flow of fuel within the injector is better known. A high speed video investigation of the spray development in the combustion chamber was designed to complete our understanding of the atomisation and vaporisation mechanisms.

5.1.3. Spray penetration

The high-speed video camera described in section 4.5.1 was used to capture the spray development for a number of injection pressures. Two high power spot lights were used to illuminate the spray on both sides (Figure 48). The camera captured the Mie scattering of light from liquid droplets and ligaments.

Liquid penetration evolutions were then computed and are shown in Figure 49. The injector being installed in the top hat, the first 23 mm of penetration were out of the field of view. Two series of penetrations are shown: with or without combustion (i.e. cold or hot intake).

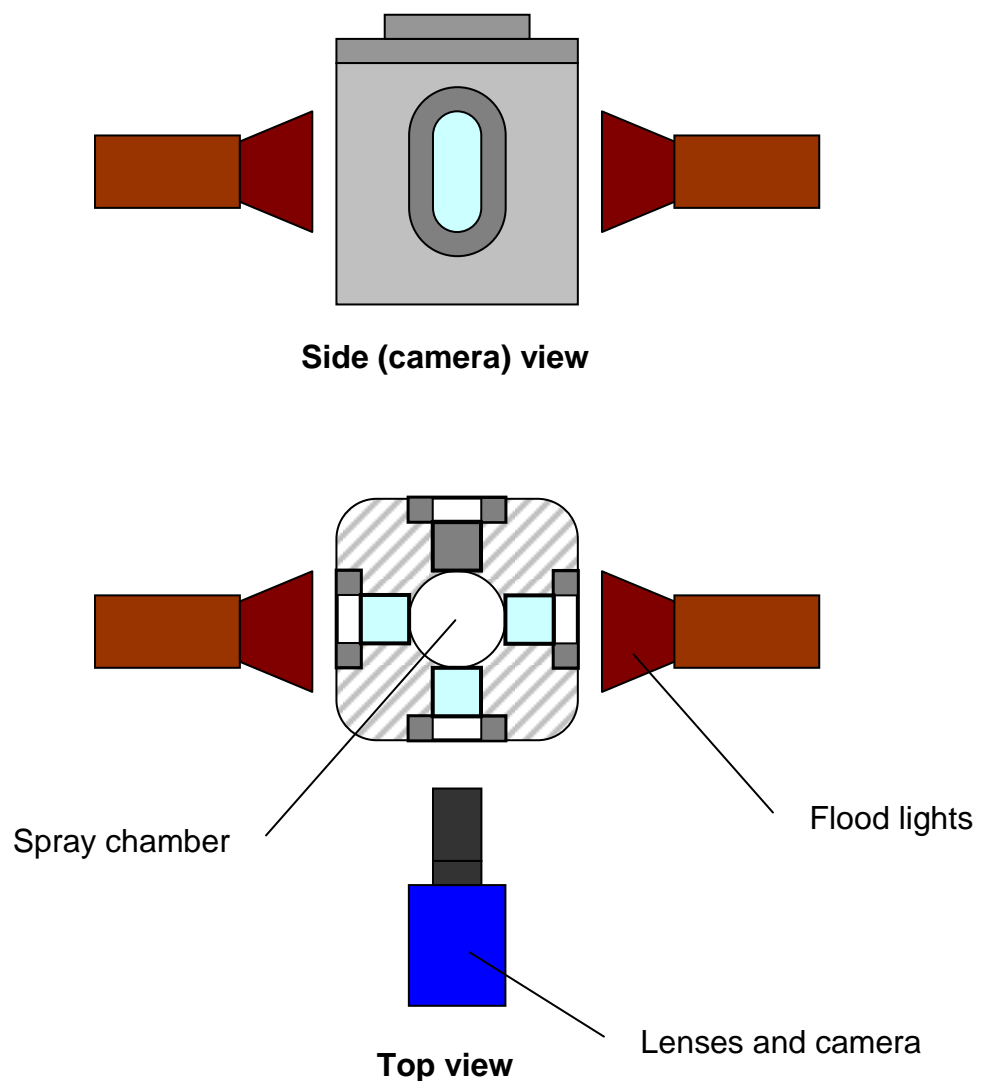


Figure 48 – High-speed video imaging of spray development

As can be expected from equation (83), the fuel velocity is greater for higher injection pressures. Furthermore, the ratio of the average velocities is close to the square root of the ratio of the pressures. For instance:

$$\sqrt{\frac{P_{160 \text{ MPa}}}{P_{60 \text{ MPa}}}} = \sqrt{\frac{160 \text{ MPa}}{60 \text{ MPa}}} = 1.63 \approx \frac{v_{160 \text{ MPa}}}{v_{60 \text{ MPa}}} = \frac{65.9 \text{ m/s}}{38.6 \text{ m/s}} = 1.70$$

The maximum penetration length is similar for all injection pressures. However, while at high injection pressure this penetration is reached before the start of combustion, at low pressure it is only reached in the non-burning conditions.

Two distinct phases of evaporation appear on the burning penetration graphs. The first phase is characterised by a rapid evaporation of the tip of the spray. This sharp decrease in penetration happens faster and is shorter for the high injection pressures. This can be associated with a better atomisation of the spray hence a shorter ignition delay and a quicker flame speed. The second phase of evaporation is steadier with liquid penetration slowly decreasing until the end of injection.

Interpolations of the penetration data over the first 23 mm confirm the timings of start of injection found with the rate tube. There are no visible variations in the penetration evolution due to the short-wave oscillations in the fuel flow.

Penetration traces can appear jerky as obtained from single-cycle data with a fairly simple threshold criterion. In the 60 and 100 MPa graphs for instance, the flame luminosity exceeds twice the luminosity threshold, yielding a flawed penetration around 2.7 and 2.85 ms aSOI respectively.

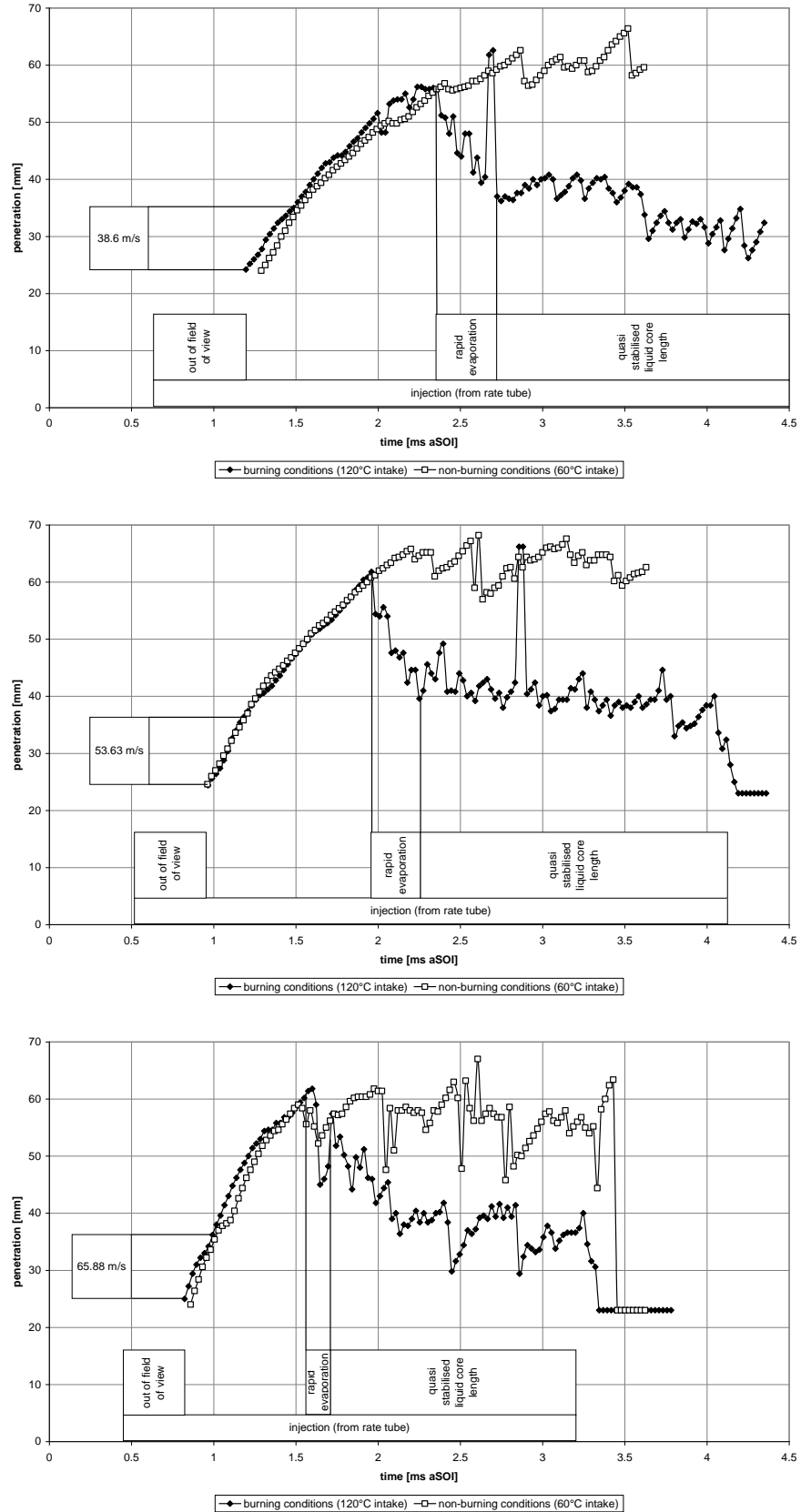


Figure 49 – Liquid fuel penetration evolution with time and injection pressure (60, 100 and 160 MPa from top to bottom – 30 mm³ of GE80 injected in an in-cylinder pressure and temperature of 5 MPa and 680K, single cycle)

The natural luminosity of the flame was also captured by the high-speed video camera and results are presented in the next section.

5.1.4. Flame development

The natural luminosity of the flame has two major origins:

- i. Chemiluminescence arising from formaldehyde (CH₂O) and CH emissions in the pre-mixed phase and OH emissions in the mixing-controlled phase (Dec and Espey, 1998, Fujimoto et al., 1998).
- ii. Gray-body radiation linked with soot emission during the mixing-controlled phase.

While most of these emissions lie within the spectral range of the camera, the broadband thermal radiation from hot soot particles is the only emission strong enough to be captured by the CMOS sensor.

The interpretation of the gray-body emission is not straightforward as it is affected by many factors such as the soot particle sizes, temperatures and optical properties (Mueller and Martin, 2002). Furthermore, this signal only gives an integrated information along the line of sight and the contributions of particles at different distances from the camera cannot be differentiated.

Nevertheless, as shown in Figure 50, natural luminosity images can be used to show regions of high soot concentration and temperature. Figure 50 demonstrates indeed the strong dependence of black-body radiation to temperature. A black body is an ideal gray-body, emitting as much radiation as it absorbs. The spectral radiance B_{λ}^b of a black-body is given by Planck's radiation law:

$$B_{\lambda}^b = \frac{2 \cdot h \cdot c}{\lambda^5} \cdot \frac{1}{\exp\left(\frac{h \cdot c}{\lambda \cdot k \cdot T}\right) - 1} \quad (85)$$

Where $h=6.62 \cdot 10^{-34}$ J.s is Planck's constant, $k=1.38 \cdot 10^{-23}$ J.k⁻¹, Boltzmann's constant, $c=2.99 \cdot 10^8$ m.s⁻¹, the speed of light, λ , the wavelength of the radiation [nm] and T , the black-body temperature [K].

The black-body equations are used to characterise and compare real radiation sources. Gray-body radiances are indeed often written as:

$$B_{\lambda} = \varepsilon(\lambda) \cdot B_{\lambda}^b \quad (86)$$

Where $\varepsilon(\lambda)$ is the spectral emissivity of the source

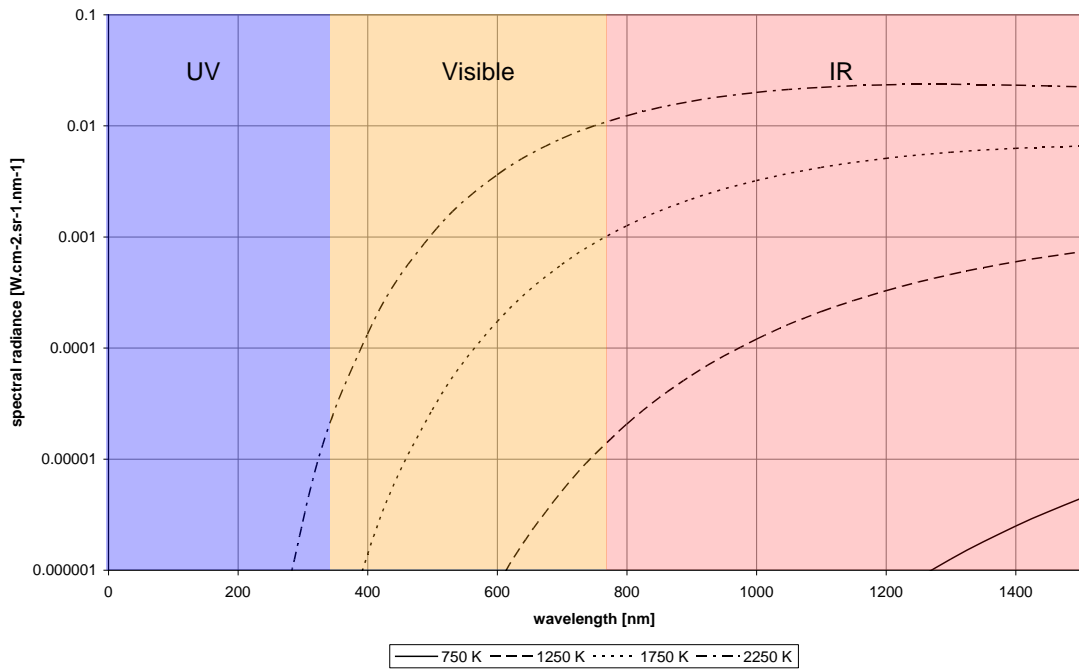


Figure 50 – Evolution of the spectral radiance of a black-body with temperature

In Figure 51, a typical injection sequence is presented. The videos were obtained with the setup presented in Figure 48. Both liquid scattering and natural luminescence of the flame are imaged at the same time. The liquid scattering is located at the top of the chamber, above the combusting zone. The oxidation of carbon yields bright flame regions in the second part of injection.

As discussed in the previous section, the liquid fuel first penetrates progressively in the combustion chamber up to its maximum penetration length.

A first rapid evaporation of the fuel is then observed at the tip of the spray. This evaporation is not associated with soot radiation and is thought to be the result of the pre-mixed combustion. This cold flame could be the source of formaldehyde and CH emissions (Dec and Espey, 1998), unfortunately too weak to be captured by the CMOS sensor. In their chemical kinetic analysis of pre-mixed diesel combustion, Flynn et al. (1999) reported similar timescales for the autoignition and early chemistry of their oxygenated fuel (40% n-heptane and 60% dimethyl ether).

Soot particles are rapidly formed in the combustion zone and thermal radiation becomes visible in a region downstream the liquid tip of the spray. Interestingly, although the liquid penetrations were found fairly constant for all injection pressures, the location of thermal radiation stays further downstream of the liquid tip for the high injection pressure cases. The soot created in the region just downstream the tip of the liquid spray seems to diffuse more radially in the case of low injection pressures and more axially in the case of high injection pressures (Figure 52). The relative position of the flame natural luminosity and the liquid fuel remains quasi-stable until the end of injection. In the late combustion phase, the natural luminosity region first extends towards the injector nozzle before slowly contracting to a zone opposite the injector nozzle. The combustion of the reference diesel fuel was found to be visibly more luminous, confirming the lower soot production of GE80.

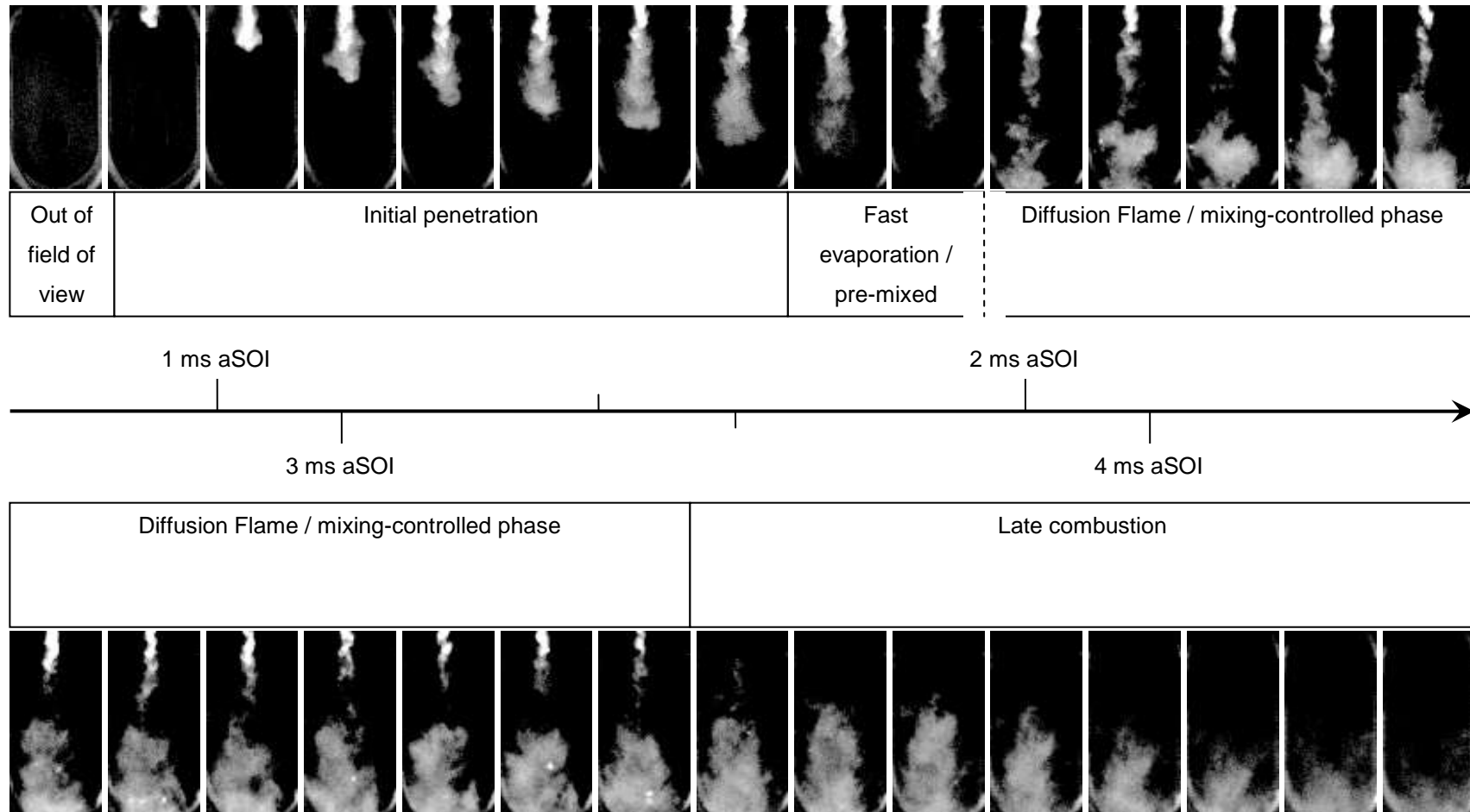


Figure 51 – High speed videos of the spray and flame development (30 mm³ of GE80 injected at 160 MPa in an in-cylinder pressure and temperature of 5 MPa and 700K). The bright regions at the top of the images are due to liquid scattering of the side illumination whereas the bottom bright regions are due to natural luminescence of flame.

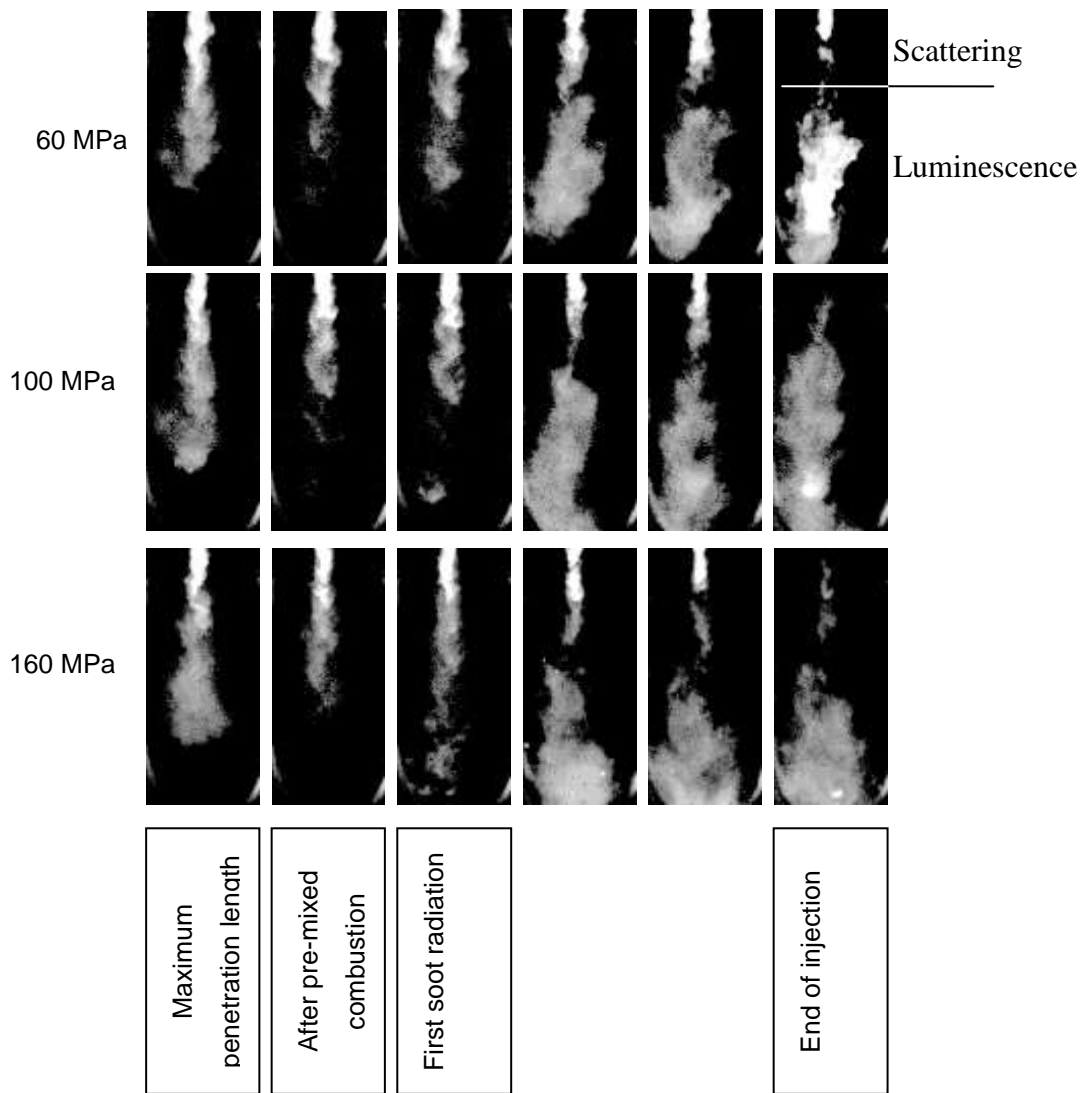


Figure 52 – High speed videos of spray and flame development at three injection pressures (30 mm^3 of GE80 in an in-cylinder pressure and temperature of 5 MPa and 720 K). The bright regions at the top of the images are due to liquid scattering of the side illumination whereas the bottom bright regions are due to natural luminescence of flame.

5.1.5. Cycle analysis

5.1.5.1. Heat release rate

In a non-optical engine, other methods than imaging have to be used to characterise the combustion. The computed heat release rate, based on the in-cylinder pressure, as presented in Appendix A, is a good indicator of the combustion development.

In this investigation, the in-cylinder pressure was measured with a water-cooled pressure transducer inserted in one of the window holders. It was estimated that the pressure trace could be up to 0.1 ms late on the actual events due to the position of the pressure transducer and the speed of pressure waves (sound) in the cylinder. The pressure data was then processed in MATLAB to remove the noise, compute the heat release rate, the ratio of specific heats γ and the spatially averaged in-cylinder temperature. The ratio of specific heats was computed assuming the compression before injection to be adiabatic. The in-cylinder temperature was computed neglecting the mass of the fuel injected and considering the chamber content as an ideal gas.

The heat release rate timing (Figure 53) matched the findings obtained with the rate tube or the high-speed video camera and the curve followed the typical diesel shape presented in the introduction (Figure 2). There was first a small period of negative rate linked with the absorption of heat by the cold liquid fuel. This drop was rapidly followed by a first spike of the heat release rate. This spike could be associated with the pre-mixed cold flame. There was a second, lower spike of heat release rate that matched the time of soot radiation and mixing-controlled combustion.

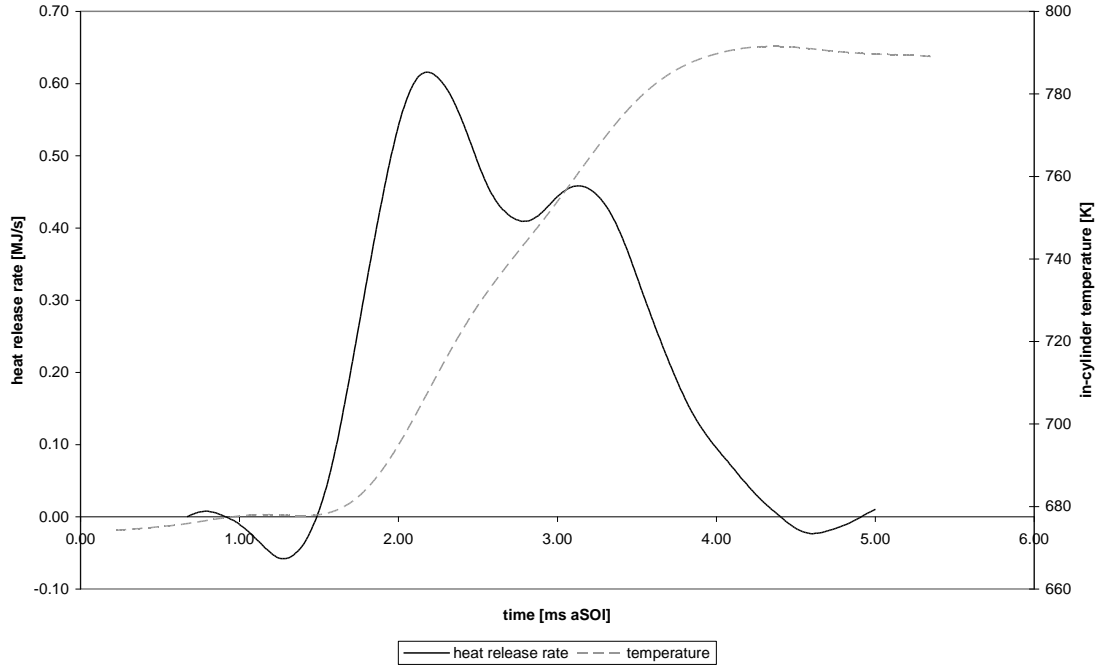


Figure 53 – Computed heat release rate and average in-cylinder temperature (30 mm³ of GE80 at 160 MPa in a in-cylinder pressure and temperature of 5 MPa and 680 K)

The heat release rate curve of Figure 53 resulted from the combination of physical processes, some corresponding to an absorption of heat (fuel heat-up and vaporisation) and some to a release of heat (pre-mixed and mixing-controlled combustion).

The heat of vaporisation and the specific heat of the GE80 are unfortunately unknown but could be assumed to be close to alcohols or alkanes of similar size (Table 21). The lower heating value of the fuel was given by (Pickett and Siebers, 2003). The energies absorbed or released are given by:

$$E_{\text{vaporisation}} = m_{\text{fuel}} \cdot \Delta_v H \quad (87)$$

$$E_{\text{heating}} = m_{\text{fuel}} \cdot c_p \cdot \Delta T \quad (88)$$

$$E_{\text{total}} = m_{\text{fuel}} \cdot LHV \quad (89)$$

Where m_{fuel} is the mass of fuel injected [kg], $\Delta_v H$, the heat of vaporisation [kJ.kg⁻¹], c_p , the specific heat [kJ.kg⁻¹.K⁻¹], ΔT , the difference between the fuel temperature in the rail and its boiling temperature [K] and LHV , the lower heating value of the fuel [MJ.kg⁻¹].

For a heat of vaporisation between 300 and 900 kJ.kg⁻¹, a specific heat between 2 and 2.5 kJ.kg⁻¹.K⁻¹, an injected volume of 30 mm³, a density of 0.93, a rail temperature of

60°C, a boiling temperature of 240°C and a lower heating value of 30.5 MJ.kg⁻¹: $E_{vaporisation}=8-24$ J; $E_{heating}=10-12$ J; $E_{total}=828$ J. The energy absorbed in processes of heat-up and vaporisation of the fuel was rather limited compared to the overall energy balance.

Table 21 – Heat of vaporisation and specific heat of some hydrocarbons of interest (Heywood, 1988)

	Heat of vaporisation [kJ.kg ⁻¹]	Specific heat [kJ.kg ⁻¹ .K ⁻¹]
Gasoline	305	2.4
Light diesel	270	2.2
Isooctane	308	2.1
Cetane	358	
Ethanol	840	2.5

The integrated area under the curve in Figure 53 was evaluated at ~845 J. The difference with the theoretical value could have several origins:

- The poor definition of the combustion boundaries. The pressure trace had to be lowpass filtered because of an interference resonance around 300 Hz. This smoothed the boundaries so the exact times of start and end of combustion are difficult to identify.
- The different assumptions made for the two calculations. The method used to compute the heat release rate assumes the gases to be ideal at a constant temperature and both the crevice flow and the heat of vaporisation were not considered. Likewise, the compression stroke was considered adiabatic and a constant value of the ratio of specific heats γ was used. In contrast, the lower heating value used to compute the theoretical energy release is a global energy balance between a fuel at 300 K and combustion gases at 400 K

5.1.5.2. Vaporisation

The calculations hereafter rely on the following observations: The mass flow rate of fuel entering the chamber could be measured with the rate tube. Moreover, the volume of liquid fuel in the chamber could be extracted from the high-speed videos. Combining these two pieces of information, and with a number of realistic assumptions, it was possible to estimate the instantaneous mass of fuel evaporated.

The calculation principle is shown in Figure 54. It is assumed that elements of liquid fuel leaving the nozzle hole at different times during the injection have the same velocity evolution in the chamber. In reality, the liquid fuel velocity is affected by varying concentrations of fuel. Likewise, the build-up of fuel within the liquid spray is not considered. Therefore, this method of calculation tends to overestimate the evaporated mass as the injected mass increases.

Given the assumption, and for a time t after maximum penetration, the time needed for the tip of the liquid spray to reach the penetration $P(t)$ is t_p , the time with corresponding penetration before combustion, as shown in Figure 54. It follows that the mass of evaporated fuel at time t is the mass of injected fuel at time $t-t_p$.

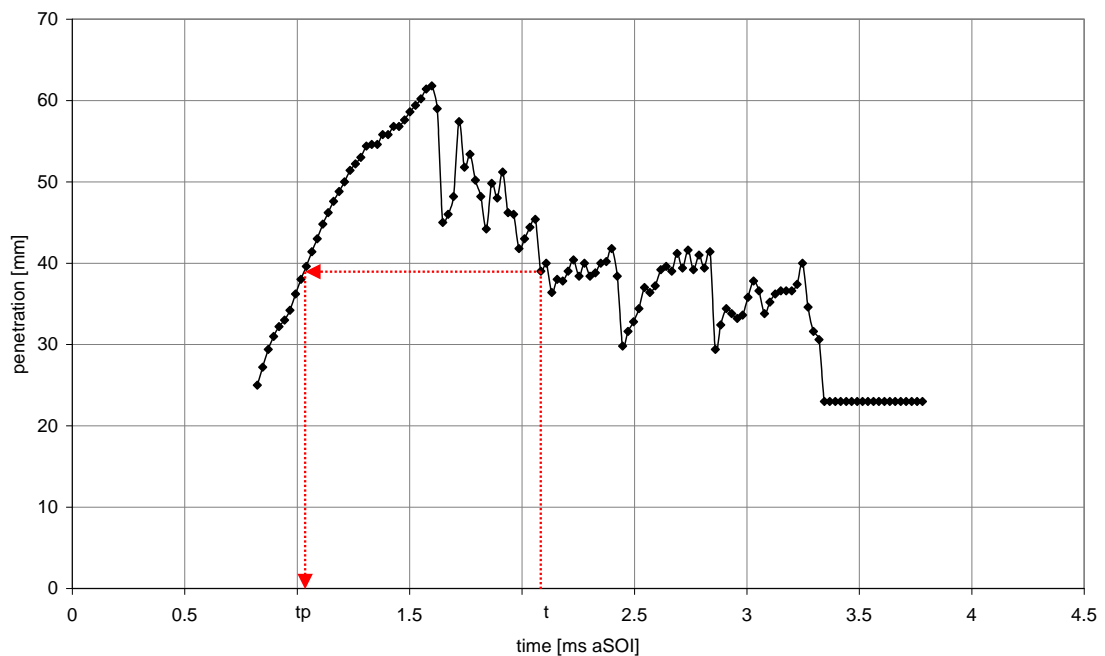


Figure 54 – Evaluation of the evaporated mass (30 mm³ of GE80 injected at 160 MPa in an in-cylinder pressure and temperature of 5 MPa and 680 K)

Unfortunately, the penetration rates measured with the videos were rather erratic and the evaporation rates calculated were difficult to interpret as such. The evaporation rate was therefore filtered with a lowpass and is shown in Figure 55. The negative evaporation rate at the beginning of the graph is an artefact due to the filter. The evaporation starts before combustion and a relatively large spike can be seen at the supposed time of pre-mixed combustion. The rate then stabilises at a lower level during the mixing-controlled phase. Finally it decreases slowly to zero as soon as the injection ends. The calculated

mass of evaporated fuel from Figure 55 is 29.7 mg, compared to the 27.6 mg really injected.

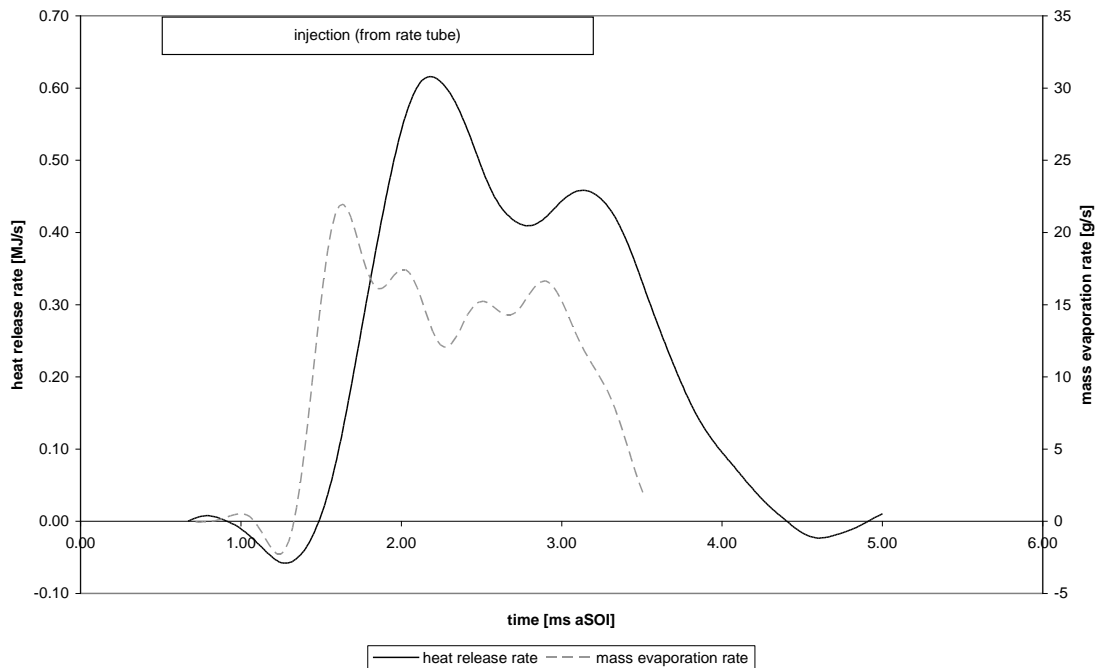


Figure 55 – Evaporation and heat release rates (30 mm³ of GE80 injected at 160 MPa in an in-cylinder pressure and temperature of 5 MPa and 680 K)

5.1.6. Conclusions

The flow, spray penetration, flame luminosity and evaporation measurements all concurred with the following development of the spray and the flame: the fuel started to flow through and out of the nozzle around 0.4 to 0.6 ms aSOI. The injection pressure influenced the time necessary to reach a steady flow as well as the penetration velocity but only faintly the maximum penetration length of the liquid core. Two distinct phases of evaporation were associated with the pre-mixed and the mixing controlled phase. The first phase was characterised by a rapid evaporation of the tip of the spray with no visible soot radiation. The evaporation was steadier in the second phase where the liquid penetration slowly decreased as the highly luminous diffusion flame developed. After the end of injection, the rest of the liquid fuel evaporated while the natural luminosity region first extended towards the injector nozzle before slowly contracting back to a zone at the tip of the plume.

5.2. LIF signal processing

In the case of a dominant collisional quenching Equation (58) can be written as:

$$F = I_{\nu_0} \cdot N_1^0 \cdot f_B \cdot V_c \cdot B_{12} \cdot \frac{h \cdot \nu_0}{c} \cdot \frac{A_{21}}{A_{21} + Q_{21}} \cdot \frac{\Omega_c}{4\pi} \cdot \varepsilon \quad (90)$$

Where I_{ν_0} is the laser irradiance at ν_0 , N_1^0 , the population density of the probed molecule in state 1 prior to laser excitation, f_B , the Boltzmann factor, V_c , the probed volume, B_{12} , the Einstein coefficient for stimulated absorption from state 1 to state 2, h , Planck's constant, ν_0 , the optical frequency of the transition, $A_{21}/(A_{21} + Q_{21}) = \Phi$, the fluorescence quantum yield or the Stern-Vollmer factor, A_{21} , the Einstein coefficient for spontaneous emission from state 2 to state 1, Q_{21} , the collisional quenching rate from state 2 to state 1 ($Q_{21} \gg A_{21}$), Ω_c is the solid angle of the collection optics, ε is the efficiency of the collection optics (includes the detection electronic gain, the quantum efficiency of the detector and any loss of signal due to the optics).

If only comparisons in similar conditions between LIF distributions are sought, the exact formulation of equation (90) can be replaced by a proportionality relation:

$$F \propto I_{\nu_0} \cdot N_1^0 \cdot f_B \cdot \phi \quad (91)$$

The review of the necessary signal corrections presented in paragraph 3.3 showed that the local temperature and molar fractions of CO₂, H₂O and O₂ must be known in order to evaluate the quenching and population distribution factors. Because these values were not easily measurable, it was decided to build a phenomenological model based on the high-speed videos of the combustion and the heat release rate. The idea here was not to construct a model based on a mathematical expression of fundamental physical processes but a model based on the experimental results that could yield orders of magnitude of what cannot be measured.

5.2.1. Calculation of the volume of the flame

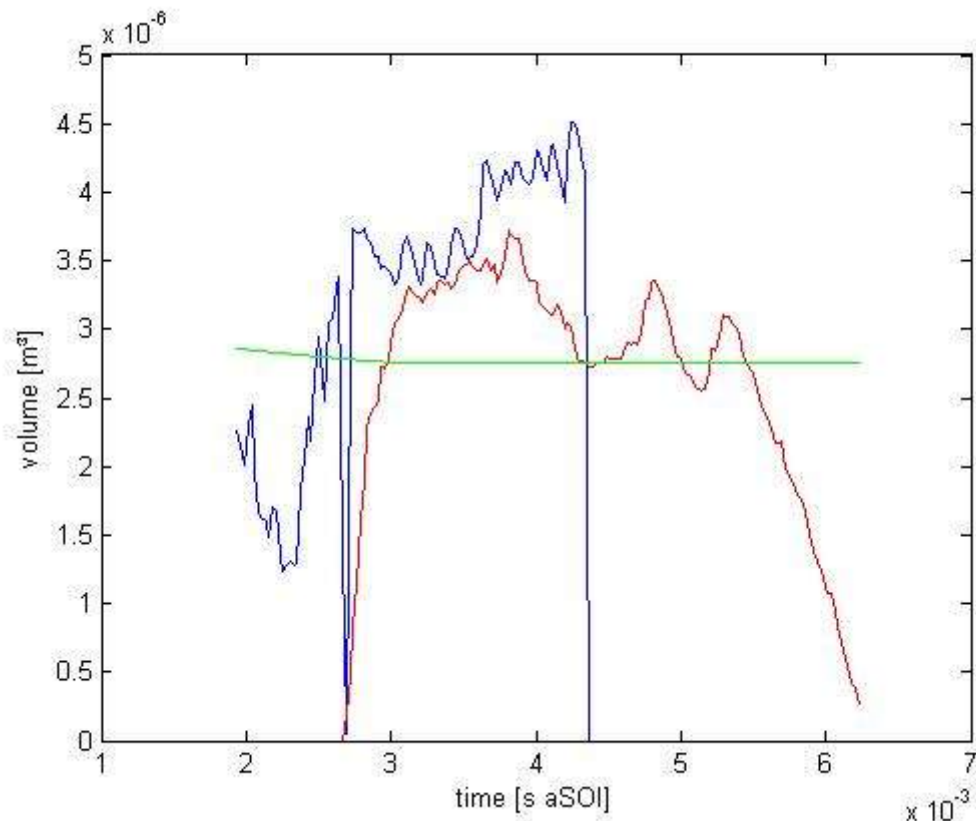


Figure 56 – Computed chamber (green 1/100), pre-mixed flame (blue) and diffusion flame (red) volumes (30 mm³ of GE80 injected at 160 MPa in an in-cylinder pressure and temperature of 5 MPa and 680 K)

If the spray is considered as a cone with varying height, the pre-mixed combustion volume can be defined as the difference in volume between the volume at maximum penetration and the volume at any time t . The diffusion flame region was defined as the area at the edge of the flame, with a thickness compatible with our OH-LIF investigations. The edge of the flame was identified using a Laplace filter. The volume of the pre-mixed flame was then calculated by integration of the flame area revolved over 180° around the central axis (Figure 56).

5.2.2. Calculation of the temperature

The heat release rate was processed to separate the pre-mix and mixing-controlled contribution. It was assumed that the diffusion flame started with the appearance of OH radicals. Similarly, it was assumed that from the height of the second spike in the heat

release rate, the contribution of the pre-mix combustion was negligible. Finally, the heat release rate of the diffusion flame was assumed to increase linearly between these two points (Figure 57). These assumptions can seem relatively far from the physical reality of the combustion, but the aim here is to construct a simple phenomenological model of the flame.

The relative importance of the pre-mixed and mixing-controlled burn can be assessed and compared for different engine conditions. Table 22, for instance, reports the effects of injection pressure on the heat release rate decomposition. As expected, the mixing controlled burn becomes relatively more important with increasing injection duration.

Table 22 – Heat release rate decomposition for two injection pressures (30 mm³ of GE80 injected at 60/160 MPa in an in-cylinder pressure and temperature of 5 MPa and 680 K)

	Heat release [J]			
	Injection pressure: 60 MPa		Injection pressure: 160 MPa	
Total	850	100%	840	100%
Pre-mixed	256	30%	320	38%
Mixing-controlled	594	70%	520	62%

The density of the chamber contents, calculated for each time step, was assumed uniform. The fuel mass was neglected. From the heat capacity of the gases and the heat release rate, a temperature evolution for each of the two flame regions could be calculated.

$$dT = \frac{hrr \cdot dt}{volume \cdot density \cdot c_p} \quad (92)$$

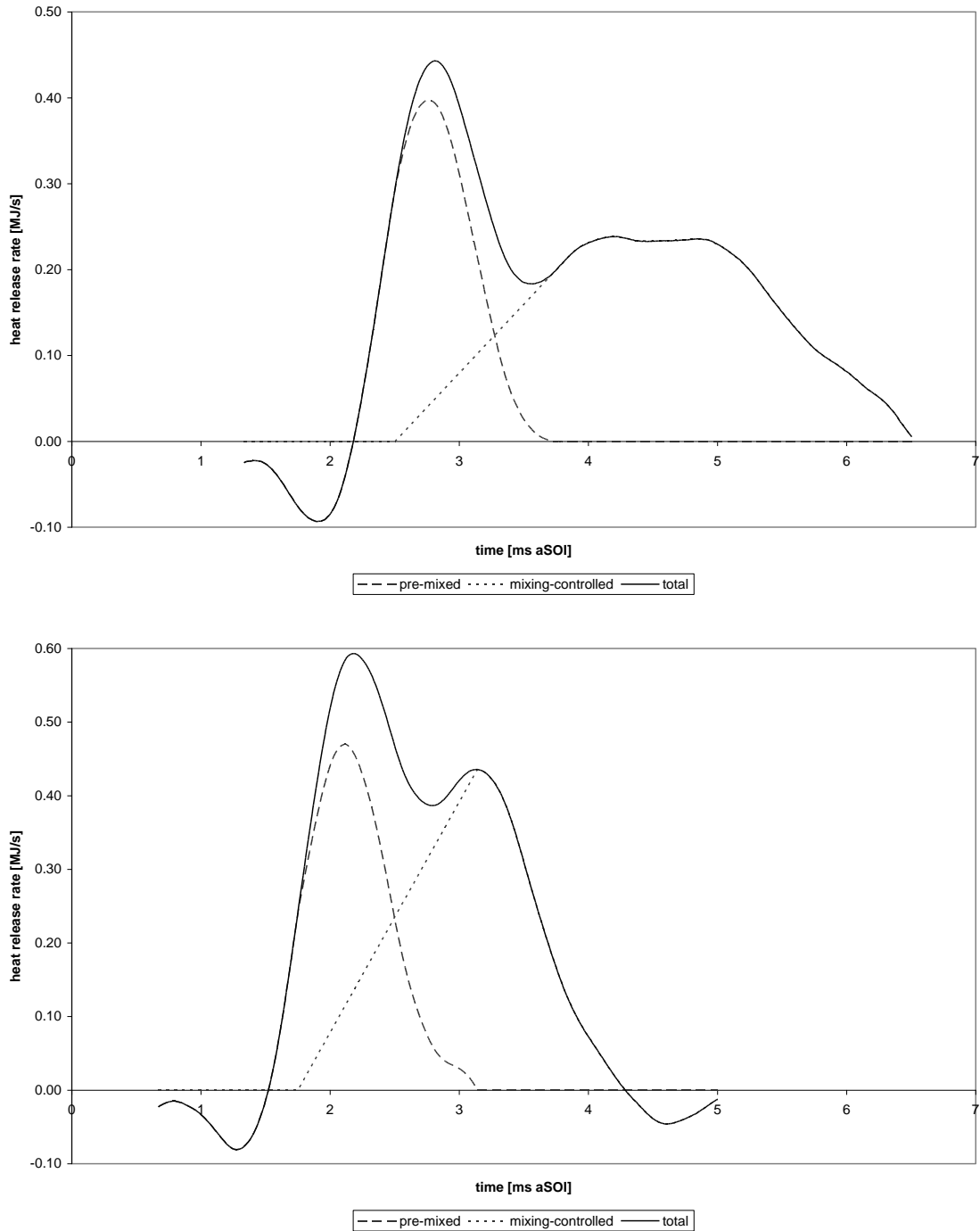


Figure 57 – Heat release decomposition (30 mm³ of GE80 at 60 MPa (top) / 160 MPa (bottom) in an in-cylinder pressure and temperature of 5 MPa and 680 K

5.2.3. Calculation of the molar fractions

Based on the investigation of heptane and oxygenated fuel combustion by Flynn *et al.* (1999), it was assumed that respectively ~10% and ~40% of the total produced CO₂ and

H₂O were formed during the pre-mixed phase. The total amount of CO₂ and H₂O produced was deduced from the quantity of fuel injected. It was then assumed that within the pre-mixed and mixing-controlled phases, the rate of production of CO₂ and H₂O could be scaled by the heat release rate. The O₂ molar fraction was uniformly set to 0.2 at the start of combustion and decreased gradually to zero in the pre-mixed phase.

5.2.4. Mixing

The optical chamber was designed to achieve a near quiescent air motion at TDC. However, the heat transfer and molecular diffusion within the chamber cannot be neglected and a Gaussian type mixing was introduced.

5.2.5. Limitations

Since parts of the optical chamber were hidden to the camera, regions of the late combustion could not be seen and the calculated mixing-controlled volume may therefore be underestimated (Figure 58). This was not an issue for the early stages of combustion. Indeed, the autoignition sites and the early flame were always within the field of view of the camera.

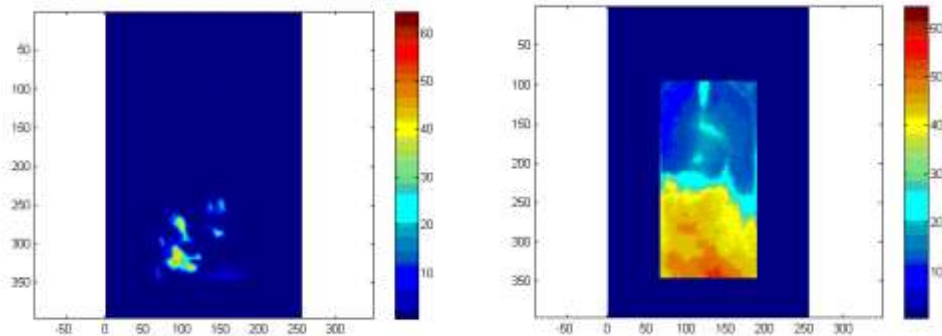


Figure 58 – Individual frames of flame high speed video, 1.9 ms aSOI (left) and 2.4 ms aSOI (right), the frames were included into a background representing the complete chamber volume (160 MPa IP, 5 MPa motored ICP, 30 mm³)

The method used to compute the heat release rate was based on several assumptions: the crevice flow was neglected, the gases were supposed ideal and at a constant temperature, and the heat of vaporisation of the fuel was not considered. Furthermore a

constant value of the ratio of the specific heats $\gamma = c_p/c_v$ derived from the analysis of the pressure curve was used.

Especially at high injection pressures, the mixing-controlled heat release rate started before the first sight of luminosity. When the first small region of soot appeared the mixing-controlled heat release rate was already substantial leading to very high temperatures in the identified region. Likewise, the early mixing-controlled heat release rate was not attributed to any region and therefore wrongly discarded.

Heat transfer and diffusion were rudimentary modelled. The heat transfer could be somewhat adjusted to match expected peak temperatures but unfortunately very little data was available on mole fractions during combustion.

5.2.6. Results and discussion

A number of maps of temperature and molar fractions of carbon dioxide are presented in Figure 59. The first distributions are typical of pre-mixed combustion with a high intensity throughout the vapour fuel region. The distributions then reflect the appearance of a flame front and the diffusion flame. Finally, the flame collapse and the gradual mixing of temperature and products can be seen.

The maximum and average temperatures calculated by the model are shown in Figure 60. The maximum temperature is seen to increase in two steps, first to around 1200 K during the pre-mixed phase and then to 1700 K within the diffusion flame. The average temperature is higher than the average temperature computed from the pressure trace which has a maximum of 760 K. The model is indeed a closed system whereas the real chamber will see heat transfer to the walls, cylinder head and piston by forced convection or radiation.

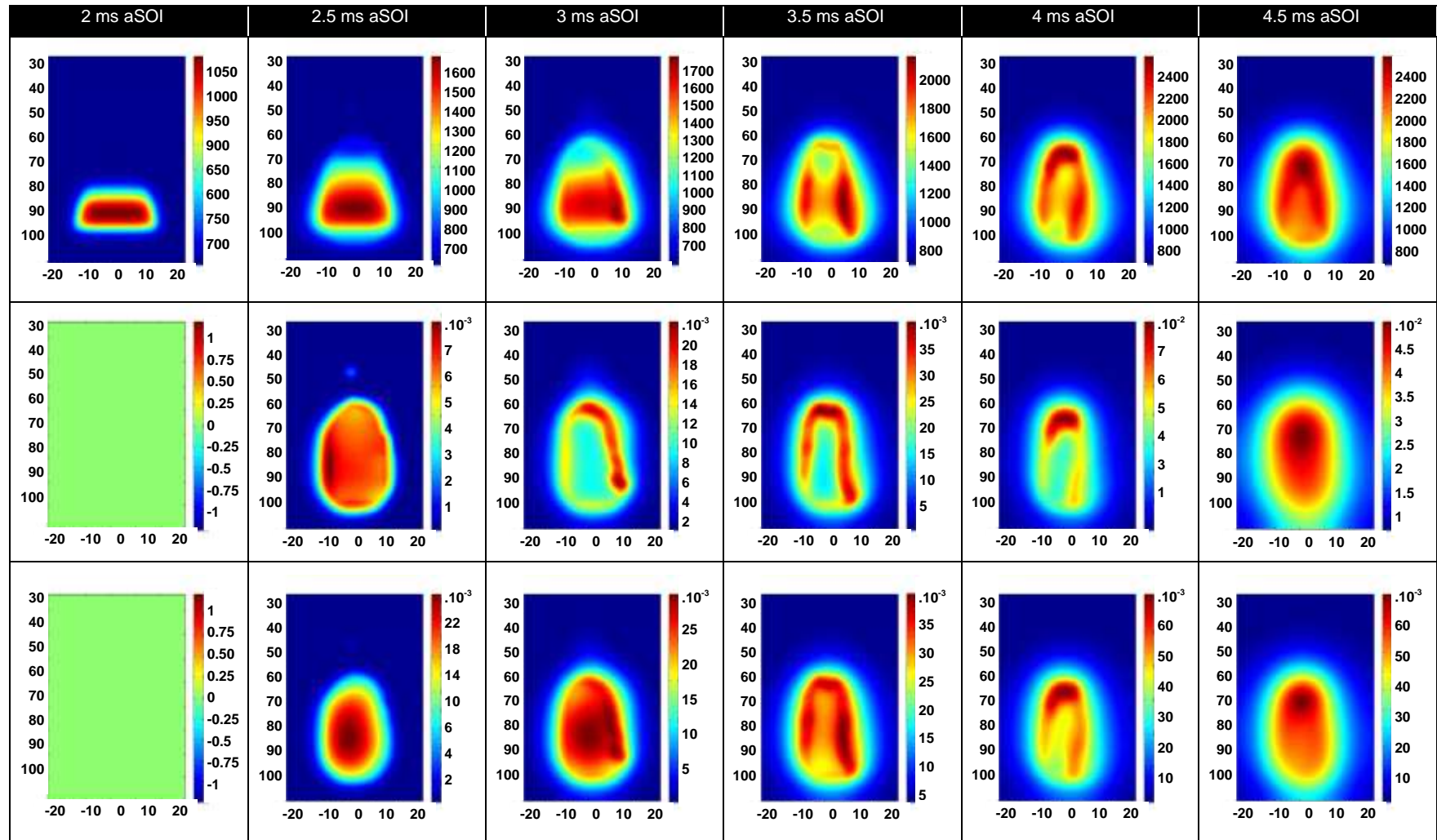


Figure 59 – Example of computed temperature (top row, colour coding in K), CO₂ molar fractions (middle row) and H₂O molar fractions (30 mm³ of GE80 injected at 100 MPa in an in-cylinder pressure and temperature of 5 MPa and 700 K). The figures on the vertical and horizontal axes correspond respectively to the axial distance from the nozzle and the radial distance from the centre of the chamber in mm.

In Figure 61 and Figure 62 the evolution of population and fluorescence yield factors with time are presented. These maps were obtained by computing the correction factors on a line 50 mm downstream the injector nozzle. These profile intensities represent the intensity variations in the LIF signal simply due to temperature and quenching variations (assuming a homogeneous mixture of OH and NO).

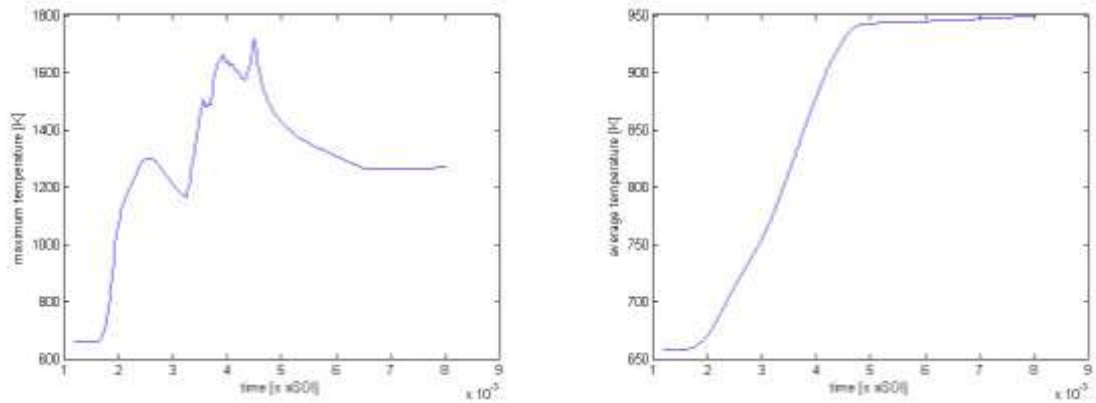


Figure 60 – Maximum (left) and average (right) computed temperatures (30 mm³ of GE80 injected at 100 MPa in an in-cylinder pressure and temperature of 5 MPa and 700 K)

The population correction depends on temperature only and it can be seen that at the time of peak temperature, the OH and NO densities will be underestimated by up to 15% in comparison with the time of coldest temperature within the combustion period. This compares favourably with the limited published data on population effects based on temperature measurements. Barlow *et al.*, for instance, found a maximum correction for population fluctuations of $\pm 10\%$ in their non-premixed turbulent flame (Barlow *et al.*, 1989).

The fluorescence yield, which depends on temperature and local molar fractions of quenching species, is found to be stronger where populations are lower. Within the combustion duration, the fluorescence yield of OH and NO for instance will vary by less than 30 and 40% respectively.

It can be noted that, whereas the fluorescence yield intensities vary in values, their distributions do not change considerably between OH and NO.

The regions with lowest population of excitable molecules generally coincide with the regions of high fluorescence yield.

Although this model proves that population distribution and especially collisional quenching have to be taken into account if a quantitative study of OH and NO

distributions is sought, they remain limited enough for the results of the present uncorrected, qualitative investigation to be meaningful.

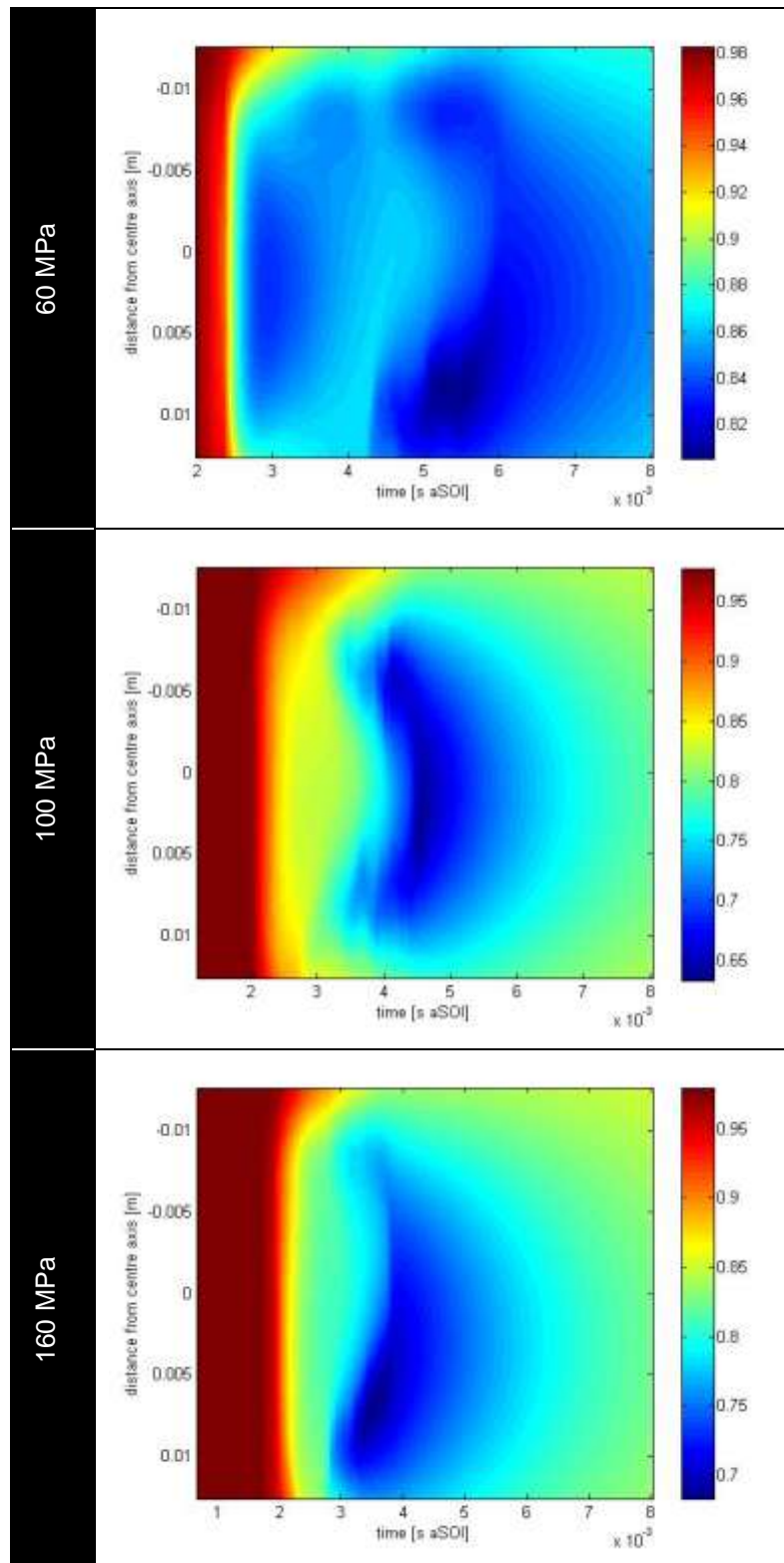


Figure 61 – Population effects on the LIF signal with time for 3 injection pressures (30 mm³ of GE80 injected in an in-cylinder pressure and temperature of 5 MPa and 700 K)

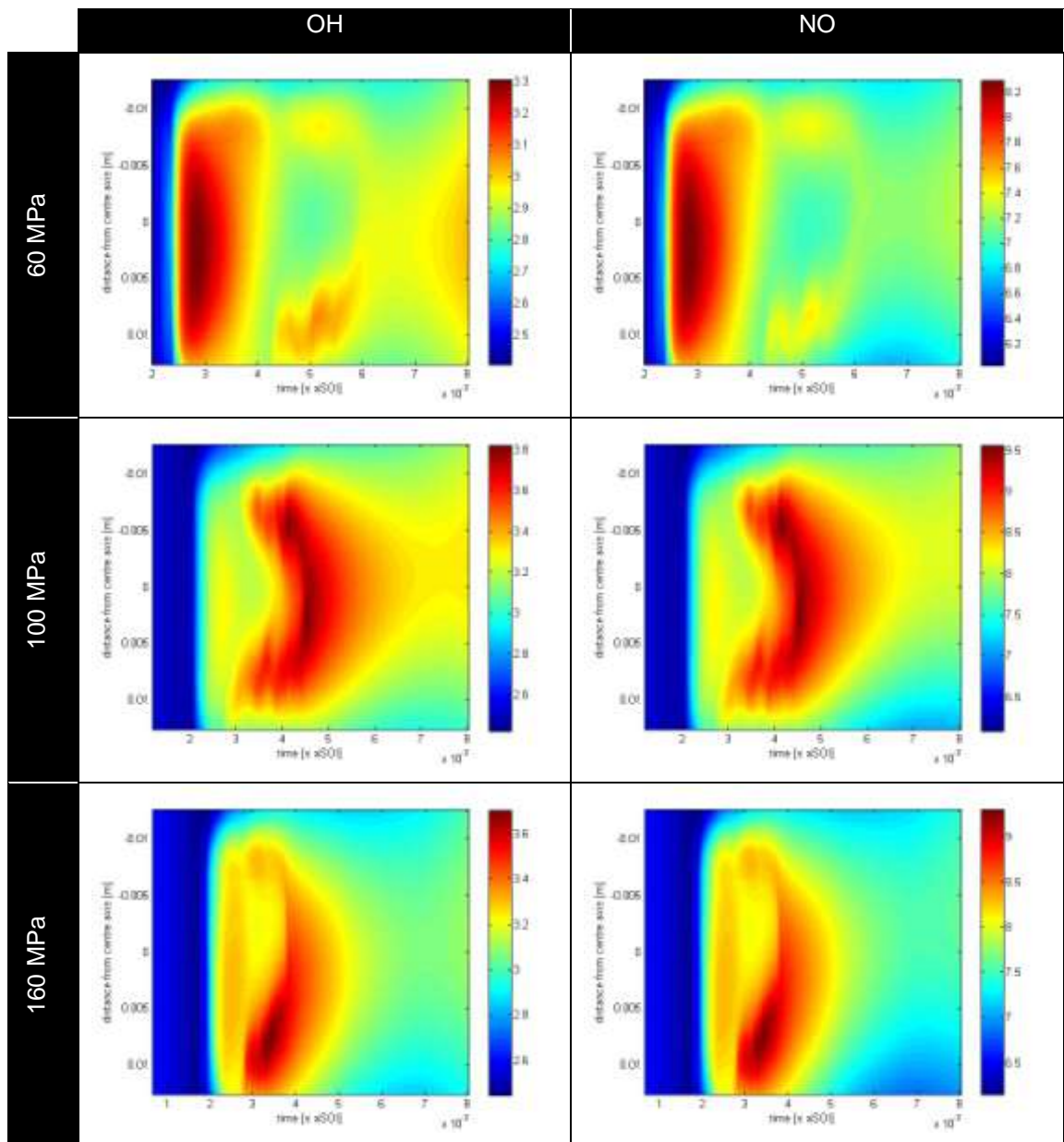


Figure 62 – Fluorescence yield effects on the OH- and NO- LIF signal with time for 3 injection pressures (30 mm³ of GE80 injected in an in-cylinder pressure and temperature of 5 MPa and 700 K)

6. LASER INDUCED FLUORESCENCE OF HYDROXYL RADICALS

In the following chapter, the excitation and collection details of the OH-LIF experiment are presented. The calibration and the choice of the excitation wavelength are then described. Finally the measurement procedure is given and the results of the experiment are presented and discussed.

6.1. Excitation

The second harmonic of the Nd:YAG laser (532 nm) was used to pump the dye laser. The output energy of the Nd:YAG laser was measured at around 300 mJ. The optics of the dye laser were aligned to maximize the power output while keeping the beam shape circular. The output wavelength of the selected dye solution was in the range 555-585 nm for mean output energies of 50 mJ/pulse. The frequency was then doubled by the use of a BBO crystal, providing a final wavelength range of 278-290 nm and a final energy of 10 mJ/pulse. Table 23 lists the hardware and settings used for the OH-PLIF investigation.

Table 23 – Hardware and settings used for OH-PLIF

Pump laser	Nd:YAG second harmonic (300 mJ at 532 nm)
Dye laser	Three-stage dye laser and BBO crystal
Camera	Intensified CCD camera
Lens	UV lens, f=105nm, f/4.5 aperture
Optical filters	Interference filter centred on 307 nm with a FWHM of 9 nm
Intensifier gate time	50 ns
Intensifier gain	800
Laser sheet dimensions	40 x 0.5 mm
Laser pulse energy	10 mJ
Pulse duration	7 ns (FWHM)
Excitation wavelength	283.96 nm (on-line), 283.86 nm (off-line)
Excitation scheme	$A^2\Sigma^+ - X^2\Pi(1,0)$

6.2. Collection

A first selection of filters based on the manufacturers' data was tested in OH-LIF experiments. Because the results seemed inconsistent, a spectrograph analysis of each filter was done. Some filters transmittances were found to be rather different than the advertised transmittances (Figure 63). Finally the IF 307, an interference filter centred on 307 nm with a FWHM of 9 nm and a maximum transmittance of 40% was selected. Indeed, this filter possesses the highest absorption around the Mie scattering wavelength and a transmittance high enough to collect a substantial part of the emitted fluorescence.

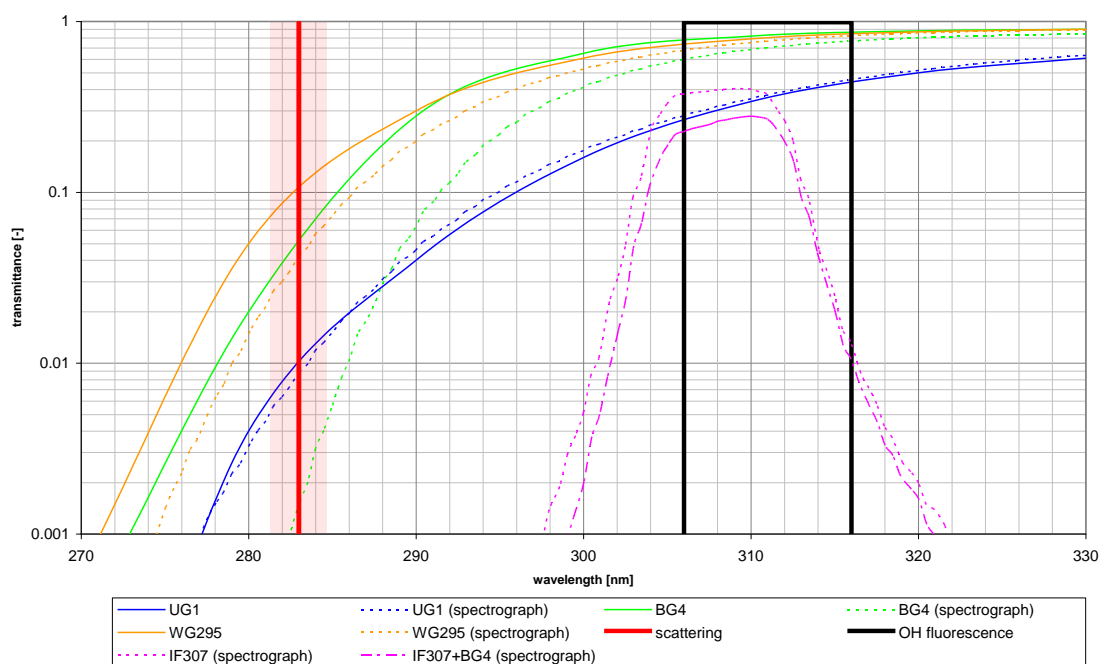


Figure 63 – Filters for OH-LIF

6.3. Calibration of OH-LIF with a candle light

Two dyes commercially available have a wavelength range compatible with the excitation of the transition $A^2\Sigma^+ - X^2\Pi(1,0)$ of OH: Coumarin 153 and Rhodamine 590. From Table 24, it appears that the latter possesses the best efficiency. However, it was feared that Rhodamine 590 would “contaminate” the dye pump circuit. If purging the solution is not sufficient to dispose of all the dye, the next investigation using the dye laser (NO-LIF with Coumarin 47) would be compromised. Therefore a test was

conducted on a candle flame to assess the relative fluorescence of OH with the two dyes.

Table 24 – Lasing Performance of the Coumarin 153 (left) and Rhodamine 590 (right) (Brackmann, 2000)

Pump		Dye Laser Characteristics						Pump		Dye Laser Characteristics				
Source	Wavelength [nm]	Peak [nm]	Range [nm]	Effic. [%]	Conc. [g/l]	Solvent	Source	Wavelength [nm]	Peak [nm]	Range [nm]	Effic. [%]	Conc. [g/l]	Solvent	
XeCl-Excimer	308	540	522-600	15	4.20	Methanol	XeCl-Excimer	308	581	569-608	16	1.20	Methanol	
Nd:YAG, 3rd	355	540	516-575	18	2.36	Methanol	Nitrogen	337	581	573-618	rel.	1.63	Methanol	
Nitrogen	337	540	517-590	rel.	3.10	Methanol	Nd:YAG, 2nd	532	566	555-585	32	0.10	Methanol	
Flashlamp	-	-	528-547	-	-	Methanol	Flashlamp	-	600	555-620	-	1.20	Ethanol	

Figure 64 shows a comparison of the candle spectrum and a simulation spectrum using a reference database: LIFBASE (Luque and Crosley, 1999). The reference database compiles all information available from transition probability calculations on OH. The small constant offset of ~0.035 nm between the two spectra was attributed to the dye laser's grating calibration. Although most of the transitions observed corresponded rather closely to a real rotational transition of OH, a number of transitions were "missed". This was to link with the low resolution of the candle spectrum (0.3 nm) and the very sharp peaks at atmospheric pressure. Of course, these wavelengths will be slightly different at the high pressures and temperatures of diesel combustion. After correction for collisional shift, the on-line excitation wavelength was set at 283.96 nm as this region exhibits a high absorption due to a number of coinciding rotational transitions (Q1(9), Q2(8), R21(17)). Furthermore, the off-line wavelength can be set only 0.1 nm away from this peak as the region around 283.86 nm shows very little absorption.

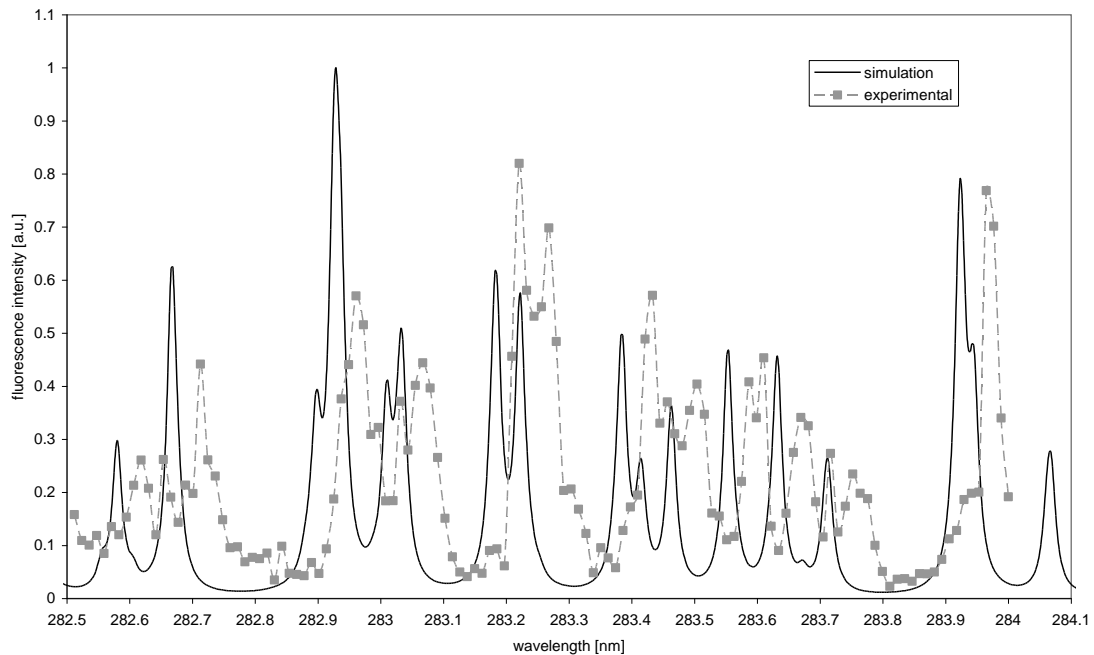


Figure 64 – Experimental candle flame and simulation spectra of OH

In Figure 65 distributions of OH in a candle flame, with respectively Coumarin 153 and Rhodamine 590 as dye, are presented for same general conditions (i.e. excitation wavelength, laser energy, intensifier gain, colour resolution...). Although both images have very low peak intensity, the OH distribution is only exploitable in the case of the Rhodamine 590. The maximum intensity in both images is of 859 and 168 counts for Rhodamine 590 and Coumarin 153 respectively. It can be noted that, even in these favourable conditions, only a small part of the 12 bits (4096 counts) range of the camera could be used (the gain of the intensifier being already at its maximum setting).

The average fluorescence intensities reported in the experimental spectrum of Figure 64 were for a region including the candle flame but excluding the area with a strong scattering on the candle top. The conditions in which these pictures were taken were obviously more favourable than in the case of a real diesel-like combustion. It was then decided that Coumarin 153 would not yield strong enough intensities and a solution of 0.10 mg/l of Rhodamine 590 in a fluorescence grade methanol was selected. A special scheme was set up to ensure that the dye pumps were run twice a day. This appeared to be sufficient to keep the dye from “contaminating” the dye circuit.

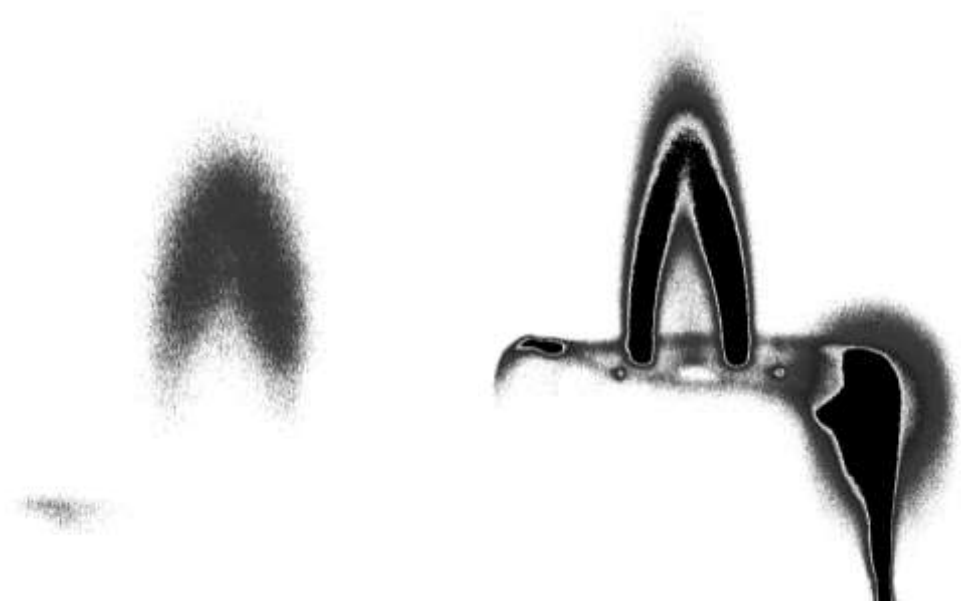


Figure 65 – Negative of OH-LIF on a candle with Coumarin 153 (left) and Rhodamine 590 (right)

6.4. Results and discussion

Planar distributions of OH radicals were captured for a number of injection and in-cylinder pressures. For each set of specific conditions the following measurement methodology was observed:

- i. A reference image of the combustion chamber was taken to identify the window outline and scaling (an example is shown in Figure 66).
- ii. The engine was warmed-up until stable conditions (in terms of water, oil and inlet temperature as well as in-cylinder pressure and engine speed) were reached.
- iii. A number of fired cycles ensured that the fuel injection equipment worked properly in a repeatable manner.
- iv. After optimising the BBO orientation for

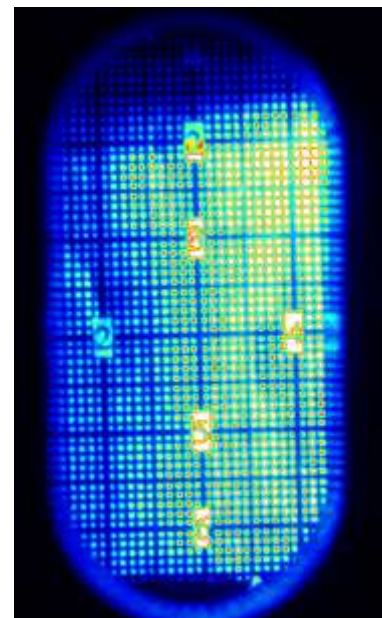


Figure 66 – Reference image of the combustion chamber

maximum output energy, the distributions for the on-line wavelength were captured (30 captures at 283.96 nm for each time step, the first 10 fired cycles being discarded).

- v. Similarly, after optimising the BBO orientation for maximum output energy, the distributions for the off-line wavelength were captured (15 captures at 283.86 nm for each time step, the first 10 fired cycles being discarded).

The distributions presented hereafter are colour-coded following the maps of Figure 67. Each set of distributions was normalised so that individual distributions intensities could be compared within the same figure.

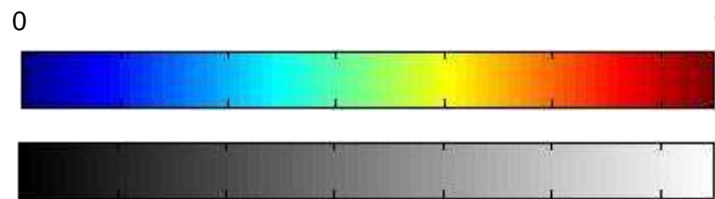


Figure 67 – Normalised colour and black & white maps used in distributions

Figure 68 presents single cycle, non-corrected, on-line OH distributions as well as single cycle spray and flame images. For each time step, the OH distribution shown was chosen to be representative of the 30 raw on-line distributions captured. The spray and flame images were obtained during a distinct investigation but for the same conditions. The high signal at 1.5 ms aSOI and part of the signal at 1.75 ms aSOI were due to strong Mie scattering from the liquid jet. Although the laser sheet height was adjusted to cover most of the combustion chamber, it can be seen at 1.5 ms aSOI that the laser energy was very weak at the top part of the spray. The two red lines in Figure 68 delimit the effective height of the laser sheet. Complete sets of raw OH distributions can be seen in Appendix .

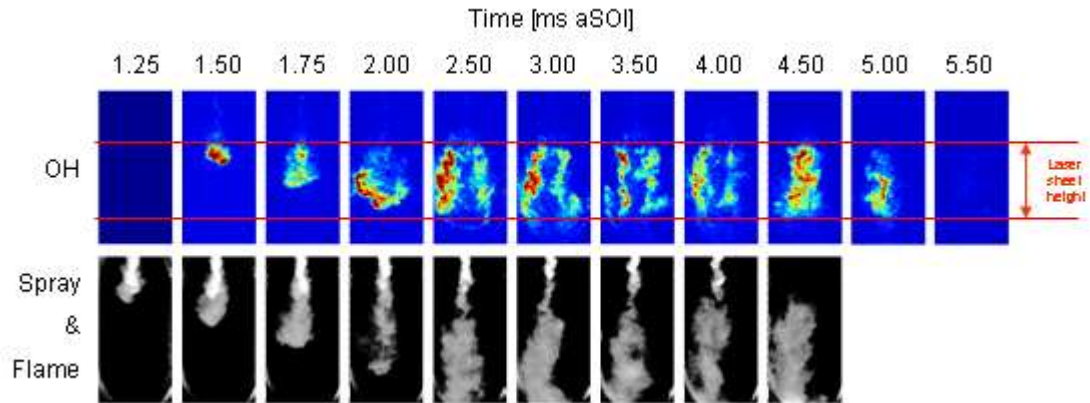


Figure 68 – Raw OH-LIF on-line distributions and spray and flame (30 mm³ of GE80 injected at 100 MPa in an in-cylinder pressure and temperature of 5 MPa and 630 K)

The energy profile of the sheet is globally Gaussian but affected by non-uniformities as can be seen in the average data of Figure 69. Indeed, some regions of the flame front appear to be consistently darker although there is no physical reason for OH concentrations to be lower at a specific height in the chamber. The alignment of the pre-amplified and amplified beams in the dye laser was set primarily for beam shape but also for output energy. This resulted in a slightly uneven laser profile. Also in Figure 69, the effects of laser light attenuation can be observed. The flame front on the side of the incoming laser light is, on average, 50% brighter than the flame front on the other side of the spray. The laser and fluorescence light is not only absorbed by nitric oxide but also by a number of broadband absorbers as well as by hot CO₂ (Hildenbrand and Schulz, 2001). The signal is therefore naturally stronger where the laser and the fluorescence travels are shorter, yielding asymmetrical distributions.

As observed by Dec and Coy (1996), the pre-mixed phase chemistry did not involve OH radicals, resulting in a negligible OH-LIF signal. The unexpected presence of strong signal in the pre-mixed phase for some injection or in-cylinder pressures can be explained by an incomplete cancellation of the strong Mie scattering of liquid droplets by the off-line subtraction method. Indeed, the spray extent seems to have changed in the time interval between the capture of the on- and off-line distributions.

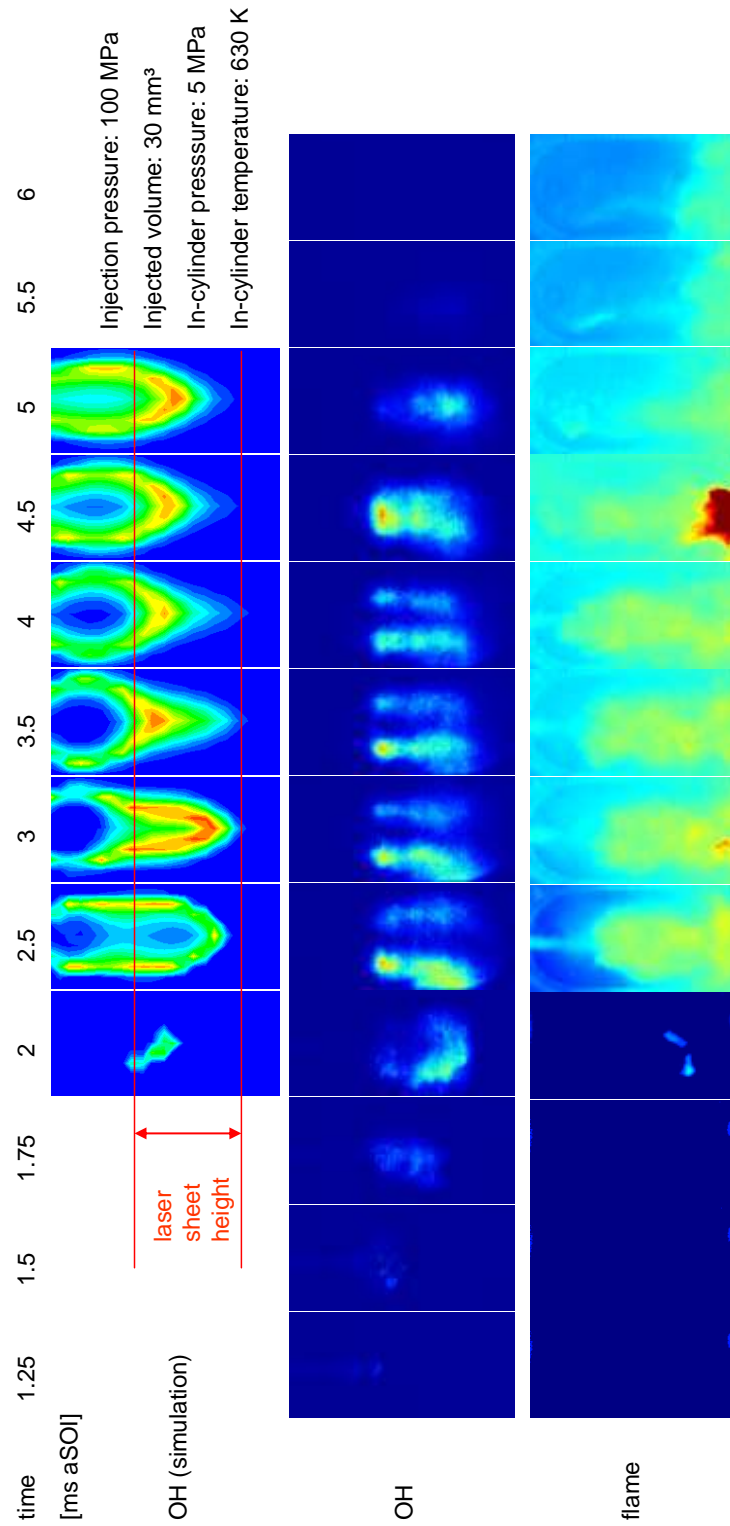


Figure 69 – Comparison of the measured OH distributions with the natural flame luminosity. The left row shows OH distribution from the KIVA 3 simulation by Dr Abdelghaffar (private communication)

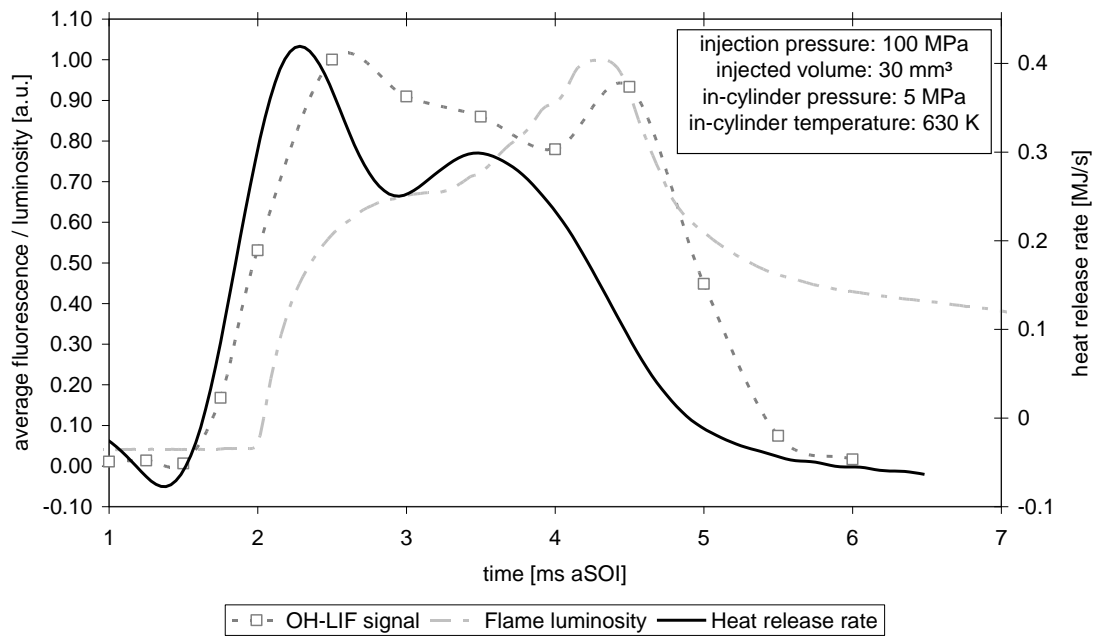


Figure 70 – Spatially averaged luminosity and OH signal compared to the heat release rate

The diffusion flame was visible as early as 0.4 ms before the pre-mixed heat-release spike (Figure 70) and started in the pre-mixed combustion products, downstream of the liquid fuel maximum penetration. It progressed downstream with the spray expansion and in 0.5 ms had evolved into a thick ellipsoidal flame front. After the peak heat-release, the flame front on the sides of the spray became fairly static while keeping a substantial thickness and exhibiting uneven ripples. These characteristics were kept until the end of injection. In contrast, the flame front moving along the spray axis became smooth and thin until no clear structure could be discriminated in the OH radicals distributions. Thus, for the main part of the mixing-controlled phase, the diffusion flame was composed of a rippled tube-like structure with high concentrations of OH radicals on its edges, and, downstream of this tube, a wider combustion zone with little OH and no discernable structure. It must be noted however that for some conditions (e.g. high injection pressures) the tip of the flame stood outside of the probed region. This is especially apparent in Figure 71 where the vertical profile intensities at 3 ms aSOI are plotted for the different injection pressures. The vertical profiles are obtained by summing the intensities for each row horizontally across the image. With increasing injection pressure, the flame moves further away from the nozzle. However, the extent of the flame appears similar for 100, 140, and 160 MPa injection pressure.

This is in fact due to the low intensity of the laser sheet above 65 mm away from the nozzle.

When the injection ended, the fairly static hollow flame collapsed on itself, slowly burning the mix of vapour and partially oxidised fuel present in the centre of the plume. This phase was associated with a high density of OH radicals throughout the flame plume.

The injection duration mainly affected the persistence of the combustion pattern described above as injections were always long enough to reach a stable diffusion flame. The fluorescence intensity slowly decreased along this phase.

The experiment was reproduced in a numerical simulation by Dr. Walid Abdelghaffar (private communication), implementing the Shell model (Halstead et al., 1977) in KIVA 3V release 2. The model was previously introduced in section 1.1. Although the results could not be quantitatively compared, the general trends of development and the associated distribution characteristics were in good agreement. Notably, the onset of the diffusion flame and its early development satisfactorily matched the measured distributions (Figure 69). In particular the timing, spatial distributions and temporal evolution of the predicted OH concentrations agreed with the experimental OH-LIF data.

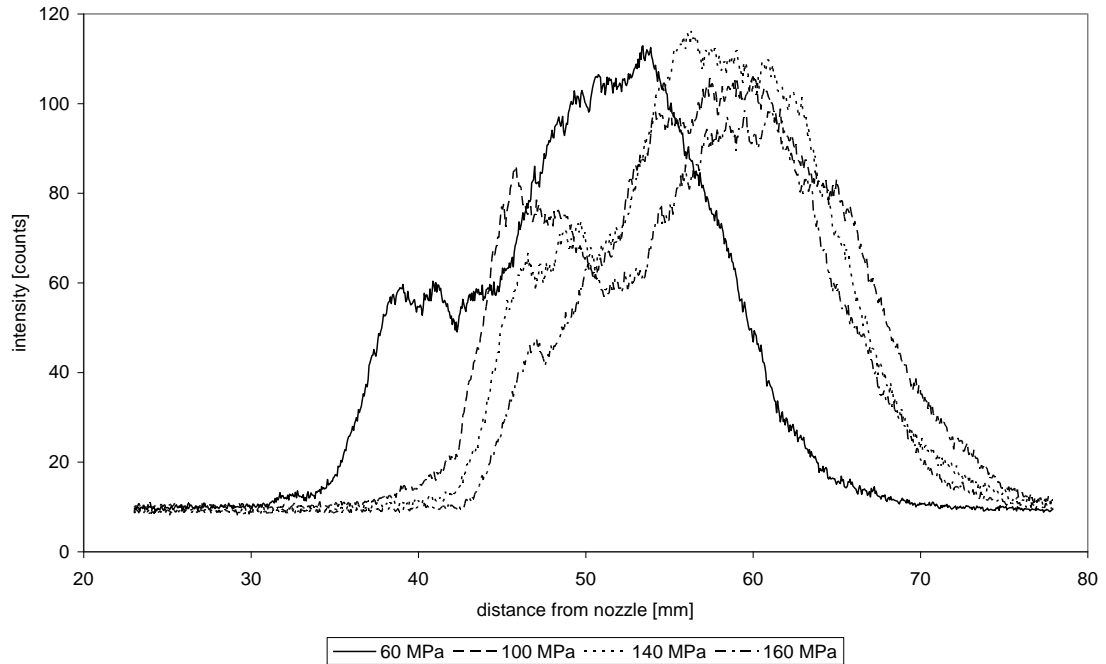


Figure 71 – Vertical intensity profile of OH distributions, 3 ms aSOI (30 mm³ of GE80 injected in an in-cylinder pressure and temperature of 5 MPa and 700K)

6.4.1. Effect of injection pressure

As seen in Figure 49, the maximum liquid fuel penetration does not increase significantly with increasing injection pressure. A similar behaviour was observed in the study of the breakup length on the same RCM by Karimi *et al.* (2006). The breakup length is a measure of the length of the liquid core before its breakup into droplets and ligaments and is therefore indicative of the fuel spray structure. Karimi *et al.* found that breakup lengths were mostly insensitive to injection pressure. However, the flame position with respect to the nozzle is clearly affected by injection pressure (Figure 71). It is believed that, for all injection pressures, liquid fuel penetrations reach a similar plateau above which only vapour fuel is present. This plateau is faster reached for high injection pressures. The vapour, on the other hand, continues to penetrate and because of its higher momentum at high injection pressure, it will be further away from the nozzle when autoignition occurs. Overall, this results in a longer vapour fuel region. This analysis is supported by the results of the Schlieren photography investigation of Crua (2002) where the vapour region is seen to increase in length with injection pressure.

The influence of the injection pressure on the diffusion flame development was consistent with what could be deduced from the vapour and heat release rate evolution: an increase in injection pressure resulted in a higher penetration of the fuel vapour and an earlier flame development (Figure 72). Apart from their timing and extent, the sequence of patterns identified above was not considerably affected by the injection pressure. The instantaneous fluorescence intensities were slightly stronger for the high injection pressures, in accordance with higher heat-release rates.

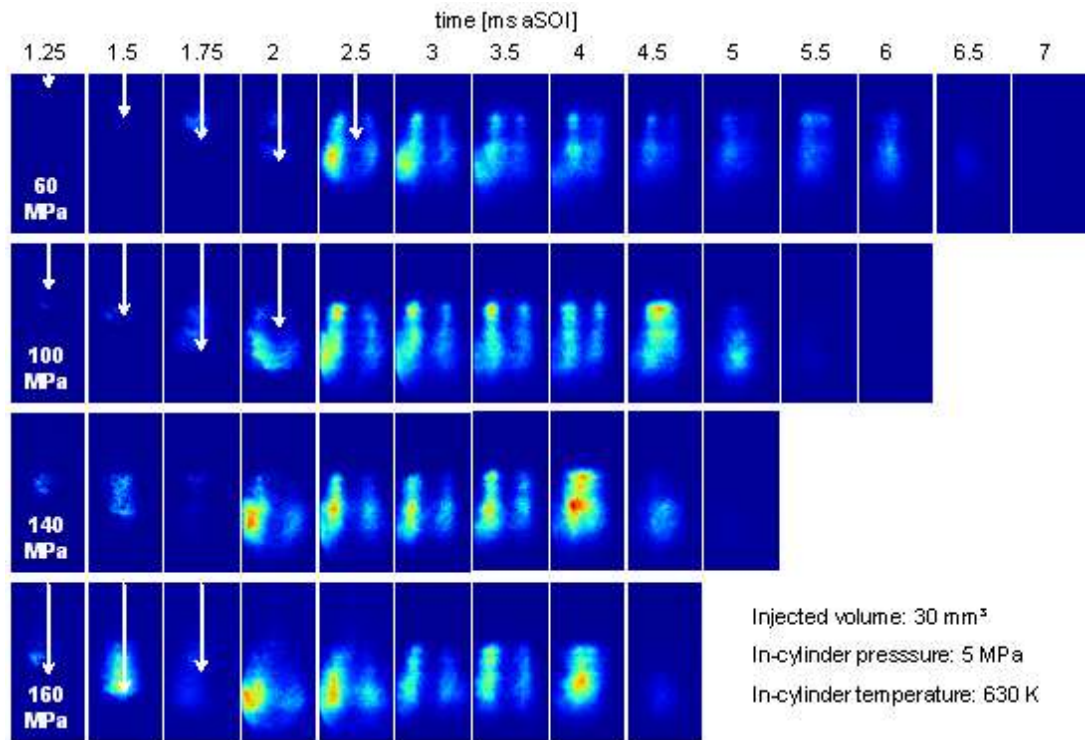


Figure 72 – Evolution of OH radicals distribution with time for four injection pressures. The white arrows indicate the liquid fuel penetration, as observed from high-speed videos (no data for 140 MPa)

The width of the flame plume and the flame front thickness appeared to stay constant with increasing injection pressure, as seen in Figure 73. This is compatible with the results of the investigation by Crua (2002), who found that the spray cone angle is not affected by the injection pressure. The horizontal profiles of Figure 73 are obtained by summing the intensities for each column vertically across the image. The finer atomisation associated with high injection pressures does not change the thickness of the combusting zone. The small offset of the plume horizontal position with respect to the central axis is due to a small angle offset in the positioning of the injector.

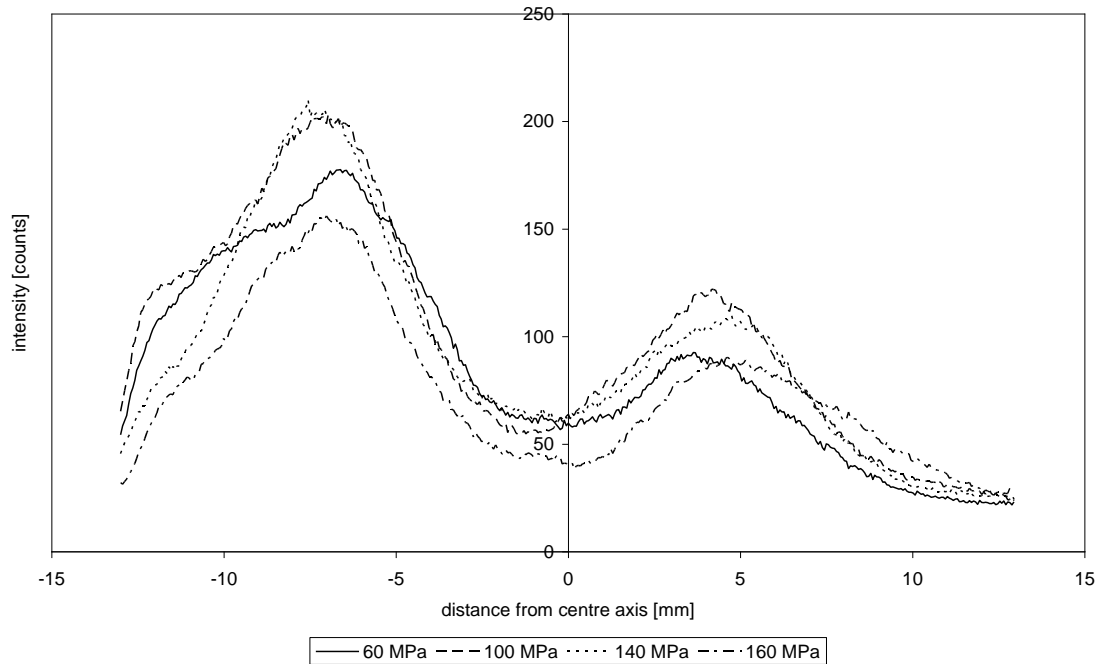


Figure 73 – Horizontal intensity profile of OH distributions, 3 ms aSOI (30 mm³ of GE80 injected in an in-cylinder pressure and temperature of 5 MPa and 700K)

6.4.2. Effect of in-cylinder pressure

Some distributions were recorded at a higher in-cylinder motored peak pressure of 6 and 7 MPa. Considering a constant in-cylinder temperature of 700 K, the investigated in-cylinder pressures of 5, 6 and 7 MPa correspond respectively to gas densities of 25, 30 and 35 kg.m⁻³. Results presented in Figure 75 show that while the combustion started earlier, it followed the development described for 5 MPa in-cylinder pressure, but with an overall weaker fluorescence signal, which was attributed to stronger three-body recombination chemistry.

Several researchers (Correa, 1992, Drake et al., 1987, Cooper and Laurendeau, 2000) noted that practical combustors employing turbulent diffusion flames have largely demonstrated a $P^{0.5}$ scaling of NO emissions with pressure. At high enough equivalence ratios, the NO formation rate becomes predominantly thermal in origin and is limited by the abundance of O atoms. The absolute concentrations of equilibrium O atoms scale approximately as $P^{0.5}$. In Figure 74, the power dependence n of OH fluorescence strength on in-cylinder pressure is presented, with:

$$\frac{OH_{P_1}}{OH_{P_2}} = \left(\frac{P_1}{P_2} \right)^n \quad (93)$$

Because of the change in combustion timing and position with in-cylinder pressure, the P^n scaling in Figure 74 varies substantially. However, the dependence is consistently negative and centred around $n=-1$. Allen *et al.* (1994) found a similar dependence ($n=-0.9$) at relatively low pressures of 0.1 to 1 MPa. This investigation extends therefore the range of verified pressure dependence up to 7 MPa. Furthermore, in this case, the data was obtained using a standard common rail injection system and high injection pressures. Contrary to O atoms, OH radicals seem to have a negative power dependence on in-cylinder pressure. However, collisional width is directly proportional to pressure and the collisional quenching of the fluorescence signal increases with pressure. A negative pressure dependence would be therefore consistent with the evolution of both the overlap integral and the fluorescence yield.

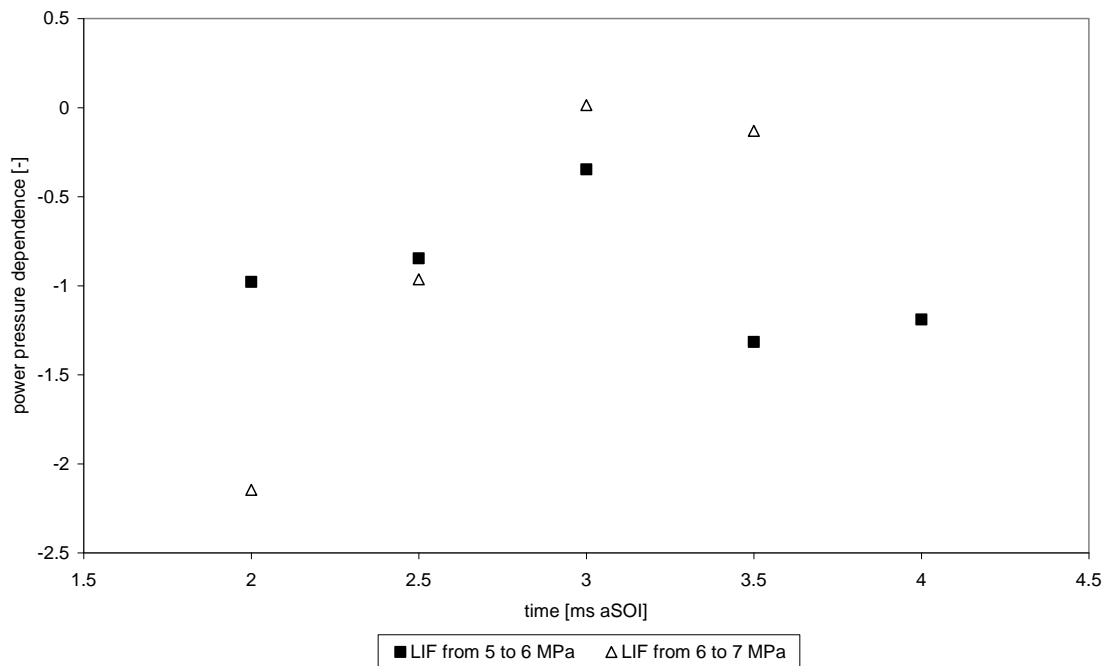


Figure 74 - In-cylinder pressure scaling of OH levels (30 mm³ of GE80 injected at 160 MPa in an in-cylinder temperature of 700 K)

As seen in Figure 76, the flame penetration decreased with increasing in-cylinder pressure. Crua (2002) reported a similar sharp decrease in vapour fuel penetration with increasing in-cylinder gas density. Figure 77 shows that, when the motored in-cylinder pressure was increased from 5 to 7 MPa, the thickness of the flame front was reduced

by 18%. The increased gas density means that all the protagonists of the combustion process can be found in a smaller layer around the spray. This is compatible with the findings of Barlow *et al.* (1989) in a non-premixed turbulent flame. They showed that OH concentrations are highly dependent on mixture fraction: the concentrations peaked for stoichiometric mixtures and decreased for richer or leaner mixtures. The increased gas density sharpens the mixture gradients, therefore leading to a thinner peak concentration of OH.

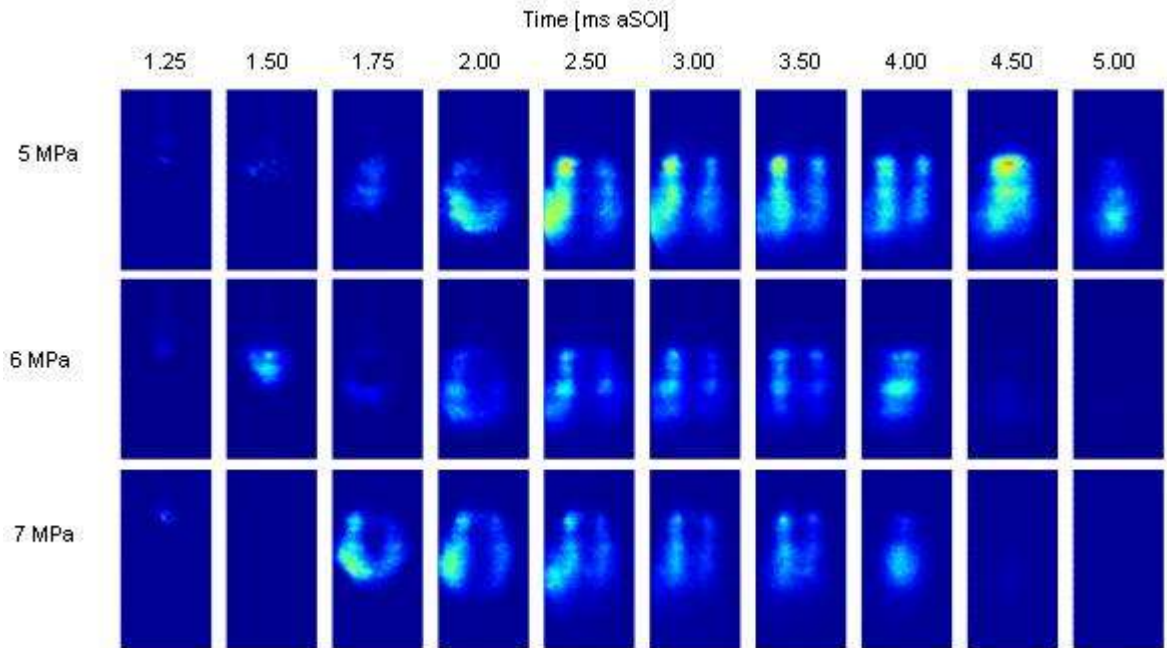


Figure 75 – Evolution of OH radicals distribution with time for three motored in-cylinder pressure (30 mm³ of GE80 injected at 160 MPa in an in-cylinder temperature of 700 K, 670 K for 6 MPa)

Similarly, the flame plume width was reduced by as much as 21% when increasing from 5 to 7 MPa ICP. Indeed, whereas the liquid spray cone angle was found to increase with increasing in-cylinder pressure, the fuel vapour region decreased in size. As presented in section 3.3.1.1, quenching of OH is dependent on pressure, temperature and molar fractions of H₂O, CO₂ and O₂. Increasing the density will decrease the importance of diffusion in the combustion process (lower Damkohler number). This more localised combustion may lead to higher concentrations of H₂O and CO₂ in the vicinity of the flame front, leading to high rates of quenching in this region.

However, as found in section 5.2.6, the effects of quenching are limited and cannot account for the differences observed. In fact, the vapour and liquid regions appear more

interwoven at high in-cylinder pressure. The widened liquid fuel spray vaporises and burns in a more restricted area and a reduced time.

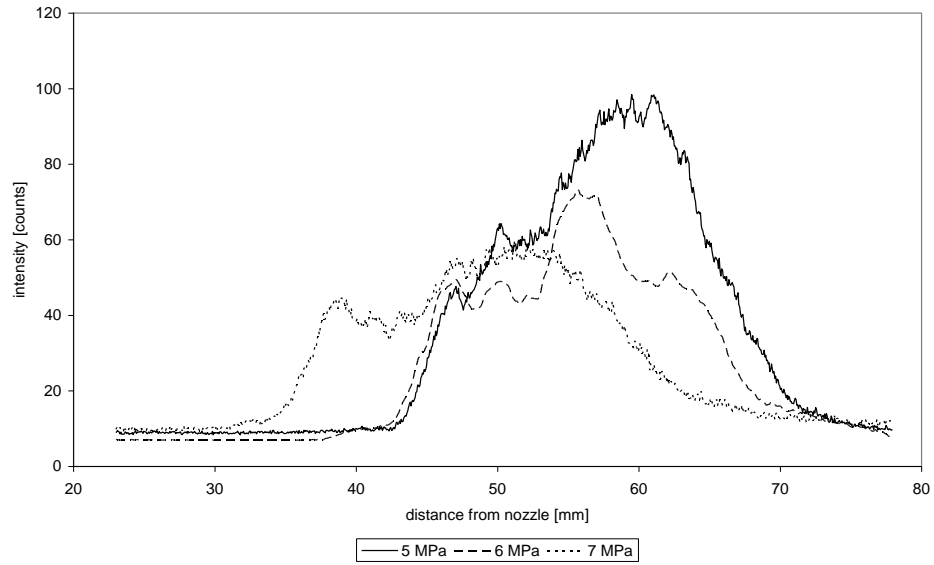


Figure 76 – Vertical intensity profile of OH distributions, 3 ms aSOI (30 mm³ of GE80 injected at 160 MPa in an in-cylinder temperature of 700 K (670 K for 6 MPa))

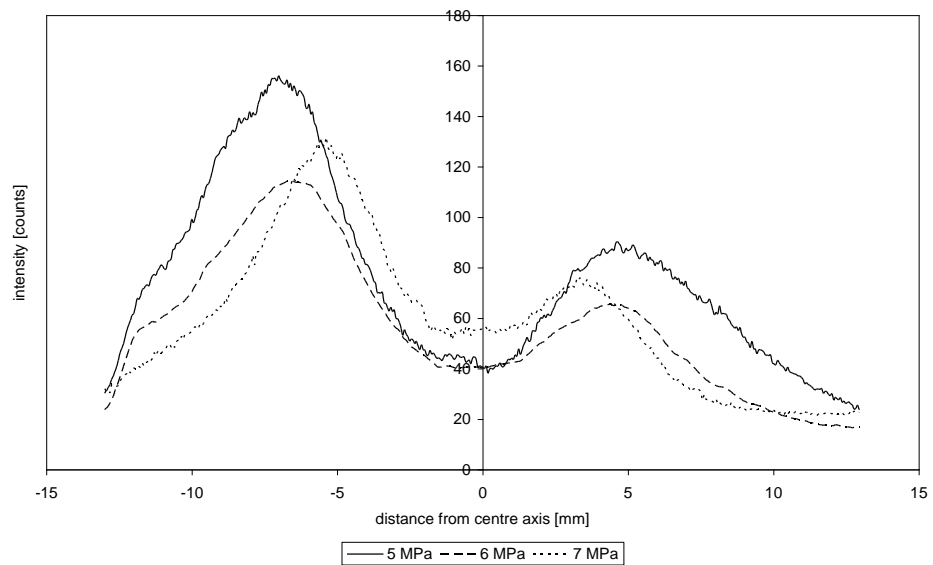


Figure 77 – Horizontal intensity profile of OH distributions, 3 ms aSOI (30 mm³ of GE80 injected at 160 MPa in an in-cylinder temperature of 700 K (670 K for 6 MPa))

6.5. Conclusions

This investigation demonstrates that the laser-induced fluorescence technique can be successfully applied to the qualitative measurement of OH radicals measurement in a diesel combusting spray at in-cylinder pressures up to 7 MPa.

When comparing the LIF results, the flame videos and the heat release rates, it was found that the pre-mixed phase was very short and mostly invisible to the optical techniques employed. This was due to the absence of soot oxidation and OH radicals during this phase. The most appropriate optical technique to study the pre-mixed phase is the analysis of the early chemiluminescence (as in Dec & Espey (1998)). In the present investigation, it was impossible to conclude on the exact location of the pre-mixed autoignition, and the observed bulk evaporation remained the best indicator of the beginning of the combustion chemistry.

The diffusion flame however could be more methodically described. The flame videos and the distributions of OH radicals suggested a varying but sometimes very early start of the diffusion flame. In the explored conditions, a substantial part of the first spike in the heat release rate could be attributed to the diffusion flame, although traditionally termed “pre-mixed spike”. The first soot oxidation was observed just at the end of the early diffusion flame development, when the flame fronts became stable.

Whereas the flame front was indeed stable downstream of the evaporation zone, the combustion near the tip of the spray was more chaotic and became increasingly richer, possibly leading to high concentrations of soot in the late part of the combustion.

The influence of injection pressure on the diffusion flame was consistent with fuel spray evolution. A higher injection pressure led to a shorter ignition delay and a longer flame. In-cylinder pressure had a stronger influence on the diffusion flame dimensions. Although the extent of the liquid spray cone angle increased with rising in-cylinder pressure, both the flame front and the plume width decreased significantly.

7. LASER-INDUCED FLUORESCENCE OF NITRIC OXIDE

In the following chapter, the excitation and collection details of the NO-LIF experiment are presented. The calibration and choice of the excitation wavelength are then described. Finally the results of the experiment are presented and discussed.

7.1. Excitation

The YAG laser output was set to 355 nm to pump efficiently the solution of 0.25 mg/l of Coumarin 47. The solvent was a fluorescence grade methanol. The output power of the YAG laser was measured at 175 mJ. The optics of the dye laser were aligned to maximize the power output while keeping the beam shape ellipsoidal. The output wavelength of the selected dye solution was in the range 444-476 nm for mean output energies of 20 mJ/pulse. The frequency was then doubled by the use of a BBO crystal, providing a final wavelength range of 222-238 nm and a final energy of 2-3 mJ/pulse. Table 25 lists the hardware and settings used for the NO-PLIF investigation.

Table 25 – Hardware and settings used for NO-PLIF

Pump laser	Nd:YAG third harmonic (175 mJ at 355 nm)
Dye laser	Three-stage dye laser and BBO crystal
Camera	Intensified CCD camera
Lens	UV lens, f=105nm, f/4.5 aperture
Optical filters	4 reflective filters centred on 248 nm (95%) FWHM of 40 nm
Intensifier gate time	50 ns
Intensifier gain	800
Laser sheet dimensions	20 x 0.5 mm
Laser pulse energy	2-3 mJ
Pulse duration	7 ns (FWHM)
Excitation wavelength	226.01 nm (on-line), 228.09 nm (off-line)
Excitation scheme	$A^2\Sigma^+ - X^2\Pi(0,0)$

One of the main issues with the $A^2\Sigma^+ - X^2\Pi(0,0)$ excitation scheme is the interferences rising from fluorescence of hot oxygen (Schulz et al., 1997, Hildenbrand et al., 2001).

Figure 78 shows the intensity of fluorescence signal for a number of excitation wavelengths against simulated absorption spectra of NO and O₂. The proportion of O₂ fluorescence in the signal collected appears non-negligible, with an overall proportion of O₂ fluorescence in the signal as high as one third. This proportion changes depending on the local temperature and gas composition, nevertheless Bessler *et al.* (2002), for instance, similarly reported a contribution of background to the overall signal of 29% for an excitation at 226.03 nm and a in-cylinder pressure of 6 MPa. Note that O₂ emission, due to a fast predissociation, is less sensitive to pressure changes than NO. The proportion of O₂ fluorescence in the signal will then be highest around peak in-cylinder pressure.

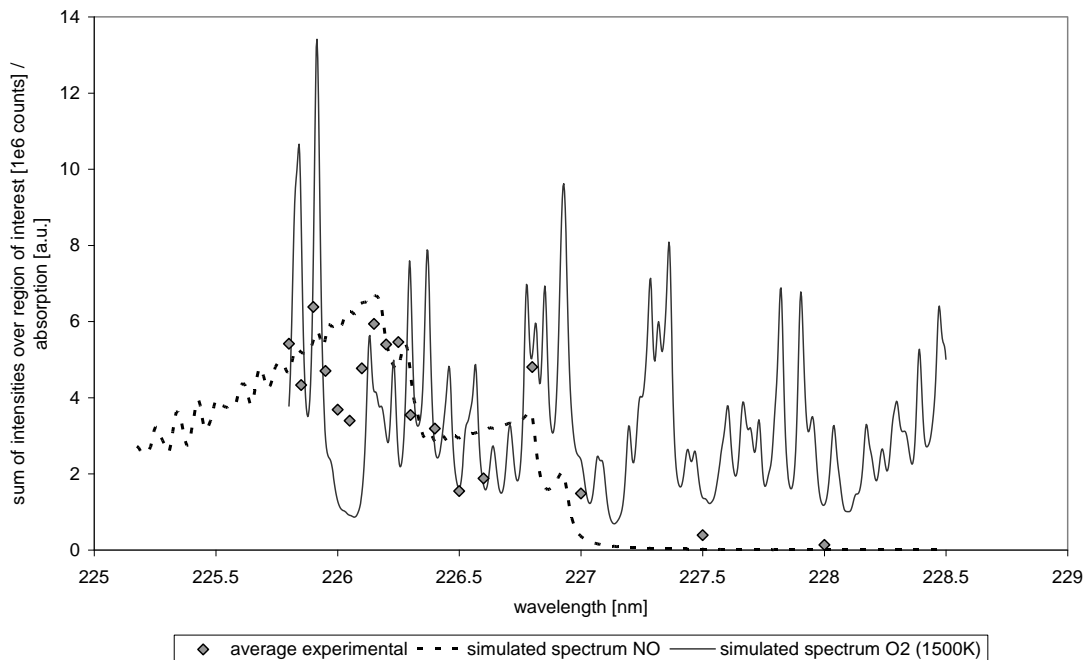


Figure 78 – Experimental absorption spectrum against NO (Luque and Crosley, 1999) and O₂ (Bessler *et al.*, 2003b) simulated spectra

The excitation wavelength was carefully selected as to minimise light absorption by hot O₂. A series of narrowband measurements proved 226.01 nm to be a good compromise, with NO absorption almost at its peak while keeping the O₂ absorption low. This dip in the O₂ absorption band has already been exploited in previously published investigations (Battles and Hanson, 1995, DiRosa *et al.*, 1996, Dec and Canaan, 1998, Bessler *et al.*, 2003a, Verbiezen *et al.*, 2006).

In order to ensure the legitimacy of the NO distributions, a second series of images was acquired for an excitation wavelength outside the NO absorption band. Narrowband

measurements showed that an excitation at 228.09 nm had the combined advantage to be clearly outside the NO absorption region and to have the same O₂ absorption level as 226.01 nm. The corrected images presented hereafter are therefore averaged images corrected for off-line signal, but also for laser energy and background noise level.

To maximise the signal to noise ratio, the height of the laser sheet was limited to 20 mm (for a width of 0.5 mm). The distributions presented are therefore combinations of two images, corresponding to two probed regions, at different distances from the nozzle. A dark strip appears in some cases between the two probed regions.

In order to obtain a reasonable PLIF signal to noise ratio, the oxygen content of the intake air was boosted. Increasing oxygen concentration in the air can be seen as the opposite measure to exhaust gas recirculation (EGR). In a similar manner as EGR is commonly used to decrease NO_x emissions, oxygen boosting can be used to increase the PLIF signal to noise ratio (Watson *et al.*, 1990). It is believed that the addition of oxygen does not fundamentally change the way NO is formed but rather increase globally the formation rates, as seen in the distributions of Nakagawa *et al.* (1997). However, the addition of oxygen will change the combustion timing, decreasing the ignition delay and potentially affect the combusting spray extent. Therefore care was taken to keep the oxygen inlet flow constant, representing a mole fraction of 25.5% of the aspirated gas in the case of 5 MPa TDC ICP.

7.2. Collection

Figure 79 summarizes the transmittance curves of a number of filters pre-selected for NO-LIF. A good filter is a filter with a high transmittance over at least two NO peaks and a very low transmittance around 226 nm and above 275 nm. As explained in Section 4.7 it is preferable not to collect too long wavelength because of possible interferences from fuel natural fluorescence, PAH fluorescence and others. Obviously, the very sooty environment of diesel combustion means that high levels of scattering can be expected. Therefore the filter must block efficiently wavelengths around 226 nm. Among the filters of Figure 79 is presented the filter originally chosen for NO-LIF. The IF254 filter is a bandpass filter centred on 254 nm. Its narrow band (10 nm FWHM) allows very low levels of scattered light and interferences to be collected. However, from a first series of measurements it appeared that not enough NO fluorescence was

collected. Indeed, it can be computed from the spectrograph results that only 4% of the 248 nm NO peak and 10% of the 259 nm NO peak were collected. Neither of the peaks at 236 nm and 272 nm was collected. This meant that the intensifier gain had to be set to the maximum setting. Moreover, the maximum laser energy output had to be reached by constantly tuning the laser set-up. Even with this highly optimised set-up NO fluorescence was hardly distinguishable.

In an attempt to increase the signal level, reflective mirrors centred on 248 nm and with a peak reflection of 90% and FWHM of 40 nm, referred as reflective filter in Figure 79 were analysed. Similar mirrors were used in previous investigations (see (Bräumer et al., 1995, Berckmüller, 1996, Schulz et al., 1997, Legris, 2005, Fissenewert et al., 2005) in Table 10). As seen in Figure 79 and noticed by Berckmüller, more than one reflective mirror is necessary to filter the very strong laser light scattering around 226 nm. A set of 4 mirrors was therefore used (Figure 80).

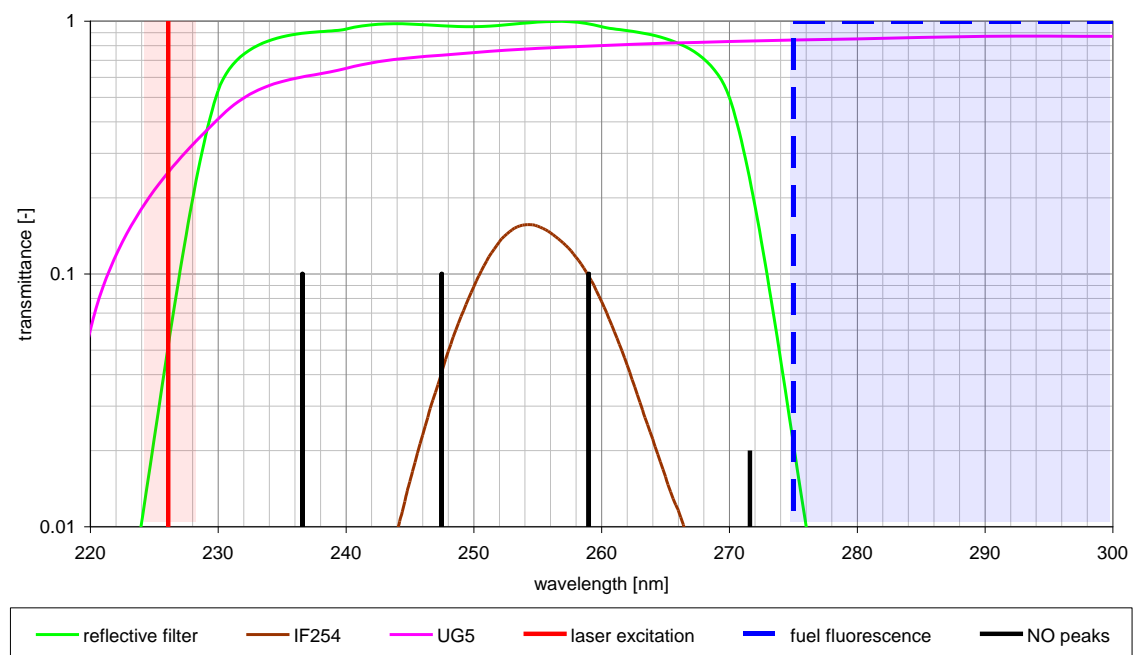


Figure 79 – Filters for NO-LIF



Figure 80 – Set of reflective filters in front of UV lens, intensifier and camera

7.3. Calibration of NO-LIF with a spectrometer

Unlike the OH spectrum, the NO spectrum is very dense. Rotational peaks often overlap, especially at high pressure. Figure 81 shows the structure of the two vibrational transitions of OH and NO exploited in this investigation. The rotational structure of OH appears clearly sparser.

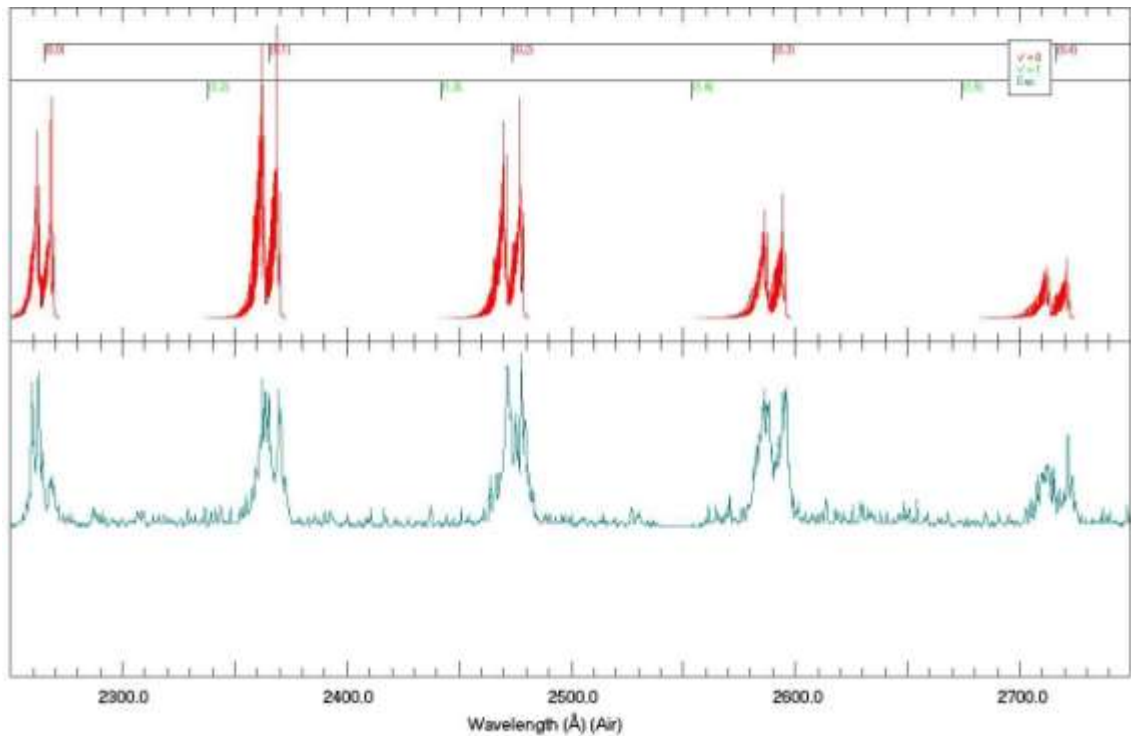


Figure 82 – Simulated (top) and measured (bottom) NO vibrational spectra (Luque and Crosley, 1999)

7.4. Results and discussion

7.4.1. Exhaust gas analysis

A series of exhaust gas analysis measurements were conducted to establish the influence of some engine parameters on NO_x emissions (Table 26). Some of the exhaust flow was cooled down and bypassed into a Horiba MEXA 7100 DEGR analyzer. The emissions reported in Table 26 are consistent with expectations and the literature. The emission trend of NO_x with oxygen air content is comparable to those of Kitamura *et al.* (2005) and Alatas *et al.* (1993), as illustrated in Figure 83.

Table 26 – Exhaust gas analysis data

In-cylinder motored peak pressure [MPa]	Injection pressure [MPa]	Number of skipped cycles	O ₂ [vol %]	CO [vol %]	CO ₂ [vol %]	THC [ppmC]	NO _x [ppm] ([α mass])
4	160	9	26.1	0	0.15	17.2	41 (0.95)
5			25.5	0	0.13	13.9	34 (1.00)
6			25.2	0	0.12	12.3	29 (1.03)
7			24.9	0	0.11	11.2	25 (1.05)
5	160	9	25.5	0	0.13	13.9	34
	140		25.6	0	0.13	13.8	36
	100		25.6	0	0.13	12	39
	60		25.6	0	0.13	11.1	41
5	160	5	25.5	0	0.19	14.9	60
		9	25.6	0	0.13	13.8	36
5	160	9	20.77	0	0.13	14.9	8.3
			25.5	0	0.13	13.9	34
			30.2	0	0.13	12.7	62

The thermal effect, associated with the change in specific heat capacity, is often cited as a possible origin for the observed variations in NO_x emissions. However, as demonstrated by Ladommatos *et al.* (1998), the dilution effect is the major responsible cause of the lower NO_x production when oxygen concentration is decreased. Indeed, the diffusion combustion being mixing-controlled (Damköhler number above unity), a higher concentration of oxygen will allow the flame to reach higher temperatures, locally rich zones falling into combusting limits faster.

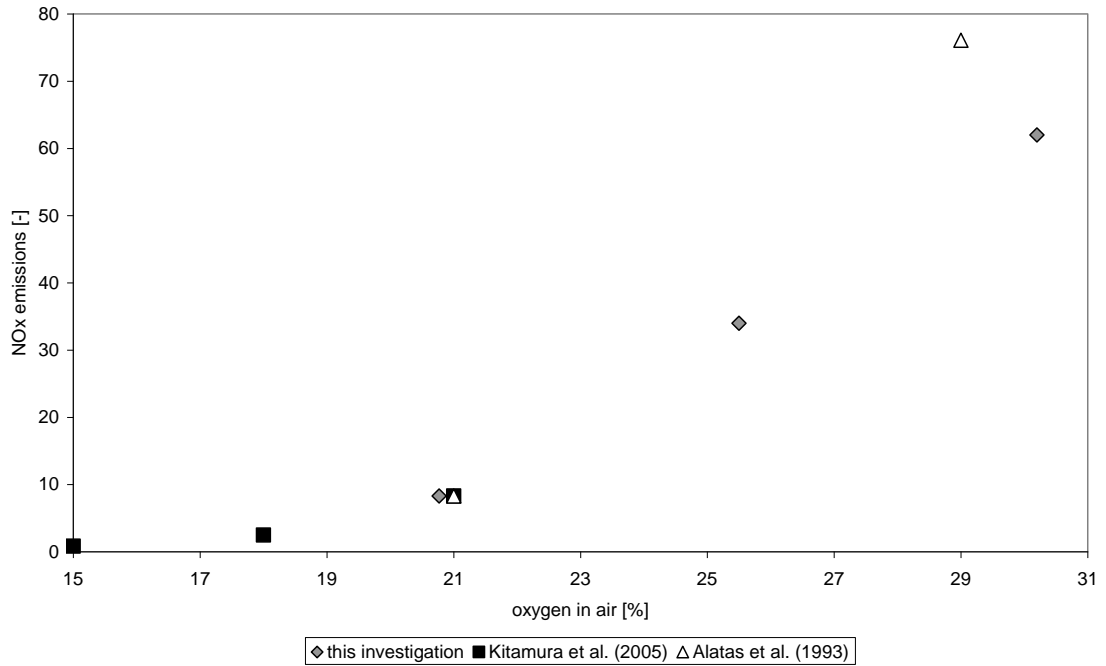


Figure 83 – NOx emission trends with oxygen level in air

The temperature of in-cylinder gases is also influenced by thermal radiation. Although it is unlikely to considerably alter the heat release rate, the peak gas temperatures can be lowered in the presence of a significant thermal radiation. It is generally accepted that thermal NO production is highly sensitive to temperature, therefore an increased radiation could lead to lower levels of NO as reported by Sazhina *et al.* (2000). Unfortunately, the influence of radiation transfer remains poorly investigated and, for instance, was not differentiated from the dilution effect in the investigation of Ladommatos *et al.* (1998).

The injection pressure only had a limited effect on exhaust NOx emissions, with a decrease of 20% when the injection pressure is increased from 60 MPa to 160 MPa. A similar trend was reported by Kitamura *et al.* (2005). The rate of NO formation was exponentially linked to the local temperature (Bowman, 1975):

$$\frac{d[NO]}{dt} = \frac{6 \cdot 10^{16}}{T^{1/2}} \exp\left(\frac{-69090}{T}\right) \cdot O_2^{1/2} \cdot N_2 \quad (94)$$

Where $d[NO]/dt$ is the rate of formation of NO [mol/cm³.s], T is the local temperature [K], and $[S]_e$ is the equilibrium concentration of species S [mol/cm³].

For a comparable combustion volume, the higher heat release rates obtained with high injection pressures should therefore lead to an increased formation. However, as shown

in Figure 84, the amount of fuel burnt in the mixing-controlled phase decreased with increased injection pressure. Thus, the overall low sensitivity of NO_x emissions to injection pressure was believed to be the consequence of a trade-off between heat release rate levels and the relative importance of the mixing-controlled phase.

Exhaust concentrations of NO_x were seen to decrease with increased in-cylinder pressure. Nevertheless, if the total mass of NO_x produced was calculated by correcting for air flow variations, NO_x emissions were seen to increase with in-cylinder pressure. Furthermore, the mass of NO_x produced needed to be corrected for the concentration of oxygen in the air as this could not be kept constant over the range of boost pressures. After making the corrections, NO_x production exhibited a power dependence on in-cylinder pressure in $P^{0.2}$.

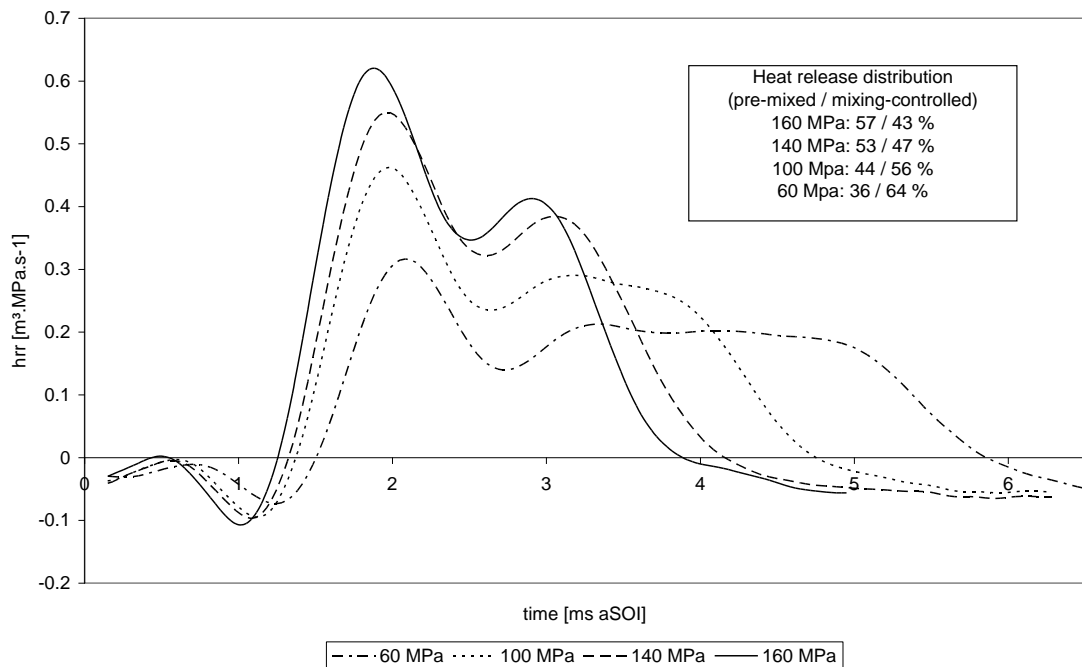


Figure 84 – Heat release rates for different injection pressures (injection of 30 mm³ of GE80 in an in-cylinder pressure and temperature of 5 MPa and 700K)

7.4.2. In-cylinder nitric oxide distributions

Planar distributions of NO were captured for a number of injection and in-cylinder pressures. For each set of specific conditions, the same measurement sequence as for the OH-LIF investigation (section 6.4) was observed.

A typical flame development is shown in Figure 85 where NO, OH distributions and flame luminosity evolutions are presented.

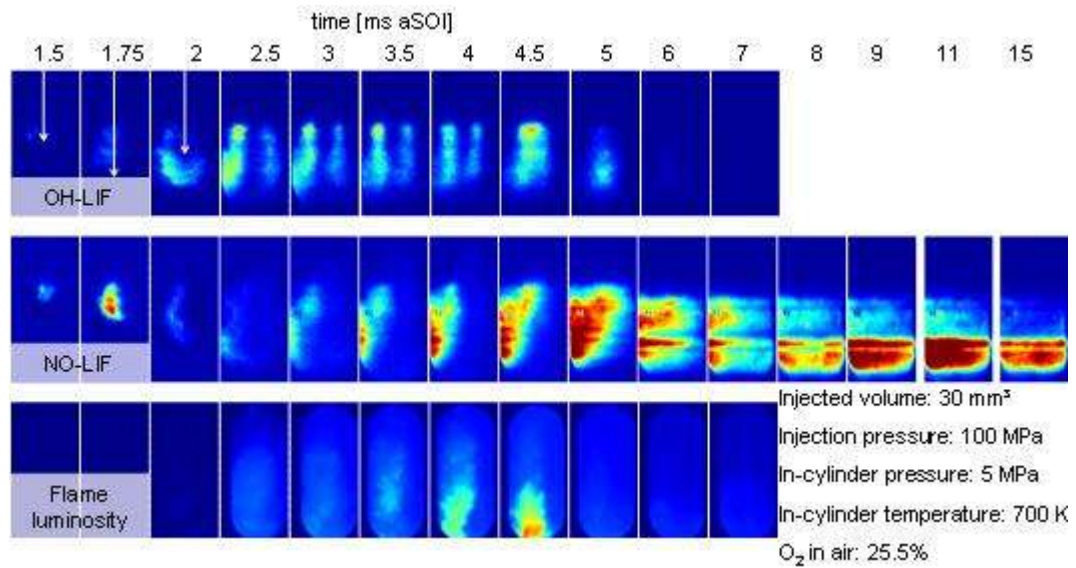


Figure 85 – Evolution of NO distributions with flame development (the white arrows represent the liquid fuel penetration)

NO first appeared 0.5 to 1 ms after the start of the diffusion flame (e.g. 2.5 ms aSOI on Figure 85), on the lean side of the flame, outside the region with a high density of OH radicals. For the same reason as for OH early distributions, the bright intensities that can be seen during the pre-mixed flame (1.75 ms aSOI in Figure 85) were not due to NO fluorescence but to liquid fuel scattering. Because there was a short time interval between the capture of the on- and off-line images, the injection and in-cylinder conditions were not perfectly identical. Consequently, the very strong Mie scattering of the liquid fuel was not always perfectly cancelled out by subtracting the off-line distribution. Pre-mixed flame NO distributions with high intensities were re-estimated using a reduced time interval between the on- and off-line measurements and the above assumption was confirmed.

A second phase with high densities of NO formation can be observed after the combustion at the bottom of the observation window (e.g. after 8 ms aSOI in Figure 85). Some of the NO seemed to be formed after the end of apparent combustion, when OH radicals had completely disappeared. The thermal-NO mechanism relies on the presence of hydroxyl radicals, atomic oxygen or atomic nitrogen (equations (28), (29)

and (30)). If due to the thermal-NO mechanism, this late formation established the presence of atomic oxygen or nitrogen after the end of combustion.

NO distributions did not exhibit an axisymmetrical pattern as OH distributions with their two flame fronts. However this could be explained by a stronger attenuation of the laser light at this low u.v. wavelength. The OH distributions, obtained with an excitation wavelength of 283 nm, were indeed already brighter on the side of the in-coming laser sheet. Furthermore, as reported by Schulz et al. (1997), attenuation at 226 nm could be 5 to 10 times stronger. The attenuation observed did not seem to be due to a weakening of the laser sheet following a substantial absorption by NO molecules. Indeed, at late timings, the distributions of NO in Figure 85 appeared homogeneous throughout the laser path. The attenuation was more likely to be due to absorption by hot CO₂ (Schulz et al., 2002) or partially decomposed fuel. CO₂ is also the collisional partner of NO with the highest collisional cross section (Battles and Hanson, 1995, Paul et al., 1994). Regions of high concentrations of hot CO₂, believed to coincide with the OH regions identified in Figure 86, would be affected by both a strong attenuation of the laser light and quenching of the fluorescence. Furthermore, if the temperature is high enough, the thermal NO mechanism would not be frozen and some of the NO would naturally decompose into N₂ and O₂. This could explain the small space gap apparent between the measured OH and NO distributions on Figure 86. The accumulating NO present in colder regions (i.e. further away from the flame front) appeared brighter due to a stronger excitation.

This complete absorption of the laser light also means that the absence of NO inside the flame plume during the combustion could not be confirmed. The NO formed at the high temperature of the flame front is likely to diffuse outwardly with respect to the plume, but some NO could be trapped inside the plume where temperatures would be low enough to quench the NO decomposition mechanism.

Figure 86 shows superimpositions of OH distributions over NO distributions during the diffusion combustion. The OH and NO captures were not simultaneous. The regions of high OH signal intensity are delimited by a white edge. The background colour coding (blue to red) corresponds to the NO signal intensity. The vertical natural flame luminosity profile is also given on the right edge of each distribution. The distributions have been corrected to take into account the difference in the collection optics. Moreover, the images were cut vertically along the spray axis in two halves. Only the side of the in-coming laser light is shown here.

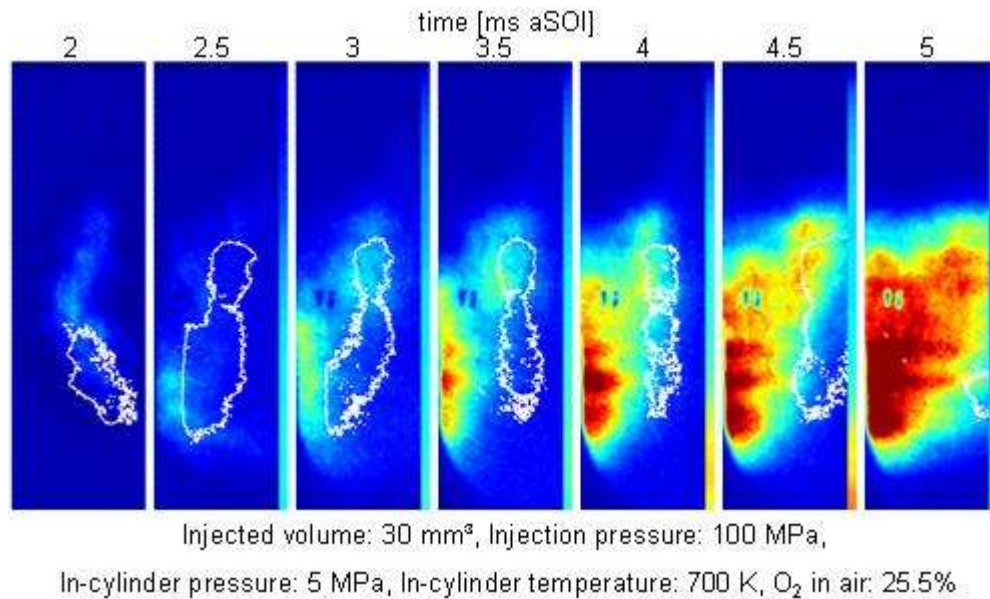


Figure 86 – Superimposition of non-simultaneous distributions of OH (white edges) and NO. The colour bar on the right of each picture represents the flame luminosity vertical profile

Whereas OH radicals have a short lifetime and disappear quickly through three-body recombination, the kinetics of NO can be frozen by decreasing temperatures. Thus, Figure 86 can be considered to combine on one hand an integrated measurement over time of NO densities and on the other an instantaneous measurement of OH formation rates. Since the kinetics of NO formation were fairly slow, there seemed to be a delay between the presence of OH – diffusion type combustion and release of heat – and the build-up of NO densities.

High OH density and high flame luminosity (soot density) did not coexist. High NO densities could be found on the side of the high OH density flame front but also later on, downstream the spray, on the outskirts of the zone with a high natural luminosity. Thus, the trade off usually observed in the exhaust gases between soot and NO_x levels did not prevent NO from being seen at the tip of the spray, adjacent to a region of high soot concentration (e.g. at 60 MPa injection pressure on Figure 87). The NO found downstream of the spray could have been formed in the vicinity of the high OH density region and from there, transported downstream via air entrainment. NO was formed throughout the combustion gases when the diffusion flame collapsed on itself and OH gradually disappeared. Whereas the NO formed during the diffusion flame depended on diffusion to reach a cold region and thus freeze its decomposition, the temperature of the centre of the plume would increase and decrease rapidly after the flame collapse, hence freezing NO mechanism on a large volume.

7.4.2.1. Effect of injection pressure

Nitric oxide distributions were captured for injection pressures varying from 60 MPa to 160 MPa and are shown in Figure 87. Here again, OH and NO were not captured simultaneously. The regions of high OH signal intensity are delimited by a white edge. The background colour coding (blue to red) corresponds to the NO signal intensity. The equivalence ratio of the pre-mixed combustion mixture was likely to change with injection pressure. Nevertheless, the NO densities stayed under the detectability limit of our setup until after the onset of the diffusion flame. Over the range of equivalence ratios explored, the formation of NO during the pre-mixed phase, either from thermal-NO or prompt-NO, was therefore negligible compared to the mixing-controlled formation.

The distributions at high injection pressures of Figure 87 exhibited surprisingly low quantities of NO on the lean side of their well-formed flame fronts. It is believed that more NO could be formed at the tip of the flame, outside the field of view. While the OH formation zone was only slightly moving downstream the nozzle with increased injection pressure, NO peak densities were moving from just below the liquid spray core to the very tip of the flame. This could be associated with a different air motion as the injection pressure increased with the hot products of combustion moving more downstream from the nozzle than sideways, perpendicular to the side flame fronts. This led to higher intensities during the second phase mentioned above for high injection pressures. This second phase of high NO densities could be associated with nitric oxide originally formed below the field of view and subsequently pushed up by the air entrained by the piston (TDC is at 5 ms aSOI). However, a similar increase of late NO formation with injection pressure was observed by Hildenbrand *et al.* (2000a) in a configuration less likely to be influenced by air entrainment. Therefore the injection pressure could influence both the location and timing of NO formation with high density regions found further away from the nozzle and later in the combustion for high injection pressures.

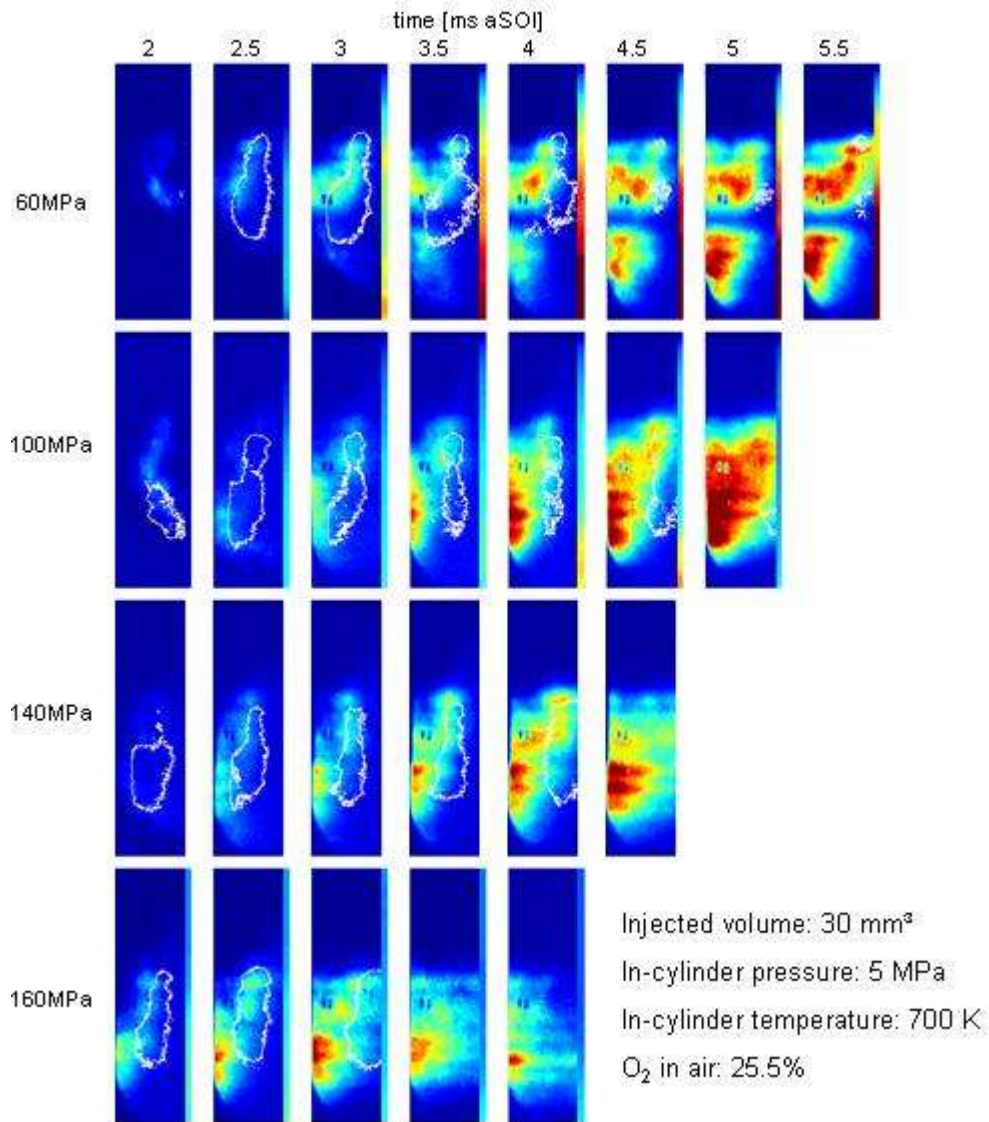


Figure 87 – Superimpositions of non-simultaneous distributions of OH (white edges) and NO for different injection pressures. The colour bar on the right of each picture represents the flame luminosity vertical profile (no data for 140 MPa)

Figure 88 reports the average distribution intensities against time after start of injection. The average intensity was severely affected by laser light attenuation and since attenuation could not be considered constant over time, the absolute value of each curve only has little meaning. However, it is interesting to notice some similarities in the shape of the curves for different injection pressures. There was no fundamental difference in the initial overall NO production rate. The slopes of the diffusion combustion curves were comparable. As explained previously, the recorded intensity before start of diffusion flame was due to unfiltered Mie scattering. The three curves showed a local increase in overall intensity just after the end of combustion of the

respective flames. This could be associated in time and space with the “collapse” of the combusting spray on itself and the high densities of OH observed subsequently. As noted previously, an increasing proportion of the NO was formed at the tip of the spray when injection pressure was raised. This NO was then pushed back into the field of view and accounted for the increase in NO signal after the end of combustion for 160 MPa and to a lesser extent 100 MPa injection pressure.

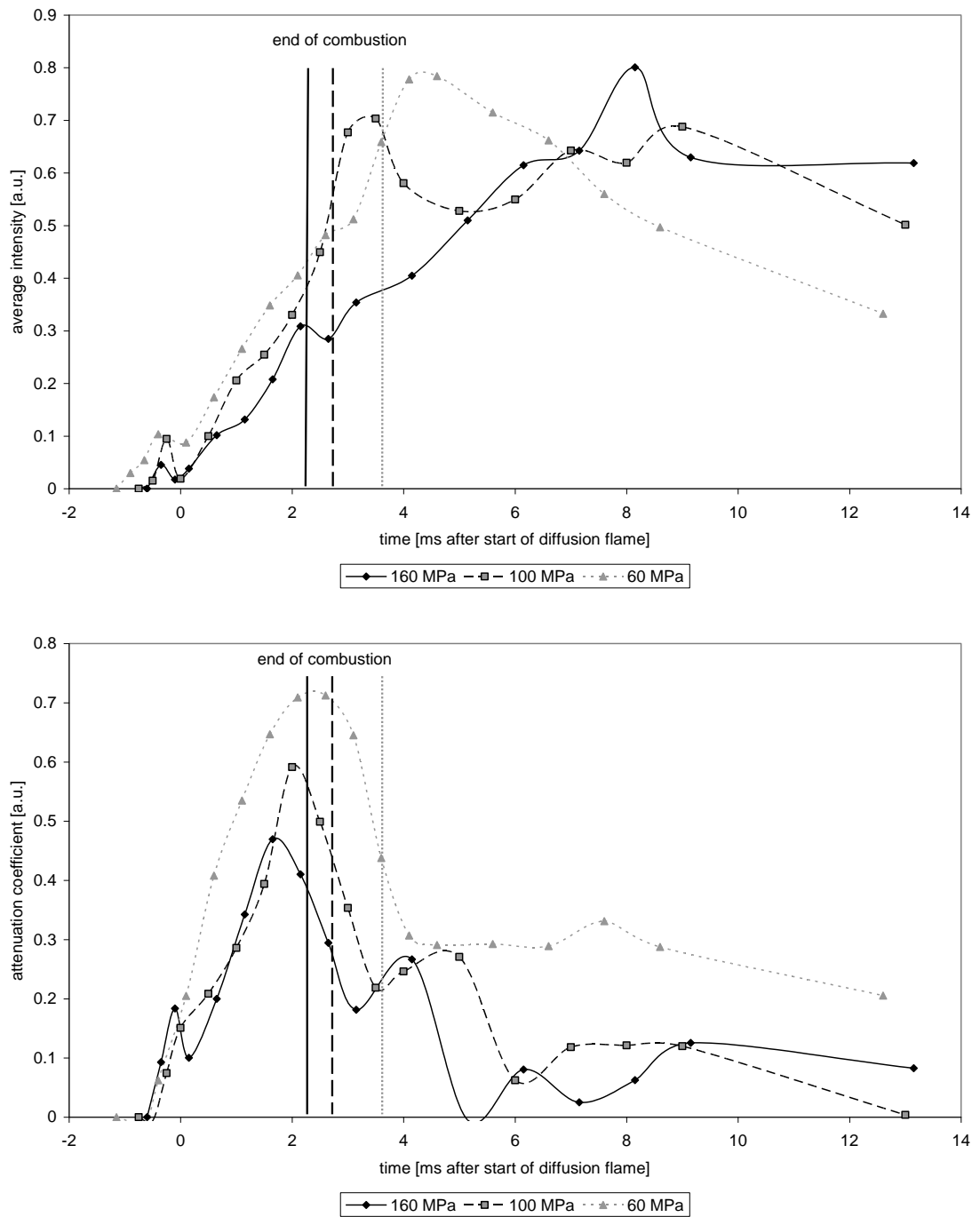


Figure 88 – Evolution of the average intensity (top) and attenuation coefficient (bottom) with time

Voiculescu & Borman (1978), Donahue *et al.* (1994) and Kitamura *et al.* (2005) reported a linear increase of the NO densities during the combustion as found in Figure 88. However they failed to report the brief shoot-out observed at the flame collapse. The overall average intensities shown here for 60 MPa are compatible with the production rates reported by Dec & Canaan (1998) with a rate plateau between 1.5 ms and 4.5 ms aSOI and an end of formation around 7 ms aSOI. Stoffels also published similar fluorescence curves with a fairly gradual formation and a small shoot-out at the end of apparent heat release (Stoffels, 1999). However, in the conditions investigated, the mixing-controlled phase was dramatically reduced. The brief shoot-out noticed at the end of combustion corresponded, therefore, to the NO produced in the entire diffusion flame period. The extended diffusion period in the present investigation allows a more detailed analysis of the evolution of NO formation rates with flame development. Thus, the flame collapse appears to be associated with an overall higher rate of NO formation than the rest of the diffusion flame. This is linked to the combined effect of the spread of the flame throughout the remainder of the spray followed by a rapid cooling of the gases.

In Figure 88, the attenuation coefficients obtained by fitting the intensity profile along the laser path to Beer's law are also reported:

$$I = I_0 \cdot \exp(-K \cdot x) \quad (95)$$

Where I is the intensity profile, I_0 the original intensity, K the attenuation coefficient, and x the laser path length.

Here again the separation between attenuation and the distributions dissymmetry cannot clearly be made. Nevertheless, the evolution with time of the attenuation coefficient agrees well with the extensive investigation of Verbiezen *et al.* (2006).

7.4.2.2. Effect of in-cylinder pressure

Figure 89 shows the evolution of the NO distributions with increasing in-cylinder pressure. The OH and NO captures were not simultaneous. The regions of high OH signal intensity are delimited by a white edge. The background colour coding (blue to red) corresponds to the NO signal intensity. Considering a constant in-cylinder temperature of 700 K, the investigated in-cylinder pressures of 5, 6 and 7 MPa correspond respectively to gas densities of 25, 30 and 35 kg.m⁻³. As seen with the

exhaust gas data, NO formation was expected to increase with ICP since a higher density of air would lead to higher local temperatures. Furthermore, a shorter spray and flame penetration would move some of the downstream NO back into the field of view.

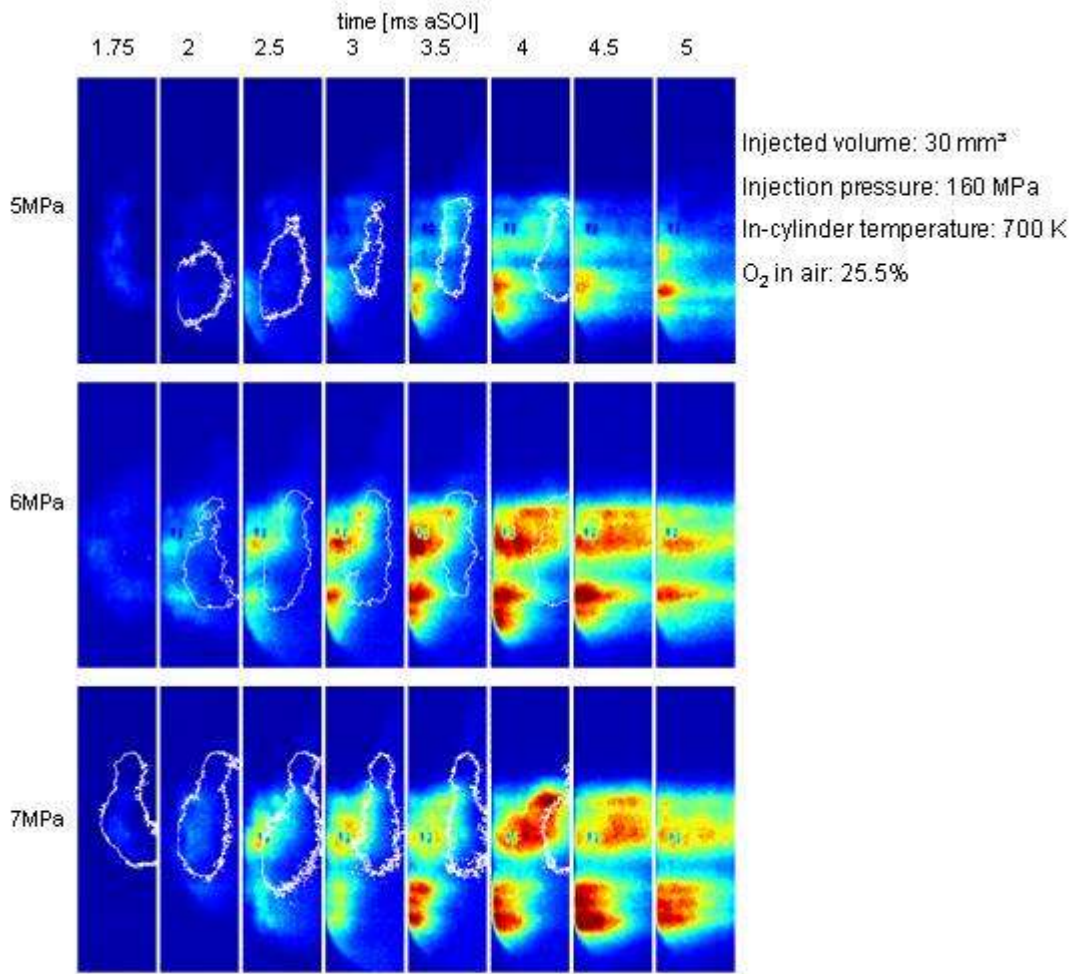


Figure 89 – Superimpositions of non-simultaneous distributions of OH (white edges) and NO for different in-cylinder pressures

The signal evolved as expected between 5 and 6 MPa with an overall increase and an especially sharp increase in the upstream part of the flame. Although the NO formation zone seemed to move further upstream when the ICP was raised to 7 MPa, the intensity of the distributions did not increase as much as previously. The gain in flame temperature itself or in the extent in space and time of high temperature regions from 6 to 7 MPa ICP could be lower than the gain from 5 to 6 MPa ICP. This was in agreement with the evolution of the heat release rate in Figure 90. The effect of a 1 MPa ICP increase on the heat release rate decreased as the ICP increased. Moreover, the exhaust gas analysis confirmed an increase in NO_x between 6 and 7 MPa as small as half the

increase recorded between 4 and 5 MPa. Finally, the small gain in flame temperature may be overcome by the increased collisional quenching.

Increasing the in-cylinder pressure also shortened the ignition delay and hence decreased the relative importance of the pre-mixed burn (Figure 90). Both OH and NO early formations were therefore seen to be boosted by an increase in ICP.

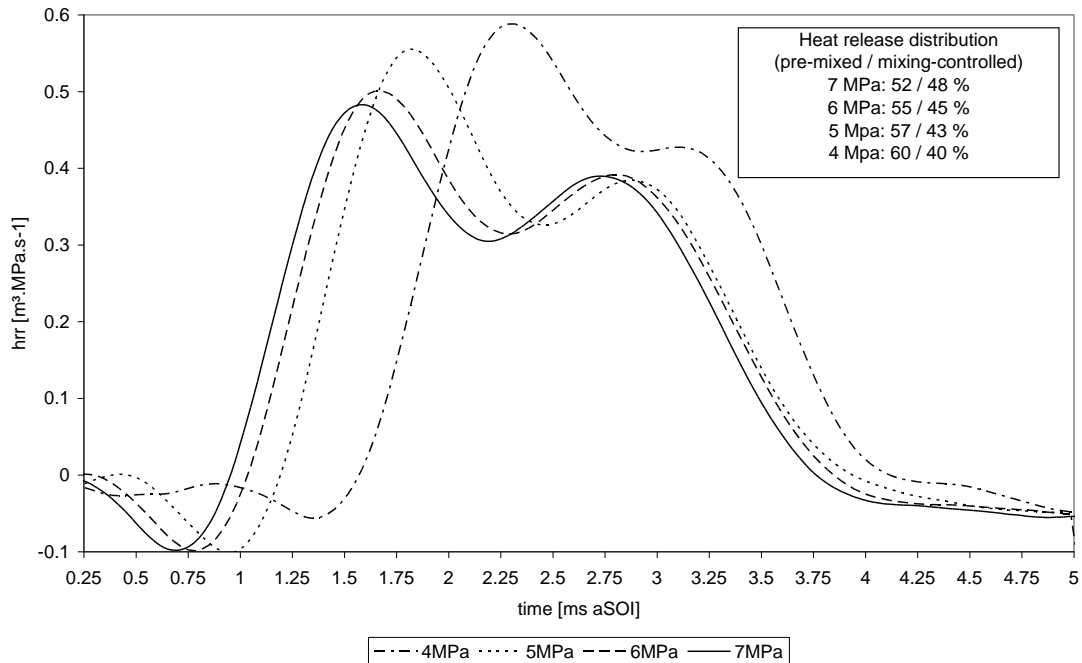


Figure 90 – Heat release rates for different in-cylinder pressures (injection of 30 mm³ of GE80 at 160 MPa in an in-cylinder temperature of 700K)

In Figure 91, the power dependence n of NO levels on in-cylinder pressure is plotted, with n given by:

$$\frac{NO_{P_1}}{NO_{P_2}} = \left(\frac{P_1}{P_2} \right)^n \quad (96)$$

Drake et al. (1987) and Cooper & Laurendeau (2000), noted that practical combustors employing turbulent diffusion flames have demonstrated a $P^{0.5}$ scaling of NO formation. Indeed, the thermal NO mechanism is normally limited by the availability of oxygen atoms, whose concentration scales as $P^{0.5}$ based on equilibrium considerations.

The LIF levels used to compute n in Figure 91 were average intensities over a section of the acquired images. Although the section was chosen to be representative of the average fluorescence level, disparities appear in the power dependences. Also, power dependences largely above 0.5 were reported. This however could be linked to the

change in the position of the flame plume with varying in-cylinder pressure. The probed region being static, it did not perfectly account for the overall NO signal evolution.

The exhaust levels of NO showed a power dependence on pressure lower than 0.5. The sensitivity of oxygen atoms availability to in-cylinder pressure may be lowered by the presence of oxygen in the fuel.

Finally, both exhaust and LIF levels show a decreased dependence on pressure with increasing ICP.

In general, it appears that other limiting factors than oxygen availability play also a role in thermal-NO formation in a diesel combusting spray. The publications cited above verified the $P^{0.5}$ dependence in experiments involving the combustion of gaseous fuels below 1 MPa ICP. Notably, the complex atomisation and vaporisation mechanisms are affected by the in-cylinder pressure and will therefore influence the P^n scaling of NO formation.

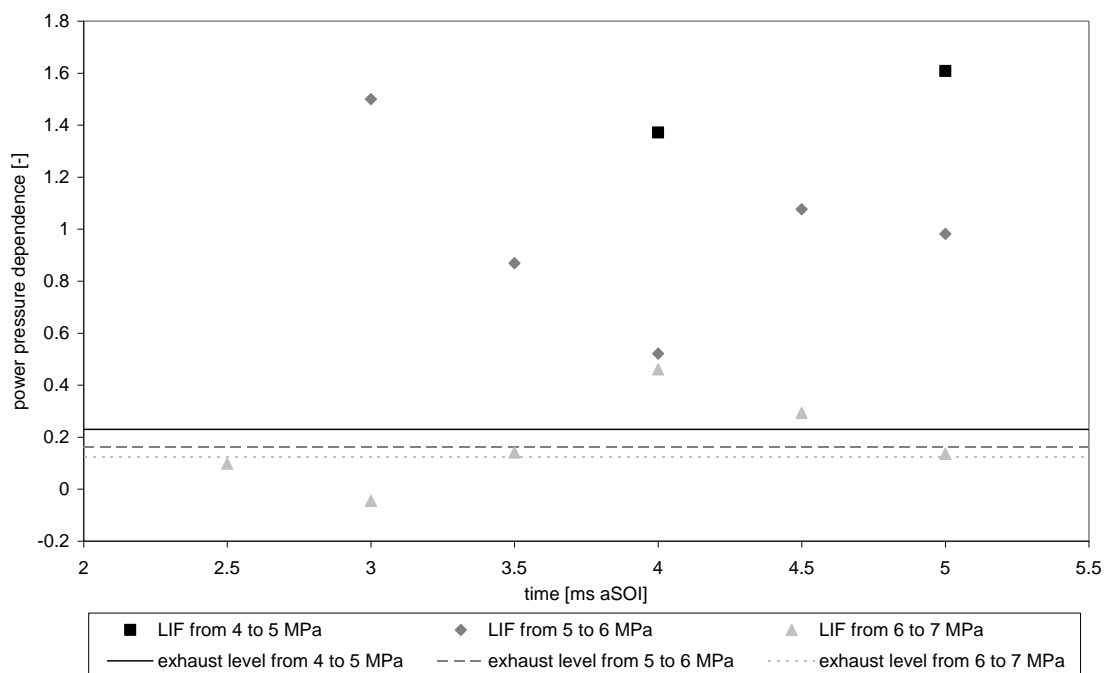


Figure 91 – In-cylinder pressure scaling of NO levels (30 mm³ of GE80 injected at 160 MPa in an in-cylinder temperature of 700 K)

Finally, the gap between observable NO and flame front was reduced by increased density. The sharper gradients of concentrations and temperatures allowed the laser light to travel further before reaching the highly attenuating flame front.

7.5. Conclusions

The NO-PLIF technique was applied to a diesel combusting spray at working in-cylinder pressures in excess of 8 MPa and injection pressures up to 160 MPa. The averaged NO distributions were analysed in conjunction with OH radical distributions and natural flame luminosity data.

NO fluorescence was first recorded slightly after the onset of the diffusion flame and until late into the expansion stroke. The early low levels of NO were located on the lean side of the high OH density zone. As NO densities gradually increased, the OH densities were restricted to the upstream part of the flame and moved inwards. High OH densities and high soot densities were not found to coexist. Finally, at the end of injection, the spray collapsed on itself thus resulting in high densities of OH and NO throughout. Some of the NO seemed to be formed after the end of apparent combustion, when OH radicals had completely disappeared

The presence of NO within the flame front or inside the flame plume could not be checked as the absorption from hot CO₂ was so intense that the laser light was completely attenuated before reaching the flame front.

Injection pressure was found to influence greatly the direction and extent of the NO diffusion. Whereas at low injection pressure NO mainly stagnated on the sides of the spray, the tip of the spray was the region with the highest NO densities at high injection pressures. On the other hand, varying injection pressures did not significantly affect the overall formation.

Increasing the in-cylinder pressure led to a shorter flame penetration and ignition delay with more NO formed early and in the upstream part of the spray. Moreover, higher local temperatures associated with the increased density led to higher formation rates.

8. CONCLUSIONS

The flow, spray penetration, flame luminosity, evaporation and LIF measurements concurred with the following development of the spray and flame (see Figure 92 for spatially averaged intensities of LIF, flame luminosity and the heat release rate):

The fuel started to flow out of the nozzle around 0.4 to 0.6 ms aSOI. The injection pressure influenced the time necessary to reach a steady flow as well as the penetration velocity but only faintly the maximum penetration length of the liquid core.

A first phase of evaporation was characterised by a rapid evaporation of the tip of the spray with no visible soot radiation. This pre-mixed phase was very short and mostly invisible to the optical techniques employed. No OH radicals or NO formation was recorded, and it is believed that only a weak chemiluminescence from intermediate species was emitted during this phase. This was verified for varying injection and in-cylinder pressures, hence varying equivalence ratio of the pre-mixed flame. It was impossible to conclude on the exact location of the pre-mixed autoignition, and the observed bulk evaporation was the best indicator of the beginning of the combustion chemistry.

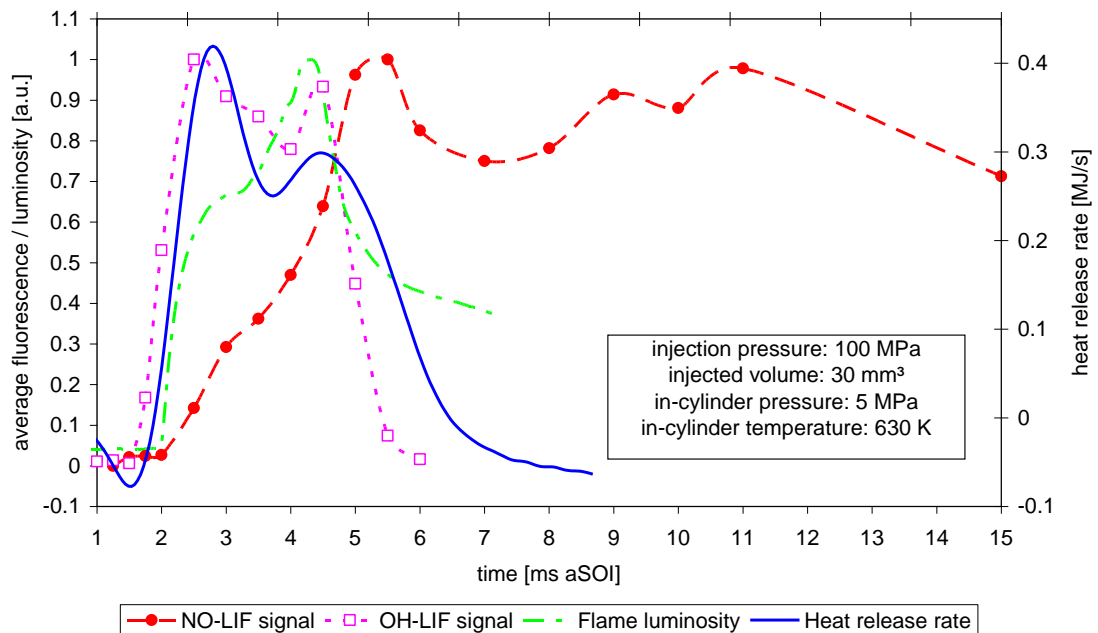


Figure 92 – Spatially averaged luminosity, OH and NO signal compared to the heat release rate

The second phase was found to have a steadier evaporation with the liquid penetration slowly decreasing as the highly luminous diffusion flame developed. The flame videos

and the distributions of OH radicals suggested a varying but sometimes very early start of the diffusion flame. In the explored conditions, a substantial part of the first spike in the heat release rate could be attributed to the diffusion combustion, although traditionally termed “pre-mixed spike”. The first soot oxidation was observed just after the overall peak OH densities, matching a sudden decrease in the oxygen content of the spray. Around this time, the first NO fluorescence was recorded. The early low levels of NO were located on the lean side of the high OH density zone. As NO densities gradually increased, the OH radicals were restricted to the upstream part of the flame and moved inwards. Furthermore, whereas the flame front was rather stable downstream of the evaporation zone, the combustion near the tip of the spray was more chaotic and became increasingly richer, leading to high concentrations of soot in the late part of the combustion. High OH densities and high soot densities were not found to spatially coexist.

Finally, at the end of injection, a third phase coincided with the collapse of the diffusion flame on the centre of the flame plume. This resulted in high densities of OH and NO throughout the plume. The natural luminosity region first extended towards the injector nozzle before slowly contracting back to the tip of the plume.

The injection pressure had a limited influence on liquid fuel penetration. This was linked with two conflicting phenomena: an increased velocity and a faster evaporation. The vapour, on the other hand, continued to penetrate and was found further away from the nozzle when autoignition occurred. This resulted in a longer vapour fuel region.

The diffusion flame was also affected by injection pressure: a decrease in injection pressure resulted in a shorter flame and a delayed flame development. However, apart from their timing and extent, the sequence of flame patterns identified above was not considerably affected by the injection pressure.

Likewise, varying injection pressure did not significantly affect the overall NO formation. However, the region probed was static whereas the combustion and region of formation of NO moved with injection pressure. Further investigations are therefore necessary to confirm the low influence of injection pressure on overall NO formation. Injection pressure was found to mainly influence the direction and extent of NO formation and transport. Whereas at low injection pressure NO stagnated on the sides of the spray, the tip of the spray was the region with the highest NO densities at high

injection pressures. It is therefore believed that the influence of in-cylinder air motion – such as swirl – on NO formation will vary according to the injection pressure.

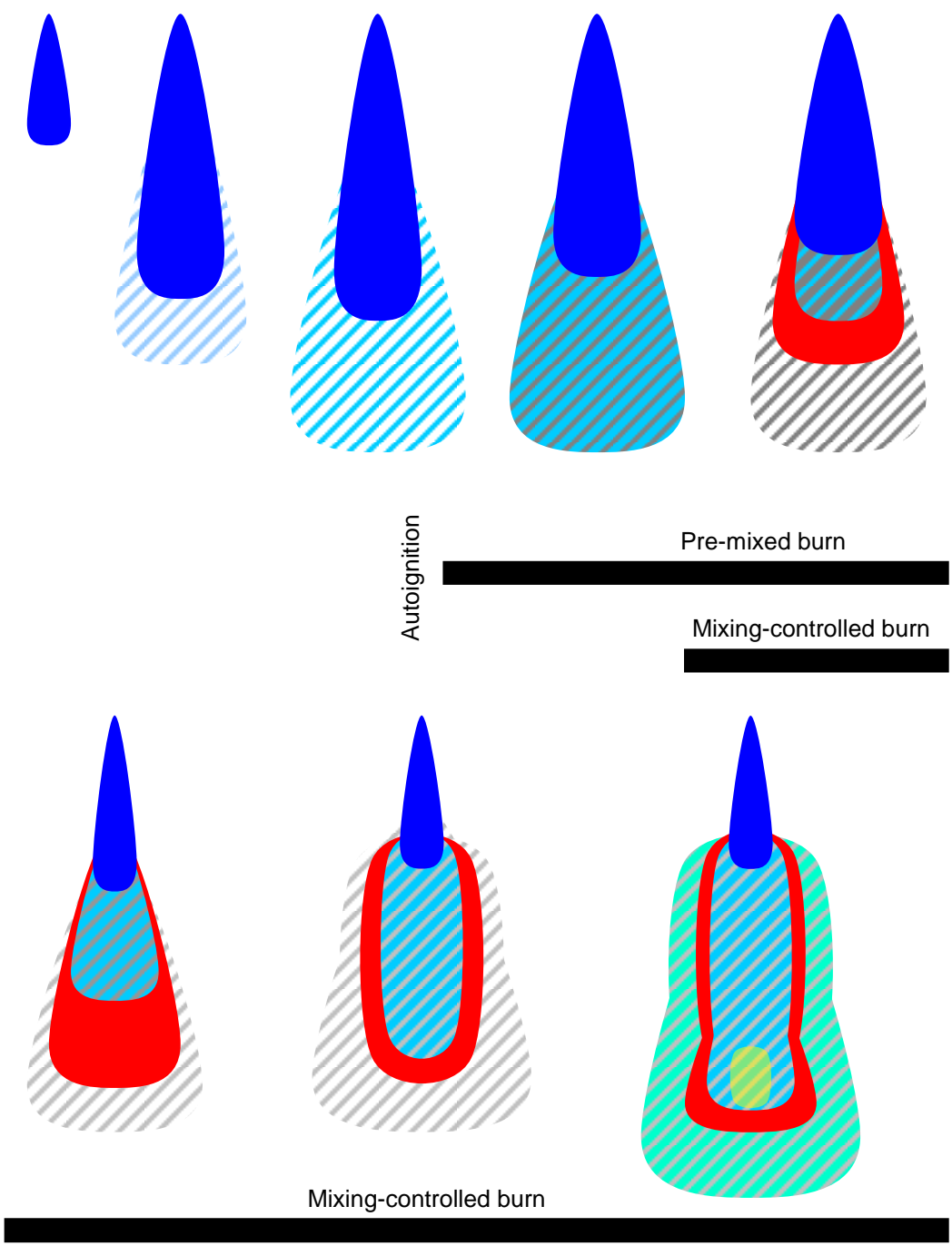
In-cylinder pressure affected both the spray penetration and dispersion resulting in a shorter, wider pre-mixed phase at higher in-cylinder pressure. Whereas the diffusion flame length followed a similar behaviour, its width decreased by as much as 20% between 5 and 7 MPa ICP. Likewise, the thickness of the flame front decreased by 18%. Increasing the in-cylinder pressure also led to an earlier formation of NO and a stronger production near the upstream part of the plume. Finally, higher local temperatures associated with the increased density led to higher overall formation rates.

Figure 93 presents a model of the flame development. It must be noted that the spray and flame front are in reality heavily rippled and Figure 93 only shows an average distribution. Furthermore, the complex atomisation and vaporisation phenomena were not investigated here (see Karimi *et al.* (2006) for a study of spray development in the same rapid compression machine). The spray evaporation process presented in Figure 93 is therefore extensively simplified.

The vapour fuel region in the centre of the flame plume is likely to be highly inhomogeneous. The evaporated fuel at the tip of the liquid core will decompose into smaller molecules and intermediates along its way to the flame front. The vapour fuel heading for the tip of the plume will have the longest residence time in this hot, rich environment. This leads to the apparition of soot precursors and a build-up of soot at the tip of the plume. The soot data presented here is based on the LII investigation of the same combusting spray by Crua (2002).

The model presented is compatible with the model published by Dec (Dec and Coy, 1996, Dec, 1997) based on measurements with an in-coming laser sheet at the tip of the flame. In the present investigation, the side lighted flame allowed a more detailed analysis of the side flame fronts. Indeed attenuation of the laser light by the tip of the flame, due to its high concentration of partially burnt fuel and soot, hindered the analysis of upstream OH in the cited investigation. Moreover, at late stages of combustion, the high concentration of soot obscured the images completely so that no distributions of the flame collapse were presented. The tube-like structure of the upstream part of the flame as well as the rapid spread of the flame throughout the spray at the end of injection could be observed in details in the present investigation.

When the injection ended, the flow of cold liquid fuel to the plume centre suddenly stopped. The diffusion flame, previously constrained to the periphery of the plume found a mix of increasingly hot and lean vapour and decomposed fuel in the centre of the plume. This led to the collapse of the diffusion flame structure on itself with high concentrations of OH radicals in a large part of the plume. The solid flame (as opposed to the hollow earlier diffusion flame), controlled by the diffusion of oxygen to the inner part of the plume (as opposed to diffusion of fuel to the periphery of the plume), lasted as long as there were hydrocarbons to oxidise.



- | | | | | | |
|---|-----------------|---|-------------------------|---|----|
|  | Liquid fuel |  | Burnt gases |  | NO |
|  | Vapour fuel |  | Pre-mixed burn products | | |
|  | Diffusion flame |  | Soot | | |

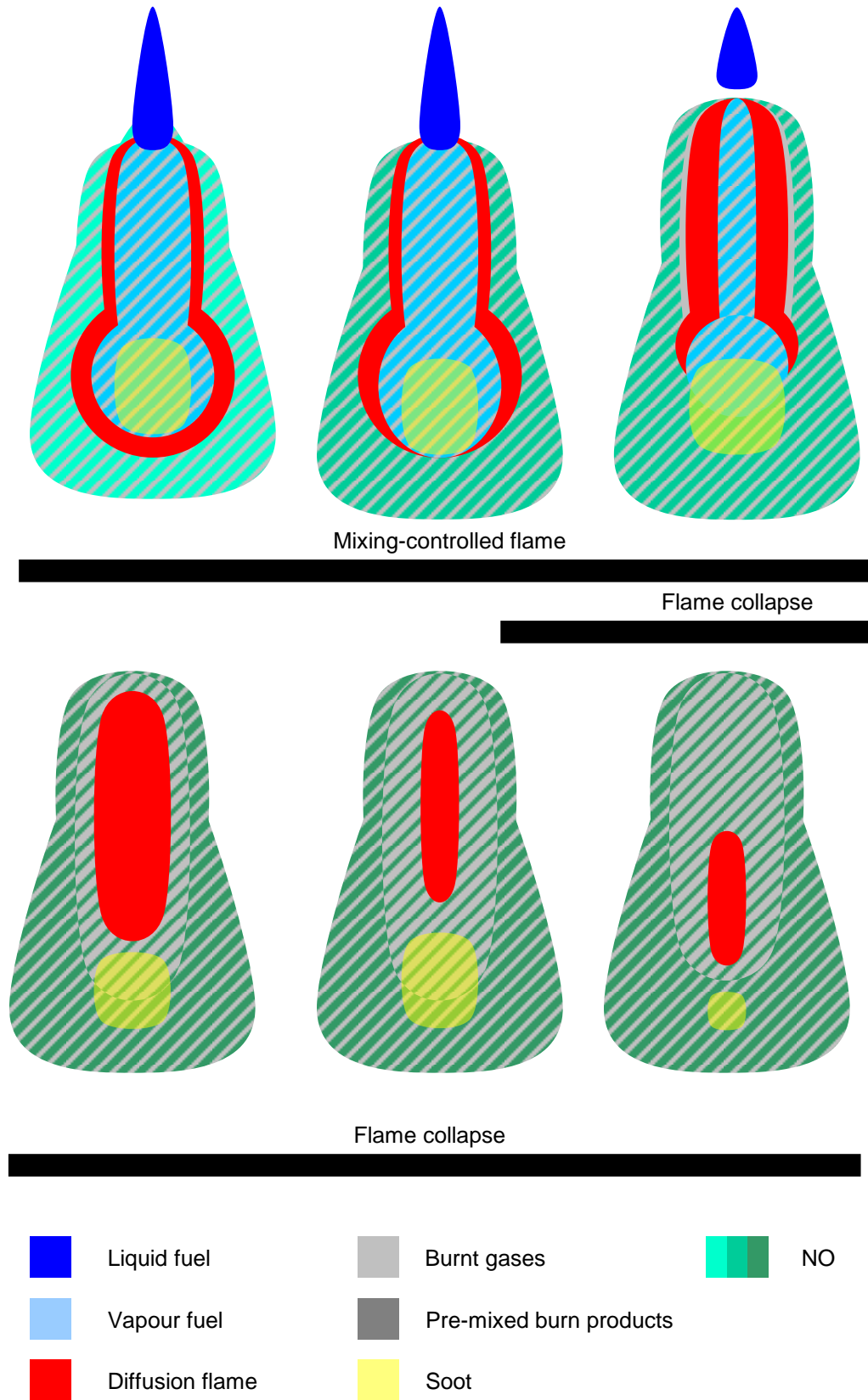


Figure 93 – Combustion process model

8.1. Future work

Seeding the intake air with a known quantity of NO could have several advantages. First, the effects of attenuation and quenching could be investigated more in details. The attenuation of the laser light by NO absorption could be, for instance, measured in motoring conditions. Likewise, the soundness of the phenomenological model developed in chapter 5 could be evaluated. Similarly, the absence of NO-LIF signal from the centre of the plume, attributed to attenuation in the flame front, could be proved independent of NO concentrations. Furthermore, the level of the NO-LIF signal at the on- and off-line excitation wavelengths could be verified without any interference. Also, the hypothesis of linear fluorescence could be verified. Finally, the late formation of NO, in the absence of OH radicals, could be confirmed and investigated more in depth.

A substantial improvement in the distribution levels could be obtained by changing the actual UV lens for a lens with a lower f-number. The lower f-number will decrease the depth of field but the imaged region being only 0.5 mm deep, all emitting molecules could be in focus. The higher collection of light and lower detectability limit associated would allow the pre-mixed phase to be investigated more thoroughly for OH and NO formation.

Comparisons with NO distributions obtained by CFD simulations could allow to assess the validity of the models for the prediction of NO formation based on thermal-NO included in such CFD codes.

Although the present investigation is believed to be representative of a modern diesel engine, some characteristics like the spray length and injection duration do not match the usual conditions in a engine running at normal load. By cutting one of the windows in the shape of a piston bowl, the influence of spray-bowl interactions on OH and NO formation could be investigated. Likewise, a similar investigation could be run for shorter injection durations and a better time resolution. This could give a better picture of the start of the mixing-controlled phase and the early diffusion flame development. This information in turn could be used to improve the heat release rate decomposition, scaling the mixing-controlled heat release build-up on the flame front development.

REFERENCES

- ALATAS, B., PINSON, J. A., LITZINGER, T. A. & SANTAVICCA, D. A. (1993) A Study of NO and Soot Evolution in a DI Diesel Engine via planar Imaging. *SAE Paper No 930973*.
- ALLEN, M. G., MCMANUS, K. R. & SONNENFROH, D. M. (1994) PLIF Imaging Measurements in High-Pressure Spray Flame Combustion. *AIAA*, 2913.
- ALLEN, M. G., MCMANUS, K. R., SONNENFROH, D. M. & PAUL, P. H. (1995) Planar Laser-Induced Fluorescence Imaging Measurements of OH and Hydrocarbon Fuel Fragments in High-Pressure Spray-Flame Combustion. *Applied Optics*, 34, 6287-6300.
- ANDRESEN, P., BATH, A., GRÖGER, W., LÜLF, H. W., MEIJER, G. & TER MEULEN, J. J. (1988) Laser-Induced Fluorescence with Tunable Excimer Lasers as a Possible Method for Instantaneous Temperature Field Measurements at High Pressures. *Applied Optics*, 27, 365-378.
- ANDRESEN, P., MEIJER, G., SCHLÜTER, H., VOGES, H., KOCH, A., HENTSCHEL, W., OPPERMAN, W. & ROTHE, E. (1990) Fluorescence imaging inside an internal combustion engine using tunable excimer lasers. *Applied Optics*, 29, 2392-2404.
- AOYAGI, Y., KAMIMOTO, T., MATSUI, Y. & MATSUOKA, S. (1980) A Gas Sampling Study on the Formation Processes of Soot and NO in a DI Diesel Engine. *SAE Paper No 800254*.
- ARNOLD, A., BECKER, H., HEMBERGER, R., HENTSCHEL, W., KETTERLE, W., KOLLNER, M., MEIENBURG, W., MONKHOUSE, P., NECKEL, H., SCHAFFER, M., SICK, V., SUNTZ, R. & WOLFRUM, J. (1990) Laser in situ monitoring of combustion processes. *Applied Optics*, 29, 4860-4872.
- ARNOLD, A., DINKELACKER, F., HEITZMANN, T., MONKHOUSE, P., SCHÄFER, M., SICK, V., WOLFRUM, J., HENTSCHEL, W. & SCHINDLER, K. P. (1992) DI diesel engine combustion visualised by combined laser techniques. *24th international symposium on combustion*. The combustion institute.
- BANWELL, C. N. & NCCASH, E. M. (1994) *Fundamentals of Molecular Spectroscopy*, McGraw-Hill.

- BARLOW, R. S., DIBBLE, R. W., CHEN, J.-Y. & LUCHT, R. P. (1990) Effect of Damköhler Number on Superequilibrium OH Concentration in Turbulent Non-premixed Jet Flames. *Combustion and Flame*, 82, 235-251.
- BARLOW, R. S., DIBBLE, R. W. & LUCHT, R. P. (1989) Simultaneous Measurement of Raman Scattering and Laser-Induced OH Fluorescence in Nonpremixed Turbulent Jet Flames. *Optics Letters*, 14, 263-265.
- BATTLES, B. E. & HANSON, R. K. (1995) Laser-Induced Fluorescence Measurements of NO and OH Mole Fraction in Fuel-Lean, High-Pressure (1-10 atm) Methane Flames: Fluorescence Modeling and Experimental Validation. *J. Quant. Spectrosc. Radiat. Transfer*, 54, 521-537.
- BECHTEL, J. H., DASH, C. J. & TEETS, R. E. (1984) *Combustion Research with Lasers*, Academic Press.
- BENGTSSON, P.-E. (1996) Simultaneous Two-Dimensional Visualization of Soot and OH in Flames Using Laser-Induced Fluorescence. 50, 1182-1186.
- BERCKMÜLLER, M. (1996) A study of mixture formation in a lean burn research engine using laser fluorescence imaging. Cranfield University.
- BESSLER, W. G., SCHULZ, C., LEE, T., JEFFRIES, J. B. & HANSON, R. K. (2003a) Carbon dioxide UV laser-induced fluorescence in high-pressure flames. *Chemical Physics Letter*, 375, 344-349.
- BESSLER, W. G., SCHULZ, C., LEE, T., SHIN, D.-I., HOFMANN, M., JEFFRIES, J. B., WOLFRUM, J. & HANSON, R. K. (2002) Quantitative NO-LIF imaging in high-pressure flames. *Appl. Phys. B*, 75, 97-102.
- BESSLER, W. G., SCHULZ, C., SICK, V. & DAILY, J. W. (2003b) A versatile modeling tool for nitric oxide LIF spectra. *Third Joint Meeting of the US Sections of The Combustion Institute*. Chicago.
- BÖCKLE, S., EINECKE, S., HILDENBRAND, F., ORLEMANN, C., C.SCHULZ, WOLFRUM, J. & SICK, V. (1999) Laser-Spectroscopic Investigation of OH-Radical Concentrations in the Exhaust Plane of Jet Engines. *Geophysical Research Letters*, 26, 1849-1852.
- BORMAN, G. L. & RAGLAND, K. W. (1998) *Combustion Engineering*, McGraw-Hill.
- BOWMAN, C. T. (1975) Kinetics of Pollutant Formation and Destruction in Combustion. *Progress in Energy and Combustion Science*, 1, 33-45.
- BRACKMANN, U. (2000) Lambdachrome Laser Dyes. *Lambda Physik AG*.

- BRÄUMER, A., SICK, V., WOLFRUM, J., DREWES, V., ZAHN, M. & MALY, R. (1995) Quantitative Two-Dimensional Measurements of Nitric Oxide and Temperature Distributions in a Transparent Square Piston SI Engine.
- BRUGMAN, T. M. (1998) Laser-based diagnostics on NO in a diesel engine. Nijmegen, Thesis Katholieke Universiteit Nijmegen.
- BRUGMAN, T. M., KLEIN-DOUWEL, R., HUIGEN, G., WALWIJK, E. V. & MEULEN, J. J. T. (1993) Laser-Induced-Fluorescence Imaging of NO in an n-Heptane- and Diesel-Fuel-Driven Diesel Engine. *Applied Physics B*, 57, 405-410.
- BRUGMAN, T. M., STOFFELS, G. G. M., DAM, N., MEERTS, W. L. & MEULEN, J. J. T. (1998) Imaging and Post-Processing of Laser-Induced Fluorescence NO in a Diesel Engine. *Applied Physics B*, 64, 717-724.
- BUCHHOLZ, B. A., MUELLER, C. J., UPATNIEKS, A., MARTIN, G. C., PITZ, W. J. & WESTBROOK, C. K. (2004) Using carbon-14 isotope tracing to investigate molecular structure effects of the oxygenate dibutyl maleate on soot emissions from a DI diesel engine. *Spring Fuels and Lubricants Conference and Exhibition*. Toulouse, France, Society of Automotive Engineers, Inc., Warrendale, Pennsylvania, USA.
- CHANG, A. Y., DIROSA, M. D. & HANSON, R. K. (1992) Temperature dependence of collision broadening and shift in the NO A \leftarrow X (0, 0) band in the presence of argon and nitrogen. *Journal of Quantitative Spectroscopy and Radiative Transfer*, 47, 375-390.
- CHEN, J.-Y. & KOLLMANN, W. (1992) PDF modeling and analysis of thermal NO formation in turbulent nonpremixed hydrogen-air jet flames. *Combustion and Flame*, 88, 397-412.
- COOPER, B., JACKSON, N. & BEASLEY, M. (2004) Technology Development to Meet the Future Demand for Passenger Car Diesel Engines with Lower Emissions and Higher Performance. *SIA International Congress, The Diesel Engine: Today and Tomorrow*. Ecole Centrale de Lyon, France, SIA.
- COOPER, C. S. & LAURENDEAU, N. M. (2000) Quantitative measurements of nitric oxide in high-pressure (2-5 atm), swirl-stabilized spray flames via laser-induced fluorescence. *Combustion and Flame*, 123, 175-188.
- CORREA, S. M. (1992) A review of NO_x Formation under Gas-Turbine Combustion. *Combust. Sci. and Tech.*, 87, 329-362.

- CRUA, C. (2002) Combustion Processes in a Diesel Engine. University of Brighton.
- DAILY, J. W. (1997) Laser Induced Fluorescence Spectroscopy in Flames. 23, 133-199.
- DAVIDSON, D. F., ROEHRIG, M., PETERSEN, E. L., ROSA, M. D. D. & HANSON, R. K. (1996) Measurements of the OH A-X(0,0) 306 nm Absorption Bandhead at 60 atm and 1735 K. *J. Quant. Spectrosc. Radiat. Transfer*, 55, 755-762.
- DE SERCEY, G., AWCOCK, G. J. & HEIKAL, M. R. (2006) Development of a calibrated technique for insitu investigation of air-fuel mixing in engines. *Imaging Science Journal*, 54, 33-45.
- DEC, J. E. (1997) Conceptual model of DI diesel combustion based on laser-sheet imaging. *SAE paper no. 970873 SAE Special Publications*, 1244, 223-252.
- DEC, J. E. & CANAAN, R. E. (1998) PLIF Imaging of NO Formation in a DI Diesel Engine. *SAE paper No. 980147*.
- DEC, J. E. & COY, E. B. (1996) OH Radical Imaging in a DI Diesel Engine and the Structure of the Early Diffusion Flame. *SAE Paper No. 960831*.
- DEC, J. E. & ESPEY, C. (1998) Chemiluminescence Imaging of Autoignition in a DI Diesel Engine. *SAE Paper No. 982685*.
- DIEKE, G. H. & CROSSWHITE, H. M. (1962) The ultraviolet bands of OH - Fundamental Data. *J. Quant. Spectrosc. Radiat. Transfer*, 2, 97-199.
- DIETSCHKE, K.-H., KLINGEBIEL, M. & MÜLLER, R. (Eds.) (2005) *Diesel Fuel-Injection System - Common Rail*, Robert Bosch GmbH.
- DIROSA, M. D., KLAVUHN, K. G. & HANSON, R. K. (1996) LIF Spectroscopy of NO and O₂ in High-Pressure Flames. *Combust. Sci. and Tech.*, 118, 257-283.
- DONAHUE, R. J., BORMAN, G. L. & BOWER, G. R. (1994) Cylinder-Averaged Histories of Nitric Oxide in a D.I. Diesel with Simulated Turbocharging. *SAE Paper No. 942046*.
- DRAKE, M. C., CORREA, S. M., PITZ, R. W., SHYY, W. & FENIMORE, C. P. (1987) Superequilibrium and Thermal Nitric Oxide Formation in Turbulent Diffusion Flames. *Combustion and Flame*, 69, 347-365.
- ECKBRETH, A. C. (1996) *Laser Diagnostics for Combustion Temperature and Species*, Gordon and Breach Publishers.
- FENIMORE, C. P. (1971) Formation of Nitric-Oxide in Premixed-Hydrocarbon Flames. *Proceedings of the Combustion Institute*, 13, 373-380.

- FERGUSON, C. R. & KIRKPATRICK, A. T. (2001) *Internal Combustion Engines - Applied Thermosciences*, John Wiley & Sons.
- FISSENEWERT, U., SICK, V. & PUCHER, H. (2005) Characterization of combustion and NO formation in a spray-guided gasoline direct-injection engine using chemiluminescence imaging, NO-PLIF, and fast NO exhaust gas analysis. *SAE 2005-01-2089*.
- FLYNN, P. F., DURETT, R. P., HUNTER, G. L., ZUR LOYE, A. O., AKINYEMI, O. C., DEC, J. E. & WESTBROOK, C. K. (1999) Diesel Combustion: An Integrated View Combining Laser Diagnostics, Chemical Kinetics, And Empirical Validation. *SAE paper no. 1999-01-0509*.
- FUJIMOTO, H., KURATA, K., ASAI, G. & SENDA, J. (1998) OH Radical Generation and Soot Formation/Oxidation in DI Diesel Engine. *SAE Paper No 982630*.
- GONZALEZ, M. A., PIEL, W., ASMUS, T., CLARK, W., GARBAK, J., LINEY, E., NATARAJAN, M., NAEGELI, D. W., YOST, D., FRAME, E. A. & III, J. P. W. (2001) Oxygenates Screening for Advanced Petroleum-Based Diesel Fuels: Part 2. The Effect of Oxygenate Blending Compounds on Exhaust Emissions. *SAE Paper No. 2001-01-3632*.
- GREENHALGH, D. A. (1988) Quantitative CARS Spectroscopy. IN CLARK, R. J. H. & HESTER, R. E. (Eds.) *Advances in Non-Linear Spectroscopy*. Wiley.
- GREENHALGH, D. A. (1994) Inelastic Scattering Laser Diagnostics; Cars, Planar LIF and Planar LII. IN LADING, L. (Ed.) *Optical Diagnostics for Flow Processes*. New York, Plenum Press.
- HALL, R. J., SMOOKE, M. D. & COLKET, M. B. (1997) Predictions of Soot Dynamics in Opposed Jet Diffusion Flames. IN SAWYER, R. F. & DRYER, F. L. (Eds.) *Physical and Chemical Aspects of Combustion: A Tribute to Irvin Glassman*. Gordon & Breach.
- HALSTEAD, M. P., KIRSCH, L. J. & QUINN, C. P. (1977) The autoignition of hydrocarbon fuels at high temperatures and pressures--Fitting of a mathematical model. *Combustion and Flame*, 30, 45-60.
- HANSON, R. K. & SALIMIAN, S. (1984) Chapter 6: Survey of Rate Constants in the N/H/O System. IN GARDINER, W. C. (Ed.) *Combustion Chemistry*. Springer-Verlag.
- HANSON, R. K., SEITZMAN, J. M. & PAUL, P. H. (1990) Planar Laser-Fluorescence Imaging of Combustion Gases. *Appl. Phys. B*, 50, 441-454.

- HAYDEN, M. & COOPER, B. G. (2004) Diesel Passenger Car & Light Commercial Vehicle Markets in Western Europe. Ricardo.
- HECHT, J. (1986) *The Laser Guidebook*, McGraw-Hill.
- HECHT, J. (1992) *The Laser Guidebook*, McGraw-Hill.
- HECHT, J. (1994) *Understanding Lasers, an Entry-Level Guide*, New York, IEEE Press.
- HEYWOOD, J. B. (1988) *Internal Combustion Engines Fundamentals*, McGraw-Hill Book Company.
- HILDENBRAND, F. & SCHULZ, C. (2001) Measurements and simulations of in-cylinder UV-absorption in spark ignition and Diesel engines. *Appl. Phys. B*, 73, 165-172.
- HILDENBRAND, F., SCHULZ, C., KELLER, F., KÖNIG, G. & WAGNER, E. (2001) Quantitative Laser Diagnostics Studies of the NO Distribution in a DI Diesel Engine with PLN and CR Injection Systems. *SAE Paper No. 2001-01-3500*.
- HILDENBRAND, F., SCHULZ, C., KELLER, F. & WAGNER, E. (2000a) Laser-Induced Fluorescence Imaging of NO in a DI Diesel Engine using KrF Excimer Radiation. *Towards Clean Diesel Engines, IFP*.
- HILDENBRAND, F., SCHULZ, C., WOLFRUM, J., KELLER, F. & WAGNER, E. (2000b) Laser Diagnostic Analysis of NO Formation in a Direct Injection Diesel Engine with Pump-Line-Nozzle and Common Rail Injection Systems. *Proceedings of the Combustion Institute*, 28, 1137-1143.
- INGLE, J. D. & CROUCH, S. R. (1988) *Spectrochemical analysis*, Prentice-Hall International Editions.
- KANAZAWA, S., OHKUBO, T., ITO, T., SHUTO, Y., NUMOTO, Y. & MIZERACZYK, J. (2001) LIF Diagnostics of NO Molecules in Atmospheric Pressure DC Streamer Coronas Used for NO_x Abatement. *Arbeitsgemeinschaft PlasmaPhysik (APP) Spring Meeting "Diagnostics of Non-Equilibrium High Pressure Plasmas"*.
- KARIMI, K., SAZHINA, E. M., ABDELGHAFAR, W. A., CRUA, C., COWELL, T., HEIKAL, M. R. & GOLD, M. R. (2006) Developments in Diesel Spray Characterisation and Modelling. *THIESEL 2006 Conference on Thermo- and Fluid Dynamic Processes in Diesel Engines*.
- KENNAIRD, D., CRUA, C., HEIKAL, M., MORGAN, R., BAR, F. & SAPSFORD, S. (2000) A New High-Pressure Diesel Spray Research Facility. *International*

Conference on Computational and Experimental Methods in Reciprocating Engines, C587/040/2000.

- KETTERLE, W., SCHÄFER, M., ARNOLD, A. & WOLFRUM, J. (1992) 2D Single-Shot Imaging of OH Radicals Using Tunable Excimer Lasers. *Applied Physics B*, B54, 109-112.
- KINSLER, L. E., FREY, A. R., COPPENS, A. B. & SANDERS, J. V. (2000) *Fundamental of acoustics*, John Wiley & Sons.
- KITAMURA, Y., MOHAMMADI, A., ISHIYAMA, T. & SHIOJI, M. (2005) Fundamental Investigation of NO_x Formation in Diesel Combustion Under Supercharged and EGR Conditions. *SAE Paper No. 2005-01-0364*.
- KOHSE-HÖINGHAUS, K. (1994) Laser Techniques for the Quantitative Detection of Reactive Intermediates in Combustion Systems. *Progress in Energy and Combustion Science*, 20.
- KOHSE-HÖINGHAUS, K. & JEFFRIES, J. B. (Eds.) (2002) *Applied Combustion Diagnostics*, Taylor & Francis.
- KOSAKA, H., NISHIGAKI, T., KAMIMOTO, T., SANO, T., MATSUTANI, A. & HARADA, S. (1996) Simultaneous 2-D Imaging of OH-Radicals and Soot in a Diesel Flame by Laser Sheet Techniques. *SAE Paper No 960834*.
- LADOMMATOS, N., ABDELHALIM, S. & ZAO, H. (1998) Control of Oxides of Nitrogen from Diesel Engines Using Diluents While Minimising the Impact on Particulate Pollutants. *Applied Thermal Engineering*, 18, 963-980.
- LADOMMATOS, N., BALIAN, R., HORROCKS, R. & COOPER, L. (1996) The Effect of Exhaust Gas Recirculation on Combustion and NO_x Emissions in a High-Speed Direct-Injection Diesel Engine. *SAE Paper No 960840*.
- LAGUITTON, O. (2005) Advanced Diesel Combustion Strategies for Ultra-Low Emissions. *School of Engineering*. Brighton, University of Brighton.
- LAVOIE, G. A., HEYWOOD, J. B. & KECK, J. C. (1970) Experimental and Theoretical Study of Nitric Oxide Formation in Internal Combustion Engines. *Combust. Sci. and Tech.*, 1, 313-326.
- LEGRIS, L. (2005) Fluorescence induite par laser du monoxyde d'azote dans un moteur a allumage commande en vue de l'etude de l'influence du melange gaz frais - gaz residuels sur la dispersion cyclique. Universite de Rouen.

- LEGRIS, L. & DOMINGUES, E. (2004) Etude bibliographique de la mise en oeuvre de la fluorescence induite par laser pour l'imagerie du monoxyde d'azote dans des conditions moteur., Coria.
- LUQUE, J. & CROSLEY, D. R. (1999) LIFBASE, Database and spectral simulation for diatomic molecules (v 1.6). *SRI International Report MP-99-009*.
- MCENALLY, C. S., SHAFFER, A. M., LONG, M. B., PFEFFERLE, L. D. & SMOOKE, M. D. (1998) Computational and Experimental Study of Soot Formation in a Coflow, Laminar Ethylene Diffusion Flame. *Twenty Seventh Symposium (International) on Combustion*. The Combustion Institute.
- MEIER, U. E., WOLFF-GABMANN, D. & STRICKER, W. (2000) LIF imaging and 2D temperature mapping in a model combustor at elevated pressure. *Aerospace Science and Technology*, 4, 403-414.
- MEROLA, S. S., VAGLIECO, B. M. & MANCARUSO, E. (2004) Multiwavelength ultraviolet absorption spectroscopy of NO and OH radical concentration applied to a high-swirl diesel-like system. *Experimental thermal and Fluid Science*, 28, 355-367.
- MILLER, J. A. & BOWMAN, C. T. (1989) Mechanism and modeling of nitrogen chemistry in combustion. *Progress in Energy and Combustion Science*, 15, 287-338.
- MINETTI, R., CARLIER, M., RIBAUCCOUR, M., THERSSEN, E. & SOCHET, L. R. (1995) A Rapid Compression Machine Investigation of Oxidation and Auto-Ignition of *n*-Heptane: Measurements and Modeling. *Combustion and Flame*, 102, 298-309.
- MOHAMED, C. (1998) Suppression of Reaction During Rapid Compression and Its Effect on Ignition Delay. *Combustion and Flame*, 112, 438-444.
- MORGAN, R., WRAY, J., KENNAIRD, D. A., CRUA, C. & HEIKAL, M. (2001) The influence of injector parameter on the formation and breakup of a Diesel spray. *2001 SAE Transactions - Journal of Engines*, 110, 389-399.
- MUELLER, C. J. & MARTIN, G. C. (2002) Effects of Oxygenated Compounds on Combustion and Soot Evolution in a D.I. Diesel Engine: Broadband Luminosity Imaging. *SAE Paper No. 2002-01-1631*.
- MURASE, E., K.HANADA, YUN, J.-H. & OPPENHEIM, A. K. (1998) Radical Emission and Fluorescence Measurements in Pulsed Flame Jet. *The Fourth International Symposium COMODIA 98*.

- NAKAGAWA, H., ENDO, H. & DEGUCHI, Y. (1998) LIF Imaging of Diesel Spray Combustion. *JSME Combustion and Modelling Symposium, COMODIA 98*. Kyoto.
- NAKAGAWA, H., ENDO, H., DEGUCHI, Y., NODA, M., OIKAWA, H. & SHIMADA, T. (1997) NO measurement in Diesel Spray Flame using Laser Induced Fluorescence. *SAE Paper No. 970874*.
- NATARAJAN, M., FRAME, E. A., NAEGELI, D. W., ASMUS, T., CLARK, W., GARBAK, J., D., M. A. G., LINEY, E., PIEL, W. & III, J. P. W. (2001) Oxygenates for Advanced Petroleum-Based Diesel Fuels: Part1. Screening and Selection Methodology for the Oxygenates. *SAE Paper No. 2001-01-3631*, 67-91.
- NGUYEN, Q. V., DIBBLE, R. W., CARTER, C. D., FIECHTNER, G. J. & BARLOW, R. S. (1996) Raman-LIF Measurements of Temperature, Major Species, OH, and NO in a Methane-Air Busen Flame. *Combustion and Flame*, 105, 499-510.
- NYGREN, J., RICHTER, M., HULT, J., KAMINSKI, C. F. & ALDEN, M. (2001) Temporally resolved single-cycle measurements of fuel- and OH- distributions in a spark ignition engine using high speed laser spectroscopy. *Fifth International Symposium on Diagnostics and Modeling of Combustion in Internal Combustion Engines (COMODIA 2001)*, 572-580.
- PASTOR, J. V., LOPEZ, J. J., JULIÁ, J. E. & BENAJES, J. (2002) Planar Laser-Induced Fluorescence Fuel Concentration Measurements in Isothermal Diesel Sprays. *Optics Express*, 10.
- PAUL, P. H., GRAY, J. A., DURANT, J. L. & THOMAN, J. W. (1994) Collisional Quenching Corrections for Laser-Induced Fluorescence Measurements of NO $A^2\Sigma^+$. *AIAA*, 32, 1670-1675.
- PICKETT, L. M. & SIEBERS, D. L. (2003) Fuel effects on soot processes of fuel jets at DI diesel conditions. *Powertrain and Fluid Systems Conference and Exhibition*. Pittsburgh, Pennsylvania, USA, Society of Automotive Engineers, Inc., Warrendale, Pennsylvania, USA.
- RAPPENGLÜCK, B., OYOLA, P., OLAETA, I. & FABIAN, P. (2000) The Evolution of Photochemical Smog in the Metropolitan Area of Santiago de Chile. *Journal of Applied Meteorology*, 39, 275-290.

- RIFE, J. & HEYWOOD, J. B. (1974) Photographic and Performance Studies of Diesel Combustion with a Rapid Compression Machine. *SAE Paper No. 740948*.
- SAZHINA, E. M., SAZHIN, S. S., HEIKAL, M. R. & BARDSLEY, M. E. A. (2000) The P-1 Model for Thermal Radiation Transfer: Application to Numerical Modeling of Combustion Processes in Diesel Engines. *16th IMACS World Congress*.
- SAZHINA, E. M., SAZHIN, S. S., HEIKAL, M. R. & MAROONEY, C. J. (1999) The Shell Autoignition Model: Applications to Gasoline and Diesel Fuels. *Fuel*, 78, 389-401.
- SCHULZ, C., JEFFRIES, J. B., DAVIDSON, D. F., KOCH, J. D., WOLFRUM, J. & HANSON, R. K. (2002) Impact of UV Absorption by CO₂ and H₂O on NO LIF in High-Pressure Combustion Applications. *Proceedings of the Combustion Institute*, 29, 2735-2742.
- SCHULZ, C., SICK, V., HEINZE, J. & STICKER, W. (1997) Laser-Induced Fluorescence Detection of Nitric Oxide in High-Pressure Flames with A-X(0,2) excitation. *Applied Optics*, 36, 3227-3232.
- SCHULZ, C., YIP, B., SICK, V. & WOLFRUM, J. (1995) A Laser-Induced Fluorescence scheme for Imaging Nitric Oxide in Engines. *Chemical Physics Letter*, 242, 259-264.
- SHER, E. (Ed.) (1998) *Handbook of Air Pollution from Internal Combustion Engines - Pollutant Formation and Control*, Academic Press.
- SMOOKE, M. D., LONG, M. B., CONNELLY, B. C., COLKET, M. B. & HALL, R. J. (2005) Soot Formation in Laminar Diffusion Flames. *Combustion and Flame*, 143, 613-628.
- SOLOMON, G. M. & BALMES, J. R. (2003) Health effects of diesel exhaust. *Clinics in Occupational and Environmental Medicine*, 3, 61-80.
- STOFFELS, G. G. M. (1999) Nitric oxide in a diesel engine: laser-based detection and interpretation. Katholieke Universiteit Nijmegen.
- STOFFELS, G. G. M., BOOM, E.-J. C. D., SPAANJAARS, C. M. I., DAM, N., MEERTS, W. L. & MEULEN, J. J. T. (1998) Laser Diagnostics of Nitric Oxide inside a Two-Stroke DI Diesel Engine. *selected papers from the 9th International Symposium, Lisbon Portugal*.
- STOFFELS, G. G. M., BOOM, E.-J. C. D., SPAANJAARS, C. M. I., DAM, N., MEERTS, W. L., MEULEN, J. J. T., DUFF, J. L. C. & RICKEARD, D. J.

- (1999) In-Cylinder measurements of NO formation in a Diesel Engine. *SAE Paper No 1999-01-1487*.
- STONE, R. (1999) *Introduction to Internal Combustion Engines*, MacMillan Press.
- TAIT, N. P. & GREENHALGH, D. A. (1993) PLIF Imaging of Fuel Fraction in Practical Devices and LII Imaging of Soot. *Ber. Bunsenges. Phys. Chem.* Heidelberg.
- TAYLOR, A. M. K. P. (Ed.) (1993a) *Instrumentation for flows with combustion*, Academic Press.
- TAYLOR, A. M. K. P. (Ed.) (1993b) *Instrumentation for Flows with Combustion*, Academic Press.
- TSUJISHITA, M., HIRANO, K., YOKOO, M., SAKURAYA, T. & TAKESHITA, Y. (1999) Accurate Thermometry Using NO and OH Laser-Induced Fluorescence in an Atmospheric Pressure Flame. 42, 119-126.
- VERBIEZEN, K., KLEIN-DOUWEL, R. J. H., VLIET, A. P. V., DONKERBROEK, A. J., MEERTS, W. L., MEERTS, N. J., DAM, N. J. & MEULEN, J. J. T. (2006) Quantitative Laser-Induced Fluorescence Measurements of Nitric-Oxide in a Heavy-Duty Diesel Engine. *Proceeding of the Combustion Institute*, 31, 765-773.
- VOICULESCU, I. A. & BORMAN, G. L. (1978) An Experimental Study of Diesel Engine Cylinder-Averaged Histories. *SAE Paper No. 780228*.
- VYRODOV, A. O., HEINZE, J. & MEIER, U. E. (1995) Collisional Broadening of Spectral Lines in the A-X(0,0) System of NO by N₂, Ar, and He at Elevated Pressures Measured by Laser-Induced Fluorescence. *J. Quant. Spectrosc. Radiat. Transfer*, 53, 277-287.
- WARNATZ, J., MASS, U. & DIBBLE, R. W. (2001) *Combustion*, Springer.
- WATSON, H. C., MILKINS, E. E. & RIGBY, G. R. (1990) A New Look at Oxygen Enrichment: 1) The Diesel Engine. *SAE Paper No. 900344*.
- WODTKE, A. M., HUWEL, L., SCHLUTER, H., MEIJER, G. & ANDRESEN, P. (1988) High-Sensitivity Detection of NO in a Flame Using a Tunable ArF Laser. *Optics Letter*, 13, 910-912.
- ZELDOVICH, J. (1946) The Oxidation of Nitrogen in Combustion and Explosions. *Acta Physicochimica U.R.S.S.*, 21, 577-628.

PAPERS PUBLISHED BY THE AUTHOR

Journals

DEMORY, R., CRUA, C. & HEIKAL, M. R. (2007) LIF Measurements of Nitric Oxide in a Combusting Diesel Spray. *Combustion and Flame*, under review.

Conferences

DEMORY, R. (2005) Laser-Based Diagnostics in a Diesel Flame: Flame Structure. *Engineering Research in Action*. Brighton.

DEMORY, R. (2006) OH and NO Distributions in Combusting Diesel Sprays. *Engineering in Action*. Brighton.

DEMORY, R., CRUA, C., GOLD, M. R. & HEIKAL, M. R. (2006) Measuring and processing in-cylinder distributions of NO and OH obtained by laser-induced fluorescence in a diesel rapid compression machine. *Applied Laser Techniques to Fluid Mechanics*. Lisbon, Portugal.

DEMORY, R., CRUA, C. & HEIKAL, M. R. (2007) Laser-Induced Fluorescence Investigation of Nitric Oxide Formation in a Diesel Rapid Compression Machine. *SAE Powertrain & Fluids*. Chicago.

APPENDIX A

Heat release rate

The first law of thermodynamics for a quasi-static open system can be written as:

$$\frac{dQ}{dt} - P \cdot \frac{dV}{dt} + \sum_i \dot{m}_i \cdot h_i = \frac{dU}{dt} \quad (97)$$

where:

$\frac{dQ}{dt}$ is the heat transfer rate across the system boundary

$P \cdot \frac{dV}{dt}$ is the rate of work transfer done by the system

\dot{m}_i is the mass flow rate through the boundaries of species i

h_i is the enthalpy of species i

U is the internal energy of the system

For direct-injection engines the only mass flows \dot{m}_i across the boundary are the fuel and the crevice flow. If crevice flows are neglected equation (97) becomes:

$$\frac{dQ}{dt} - P \cdot \frac{dV}{dt} + \dot{m}_f \cdot h_f = \frac{dU}{dt} \quad (98)$$

The cylinder contents are assumed to be at uniform temperature at each instant in time during the combustion process. U and h_f are taken to be sensible internal energy of the cylinder contents and sensible enthalpy of the injected fuel ($U = U(T) - U(298 K)$ and $h_f = h_f(T) - h_f(298 K)$).

Since $h_f(T) \approx 0$, equation (98) becomes:

$$\frac{dQ_n}{dt} = P \cdot \frac{dV}{dt} + \frac{dU}{dt} \quad (99)$$

Where $\frac{dQ_n}{dt}$ is the net-heat release rate, the gross heat release minus the lost heat at the walls. If the contents of the cylinders are modelled as an ideal gas:

$$\frac{dQ_n}{dt} = P \cdot \frac{dV}{dt} + m \cdot c_v \frac{dT}{dt} \quad (100)$$

Where c_v is the specific heat at constant volume and m the gas mass. Differentiating the ideal gas law and substituting in equation (100), it follows:

$$\frac{dQ_n}{dt} = \frac{\gamma}{\gamma - 1} \cdot P \cdot \frac{dV}{dt} + \frac{1}{\gamma - 1} \cdot V \cdot \frac{dP}{dt} \quad (101)$$

Where γ is the ratio of specific heats c_p/c_v .

APPENDIX B

Emission standards

Data from www.dieseln.net

Europe

Table 27 – EU emission standards for passenger cars [$\text{g}\cdot\text{km}^{-1}$]

Tier	Year	CO	HC	HC+NO _x	NO _x	PM
Diesel						
Euro 1†	1992.07	2.72 (3.16)	-	0.97 (1.13)	-	0.14 (0.18)
Euro 2, IDI	1996.01	1.0	-	0.7	-	0.08
Euro 2, DI	1996.01 ^a	1.0	-	0.9	-	0.10
Euro 3	2000.01	0.64	-	0.56	0.50	0.05
Euro 4	2005.01	0.50	-	0.30	0.25	0.025
Petrol (Gasoline)						
Euro 1†	1992.07	2.72 (3.16)	-	0.97 (1.13)	-	-
Euro 2	1996.01	2.2	-	0.5	-	-
Euro 3	2000.01	2.30	0.20	-	0.15	-
Euro 4	2005.01	1.0	0.10	-	0.08	-
† Values in brackets are conformity of production (COP) limits.						
a - until 1999.09.30 (after that date DI engines must meet the IDI limits)						

The ECE+EUDC test cycle is performed on a chassis dynamometer. The cycle—also known as the MVEG-A cycle—is used for emission certification of light duty vehicles in Europe (*EEC Directive 90/C81/01*).

The entire cycle includes four ECE segments, Figure 1, repeated without interruption, followed by one EUDC segment, Figure 2. Before the test, the vehicle is allowed to soak for at least 6 hours at a test temperature of 20-30°C. It is then started and allowed to idle for 40s.

Effective year 2000, that idling period has been eliminated, i.e., engine starts at 0s and the emission sampling begins at the same time. This modified cold-start procedure is sometimes referred to as the “new European driving cycle” or NEDC.

Emissions are sampled during the cycle according to the “Constant Volume Sampling” technique, analyzed, and expressed in g/km for each of the pollutants.

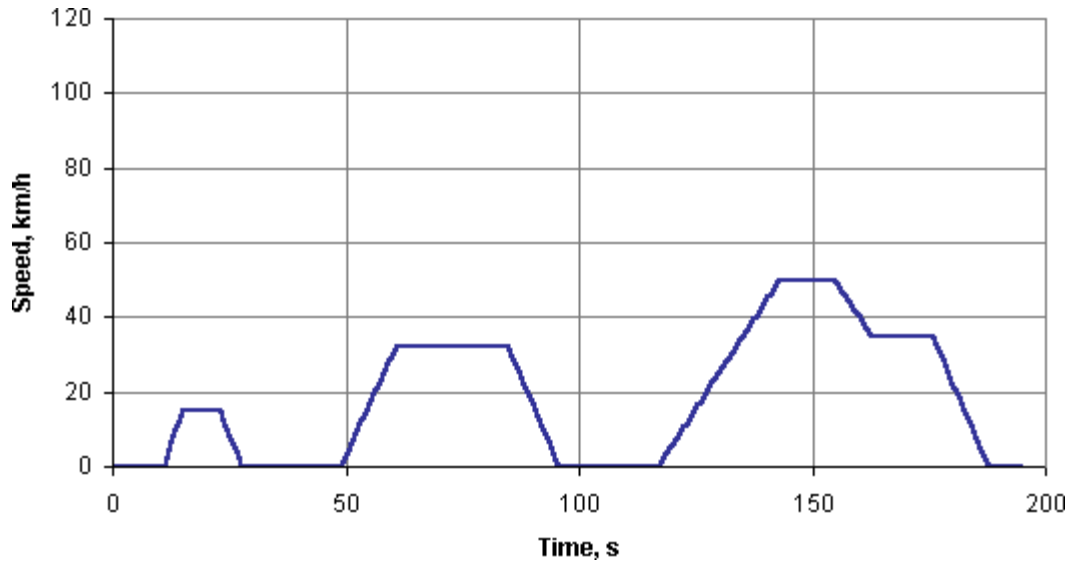


Figure 94 – ECE 15 cycle

The ECE cycle is an urban driving cycle, also known as UDC. It was devised to represent city driving conditions, e.g. in Paris or Rome. It is characterized by low vehicle speed, low engine load, and low exhaust gas temperature.

The above urban driving cycle represents Type I test, as defined by the original ECE 15 emissions procedure. Type II test is a warmed-up idle tailpipe CO test conducted immediately after the fourth cycle of the Type I test. Type III test is a two-mode (idle and 50 km/h) chassis dynamometer procedure for crankcase emission determination.

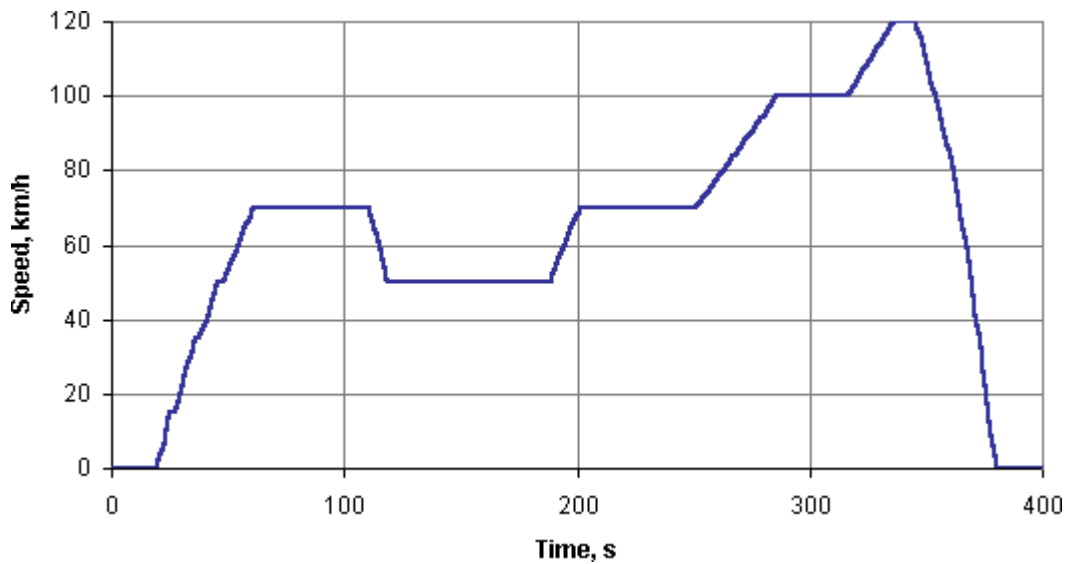


Figure 95 – EUDC Cycle

The EUDC (Extra Urban Driving Cycle) segment has been added after the fourth ECE cycle to account for more aggressive, high speed driving modes. The maximum speed of the EUDC cycle is 120 km/h. An alternative EUDC cycle for low-powered vehicles has been also defined with a maximum speed limited to 90 km/h (Figure 3).

Table 28 – Summary of the parameters for the ECE and EUDC cycles

Characteristics	Unit	ECE 15	EUDC
Distance	km	4×1.013=4.052	6.955
Duration	s	4×195=780	400
Average Speed	km/h	18.7 (with idling)	62.6
Maximum Speed	km/h	50	120

Japan

Table 29 – Japanese emission standards for diesel passenger cars [g/km]

Vehicle Weight	Date	Test	CO	HC	NOx	PM
			mean (max)	mean (max)	mean (max)	mean (max)
< 1250 kg*	1986	10-15 mode	2.1 (2.7)	0.40 (0.62)	0.70 (0.98)	
	1990		2.1 (2.7)	0.40 (0.62)	0.50 (0.72)	
	1994		2.1 (2.7)	0.40 (0.62)	0.50 (0.72)	0.20 (0.34)
	1997		2.1 (2.7)	0.40 (0.62)	0.40 (0.55)	0.08 (0.14)
	2002 ^a		0.63	0.12	0.28	0.052
	2005 ^b	New mode ^c	0.63	0.024 ^d	0.14	0.013
> 1250 kg*	1986	10-15 mode	2.1 (2.7)	0.40 (0.62)	0.90 (1.26)	
	1992		2.1 (2.7)	0.40 (0.62)	0.60 (0.84)	
	1994		2.1 (2.7)	0.40 (0.62)	0.60 (0.84)	0.20 (0.34)
	1998		2.1 (2.7)	0.40 (0.62)	0.40 (0.55)	0.08 (0.14)
	2002 ^a		0.63	0.12	0.30	0.056
	2005 ^b	New mode ^c	0.63	0.024 ^d	0.15	0.014

* - equivalent inertia weight (EIW); vehicle weight of 1265 kg
a - 2002.10 for domestic cars, 2004.09 for imports
b - full implementation by the end of 2005
c - full phase-in by 2011
d - non-methane hydrocarbons

The 10-15 mode cycle is currently used in Japan for emission certification and fuel economy for light duty vehicles. It is derived from the 10 mode cycle by adding another 15-mode segment of a maximum speed of 70 km/h. Emissions are expressed in g/km (*Japanese Industrial Safety and Health Association, JISHA 899, 1983*).

The entire cycle includes a sequence of a 15 minute warm-up at 60 km/h, idle test, 5 minute warm-up at 60 km/h, and one 15-mode segment, followed by three repetitions of 10-mode segments and one 15-mode segment. Emissions are measured over the last four segments (3×10-mode + 1×15-mode, Figure 1).

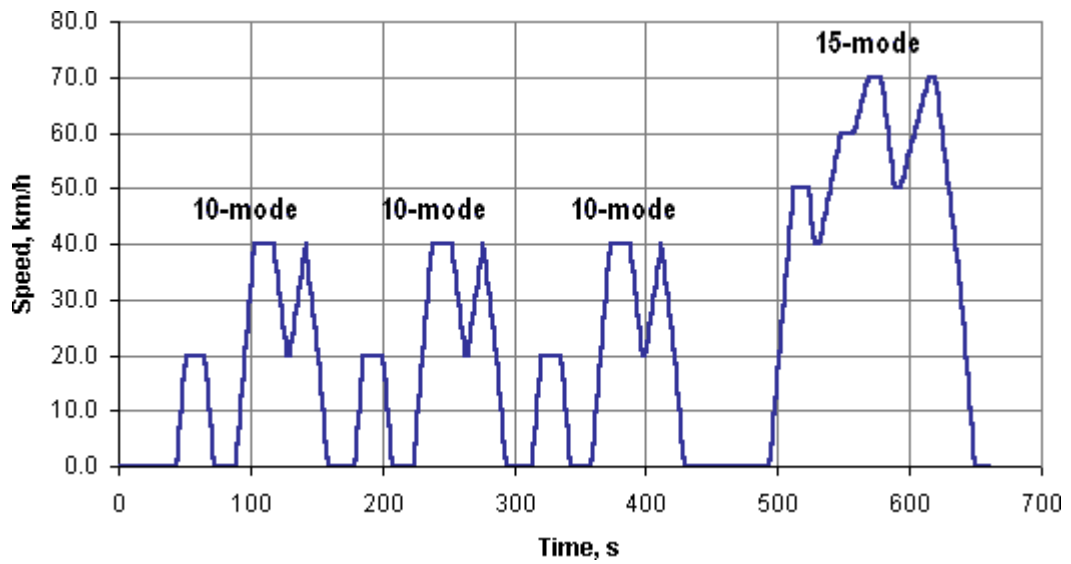


Figure 96 – 10-15 mode cycle

The distance of the cycle is 4.16 km, average speed 22.7 km/h, duration 660 s (or 6.34 km, 25.6 km/h, 892 s, respectively, including the initial 15 mode segment).

USA

Table 30 – EPA Tier 1 emission standards for passenger cars [g/miles]

Category	50,000 miles/5 years						100,000 miles/10 years ¹					
	THC	NMHC	CO	NO _x dies.	NO _x gas.	PM	THC	NMHC	CO	NO _x dies.	NO _x gas.	PM
Passenger cars	0.41	0.25	3.4	1.0	0.4	0.08	-	0.31	4.2	1.25	0.6	0.10
LLDT, LVW <3,750 lbs	-	0.25	3.4	1.0	0.4	0.08	0.80	0.31	4.2	1.25	0.6	0.10
LLDT, LVW >3,750 lbs	-	0.32	4.4	-	0.7	0.08	0.80	0.40	5.5	0.97	0.97	0.10
HLDT, ALVW <5,750 lbs	0.32	-	4.4	-	0.7	-	0.80	0.46	6.4	0.98	0.98	0.10
HLDT, ALVW >5,750 lbs	0.39	-	5.0	-	1.1	-	0.80	0.56	7.3	1.53	1.53	0.12

1 - Useful life 120,000 miles/11 years for all HLDT standards and for THC standards for LDT

Abbreviations:
 LVW - loaded vehicle weight (curb weight + 300 lbs)
 ALVW - adjusted LVW (the numerical average of the curb weight and the GVWR)
 LLDT - light light-duty truck (below 6,000 lbs GVWR)
 HLDT - heavy light-duty truck (above 6,000 lbs GVWR)

Table 31 – EPA Tier 2 emission standards [g/miles]

Bin#	50,000 miles					120,000 miles				
	NMOG	CO	NOx	PM	HCHO	NMOG	CO	NOx*	PM	HCHO
Temporary Bins										
MDPV ^c						0.280	7.3	0.9	0.12	0.032
10 ^{a,b,d,f}	0.125 (0.160)	3.4 (4.4)	0.4	-	0.015 (0.018)	0.156 (0.230)	4.2 (6.4)	0.6	0.08	0.018 (0.027)
9 ^{a,b,e}	0.075 (0.140)	3.4	0.2	-	0.015	0.090 (0.180)	4.2	0.3	0.06	0.018
Permanent Bins										
8 ^b	0.100 (0.125)	3.4	0.14	-	0.015	0.125 (0.156)	4.2	0.20	0.02	0.018
7	0.075	3.4	0.11	-	0.015	0.090	4.2	0.15	0.02	0.018
6	0.075	3.4	0.08	-	0.015	0.090	4.2	0.10	0.01	0.018
5	0.075	3.4	0.05	-	0.015	0.090	4.2	0.07	0.01	0.018
4	-	-	-	-	-	0.070	2.1	0.04	0.01	0.011
3	-	-	-	-	-	0.055	2.1	0.03	0.01	0.011
2	-	-	-	-	-	0.010	2.1	0.02	0.01	0.004
1	-	-	-	-	-	0.000	0.0	0.00	0.00	0.000
<p>* - average manufacturer fleet NOx standard is 0.07 g/mi</p> <p>a - Bin deleted at end of 2006 model year (2008 for HLDTs)</p> <p>b - The higher temporary NMOG, CO and HCHO values apply only to HLDTs and expire after 2008</p> <p>c - An additional temporary bin restricted to MDPVs, expires after model year 2008</p> <p>d - Optional temporary NMOG standard of 0.195 g/mi (50,000) and 0.280 g/mi (120,000) applies for qualifying LDT4s and MDPVs only</p> <p>e - Optional temporary NMOG standard of 0.100 g/mi (50,000) and 0.130 g/mi (120,000) applies for qualifying LDT2s only</p> <p>f - 50,000 mile standard optional for diesels certified to bin 10</p>										

The FTP-75 (Federal Test Procedure) has been used for emission certification of light duty vehicles in the U.S. Effective model year 2000, vehicles have to be additionally tested on two Supplemental Federal Test Procedures (SFTP) designed to address shortcomings with the FTP-75 in the representation of (1) aggressive, high speed driving, and (2) the use of air conditioning.

The FTP-75 cycle is derived from the FTP-72 cycle by adding a third phase of 505s, identical to the first phase of FTP-72 but with a hot start. The third phase starts after the engine is stopped for 10 minutes. Thus, the entire FTP-75 cycle consists of the following segments: cold start phase, transient phase, hot start phase.

Table 32 – Summary of the parameters for the FTP-75 cycle

Characteristics	Unit	FTP-75
Distance	km	11.04 miles (17.77 km)
Duration	s	1874 s
Average Speed	km/h	21.2 mph (34.1 km/h)

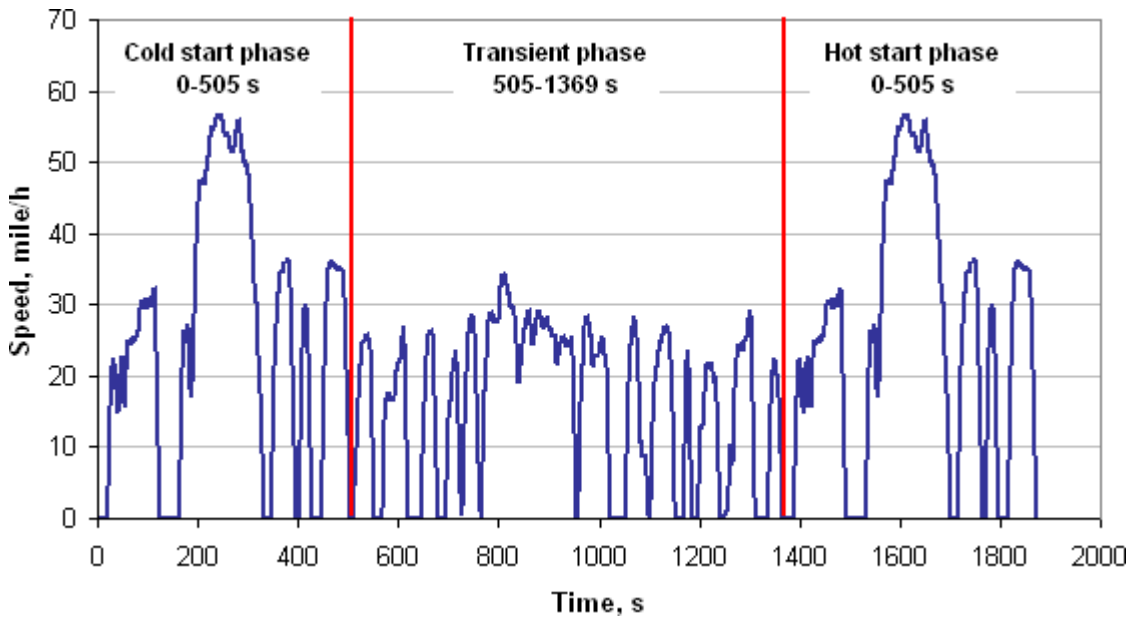


Figure 97 – FTP-75 cycle

The emissions from each phase are collected in a separate teflon bag, analyzed and expressed in g/mile (g/km). The weighting factors are 0.43 for the cold start, 1.0 for the transient phase and 0.57 for the hot start phase.

The FTP-75 cycle is known in Australia as the ADR 37 (Australian Design Rules) cycle.

APPENDIX C

Raw OH distributions

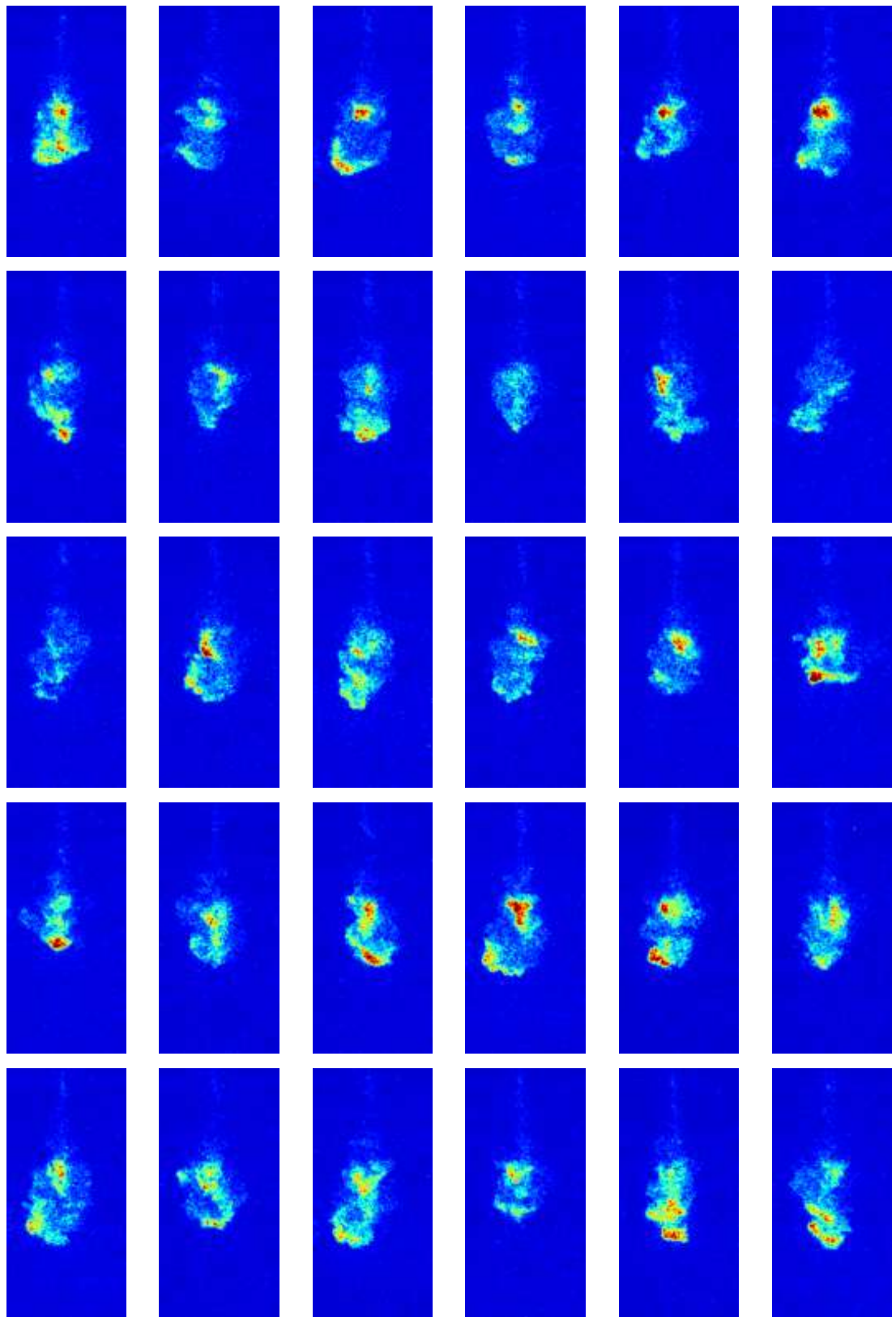


Figure 98 – Raw OH on-line distributions – 1.75 ms aSOI, initial development of the diffusion flame (injection of 30 mm³ of GE80 at 100 MPa in an in-cylinder pressure and temperature of 5 MPa and 700 K)

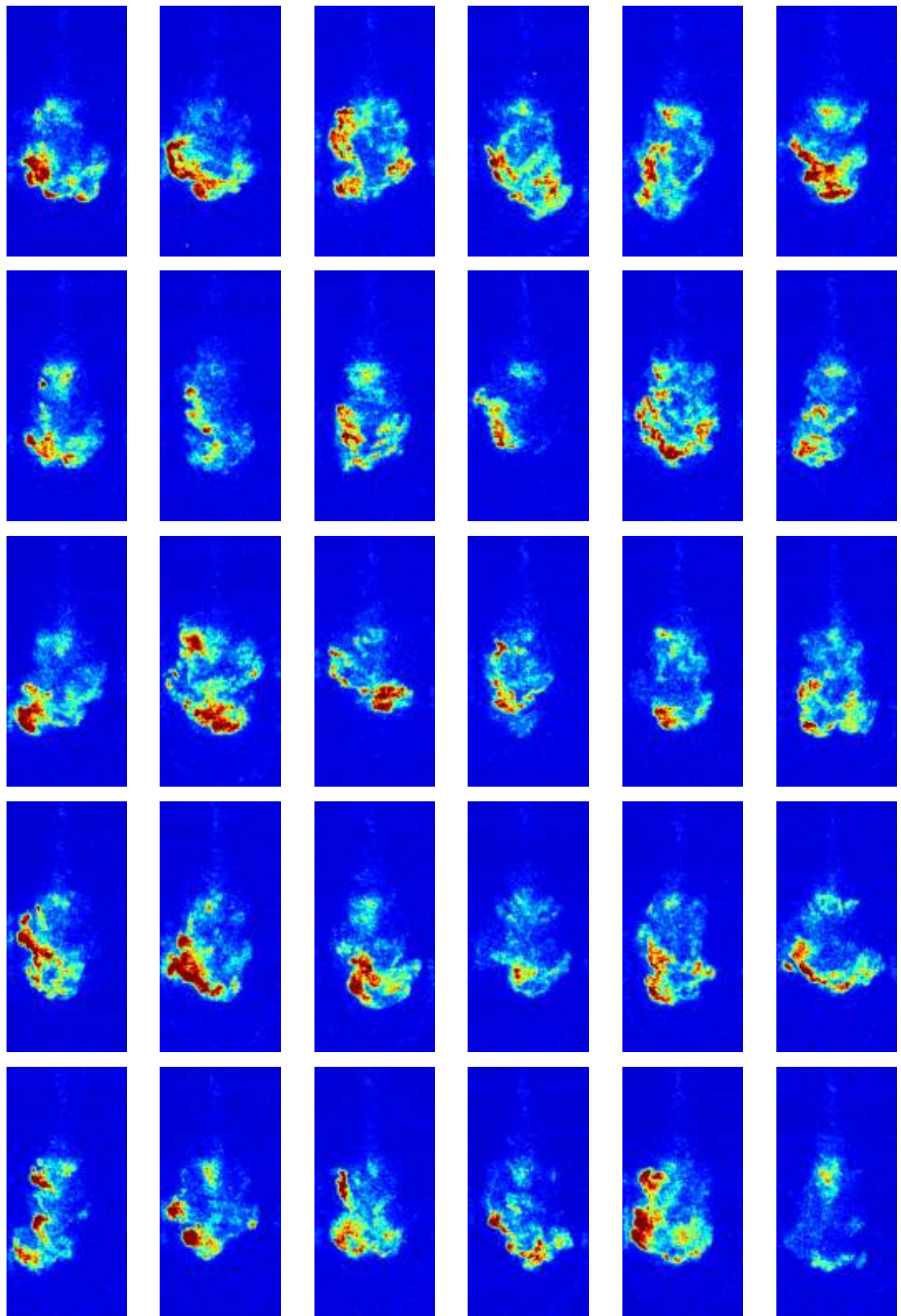


Figure 99 – Raw OH on-line distributions – 2 ms aSOI, initial development of the diffusion flame (injection of 30 mm³ of GE80 at 100 MPa in an in-cylinder pressure and temperature of 5 MPa and 700 K)

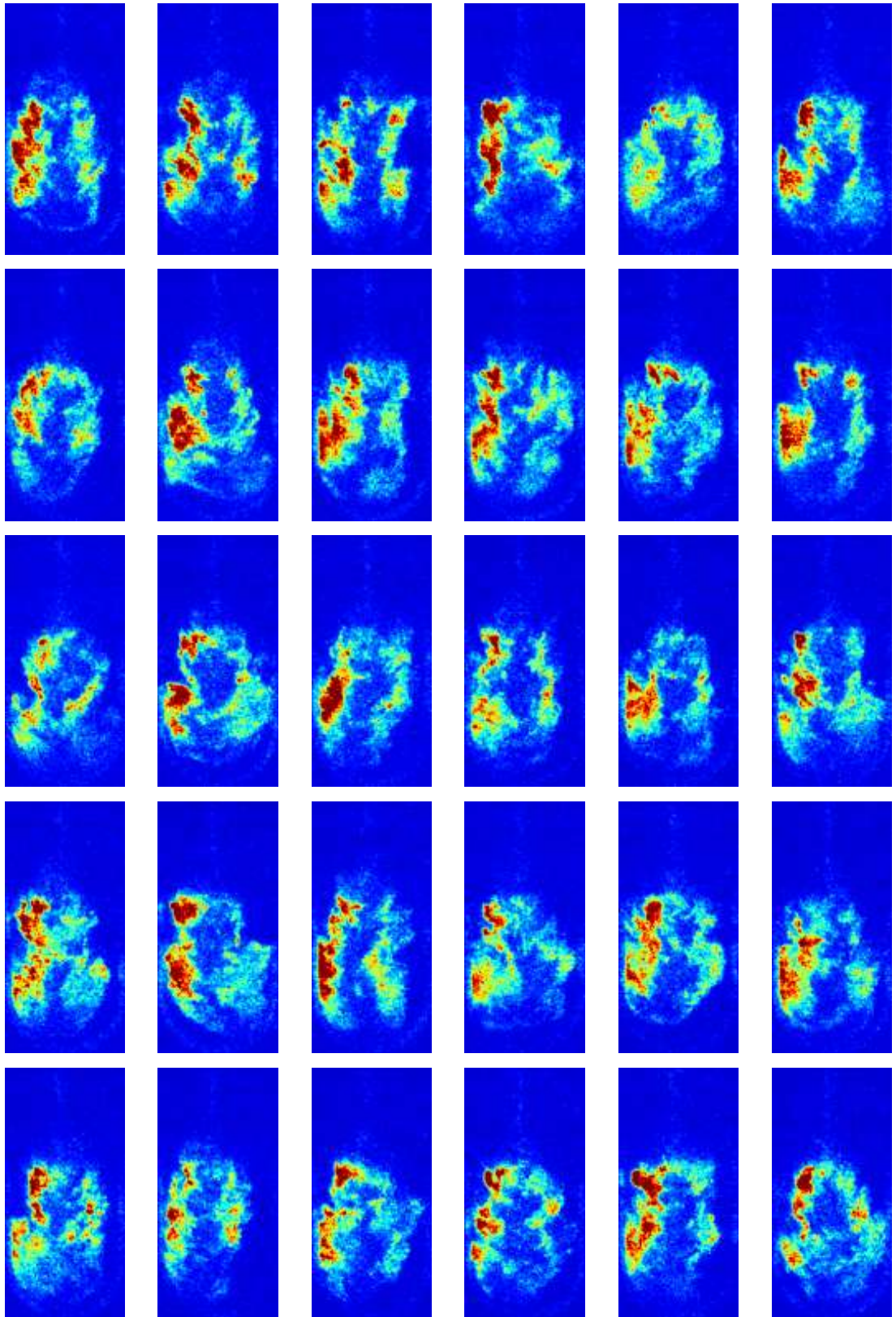


Figure 100 – Raw OH on-line distributions – 2.5 ms aSOI, static diffusion flame (injection of 30 mm³ of GE80 at 100 MPa in an in-cylinder pressure and temperature of 5 MPa and 700 K)

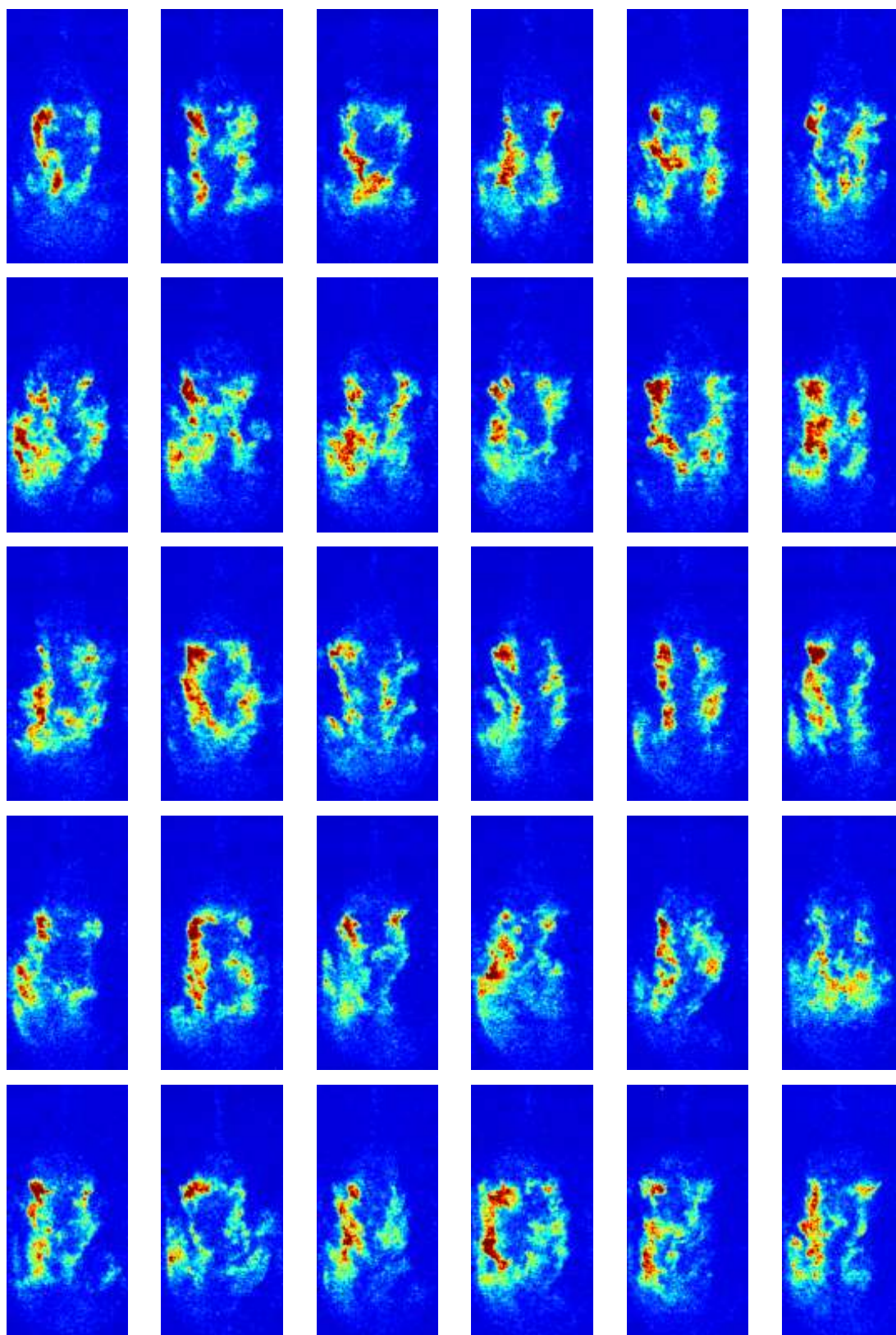


Figure 101 – Raw OH on-line distributions – 3.5 ms aSOI, flame collapse (injection of 30 mm³ of GE80 at 100 MPa in an in-cylinder pressure and temperature of 5 MPa and 700 K)

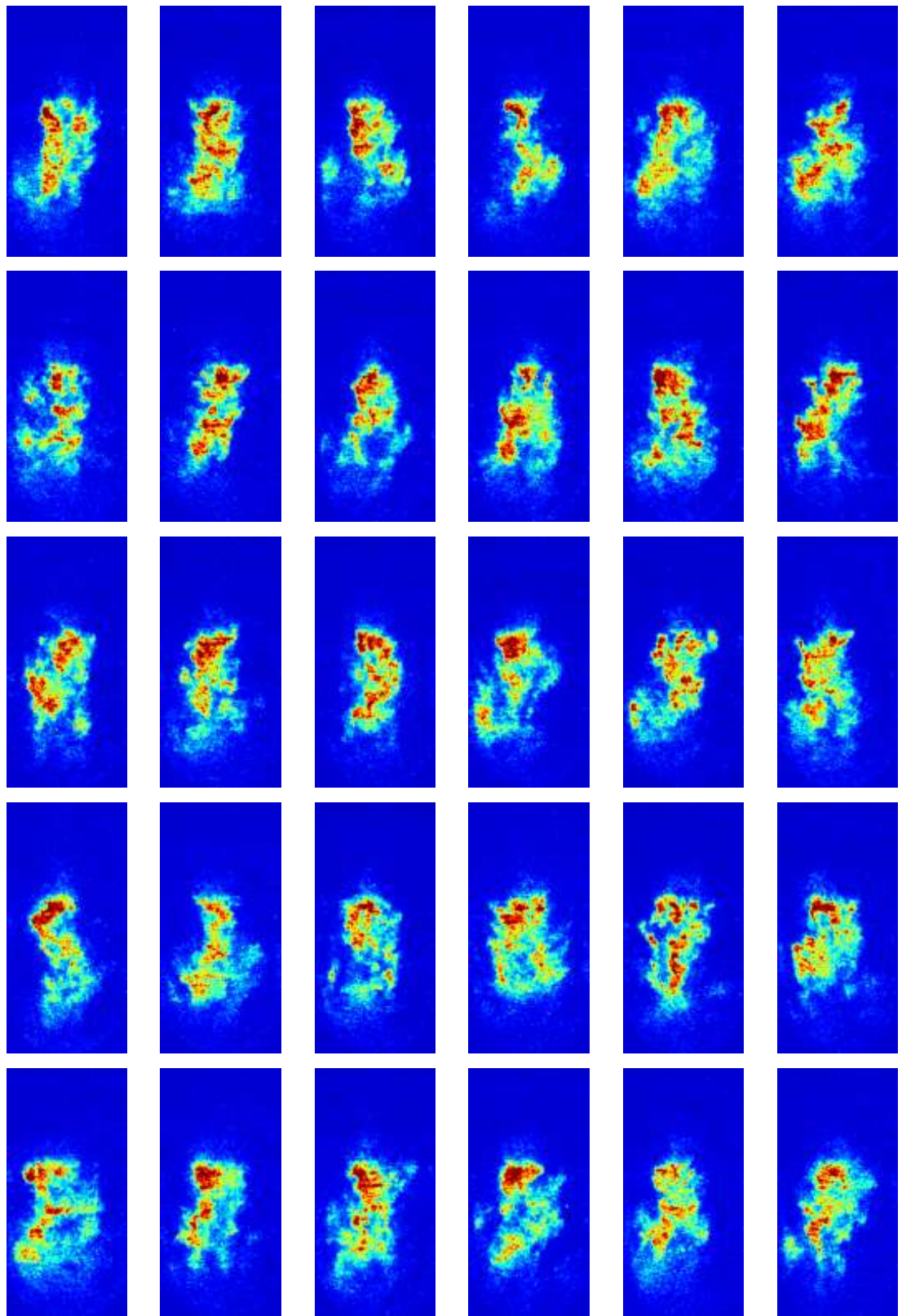


Figure 102 – Raw OH on-line distributions – 4.5 ms aSOI, flame collapse (injection of 30 mm³ of GE80 at 100 MPa in an in-cylinder pressure and temperature of 5 MPa and 700 K)

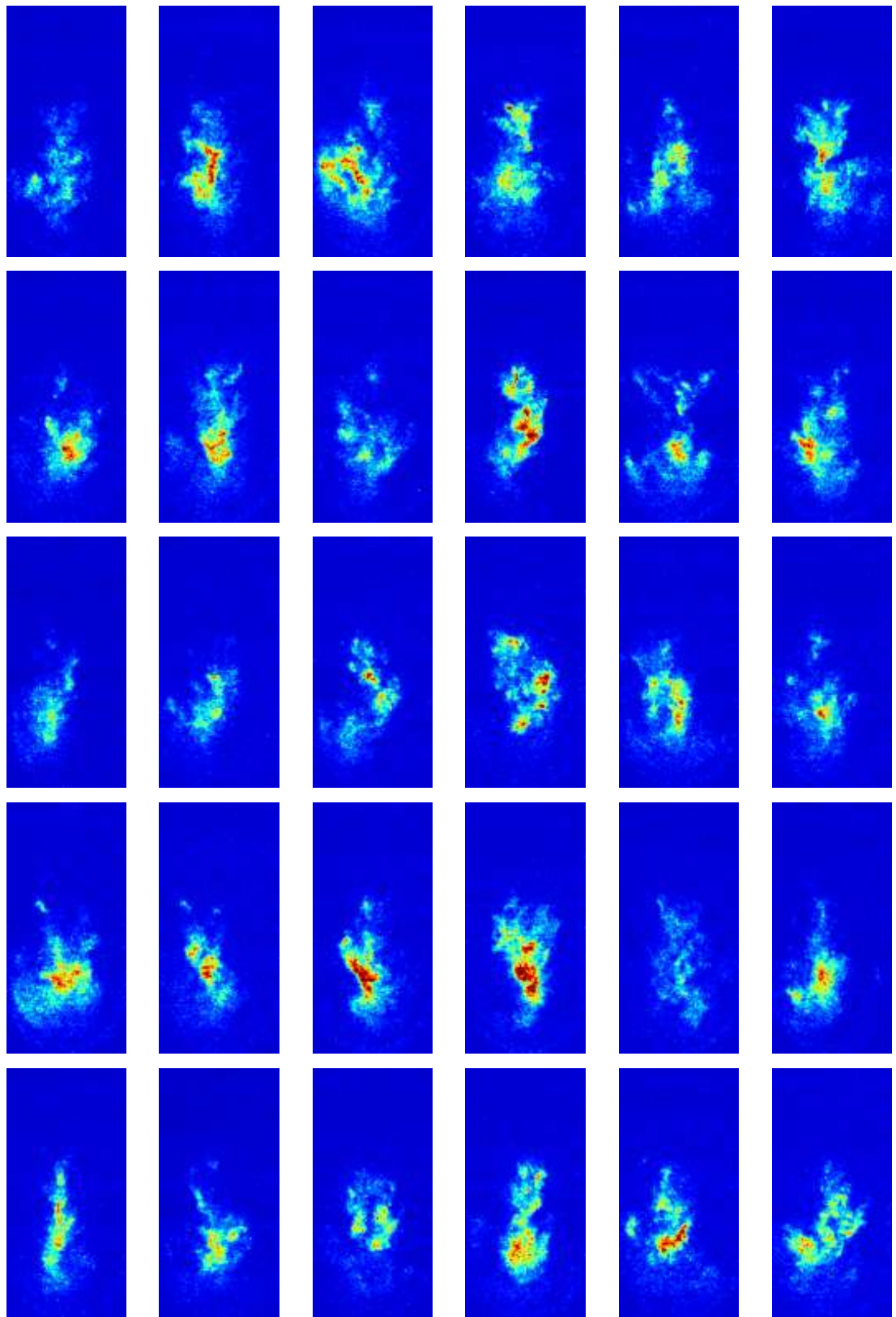


Figure 103 – Raw OH on-line distributions – 5 ms aSOI, flame collapse (injection of 30 mm³ of GE80 at 100 MPa in an in-cylinder pressure and temperature of 5 MPa and 700 K)